JSCSEN 76(6)805–946(2011)

International Year of CHEMISTRY 2011

Journal of the Serbian Chemical Society

Electronic Version

VOLUME 76

No 6

BELGRADE 2011

Available on line at

www.shd.org.rs/JSCS/

The full search of JSCS is available through

DOAJ DIRECTORY OF OPEN ACCESS JOURNALS

www.doaj.org

Journal of the Serbian Chemical Society
JSCS-info@shd.org.rs • www.shd.org.rs/JSCS

J. Serb. Chem. Soc. Vol. 76, No. 6 (2011)

CONTENTS

Published by the Serbian Chemical Society
Karnegijeva 4/III, 11000 Belgrade, Serbia
Printed by the Faculty of Technology and Metallurgy
Karnegijeva 4, P.O. Box 35-03, 11120 Belgrade, Serbia

Journal of the Serbian Chemical Society
JSCS-info@shd.org.rs • www.shd.org.rs/JSCS
J. Serb. Chem. Soc. 76 (6) 805–822 (2011)
JSCS–4161
UDC 537.3+532.14+544.6.076.2:519.87
Authors' review

AUTHORS' REVIEW

A mathematical model of the current density distribution in electrochemical cells

KONSTANTIN I. POPOV[1,2*#], PREDRAG M. ŽIVKOVIĆ[1] and NEBOJŠA D. NIKOLIĆ[2#]

[1]Faculty of Technology and Metallurgy, University of Belgrade, Karnegijeva 4, 11120 Belgrade and [2]ICTM – Institute of Electrochemistry, University of Belgrade, Njegoševa 12, Belgrade, Serbia

(Received 12 March 2010, revised 4 March 2011)

Abstract: An approach based on the equations of electrochemical kinetics for the estimation of the current density distribution in electrochemical cells is presented. This approach was employed for a theoretical explanation of the phenomena of the edge and corner effects. The effects of the geometry of the system, the kinetic parameters of the cathode reactions and the resistivity of the solution are also discussed. A procedure for a complete analysis of the current distribution in electrochemical cells is presented.

Keywords: current distribution; edge effect; corner effect.

CONTENTS

* Corresponding author. E-mail: kosta@tmf.bg.ac.rs
# Serbian Chemical Society member.
doi: 10.2298/JSC100312079P

1. BASIC FACTS

It is known that electrodeposited metals can have different morphologies at different positions of the electrode surface. This means that the local current density during electrodeposition of metals varies from point to point on the electrode surface. Even for a simple electrode configuration, the calculation of the current distribution in a classical manner is a complex problem, which becomes more complicate with an increasing complexity of the geometry, especially if the limiting diffusion current density varies over the electrode due to different geometric and hydrodynamic conditions.[1–4]

Recently, a method for the determination of the current density distribution based on a simple equation of the electrode kinetics was developed in a manner presented in the literature.[5–17] The aim of this work is to review them.

2. A STATEMENT OF THE PROBLEM

The current density distribution in electrochemical cells depends on:

a) the geometry of the system,

b) the conductivity of both the solution and the electrodes,

c) the polarization characteristics of electrodes and

d) the hydrodynamics of the system.

In this review, the effects of the geometry of the system, the conductivity of the solution and electrodes and the polarization characteristics of electrodes will be considered. It will be assumed that the diffusion layer thickness is the same over all electrode surfaces.

The simplest representation of an electrochemical cell is presented in Fig. 1.

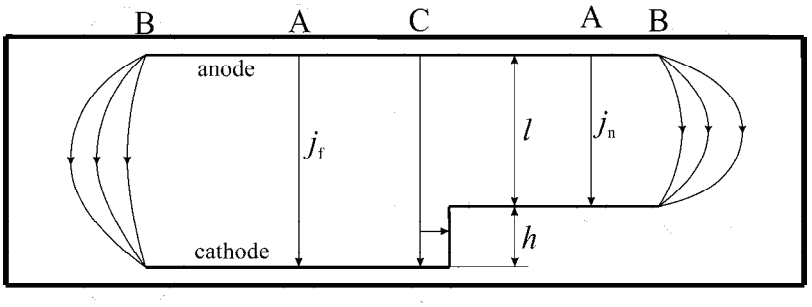

Fig. 1. Schematic representation of an electrochemical cell.

If electrodes are placed in the cell as shown in Fig. 1, three ways for the propagation of the current lines between the anode and cathode are possible.

I. there is only one current line between two symmetrically positioned points on the cathode and anode in the homogenous field (A in Fig. 1),

II. there are many current lines between two symmetrically positioned points at the edges of both the cathode and anode (B in Fig. 1),

III. there is a division of a current line into two parts at the corner of the cathode (C in Fig. 1).

All these cases will be treated separately.

3. THE CURRENT DENSITY DISTRIBUTION IN HOMOGENOUS FIELDS

The current density distribution between parts of the electrode surface with smaller and larger distance between cathode and anode can be calculated as follows.

The voltage, U, imposed on a cell shown in Fig. 1 is given by:

$$U - E = b_a \log \frac{j_f}{j_{0,a}} + b_c \log \frac{j_f}{j_{0,c}} \frac{j_L}{j_L - j_f} + \rho(l+h) j_f \quad (1)$$

as well as by:

$$U - E = b_a \log \frac{j_n}{j_{0,a}} + b_c \log \frac{j_n}{j_{0,c}} \frac{j_L}{j_L - j_n} + \rho l j_n \quad (2)$$

being valid within the Tafel region and at larger overpotentials, where E is a equilibrium potential difference, b_a and b_c and $j_{0,a}$ and $j_{0,c}$ are the anodic and cathodic Tafel slopes and exchange current densities, respectively, j_L is the limiting diffusion current density for the cathodic process, ρ is the specific ohmic resistivity of the solution and the current densities for the part of the cathode at larger, j_f and smaller, j_n distances from the anode, respectively. For soluble anode considered in this case, it will be $j_{0,a} = j_{0,c} = j_0$ and $E = 0$. In these calculations, absolute values of both the cathodic and anodic current densities, as well as the cathodic and anodic overpotentials are taken. The meanings of l and h are seen from Fig. 1. It is obvious from Eqs. (1) and (2) that:

$$j_n = j_f \quad (3)$$

if $\rho = 0$ and if the system is under complete diffusion control, *i.e.*, if

$$j_n = j_f = j_L \quad (4)$$

It follows from Eq. (3) that the dominant effect on current distribution is the effect of the resistivity of the solution.

On the other hand, if the electrochemical part of Eqs. (1) and (2) can be neglected relative to the ohmic voltage drop, complete ohmic control appears and the relation:

$$j_n = j_f \frac{l+h}{l} = j_f \left(1 + \frac{h}{l}\right) \quad (5)$$

is valid, corresponding to the primary current distribution.

An estimation of the effect of different parameters on the current density distribution can be made from Fig. 2, which shows the dependences of the current

densities at the closer, j_n, and further, j_f, part of the cathode from the anode on the cell voltage, U, for different solution resistivities.[13]

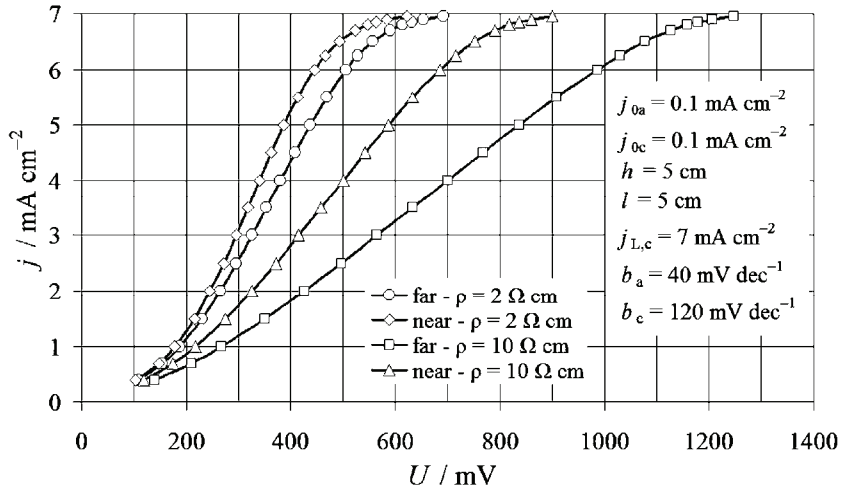

Fig. 2. The dependences of the current densities at parts of the cathode closer to and further from the anode on the cell voltage for different solution resistivities.

As can be seen, the larger is the conductivity of the electrolyte, the more uniform is the current density distribution. A similar but less pronounced effect of the increase of the cathodic Tafel slope can be seen, while the change of j_0 does not affect the current density distribution. It is necessary to note that a soluble anode is considered in this case and, hence, the anodic and cathodic exchange current densities are the same.[13]

Finally, the effect of the h/l ratio will be discussed. As expected, for $h/l \rightarrow 0$, the current density distribution approaches to a uniform one, while for $h/l >> 1$, it is similar to the primary current distribution. Based on the above results, it follows that the ohmic resistance of the solution is the most important parameter producing an effect on the current density distribution in electrochemical cells. If $h/l>>1$, the effect of the geometry of the system can also be important, but an auxiliary anode adjusted to the cathode shape should be used in this case, as illustrated in Fig. 3.

4. THE EDGE EFFECT

The current density distribution in a cell with plane parallel electrodes, with edges not touching the cell wall, is illustrated in Fig. 4.

It can be assumed that a homogenous electric field and, consequently, a uniform current distribution are present over the entire electrode surface up to the very edge of the electrode, where the current density increases abruptly. This problem has been studied in detail in numerous references[8–10,12,17] and a rela-

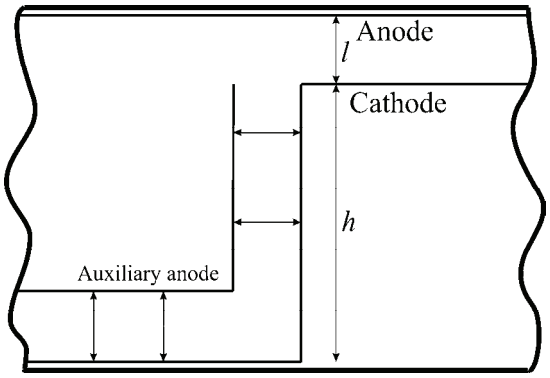

Fig. 3. The auxiliary anode adjusted to the cathode shape in order to improve the current density distribution.

tively rough approximation will be used here. There is only one current line between two symmetrically positioned points on the anode and cathode in a homogenous field, and current density in the homogenous field should be lower than current density at the edges.

There is an infinitely large number of the current lines between two symmetrically placed points at the edges of the electrodes. Hence, it can be taken that the overall resistance between these two points will be equal to an infinitely large number of resistances connected in parallel, being lower than in the homogeneous field. This approximation is more appropriate for the tip of a stationary wire electrode due to the dissipation occurring through the space in this case.[10] On the other hand, in the case of the edges of plane parallel electrodes, it occurs in one plane normal to the electrodes to which the two symmetrically positioned points belong.

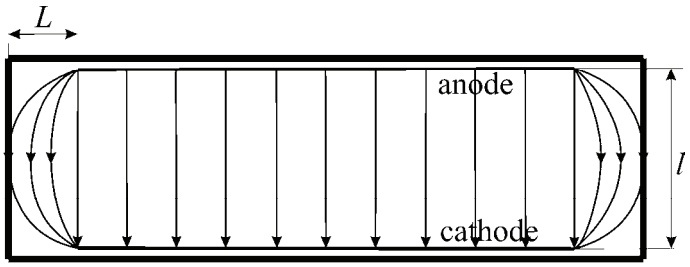

Fig. 4. The current density distribution in a cell with planparallel electrodes the edges of which edges do not touch the cell walls.

5. TWO EQUAL PLANE PARALLEL ELECTRODES ARRANGEMENT

The cell with two equal plane parallel electrodes represents the elementary cell of the electrode arrangement in electrochemical metal refining and winning processes.

It is a well-known fact that in a cell with parallel electrodes (if the electrode edges do not touch the side walls of the cell), the current density is higher at the

edges than at the centre of the electrode. This is because the current flow passes partially around the rectangular space between the electrodes. The increased current density at the edges of the electrodes can be easily noticed by observing the quality of the metal electrodeposit at the cathode. In some cases, the deposit in the central part of the cathode may be compact and flat, whereas the formation of dendrites is observed at the edges. The appearance of dendrites at the edges of cathodes in such situations is the most important problem of the current density distribution, because the growing dendrites could cause short circuits followed by a decrease in the current efficiency, or even damage to the power supply.

The aim of this section is to show in which way dendritic growth at the cathode edges can be avoided in electrowinning and refining processes.

5.1 Ohmic resistance of the cell

The current density distribution in a rectangular electrolytic cell in which parallel electrodes cover only part of the wall and the linear approximation of the current distribution are presented schematically in Fig. 5.

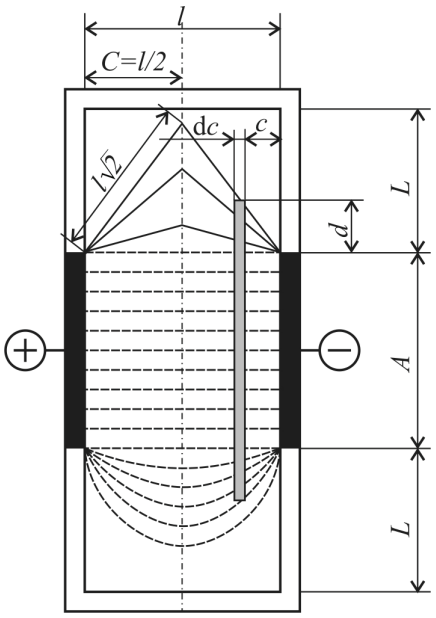

Fig. 5. Schematic presentation of the current distribution in a parallel plate electrode geometry and the linear approximation model showing the current flow passing the space between the plane parallel electrodes (*A* is the electrode width, *L* is the distance between the edge of the electrode and the side walls and *l* is the distance between the electrodes).[5,9]

The analysis performed here for the current distribution between the electrode edges and the cell side walls is obviously valid also for the situation in which there are gaps between the upper edges of the electrodes and the free surface of the solution and the lower edges to the bottom of the cell. In the case under consideration, these two distances are zero.

The resistance d*R* of a section of the electrolyte of thickness d*c* is given by:

$$dR = \frac{\rho}{B}\frac{dc}{A+2d} \tag{6}$$

where B is the height of the electrode and ρ is the specific resistance of the electrolyte. From the linear approximation, it follows:[5]

$$d = \frac{L}{C}c \tag{7}$$

The parameters d and c are indicated in Fig. 5.

The resistance of the whole electrolyte is then given by:[5]

$$R = \frac{\rho\, C}{BL}\ln\left(\frac{A+2L}{A}\right) \tag{8}$$

and for $L \to 0$, by:

$$\lim_{L\to 0} R = \frac{2\rho\, C}{BA} = \frac{\rho l}{BA} = R_h \tag{9}$$

where R_h corresponds to the resistance of a system with a homogeneous current density distribution (the side walls touch the edges of the electrodes). For $0 \le L << << \infty$, L can be related to A by a linear coefficient k as follows:

$$L = kA \tag{10}$$

which transforms Eq. (8) to:

$$R = \frac{R_h}{2k}\ln(1+2k) \tag{11}$$

and

$$l_{eff} = \frac{l}{2k}\ln(1+2k) \tag{12}$$

taking into account Eq. (9), where l_{eff} represents the interelectrode distance in a cell with L=0, the resistance of which is equal to the resistance of a cell in which the interelectrode distance is l and $L > 0$.

The good agreement between the experimental results and the values predicted by Eq. (11) extends to $k \approx 1$. It can be concluded that for this system, Eq. (11) is valid for $k < 1$. This means that the maximum penetration of the current lines occurs when $L = C = A$ in this case, and that the maximum length of the current line, l', is $l\sqrt{2}$.

5.2 The very edge ohmic resistance

This consideration of the very edge current density can be elaborated mathematically in the following way.[9] Assuming total ohmic control, the voltage drop in the solution between the electrodes inside the homogenous field is given by:

$$U - E = \rho l j \tag{13}$$

and outside of the homogeneous field by:

$$U - E = \rho l_i j_i \tag{14}$$

where U is the cell voltage, E is the equilibrium potential difference, ρ is the specific resistivity of the electrolyte, l the interelectrode distance, j is the current density, l_i is the length of the i-th current line and j_i is the current density corresponding to the i-th current line, as can be seen from Fig. 6.

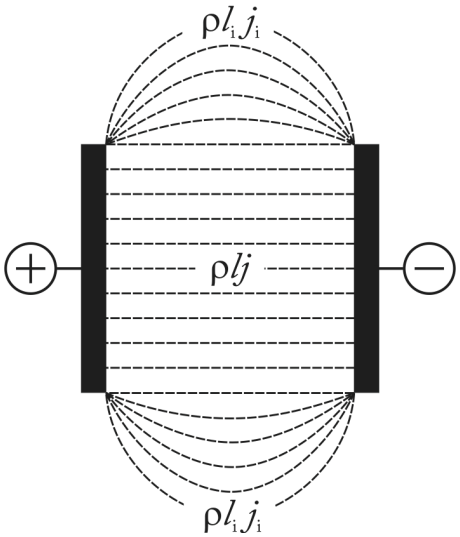

Fig. 6. Current lines between electrodes with edges not touching the side walls of the cell.[9]

The difference in the current lines outside of the homogeneous field is given by:

$$j_i + \Delta j_i - j_i = \frac{U - E}{\rho}\left(\frac{1}{l_i} - \frac{1}{l_i + \Delta l_i}\right) \tag{15}$$

or in the differential form:

$$\frac{\mathrm{d}\, j_i}{\mathrm{d}l_i} = \frac{U - E}{\rho}\frac{1}{l_i^2} \tag{16}$$

When Eq. (16) is integrated from the interelectrode distance l to the maximum length of the current line l', the maximum contribution to the edge current density j', due to current line propagation between the electrode edges and the side walls of the cell, is obtained:

$$j' = \frac{U - E}{\rho}\left(\frac{1}{l} - \frac{1}{l'}\right) = \frac{U - E}{\rho l}\frac{l' - l}{l'} \tag{17}$$

Taking into accounts Eq. (13), one obtains:

$$j' = j\frac{l'-l}{l'} \tag{18}$$

The edge current density, j_e, can be written as:

$$j_e = j + j' \tag{19}$$

The maximum value of j' is obtained from Eq. (18) as:

$$j'_{max} = j\frac{2-\sqrt{2}}{2} \tag{20}$$

Combining Eqs. (19) and (20), the maximum edge current density can be given as:[11]

$$j_{e,\,max} = \left(2-\frac{\sqrt{2}}{2}\right) j \approx 1.3\, j \tag{21}$$

for $l' = l\sqrt{2}$, as follows from Fig. 1.
This means that the very edge resistance is lower than that in the homogenous field and that the minimum effective interelectrode distance, $l_{eff,e,min}$ between the edges of the anode and cathode will be:

$$l_{eff,e,min} = \frac{2}{4-\sqrt{2}} l \tag{22}$$

because:

$$\rho l j = \rho\, l_{eff,e,min}\, j_{e,max} \tag{23}$$

5.3 The edge effect on the current density distribution

In a cell with parallel plate electrodes, if the electrode edges do not touch the cell side walls, the potential difference between two points in the homogenous field symmetrically positioned on the electrodes is given by:

$$U = E + \eta_a + \eta_c + \rho l j \tag{24}$$

Analogously, the cell voltage at the edges can be expressed as:

$$U = E + \eta_{a,e} + \eta_{c,e} + \rho l_{eff,e} j_e \tag{25}$$

where η_a and η_c are the anodic and cathodic overpotentials corresponding to the homogenous field, respectively, and $\eta_{a,e}$ and $\eta_{c,e}$ are the anodic and cathodic overpotentials corresponding to the edges, respectively.

Elimination of U from Eqs. (24) and (25) gives:

$$\eta_{a,e} + \eta_{c,e} = \eta_a + \eta_c + \rho l j - \rho l_{eff,e} j_e \tag{26}$$

In this case $\rho l j > \rho l_{eff,e} j_e$, because the increase of the current density also leads to the increase of the cathodic and anodic overpotentials.

In this way, a part of the ohmic potential drop in a homogenous field transforms into electrochemical overpotential for points at the plane electrode edges, or in a similar position, meaning the edge current density is larger than in the homogenous field. In this way it is possible to explain the change in the quality of the metal deposit near the edge and at the very edge of an electrode. It should be noted, however, that according to the proposed model, the entire edge current is located at the very edge of the electrode. In other words, a homogeneous electric field and, consequently, a uniform current distribution is assumed over the entire electrode surface up to the very edge of the electrode, where the current density increases abruptly, which is quite close to the real state described by other authors.[2,18]

5.4 The depth of the penetration of a current line between the electrode edges and the cell side walls

Equation (17) can be rewritten in the form:

$$l' = \frac{l}{1 - \frac{\rho l j'}{U - E}} \tag{27}$$

and if j' is replaced with $j(2-\sqrt{2})/2$, then l' becomes:

$$l' = \frac{l}{1 - \frac{\rho l j}{U - E}\frac{2-\sqrt{2}}{2}} \tag{28}$$

as the maximum length of a current line. ($U - E$) in Eqs. (27) and (28) is the ohmic potential drop, but it can be substituted by the cell potential due to the following facts.

The current along each line should be very low and because of this, the electrochemical overpotentials at the edges of electrodes due to one current line can be neglected relative to the ohmic potential drop. Hence, the cell potential transforms into the ohmic potential drop along each current line and ($U - E$) in Eq. (28) can be substituted by the cell potential from Eq. (24).

Substitution of ($U - E$) from Eq. (24) in Eq. (28) gives:

$$l' = \frac{l}{1 - \frac{\rho l j}{\eta_a + \eta_c + \rho l j}\frac{2-\sqrt{2}}{2}} \tag{29}$$

or after rearrangement:

$$l' = l\frac{\eta_a + \eta_c + \rho l j}{\eta_a + \eta_c + \frac{\sqrt{2}}{2}\rho l j} \tag{30}$$

Assuming a linear approximation of the propagation of a current line, the relation between L', the maximum depth of the propagation of a current line penetration into the space between the edges of the electrodes and the cell side walls, l and l', is given by:

$$L' = \frac{1}{2}\sqrt{l'^2 - l^2} \tag{31}$$

Substituting l' from Eq. (30) into Eq. (31) and rearranging gives:

$$L' = \frac{l}{2}\left[\left(\frac{\eta_a + \eta_c + \rho l j}{\eta_a + \eta_c + \frac{\sqrt{2}}{2}\rho l j}\right)^2 - 1\right]^{1/2} \tag{32}$$

It can be shown that if:

$$\eta_a + \eta_c >> \rho\, l j \tag{33}$$

then $l' \to l$ and $L' \to 0$ and, in the opposite case, $l' = l\sqrt{2}$ and $L' \to l/2$. This shows that the ability of an electrolyte to distribute the current density uniformly increases with decreasing ρlj product, *i.e.*, with decreasing ohmic polarization. Furthermore, it is to be expected that with a larger spacing (the distance between the polarization $j - U$ curves for $L = 0$ and $L > 0$), the current density distribution will become worse.

5.5 The dendritic growth initiation at the edges of the cathode

The equation for the polarization curve is given by:[17]

$$j = \frac{j_0 f_c}{1 + \frac{j_0 f_c}{j_L}} \tag{34}$$

for $f_c >> f_a$, where $f_c = 10^{\eta/b_c}$ and $f_a = 10^{-\eta/b_a}$. The critical overpotential for dendritic growth initiation, η_i, is given by:

$$\eta_i = \frac{b_c}{2.3} \ln \frac{j_L}{j_0} \tag{35}$$

Substitution of η_i from Eq. (35) into Eq. (34) and further rearranging gives:

$$j_i = \frac{1}{2} j_L \tag{36}$$

where j_i is the critical current density for dendritic growth initiation.

If $L > L'$, the edge current density could be obtained by combining Eqs. (18), (19) and (30) as:

$$j_e = j\frac{\eta_a + \eta_e + \left(2 - \frac{\sqrt{2}}{2}\right)\rho l j}{\eta_a + \eta_e + \rho l j} \tag{37}$$

Assuming that the maximum edge current density at which dendrites do not grow is given by Eq. (36), the maximum current density, j_{max}, in the homogeneous field at which dendrites at the edges do not grow is obtained after the substitution of j_e in Eq. (37) with j_i and after combination of Eqs. (36) and (37) as:

$$j_{max} = \frac{1}{2}\frac{\eta_a + \eta_e + \rho l j}{\eta_a + \eta_e + \left(2 - \frac{\sqrt{2}}{2}\right)\rho l j} j_L \tag{38}$$

It follows from Eq. (38) that $j_{max} \approx 0.5\, j_L$ for:

$$\eta_a + \eta_c >> \rho l j \tag{39}$$

and $j_{max} \approx 0.4 j_L$ for:

$$\eta_a + \eta_c << \rho l j \tag{40}$$

The maximum current density in both cases is larger than the current density corresponding to the end of the Tafel linearity, which is the optimum current density for the deposition of compact metal. Hence, if the deposition current density corresponds to the end of the Tafel linearity, dendrites will not grow at the edges of the electrode. It should be noted that in metal electrorefining, the working current density can be determined relative to the initial concentration of depositing ions, because it remains constant or increases during the refining process. In electrowinning processes, the working current density must be determined relative to the final concentration of depositing ions, because it is lower than initial one. The same reason is valid in the case of $L < L'$; meaning, in general, that if the current density in the cell is lower than $0.4 j_L$, dendrites and probably carrot-like protrusion on the electrode edges do not grow.

Equations (39) and (40) are in qualitative agreement with experimental findings, but this topic requires some additional, carefully performed investigations.

6. THE CORNER EFFECT

"Corner weakness" occurs in heavy deposits of electroformed metal at screened cathode parts, *i.e.*, corners. At these areas, the deposit is thinner and, in extreme cases, there is no deposition at all along the line of the corner bisector. A number of microphotographs of deposit cross-sections, illustrating the "corner weakness" effect can be found in the literature.[19,20] It can be seen that the cal-

culated deposit profile,[12] with a crack appearing along the corner bisector, looks very similar to that typically obtained in plating practice.[19,20] The consequence is the emergence of a fracture under negligible load along the line of the corner bisection, instead of a fracture at much higher loads across the narrowest cross-section of an electroformed deposit normal to the line of pull.

A theoretical analysis of this phenomenon has been reported using the following assumptions:

– the potential difference between each two points on the anode and cathode is equal to the cell voltage,

– the current lines are normal to the electrode surface,

– the corresponding ohmic resistance of a solution exists along each current line and the current lines are independent and insulated from each other,

– current lines in the vicinity of a protrusion divide into components which are normal to the electrode surface and

– the Kirchoff Laws are valid for current lines branching.

The current distribution in a cell with the electrode arrangement given in Fig. 1 near to an elevation at the cathode can be envisaged as shown in Fig. 7.

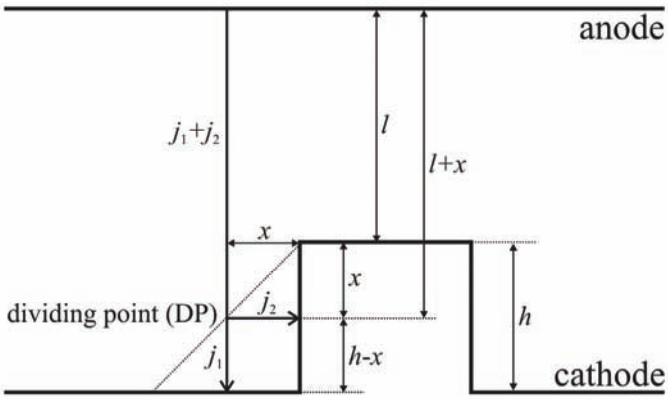

Fig. 7. The assumed model of the line division of the current at the corner on the cathode surface.[12]

According to the assumed model of current line division, it follows that there is no deposition along the line of bisection (Fig. 7). If division of current lines occurs along the line indicated by the dashed line, this is in perfect agreement with some earlier experimental findings.[12] It can be seen that this configuration provides the same density of current lines at the cathode as at the anode.

The overall current density along the current line from the anode to the dividing point (DP) is obviously the sum of the partial ones branching at the DP, *i.e.*, $(j_1 + j_2)$. For a cell with a soluble anode, following relations are valid:

$$U_{\text{cell}} = \frac{b_a}{2.3}\ln\frac{j_1+j_2}{j_0} + \rho(l+x)(j_1+j_2) + \frac{b_c}{2.3}\ln\frac{j_1 j_L}{j_0(j_L-j_1)} + \rho j_1(h-x) \quad (41)$$

$$U_{\text{cell}} = \frac{b_a}{2.3}\ln\frac{j_1+j_2}{j_0} + \rho(l+x)(j_1+j_2) + \frac{b_c}{2.3}\ln\frac{j_2 j_L}{j_0(j_L-j_2)} + \rho j_2 x \quad (42)$$

The proposed model implies that there is no current component in the direction of the corner vertex and the appearance of a crack along the corner bisector is expected.

A deposit cannot be obtained in the corner of the cathode directly but rather by the buildup of the deposit in the x and y direction. An overlap of the x and y oriented deposits should occur when current density virtually does not depend on the distance from the very corner.

However, if the current density decreases upon approaching the corner vertex, the deposits would not overlap and a flaw would be created.[12]

An improved procedure for the determination of j_1 and j_2 as compared to the one presented earlier[12] is presented here. It follows from Eqs. (41) and (42) that:

$$E_{\text{DPC}} = b_c \log\frac{j_1 j_L}{j_0(j_L-j_1)} + \rho j_1(l-x) \quad (43)$$

and

$$E_{\text{DPC}} = b_c \log\frac{j_2 j_L}{j_0(j_L-j_2)} + \rho j_2 x \quad (44)$$

E_{DPC} should be calculated using Eq. (43) for x = 0.1h, 0.5h and 0.9h and j_1 = = 1, 2, 3, 4, 5 and 6 mA/cm^2 and ρ = 5 Ω cm, j_0 = 0.1 mA cm^{-2}, l = 5 cm, h = 5 cm, j_L = 7 mA cm^{-2}, b_a = 40 mV dec^{-1} and b_c = 120 mV dec^{-1}. Then, j_2 can be calculated using Eq. (44) and U is obtained as:

$$U = b_a \log\frac{j_1+j_2}{j_0} + (l+x)(j_1+j_2) + E_{\text{DPC}} \quad (45)$$

The calculation should be performed for each x and the obtained values plotted as shown in Figs. 8–10. Taking the calculated values of the current densities, it is possible to visualize the current density distribution in the electrochemical cell schematically presented in Fig. 11. Taking that j_f corresponds to a distance of 1 cm, the j_n, j_f, j_1 and j_2 values for each x can be calculated and the current density distribution can be presented as in Fig. 11 for different values of U, being in agreement with experimental data.[19,20]

The current density distribution effect is of a high technological significance for the creation of open porous metal structures, denoted as honeycomb-like ones,

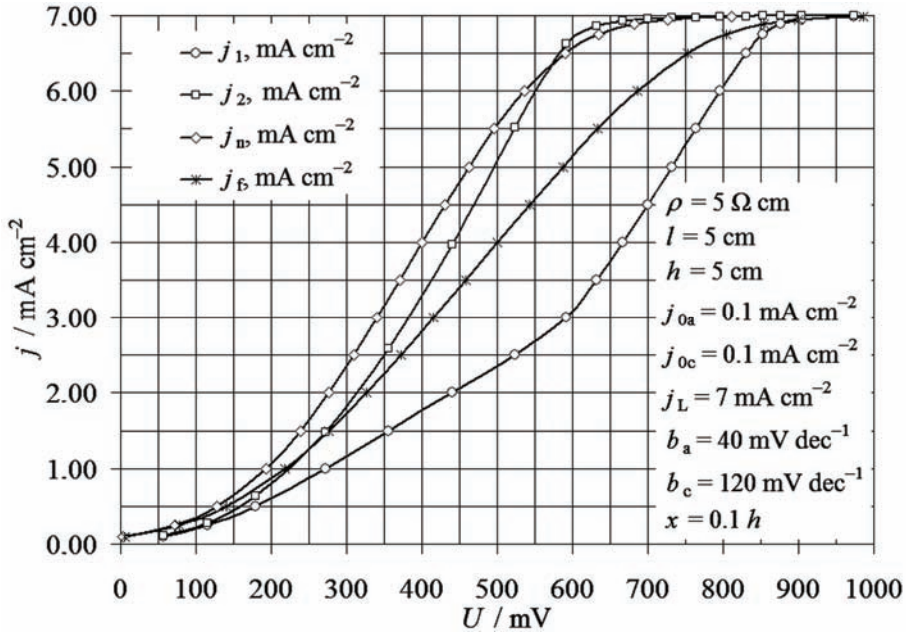

Fig. 8. The dependences of the current densities at the near and at far parts of an electrode on the cell voltage, as well as the j_1 and j_2 for $x = 0.1$.

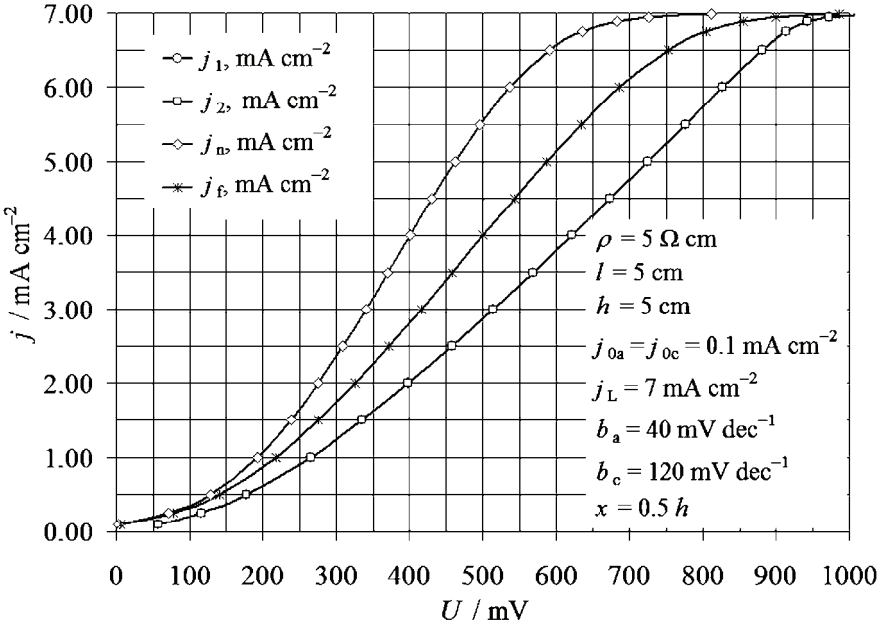

Fig. 9. The dependences of the current densities at the near and at far parts of an electrode on the cell voltage, as well as the j_1 and j_2 for $x = 0.5$.

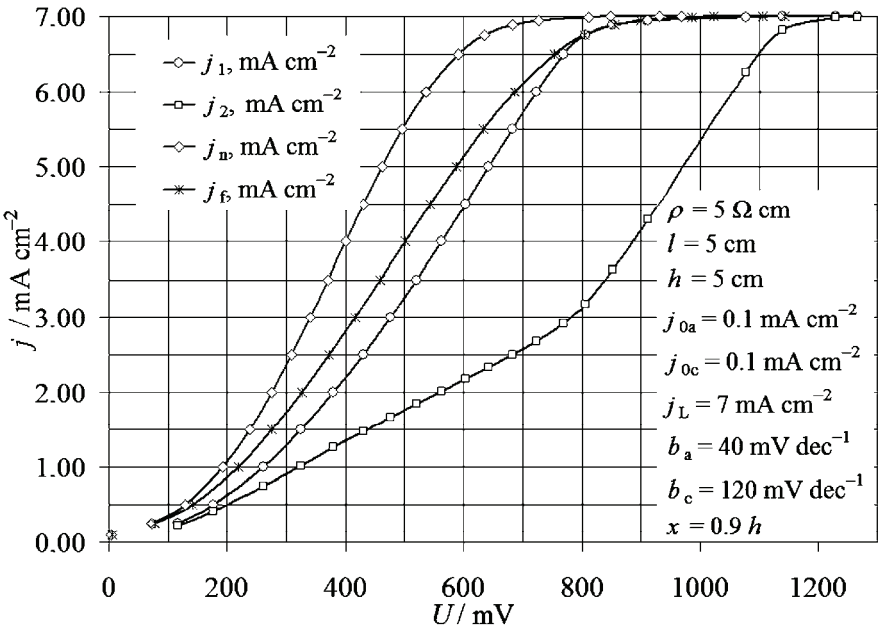

Fig. 10. The dependences of the current densities at the near and at far part of an electrode on the cell voltage, as well as the j_1 and j_2 for $x = 0.9$.

which are ideally suited for electrodes in many electrochemical devices, such as fuel cells, sensors and batteries.[21] Copper structures of this type are formed from acid sulfate solutions of different $CuSO_4$ and H_2SO_4 concentrations,[22] characterized by different values of the exchange current density, j_0.[23] Due to the effect of the current density distribution effect, improvement of the micro- and nanostructural characteristics of the honeycomb-like structures can be attained by application of periodically changing regimes of electrolysis, such as the pulsating overpotential (PO) regime.[24]

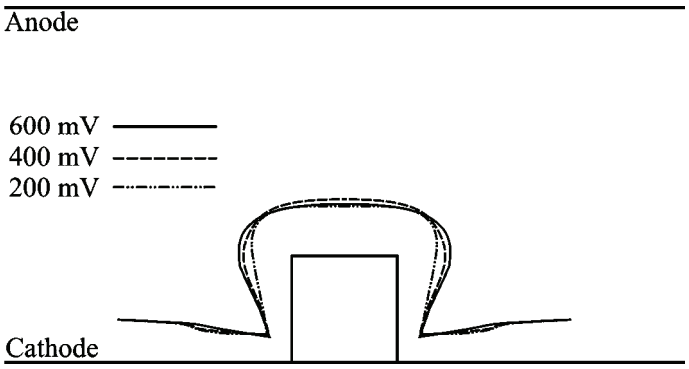

Fig. 11. Visualization of current density distribution for $U = 200$, 400 and 600 mV.

7. CONCLUSIONS

A concise review of earlier results and an improved method for the estimation of the current density distribution in electrochemical cells is presented. The method is based on the simple equations of electrode kinetics and the physical essence of the phenomena is clearly demonstrated.

Acknowledgments. The work was supported by the Ministry of Education and Science of the Republic of Serbia under the research project: "Electrochemical synthesis and characterization of nanostructured functional materials for application in new technologies" (No. 172046).

И З В О Д

МАТЕМАТИЧКИ МОДЕЛ РАСПОДЕЛЕ ГУСТИНЕ СТРУЈЕ У ЕЛЕКТРОХЕМИЈСКИМ ЋЕЛИЈАМА

КОНСТАНТИН И. ПОПОВ[1,2], ПРЕДРАГ М. ЖИВКОВИЋ[1] и НЕБОЈША Д. НИКОЛИЋ[2]

[1]*Технолошко–металуршки факултет, Универзитет у Београду, Карнегијева 4, 11 000 Београд и*
[2]*ИХТМ – Центар за електрохемију, Универзитет у Београду, Његошева 12, 11 000 Београд*

Приказан је сажети преглед ранијих резултата и представљен је побољшан приступ процени расподеле струје у електрохемијским ћелијама. Овај приступ, заснован на једначинама електрохемијске кинетике, употребљен је за теоријско објашњење ивичних и угаоних ефеката. Такође су дискутовани утицаји геометрије система, кинетичких параметара катодних реакција и отпорности раствора. Представљена је процедура за комплетну анализу расподеле струје у електрохемијским ћелијама.

(Примљено 12. марта 2010, ревидирано 4. марта 2011)

REFERENCES

1. C. Wagner, *J. Electrochem. Soc.* **98** (1951) 116
2. N. Ibl, *Oberfläche - Surface* **16** (1975) 23
3. N. Ibl, *Current distribution* in *Comprehensive Treatise of Electrochemistry*, Vol. 6, E. E. Jeager, J. O' M. Bockris, B. E. Conway, S. Sarangapani, Eds., Plenum Press, New York, NY, 1983
4. U. Landau, *Current Distribution in Electrochemical Cells: Analytical and Numerical Modeling, in Modern Aspects of Electrochemistry: Modelling and Numerical Simulations II*, M. Schlesinger, Ed., Springer Science+Business Media LLC, 2009, p.p. 451–501.
5. K. I. Popov, M. D. Maksimović, D. Ć. Totovski, V. N. Nakić, *Surf. Technol.* **19** (1983) 173
6. K. I. Popov, N. V. Krstajić, S. R. Popov, *Surf. Technol.* **22** (1984) 245
7. K. I. Popov, Z. P. Rodaljević, N. V. Krstajić, S. D. Novaković, *Surf. Technol.* **25** (1985) 217
8. K. I. Popov, S. K. Zečević, S. M. Pešić, *J. Serb. Chem. Soc.* **60** (1995) 307
9. K. I. Popov, S. K. Zečević, S. M. Pešić, *J. Serb. Chem. Soc.* **61** (1996) 583
10. K. I. Popov, M. G. Pavlović, E. R. Stojilković, Z. Ž. Stevanović, *Hydrometallurgy* **46** (1997) 321
11. K. I. Popov, S. M. Pešić, T. M. Kostić, *J. Serb. Chem. Soc.* **64** (1999) 795
12. K. I. Popov, R. M. Stevanović, *J. Serb. Chem. Soc.* **65** (2000) 905
13. K. I. Popov, R. M. Stevanović, P. M. Živković, *J. Serb. Chem. Soc.* **66** (2001) 131
14. K. I. Popov, S. M. Pešić, P. M. Živković, *J. Serb. Chem. Soc.* **66** (2001) 491

15. K. I. Popov, S. M. Pešić, P. M. Živković, *J. Serb. Chem. Soc.* **67** (2002) 273
16. K. I. Popov, S. M. Pešić, P. M. Živković, *J. Serb. Chem. Soc.* **70** (2005) 251
17. K. I. Popov, S. S. Djokić, B. N. Grgur, *Fundamental Aspects of Electrometallurgy*, Kluwer Academic/Plenum Publishers, New York, 2002, pp. 101–143
18. J. S. Newman, *Electrochemical Systems*, Prentice-Hall, Inc., Englewood Cliffs, NJ, USA, 1973, p 177
19. P. Spiro, *Electroforming*, Robert Drapper, Teddington, UK, 1968, p. 62
20. G. A. Sadakov, *Galvanoplastika*, Mashinostroienie, Moscow, 1987, p. 17
21. H.–C. Shin, J. Dong, M. Liu, *Adv. Mater.* **15** (2003) 1610
22. N. D. Nikolić, Lj. J. Pavlović, G. Branković, M. G. Pavlović, K. I. Popov, *J. Serb. Chem. Soc.* **73** (2008) 753
23. P. M. Živković, N. D. Nikolić, M. Gvozdenović, K. I. Popov, *J. Serb. Chem. Soc.* **74** (2009) 291
24. N. D. Nikolić, V. Maksimović, M. G. Pavlović, K. I. Popov, *J. Serb. Chem. Soc.* **74** (2009) 689.

Journal of the Serbian Chemical Society
JSCS-info@shd.org.rs • www.shd.org.rs/JSCS
J. Serb. Chem. Soc. 76 (6) 823–830 (2011)
JSCS–4162
UDC 547.831+547.592+547.447:542.913
Original scientific paper

An efficient, microwave-assisted, one-pot synthesis of novel 5,6,7,8-tetrahydroquinoline-3-carbonitriles

DIPTI K. DODIYA*, HARESH K. RAM, AMIT R. TRIVEDI and VIRESH H. SHAH

Department of Chemistry, Saurashtra University, Rajkot-360 005, Gujarat, India

(Received 2 July 2010, revised 9 January 2011)

Abstract: An efficient, microwave-assisted synthesis of novel 2-alkoxy-5,6,7,8--tetrahydroquinoline-3-carbonitriles, which have not hitherto been reported, *via* reactions of cyclohexanone and arylidene malononitriles in the corresponding alcohols in presence of sodium is described. All the newly synthesized compounds were characterized by the IR, ^{1}H-NMR, ^{13}C-NMR and mass spectrescopic techniques and by elemental analyses. The newly synthesized compounds were evaluated for their antibacterial and antifungal activities.

Keywords: 2-alkoxytetrahydroquinoline-3-carbonitriles; quinoline-3-carbonitriles; one-pot synthesis; microwave-assisted synthesis; cyclohexanone; arylidene malononitriles.

INTRODUCTION

As a privileged fragment, quinoline is a ubiquitous subunit in many quinoline-containing natural products with remarkable biological activities. Members of this family have wide applications in medicinal chemistry, being used as antimalarial, anti-inflammatory, antiasthmatic, antibacterial, antihypertensive and tyrosine kinase inhibiting agents.[1] Because of their importance as substructures in a broad range of natural and designed products, significant efforts continue to be directed into the development of new quinoline-based structures.[2]

Among quinoline derivatives, tetrahydroquinolines are an important structural subunit of natural products and many tetrahydroquinoline derivatives exhibit interesting biological and pharmaceutical activities,[3] including anti-HIV,[4,5] anticancer,[6] antimalarial,[7] cholesteryl ester transfer protein inhibitors,[8] anti-diabetic,[9] *etc*. Consequently, synthetic methodologies for preparing tetrahydroquinoline derivatives have attracted considerable interest and several methods offering good results have been reported. However, most of them describe the synthesis of

* Corresponding author. E-mail: diptid85@gmail.com
doi: 10.2298/JSC100702071D

the 1,2,3,4-tetrahydroquinoline nucleus,[10–12] and concise methods to access usefully functionalized 5,6,7,8-tetrahydroquinolines are scarce in the literature.[13]

Recently, 5,6,7,8-tetrahydroquinolines have drawn considerable attention due to their interesting pharmacological applications as RET tyrosine kinase inhibitors,[14] anti-HIV,[15,16] anti-fungal,[17] anti-cancer[18] and C5a receptor antagonists agents.[19] The development of simple synthetic routes for widely used organic compounds from readily available reagents is one of the major tasks in organic synthesis. Application of microwave irradiation in achieving this task has been the focus of considerable attention in recent years and is becoming an increasingly popular technology.[20,21]

In view of these observations and as part of a continuing effort in our laboratory towards the development of new methods for the expeditious synthesis of biologically relevant heterocyclic compounds,[22] herein, a simple and efficient microwave-assisted synthesis of functionalized novel 2-alkoxy-5,6,7,8-tetrahydroquinoline-3-carbonitriles, which are also structurally relevant to recently reported bioactive 5,6,7,8-tetrahydroquinolines,[16–19] is described (Fig. 1).

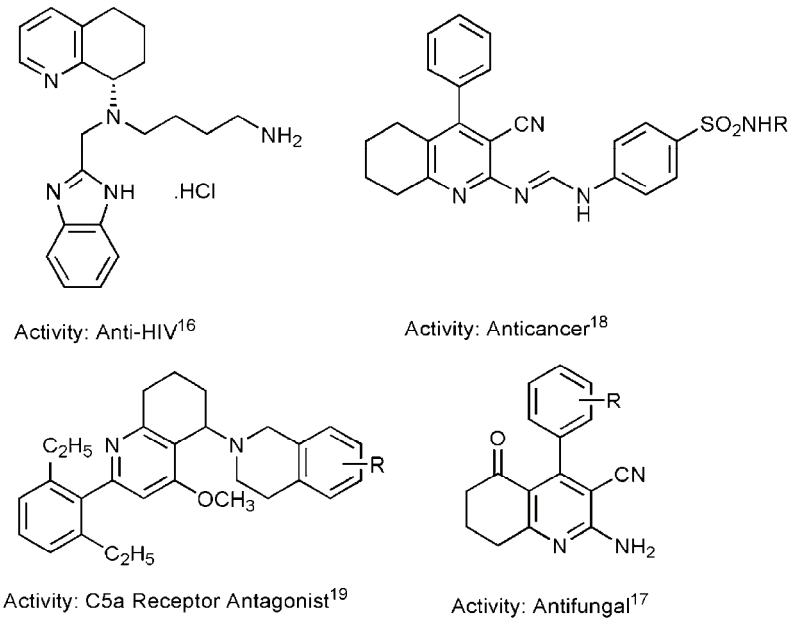

Fig. 1. Examples of some bioactive 5,6,7,8-tetrahydroquinolines structurally relevant to the synthesized 5,6,7,8-tetrahydroquinoline-3-carbonitriles.

All the newly synthesized compounds **3a**–**j** were evaluated for their antibacterial and antifungal activity. The biological activity of the synthesized compounds was compared with reference standard drugs.

RESULTS AND DISCUSSION

Chemistry

There are very few reports in literature for the synthesis of 2-alkoxypyridine--3-carbonitriles,[23,24] but most of them do not describe the synthesis of fused pyridines or benzo-fused pyridines, *i.e.*, quinolines. During an extensive literature survey, only one such synthesis of benzothiepino-fused 2-alkoxy-pyridine-3-carbonitriles was found.[25] Herein, the efficient and rapid microwave-assisted one--pot synthesis of functionalized novel 2-alkoxy-5,6,7,8-tetrahydroquinoline-3--carbonitriles, which have not hitherto been reported, *via* the reactions of cyclohexanone, arylidene malononitriles in the corresponding alcohol in the presence of sodium is reported.

The arylidene malononitriles **2** were prepared following a reported literature procedure.[26] Treatment of cyclohexanone **1** with arylidene malononitriles **2** in the corresponding alcohol in the presence of sodium under microwave irradiation at 300 W afforded the 2-alkoxy-5,6,7,8-tetrahydroquinoline-3-carbonitriles **3a**–**j** in excellent yields (88–95 %) in a very short time (Scheme 1) as compared to conventional heating, which results in lower yields after longer reaction times (5––10 h).

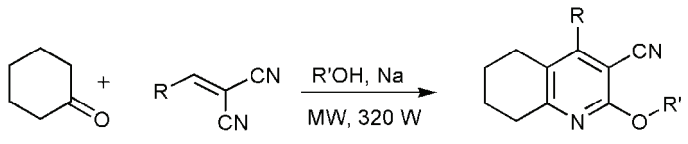

1 2 3

3a R= phenyl,
3b R= 4-chlorophenyl,
3c R= 4-fluorophenyl,
3d R= 4-methoxyphenyl,
3e R= 4-hydroxyphenyl
3f R= phenyl,
3g R= 4-chlorophenyl,
3h R= 4-fluorophenyl,
3i R= 4-methoxyphenyl
3j R= 4-hydroxyphenyl

3a-e R' = methyl,
3f-j R' = ethyl

Scheme 1. Microwave-assisted synthesis of 2-alkoxy-5,6,7,8--tetrahydroquinoline-3-carbonitriles.

The proposed mechanism[27] involves Michael addition between **1** and **2** to generate intermediate **A**, followed by nucleophilic alkoxide attack at one of the nitrile groups of **A** with dehydration and subsequent dehydrogenation to give the tetrahydroquinoline **3** (Scheme 2).

All the newly synthesized 2-methoxy- and 2-ethoxy-5,6,7,8-tetrahydroquinolines **3a–j** were characterized by IR, ^{1}H-NMR, ^{13}C-NMR, mass spectroscopy

and elemental analyses (Supplementary material). The IR spectra of **3a–j** revealed the appearance of confirmatory bands characteristics of the stretching vibrations of the –CN and C=N groups at 2231–2225 cm^{-1} and 1635–1566 cm^{-1}, respectively. Furthermore, asymmetric and symmetric stretching vibration bands of the ether (C–O–C) linkage were also present in the IR spectra in the range of 1296–1263 cm^{-1} and 1097–1018 cm^{-1}, respectively, which confirmed the presence of 2-alkoxy groups. The ^{1}H-NMR spectra of compounds **3a–e** showed confirmatory signals in the δ range 3.75–3.80 ppm as a singlet for ($-OCH_3$), while the ^{1}H-NMR spectra of compounds **3f–j** revealed signals at δ 1.27–1.44 ppm as a triplet for the ($-CH_2-C\mathbf{H}_3$) and signals at δ 4.15–4.51 ppm as a quartet for ($-C\mathbf{H}_2-CH_3$) of the 2-ethoxy group in the title compounds, which confirmed the structure. The ^{13}C-NMR signals were also found to be in full agreement with the proposed structure.

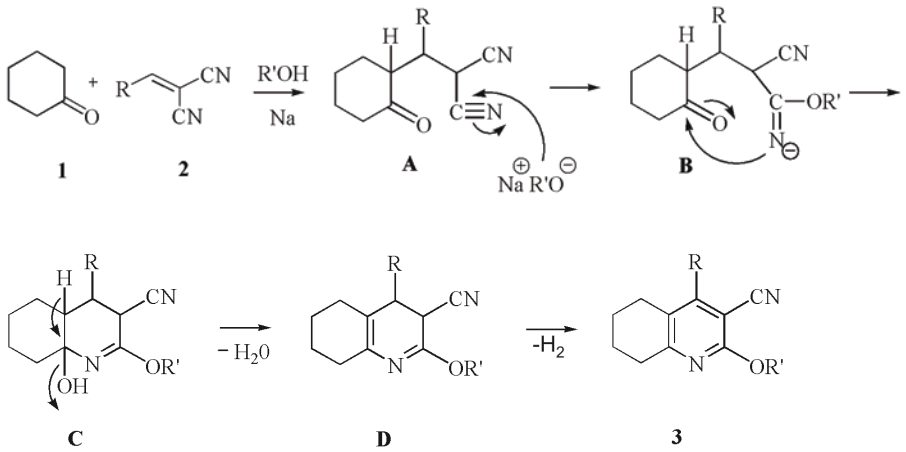

Scheme 2. Proposed mechanism for synthesis of 2-alkoxy-5,6,7,8--tetrahydroquinoline-3-carbonitriles

Biological screening

All the synthesized compounds **3a–j** exhibited moderate to good antimicrobial activity. Compound **3i** showed the highest activity against all the bacteria and fungi. Compounds **3c** and **3g** also showed quite good antibacterial activity as compared to the standard drugs ampicillin and chloramphenicol. Compounds **3c**, **3g** and **3h** exhibited good antifungal activity against *A. niger* as compared to the standard griseofulvin.

EXPERIMENTAL

Chemistry

All chemicals were supplied either by E. Merck (Germany) or by S. D. Fine Chemicals (India). Melting points were determined in open capillaries and are uncorrected. The IR spec-

tra were recorded on a Shimadzu-FT-IR-8400 (Fourier transform infrared (FTIR)). The IR spectra were taken using KBr pellets. The ^{1}H- and ^{13}C-NMR spectra were recorded on a Bruker AMX-400 spectrometer at 400 MHz and 100 MHz, respectively, in DMSO-d_6 with TMS as an internal standard. Gas chromatography–mass spectrometry (GC–MS) was performed on a Shimadzu-GCMS QP2010 series instrument and elemental analysis was performed using a Heraus CHN rapid analyzer. The microwave-assisted reactions were realised in a QPro-M microwave synthesizer.

*General procedure for the synthesis of 2-alkoxy-5,6,7,8-tetrahydroquinoline-3-carbonitriles (**3a–j**)*

A mixture of cyclohexanone **1** (2.5 mmol), arylidene malononitrile **2** (2.5 mmol) in the appropriate alcohol (15 mL) containing sodium (0.05 g) was irradiated under microwaves at 300 W for an appropriate time (Table I). The separated solid was collected, washed with water and then with methanol affording the corresponding **3a**–**j** in good purity. Further purification of the product was not required by recrystallization or any other method.

TABLE I. Microwave assisted synthesis of 2-alkoxy-5,6,7,8-tetrahydroquinoline-3-carbonitriles

Compound	R	R’	Yield, %	Time, min
3a	Phenyl	$–CH_3$	91	4
3b	4-Chlorophenyl	$–CH_3$	95	5
3c	4-Fluorophenyl	$–CH_3$	92	5
3d	4-Methoxyphenyl	$–CH_3$	89	5
3e	4-Hydroxyphenyl	$–CH_3$	94	7
3f	Phenyl	$–C_2H_5$	89	5
3g	4-Chlorophenyl	$–C_2H_5$	94	7
3h	4-Fluorophenyl	$–C_2H_5$	92	6
3i	4-Methoxyphenyl	$–C_2H_5$	92	6
3j	4-Hydroxyphenyl	$–C_2H_5$	88	8

Biological screening

Antimicrobial activity. All the title compounds **3a**–**j** were evaluated for their *in vitro* antimicrobial activity against two Gram-positive bacterial strains, *Streptococcus pyogenes*, *Staphylococcus aureus* and two Gram-negative bacterial strains *Escherichia coli*, *Bacillus subtilis* and one fungal strain *Aspergillus niger* at a concentration of 50 μg mL^{-1} in *N*,*N*-dimethylformamide using the cup plate method.[28] The solvent, *N*,*N*-dimethylformamide, showed no zone of inhibition. After 24 h of incubation at 37 °C, the zones of inhibition were measured in mm. The activities were compared with those of some known antibiotics, *i.e.*, ampicillin, chloramphenicol, ciprofloxacin, as well as griseofulvin at the same concentration. The results are summarized in Table II.

TABLE II. Antimicrobial activity of 2-alkoxy-5,6,7,8-tetrahydroquinoline-3-carbonitriles **3a**–**j**

No.	R	Zone of inhibition, mm				
		S. pyogenes	*S. aureus*	*E. coli*	*B. subtilis*	*A. niger*
3a	Phenyl	13	13	10	09	11
3b	4-Chlorophenyl	11	14	12	12	12
3c	4-Fluorophenyl	14	13	12	11	14

TABLE II. Continued

No.	R	Zone of inhibition, mm				
		S. pyogenes	*S. aureus*	*E. coli*	*B. subtilis*	*A. niger*
3d	4-Methoxyphenyl	13	13	10	10	12
3e	4-Hydroxyphenyl	9	12	10	10	12
3f	Phenyl	12	12	11	11	11
3g	4-Chlorophenyl	14	15	15	14	13
3h	4-Fluorophenyl	10	12	12	12	12
3i	4-Methoxyphenyl	14	13	13	16	18
3j	4-Hydroxyphenyl	13	14	10	10	10
Ampicillin		16	18	16	18	–
Chloramphenicol		18	16	19	16	–
Ciprofloxacin		23	17	20	19	–
Griseofulvin		–	–	–	–	20

CONCLUSIONS

A new and efficient microwave-assisted synthesis of novel functionalized 2-alkoxy-5,6,7,8-tetrahydroquinoline-3-carbonitriles from cyclohexanone and arylidene malononitriles has been reported. Considering the availability of the starting materials, the simple reaction procedure, simple work-up and robust nature, this chemical process provides a very straightforward route to construct various highly functionalized tetrahydroquinoline-3-carbonitriles.

The newly synthesized heterocycles exhibited moderate to promising antimicrobial activity against standard strains. These results make them interesting lead molecules for further synthetic and biological evaluation. It can be concluded that this class of compounds certainly hold great promise towards the pursuit of discovering novel classes of antimicrobial agents. Further studies to acquire more information concerning structure–activity relationships are in progress.

SUPPLEMENTARY MATERIAL

The results of IR, ^{1}H-NMR, ^{13}C-NMR, mass spectroscopy and elemental analyses of synthesized compounds are available electronically at http://www.shd.org.rs/JSCS/, or from the corresponding author on request.

Acknowledgements. The authors are thankful to the Department of Chemistry, Saurashtra University for providing the laboratory facilities. Ms. Dipti K. Dodiya is thankful to UGC, New Delhi for providing financial support in the form of a Research Fellowship in Sciences for Meritorious Students.

И З В О Д

ЕФИКАСНА СИНТЕЗА 5,6,7,8-ТЕТРАХИДРОХИНОЛИН-3-КАРБОНИТРИЛА ОЗРАЧИВАЊЕМ МИКРОТАЛАСИМА

DIPTI K. DODIYA*, HARESH K. RAM, AMIT R. TRIVEDI и VIRESH H. SHAH

Department of Chemistry, Saurashtra University, Rajkot-360 005, Gujarat, India

Описана је ефикасна синтеза нових 2-алкокси-5,6,7,8-тетрахидрохинолин-3-карбонитрила, озрачивањем микроталасима, полазећи од циклохексанона и арилиден-малононитрила

у одговарајућем алкохолу, у присуству натријума. Сва нова једињења окарактерисана су IC, ^{1}H-NMR и ^{13}C-NMR спектроскопијом и масеном спектрометријом и елементалном анализом. Испитана је антибактеријска и антифунгална активност нових синтетисаних једињења.

(Примљено 2. јула 2010, ревидирано 9. јануара 2011)

REFERENCES

1. a) R. D. Larsen, E. G. Corley, A. O. King, J. D. Carrol, P. Davis, T. R. Verhoeven, P. J. Reider, M. Labelle, J. Y. Gauthier, Y. B. Xiang, R. Zamboni, *J. Org. Chem.* **61** (1996) 3398; b) Y. L. Chen, K. C. Fang, J. Y. Sheu, S. L. Hsu, C. C. Tzeng, *J. Med. Chem.* **44** (2001) 2374; c) M. D. Roma, G. Braccio, M. Chia, *Eur. J. Med. Chem.* **35** (2000) 1021; d) D. Doube, M. Bloun,; C. Brideau, C. Chan, S. Desmarais, D. Eithier, J. P. Falgueyeret, R. W. Friesen, M. Girad, Y. Girad,; J. Guay, P. Tagari, R. N. Yong, *Bioorg. Med. Chem. Lett.* **8** (1998) 1255; e) M. P. Maguire, K. R. Sheets, K. McVety, A. P. Spada, A. Zilberstein, *J. Med. Chem.* **37** (1994) 2129
2. M. Z. Hoemann, G. Kumaravel, R. L. Xie, R. F. Rossi, S. Meyer, A. Sidhu, G. D. Cuny, J. R. Hauske, *Bioorg. Med. Chem. Lett.* **10** (2000) 2675
3. a) M. P. Mertes, A. J. Lin, *J. Med. Chem.* **13** (1970) 276; b) M. Romesh, P. S. Moham, P. A. Shanmugam, *Tetrahedron* **40** (1984) 4041; c) N. B. Perry, J. W. Blunt, J. D. McCombs, M. H. Munro, *J. Org. Chem.* **51** (1986) 5476; d) N. M. Williamson, P. R. March, A. D. Ward, *Tetrahedron Lett.* **36** (1995) 7721; e) N. DeKempe, M. Keppens, *Tetrahedron* **52** (1996) 3705; f) A. Padwa, M. A. Brodney, B. Liu, K. Satake, T. A. Wu, *J. Org. Chem.* **64** (1999) 3595; g) R. Hiessbock, C. Wolf, E. Richter, M. Hitzler, P. Chiba, M. Kratzel, G. Ecker, *J. Med. Chem.* **42** (1999) 1921; h) D. B. Dimon, W. Robert, JP 2001163859 (2001); i) R. N. Asolkar, D. Schroder, R. Heckmann, S. Lang, I. Wagner-Dobler, H. Laatsch, , *J. Antibiotics* **57** (2004) 17
4. D. S. Su, A. J. Neville, J. J. Lim, E. Tinney, T. M. Williams, PCT Int. Appl. (2007)
5. R. T. Skerlj, G. J. Bridger, A. Kaller, E. J. McEachern, J. B. Crawford, Y. Zhou, B. Atsma, J. Langille, S. Nan, D. Veale, T. Wilson, C. Harwig, S. Hatse, K. Princen, E. De Clercq, D. Schols, *J. Med. Chem.* **53** (2010) 3376
6. a) E. Lukevics, T. Lapina, I. Segals, I. Augustane, V. N. Verovskii, *Khim.-Furm. Zh.* **22** (1988) 947; b) C. Ramesh, T. K. Nayak, R. Burai, M. K. Dennis, H. J. Hathaway, L. A. Sklar, E. R. Prossnitz, J. B. Arterburn, *J. Med. Chem.* **53** (2010) 1004
7. V. J. Bulbule, K. Rivas, C. L. Verlinde, W. C. Van-Voorhis, M. H. Gelb, *J. Med. Chem.* **51** (2008) 384
8. T. A. Rano, E. Sieber-McMaster, P. D. Pelton, M. Yang, K. T. Demarest, G. H. Kuo, *Bioorg. Med. Chem. Lett.* **19** (2009) 2456
9. C. Parmenon, J. Guillard, D.-H. Caignard, N. Hennuyer, B. Staels, V. Audinot-Bouchez, J. Boutin, C. Dacquet, A. Ktorza, M.-C. Viaud, *Bioorg. Med. Chem. Lett.* **18** (2008) 1617
10. a) S. Murahashi, Y. Imada, Y. Hirai, *Tetrahedron Lett.* **28** (1987) 77; b) J. N. Reed, J. Rotchford, D. Strickland, *Tetrahedron Lett.* **29** (1988) 5725; c) E. Borrione, M. Prato, G. Scorrano, M. Stivanello, V. Lucchini, G. Valle, *J. Chem. Soc., Perkin Trans. 1* (1989) 2245; d) L. Basolo, E. Beccalli, E. Borsini, G. Broggini, S. Pellegrino, *Tetrahedron* **64** (2008) 8182; e) V. Shridharan, C. Avendano, J. C. Menendez, *Synthesis* (2008) 1039; f) D. L. J. Clive, J. Peng, S. P. Fletcher, V. E. Ziffle, D. Wingert, *J. Org. Chem.* **73** (2008) 2330; g) S. V. Ryabukhin, A. S. Plaskon, D. M. Volochnyuk, S. E. Pipko, A. A. Tolmachev, *Synth. Commun.* **38** (2008) 3032; h) A. R. Jagdale, R. S. Reddy, A. Sudalai, *Org. Lett.* **11** (2009) 803; i) A. Patti, S. Pedotti, *Tetrahedron* **66** (2010) 5607; j) H.-G. Cheng,

C.-B. Chen, F. Tan, N.-J. Chang, J.-R. Chen, W.-J. Xiao, *Eur. J. Org. Chem.* **26** (2010) 4976
11. For leading references see: a) T. Nishio, M. Tabata, H. Koyama, M. Sakamoto, *Helv. Chim. Acta* **88** (2005) 78; b) A. R. Katritzky, S. Rachwal, B. Rachwal, *Tetrahedron* **52** (1996) 15031; c) G.-D. Isabelle, P. Gastaud, T. V. RajanBabu, *Org. Lett.* **3** (2001) 2053
12. a) V. Sriramurthy, O. Kwon, *Org. Lett.* 12 (2010) 1084; b) T. H. Babu, G. Shanthi, P. T. Perumal, *Tetrahedron Lett.* 50 (2009) 2881; c) D. L. J. Clive, J. Peng, S. P. Fletcher, V. E. Ziffle, D. Wingert, *J. Org. Chem.* **73** (2008) 2330
13. K. A. Skupinska, E. J. McEachern, R. T. Skerlj, G. J. Bridger, *J. Org. Chem.* **67** (2002) 7890
14. W. Brandt, L. Mologni, L. Preu, T. Lemcke, C. Gambacorti-Passerini, C. Kunick, *Eur. J. Med. Chem.* **45** (2010) 2919
15. K. S. Gudmundsson, S. D. Boggs, J. G. Catalano, A. Svolto, A. Spaltenstein, M. Thomson, P. Wheelan, S. Jenkinson, *Bioorg. Med. Chem. Lett.* **19** (2009) 6399
16. J. B. Crawford, G. Chen, D. Gauthier, T. Wilson, B. Carpenter, I. R. Baird, E. McEachern, A. Kaller, C. Harwig, B. Atsma, R. T. Skerlj, G. J. Bridger, *Org. Process Res. Dev.* **12** (2008) 823
17. A. R. Gholap, K. S. Toti, F. Shirazi, R. Kumari, M. Bhat, M. V. Deshpande, K. V. Srinivasan, *Bioorg. Med. Chem.* **15** (2007) 6705
18. M. M. Ghorab, F. A. Ragab, M. M. Hamed, *Eur. J. Med. Chem.* **44** (2009) 4211
19. J. K. Barbay, Y. Gong, M. Buntinx, J. Li, C. Claes, P. J. Hornby, G. V. Lommen, J. V. Wauweb, W. Hea, *Bioorg. Med. Chem. Lett.* **18** (2008) 2544
20. For recent reviews and books on microwave-assisted organic synthesis, see: a) C. Oliver Kappe, *Angew. Chem. Int. Ed.* **43** (2004) 6250; b) A. Loupy, *Microwaves in Organic Synthesis*, 2nd ed., Wiley-VCH, Weinheim, 2006; c) V. Polshettiwar, R. S. Varma, *Acc. Chem. Res.* **41** (2008) 629; d) P. Appukkuttan, E. V. Eycken, *Eur. J. Org. Chem.* (2008) 1133; e) A. Barge, S. Tagliapietra, L. Tei, P. Cintas, G. Cravotto, *Curr. Org. Chem.* **12** (2008) 1588; f) M. Pineiro, T. Pinho-e-Melo, *Eur. J. Org. Chem.* (2009) 5287
21. For recent examples of papers on microwave activation, see: a) E. M. Beccalli, G. Broggini, M. Martinelli, G. Paladino, E. Rossi, *Synthesis* (2006) 2404; b) H. Tsukamoto, T. Matsumoto, Y. Kondo, *J. Am. Chem. Soc.* **130** (2008) 388; c) M. Andaloussi, J. Lindh, J. Savmarker, P. J. R. Sjoberg, M. Larhed, *Chem. Eur. J.* **15** (2009) 13069; d) A. Reichelt, J. R. Falsey, R. M. Rzasa, O. R. Thiel, M. M. Achmatowicz, R. D. Larsen, D. Zhang, *Org. Lett.* **12** (2010) 792; e) B. Roberts, D. Liptrot, L. Alcaraz, *Org. Lett.* **12** (2010) 1264; f) E. M. Beccalli, A. Bernasconi, E. Borsini, G. Broggini, M. Rigamonti, G. Zecchi, *J. Org. Chem.* **75** (2010) 6923
22. a) D. K. Dodiya, A. R. Trivedi, S. H. Jarsania, S. J. Vaghasiya, V. H. Shah, *J. Serb. Chem. Soc.* **73** (2008) 683; b) A. R. Trivedi, A. B. Siddiqui, D. K. Dodiya, M. J. Soalnki, V. H. Shah, *J. Sulfur Chem.* **30** (2009) 590
23. F. E. Goda, A. A.-M. Abdel-Azizb, O. A. Attefc, *Bioorg. Med. Chem.* **12** (2004) 1845
24. J. N. Godhasra, M. C. Patel, N. N. Kansagara, B. P. Thanki, V. R. Shah, *Indian J. Heterocycl. Chem.* **18** (2009), 369
25. A. S. Girgis, N. Mishriky, M. Ellithey, H. M. Hosnia, H. Farag, *Bioorg. Med. Chem.* **15** (2007) 2403
26. N. M. Abd El-Rahman, A. A. El-Kateb, M. F. Mady, *Synth. Commun.* **37** (2007) 3961
27. O. Sangtae, J. H. In, A. M. Chan, S. Woon-Seob, L. Seokjoon, *Bioorg. Med. Chem.* **12** (2004) 3783
28. *Practical medical microbiology*, 14th ed., G. Collee, J. P. Duguid, A. G. Froser, B. P. Marmion, Eds., Churchill Livingstone, Edinburgh, UK, 1996.

Journal of the Serbian Chemical Society
JSCS@tmf.bg.ac.rs • www.shd.org.rs/JSCS
J. Serb. Chem. Soc. 76 (6) S1–S3 (2011) *Supplementary material*

SUPPLEMENTARY MATERIAL TO

An efficient, microwave-assisted, one-pot synthesis of novel 5,6,7,8-tetrahydroquinoline-3-carbonitriles

DIPTI K. DODIYA*, HARESH K. RAM, AMIT R. TRIVEDI and VIRESH H. SHAH

Department of Chemistry, Saurashtra University, Rajkot-360 005, Gujarat, India

J. Serb. Chem. Soc. 76 (6) (2011) 823–830

ANALYTICAL AND SPECTRAL DATA OF SYNTHESIZED COMPOUNDS

*2-Methoxy-4-phenyl-5,6,7,8-tetrahydroquinoline-3-carbonitrile (**3a**).* Yield: 91 %; m.p. 189–192 °C; Anal. Calcd. for $C_{17}H_{16}N_2O$: C, 77.25; H, 6.10; N, 10.6 %. Found: C, 77.13; H, 6.02; N, 10.68 %. IR (KBr, cm^{-1}): 2225, 1606, 1263, 1066. ^{1}H-NMR (400 MHz, DMSO-d_6, δ / ppm): 1.66–2.83 (8H, *m*, 4 –CH_2), 3.75 (3H, *s*, –OCH_3), 7.06–7.37 (5H, *m*, Ar–H). ^{13}C-NMR (100 MHz, DMSO--d_6, δ / ppm): 23.1, 23.6, 24.8, 32.1, 55.9, 96.2, 117.7, 122.6, 127.5, 130.2, 138.7, 152.2, 160.2, 163.7. MS (*m*/*z*): 264 (M^+).

*2-Methoxy-4-(4-chlorophenyl)-5,6,7,8-tetrahydroquinoline-3-carbonitrile (**3b**).* Yield: 96 %; m.p. 213–215 °C; Anal. Calcd. for $C_{17}H_{15}ClN_2O$: C, 68.34; H, 5.06; N, 9.38 %. Found: C, 68.25; H, 5.12; N, 9.26 %. IR (KBr, cm^{-1}): 2225, 1608, 1263, 1068. ^{1}H-NMR (400 MHz, DMSO-d_6, δ / ppm): 1.68–2.89 (8H, *m*, 4–CH_2), 3.80 (3H, *s*, –OCH_3), 7.10–7.12 (2H, *d*, *J* = 8.36 Hz, Ar–H), 7.35–7.37 (2H, *d*, *J* = 8.32 Hz, Ar–H). ^{13}C-NMR (100 MHz, DMSO-d_6, δ / ppm): 23.4, 23.8, 24.5, 32.5, 55.7, 96.5, 117.4, 123.0, 128.2, 129.5, 134.4, 136.7, 151.7, 160.5, 162.8. MS (*m*/*z*): 298 (M^+).

*2-Methoxy-4-(4-fluorophenyl)-5,6,7,8-tetrahydroquinoline-3-carbonitrile (**3c**).* Yield: 92 %; m.p. 224–226 °C; Anal. Calcd. for $C_{17}H_{15}FN_2O$: C, 72.32; H, 5.36; N, 9.92 %. Found: C, 72.21; H, 5.28; N, 9.80 %. IR (KBr, cm^{-1}): 2222, 1604, 1278, 1066. ^{1}H-NMR (400 MHz, DMSO-d_6, δ / ppm): 1.62–2.90 (8H, *m*, 4–CH_2), 3.77 (3H, *s*, –OCH_3), 6.98–7.00 (2H, *t*, Ar–H), 7.24–7.26 (2H, *m*, Ar–H). ^{13}C-NMR (100 MHz, DMSO-d_6, δ / ppm): 23.2, 23.7, 24.2, 31.9, 55.6, 96.2, 116.8, 117.6, 122.8, 129.3, 133.8, 151.4, 159.9, 162.9, 163.5. MS (*m*/*z*): 282 (M^+).

* Corresponding author. E-mail: diptid85@gmail.com

2-Methoxy-4-(4-methoxyphenyl)-5,6,7,8-tetrahydroquinoline-3-carbonitrile ***(3d)***. Yield: 89 %; m.p. 193–195 °C; Anal. Calcd. for $C_{18}H_{18}N_2O_2$: C, 73.45; H, 6.16; N, 9.52 %. Found: C, 73.36; H, 6.03; N, 9.39 %. IR (KBr, cm^{-1}): 2227, 1597, 1263, 1066. ^{1}H-NMR (400 MHz, DMSO-d_6, δ / ppm): 1.71–2.81 (8H, *m*, 4–CH_2), 3.75 (3H, *s*, –OCH_3), 3.89 (3H, *s*, –OCH_3), 6.76–6.78 (2H, *d*, *J* = 7.96 Hz, Ar–H), 6.98–7.00 (2H, *d*, *J* = 8.08 Hz, Ar–H). ^{13}C-NMR (100 MHz, DMSO--d_6, δ / ppm): 23.4, 23.9, 24.6, 32.3, 55.7, 96.5, 114.9, 117.1, 122.8, 129.1, 130.5, 151.5, 160.3, 161.7, 162.8. MS (*m*/*z*): 294 (M^+).

2-Methoxy-4-(4-hydroxyphenyl)-5,6,7,8-tetrahydroquinoline-3-carbonitrile ***(3e)***. Yield: 94 %; m.p. 207–210 °C; Anal. Calcd. for $C_{17}H_{16}N_2O_2$: C, 77.67; H, 6.52; N, 10.06 %. Found: C, 77.72; H, 6.41; N, 9..93 %. IR (KBr, cm^{-1}): 2231, 1606, 1276, 1037. ^{1}H-NMR (400 MHz, DMSO-d_6, δ / ppm): 1.62–2.85 (8H, *m*, 4–CH_2), 3.80 (3H, *s*, –OCH_3), 4.71 (1H, *s*, –OH), 7.14–7.16 (2H, *d*, *J* = 8.1 Hz, Ar–H), 7.23–7.25 (2H, *d*, *J* = 8.15 Hz, Ar–H). ^{13}C-NMR (100 MHz, DMSO-d_6, δ / ppm): 23.2, 23.7, 24.2, 31.9, 55.4, 95.8, 117.3, 122.6, 127.3, 129.8, 136.1, 138.5, 151.6, 160.3, 162.8. MS (*m*/*z*): 280 (M^+).

2-Ethoxy-4-phenyl-5,6,7,8-tetrahydroquinoline-3-carbonitrile ***(3f)***. Yield: 89 %; m.p. 233–235 ºC; Anal. Calcd. for $C_{18}H_{18}N_2O$: C, 77.67; H, 6.52; N, 10.06 %; Found: C, 77.52; H, 6.38; N, 10.18 %. IR (KBr, cm^{-1}): 2225, 1627, 1292, 1097. ^{1}H-NMR (400 MHz, DMSO-d_6, δ / ppm): 1.31–1.36 (3H, *t*, –CH_3), 1.64––2.85 (8H, *m*, 4–CH_2), 4.39–4.45 (2H, *q*, –CH_2), 6.91–7.44 (5H, *m*, Ar–H). ^{13}C--NMR (100 MHz, DMSO-d_6, δ / ppm): 14.3, 23.1, 23.9, 24.0, 31.5, 65.4, 96.5, 117.4, 122.8, 127.8, 129.8, 138.3, 152.2, 159.9, 162.8. MS (*m*/*z*): 278 (M^+).

2-Ethoxy-4-(4-chlorophenyl)-5,6,7,8-tetrahydroquinoline-3-carbonitrile ***(3g)***. Yield: 94 %; m.p. 216–218 °C; Anal. Calcd. for $C_{18}H_{17}ClN_2O$: C, 69.12; H, 5.48; N, 8.96 %. Found: C, 69.19; H, 5.42; N, 8.89 %. IR (KBr, cm^{-1}): 2222, 1602, 1278, 1064. ^{1}H-NMR (400 MHz, DMSO-d_6, δ / ppm): 1.40–1.44 (3H, *t*, –CH_3), 1.68–2.85 (8H, *m*, 4–CH_2), 4.44–4.50 (2H, *q*, CH_2), 6.98–7.00 (2H, *d*, *J* = 7.9 Hz, Ar–H), 7.23–7.25 (2H, *d*, *J* = 8.28 Hz, Ar–H). ^{13}C-NMR (100 MHz, DMSO-d_6, δ / ppm): 14.5, 22.9, 23.8, 24.7, 32.1, 65.4, 96.1, 117.7, 122.8, 128.4, 129.1, 134.8, 137.1, 151.7, 161.2, 162.9. MS (*m*/*z*): 312 (M^+).

2-Ethoxy-4-(4-fluorophenyl)-5,6,7,8-tetrahydroquinoline-3-carbonitrile ***(3h)***. Yield: 92 %; m.p. 244–226 °C; Anal. Calcd. for $C_{18}H_{17}FN_2O$: C, 72.95; H, 5.78; N, 9.45 %. Found: C, 72.87; H, 5.69; N, 9.52 %. ^{1}H-NMR (400 MHz, DMSO-d_6, δ / ppm): 1.41–1.44 (3H, *t*, –CH_3), 1.63–2.88 (8H, *m*, 4–CH_2), 4.45–4.51 (2H, *q*, –CH_2), 7.26–7.28 (2H, *t*, Ar–H), 7.82–7.84 (2H, *t*, Ar–H). ^{13}C-NMR (100 MHz, DMSO-d_6, δ / ppm): 14.4, 23.1, 23.8, 24.5, 31.5, 64.9, 96.4, 117.1, 117.8, 123.1, 129.6, 133.7, 151.2, 160.2, 162.7, 163.2. MS (*m*/*z*): 296 (M^+).

2-Ethoxy-4-(4-methoxyphenyl)-5,6,7,8-tetrahydroquinoline-3-carbonitrile ***(3i)***. Yield: 92 %; m.p 188–190 °C; Anal. Calcd. for $C_{19}H_{20}N_2O_2$: C, 74.00; H, 6.54; N, 9.08 %. Found: C, 73.89; H, 6.45; N, 9.12 %. IR (KBr, cm^{-1}): 2227, 1589,

1296, 1093. ^{1}H-NMR (400 MHz, DMSO-d_6, δ / ppm): 1.41–1.44 (3H, *t*, –CH_3), 1.62–2.87 (8H, *m*, 4–CH_2), 3.80 (3H, *s*, –OCH_3), 4.45–4.48 (2H, *q*, –CH_2), 7.49––7.51 (2H, *d*, *J* = 8.13 Hz, Ar–H), 7.78–7.80 (2H, *d*, *J* = 8.32 Hz, Ar–H). ^{13}C--NMR (100 MHz, DMSO-d_6, δ / ppm): 14.5, 23.2, 23.9, 24.2, 31.9, 55.7, 65.2, 96.5, 114.6, 117.5, 123.1, 129.4, 130.3, 151.2, 160.8, 161.9, 162.5. MS (*m*/*z*): 308 (M^+).

*2-Ethoxy-4-(4-hydroxyphenyl)-5,6,7,8-tetrahydroquinoline-3-carbonitrile (**3j**)*. Yield: 88 %; m.p. 232–234 °C; Anal. Calcd. for $C_{18}H_{18}N_2O_2$: C, 78.05; H, 6.89; N, 9.58 %; Found: C, 78.17; H, 6.72; N, 9.43 %. IR (KBr, cm^{-1}): 2222, 1635, 1278, 1097. ^{1}H-NMR (400 MHz, DMSO-d_6, δ / ppm): 1.27–1.31 (3H, *t*, –CH_3), 1.63–2.85 (8H, *m*, 4–CH_2), 4.15–4.20 (2H, *q*, –CH_2), 4.77 (1H, *s*, –OH), 6.76––6.78 (2H, *d*, *J* = 7.89 Hz, Ar–H), 6.98–7.00 (2H, *d*, *J* = 8.03 Hz, Ar–H). ^{13}C--NMR (100 MHz, DMSO-d_6, δ / ppm): 14.8, 22.9, 23.2, 23.9, 31.4, 64.9, 95.9, 117.5, 122.2, 127.4, 129.8, 135.8, 139.1, 151.2, 160.7, 163.2. MS (*m*/*z*): 294 (M^+).

Journal of the Serbian Chemical Society
JSCS-info@shd.org.rs • www.shd.org.rs/JSCS
J. Serb. Chem. Soc. *76* (6) 831–840 (2011)
JSCS–4163
UDC 547.867.6+547.16+543.42+548.7:547.233+547.264
Original scientific paper

Synthesis and spectroscopic properties of geminal-bis(*tert*-butylamino)cyclotriphosphazenes obtained by the reaction of spiro and ansa phenoxycyclotriphosphazenes with the *tert*-butylamine and the crystal structure of 4,4'-bis(*tert*-butylamino)-2,6',6',10--tetrachloro-4',4',6',6'-tetrahydrospyro[12*H*-dibenzo[*d*,*g*]-[1,3,2]dioxaphosphocin-6,2'λ^5-[1,3,5,2,4,6]-triazaphosphorine]

DİĞDEM ERDENER[1], MUSTAFA YILDIZ[1]*, HÜSEYİN ÜNVER[2], NAZAN OCAK İSKELELİ[3] and TAHSİN NURİ DURLU[2]

[1]*Department of Chemistry, Faculty of Science and Arts, Çanakkale Onsekiz Mart University, TR-17100 Çanakkale,* [2]*Department of Physics, Faculty of Science, Ankara University, TR-06100 Tandoğan, Ankara and* [3]*Department of Physics, Faculty of Science and Arts, Ondokuz Mayıs University, TR-55139 Kurupelit, Samsun, Turkey*

(Received 22 July 2010, revised 7 January 2011)

Abstract: The condensation reactions of partly substituted spiro and ansa phenoxycyclotriphosphazenes **1** and **2** with *tert*-butylamine produce disubstituted geminal-bis(*tert*-butylamino)phenoxycyclotriphosphazene derivatives (**3** and **4**). The structures of these compounds were characterized by elemental analysis, and IR, ^{1}H-, ^{13}C-, ^{31}P-NMR and mass spectroscopic techniques. Compound **3** was also examined by X-ray crystallography and found to be crystallized in the monoclinic space group $P2_1/n$ with the unit cell parameters: a = = 10.842(4), b = 9.375(5), c = 29.104(11) Å, β = 99.25(3)°, V = 2920(2) Å^3, D_x = 1.404 g cm^{-3}.

Keywords: phenoxyphosphazenes; spectroscopy; spiro; ansa; crystal structure.

INTRODUCTION

The reactions of trimeric phosphazene ($N_3P_3Cl_6$) with primary and secondary amines, diamines, polyamines [1–4] and aryloxides [5–14] under different conditions have been studied. The phenoxy derivatives of trimeric phosphazene ($N_3P_3Cl_6$) and tetrameric phosphazene ($N_4P_4Cl_8$) were used in the synthesis of new, small-molecule organocyclophosphazenes.[15] Polymeric phosphazene derivatives with inorganic backbones and aryloxy side groups are widely used as high refractive index glasses,[16] ferroelectric and non-linear optical devices,[17]

* Corresponding author. E-mail: myildiz@comu.edu.tr
doi: 10.2298/JSC100722070E

liquid crystalline materials,[18] and as biomedical materials.[19] Additionally, they can be used to create small molecule models for the corresponding linear phosphazene macromolecules. The organic, inorganic or organometallic side groups are highly effective in determining the specific physical or chemical properties of phosphazene polymers. Although the partial and complete aminolysis reactions of *tert*-butylamine [$NH_2C(CH_3)_3$] were studied[20] to obtain geminal *tert*-butylamino products, there have not been sufficient studies yet on the partial and complete aminolysis reactions of *tert*-butylamine for spiro or ansa phosphazene compounds. In the present study, the reaction of 2,4',4',6',6',10-hexachloro--4',4',6',6'-tetrahydrospiro[12*H*-dibenzo[*d*,*g*][1,3,2]dioxaphosphocin-6,2'λ^5--[1,3,5,2,4,6]triazaphosphorine] (spiro) (**1**) and 2,6,8,8,10,14-hexachloro-8,8--dihydro-6*H*-6λ^5,10λ^5-nitrilo-10*H*,16*H*-dibenzo[*h*,*k*][1,7,3,5,2,4,6]-dioxadiazatriphosphacyclododecine (ansa) (**2**) with *tert*-butylamine (Scheme 1) were examined and the new *gem*-diamino-spiro (**3**) (Fig. 1) and ansa (**4**) phenoxycyclotriphosphazene derivatives were isolated.

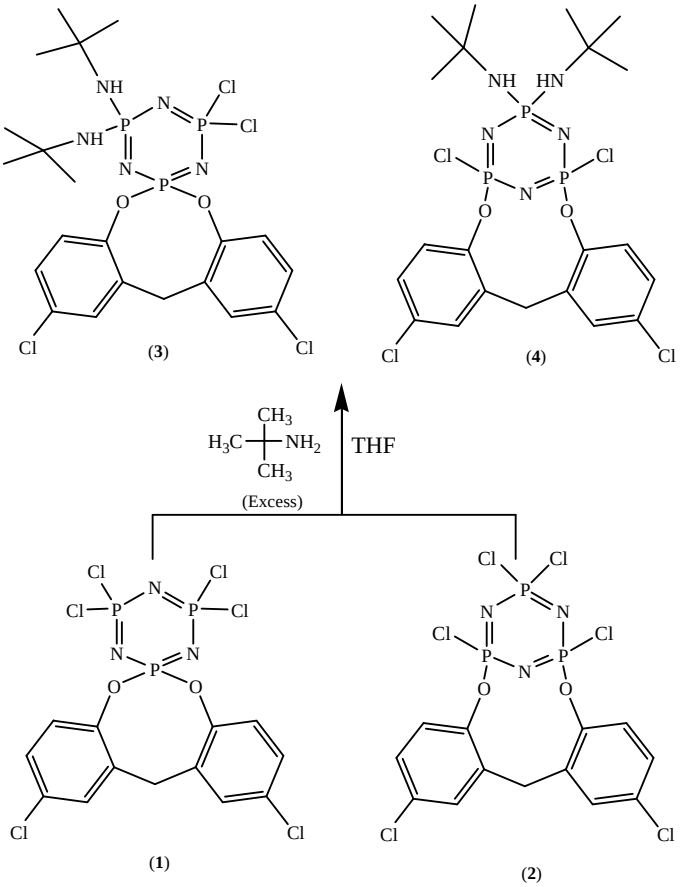

Scheme 1. Synthesis of compounds **3** and **4**.

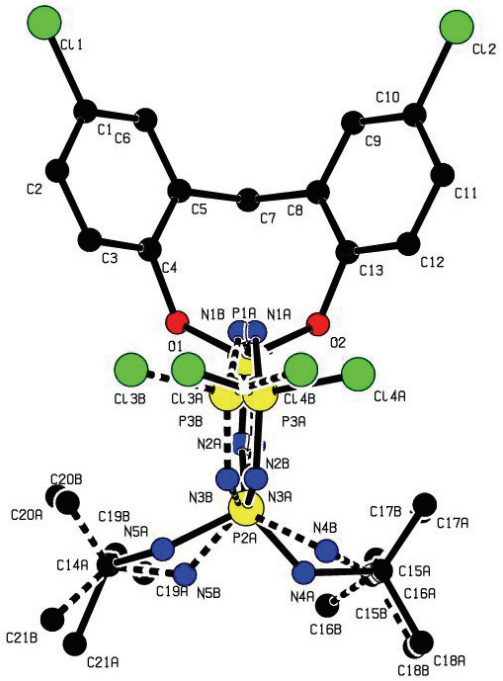

Fig. 1. The molecular structure of compound **3**; the H atoms have been omitted for clarity.[21]

RESULTS AND DISCUSSION

Analytical, IR and MS spectral data

*4,4'-Bis(*tert*-butylamino)-2,6',6',10-tetrachloro-4',4',6',6'-tetrahydrospyro-[12*H*-dibenzo[*d,g*][1,3,2]dioxaphosphocin-6,2'λ^5-[1,3,5,2,4,6]-triazaphosphorine] (spiro)* (**3**). Yield: 32 %; m.p.: 238 °C; Anal. Calcd. for $C_{21}H_{28}O_2N_5P_3Cl_4$: C, 40.84; H, 4.53; N, 11.34 %. Found: C, 40.99; H, 4.63; N, 11.31 %. IR (KBr, cm^{-1}): 3382 (*s*, N–H), 3081 (*w*, Ar–H), 2969 (*s*, C–H, aliphatic), 1481 (*s*, C=C), 1383 (*m*, C–O), 1276 (*s*, P–O), 1222 (*s*, P=N), 1178–1156–1110 (*s*, P–O–C), 581 + 525 (*s*, P–Cl). MS (highest peak in multiplet, based on Cl^{35}) (*m*/*z*): 617 (M^+, 100 %), 543 ((M – *tert*-BuNH), 10 %), 279 ((M – $CH_2(OArCl)_2Cl_2$), 13 %).

*8,8-Bis(*tert*-butylamino)-2,6,10,14-tetrachloro-8,8-dihydro-6*H*-6λ^5,10λ^5-nitrilo-10*H*,16*H*-dibenzo[*h,k*][1,7,3,5,2,4,6]-dioxadiazatriphosphacyclododecine (ansa) (**4**)*. Yield: 30 %; m.p.: 261 °C; Anal. Calcd. for $C_{21}H_{28}O_2N_5P_3Cl_4$: C, 40.84; H, 4.53; N, 11.34 %. Found: C, 40.89; H, 4.55; N, 11.33 %. IR (KBr, cm^{-1}): 3446 (*m*, N–H), 3086 (*w*, Ar–H), 2927 (*m*, C–H, aliphatic), 1481 (*s*, C=C), 1393 (*w*, C–O), 1261 (*s*, P–O), 1205 (*s*, P=N), 1159–1110 (*s*, P–O–C), 562 + 530 (*s*, P–Cl). MS (highest peak in multiplet, based on Cl^{35}) (*m*/*z*): 617 (M^+, 18 %), 543 ((M – *tert*-BuNH), 3 %), 279 ((M – $CH_2(OArCl)_2Cl_2$), 15 %).

IR, ^{1}H-NMR, ^{13}C-NMR, ^{31}P-NMR and MS spectroscopy

In the IR spectra, the characteristic P=N, P–O and P–O–C bands with wave numbers 1222 , 1205 (ν(P=N)), 1276, 1261 (ν(P–O)) and 1178–1156–1110, 1159––1110 (ν(P–O–C)) were observed for compounds **3** and **4**, respectively. In addition, the asymmetric and symmetric vibrations of PCl_2 were found at 581 and 562, and 525 and 530 for **3** and **4,** respectively.

The NMR spectral data for compounds **3** and **4** are presented in Table I. In solution, the structures are symmetrical according to the ^{1}H-NMR and ^{13}C-NMR spectral data. The Ar–CH_2–Ar protons are quartered due to the geminal proton couplings with the P atom ($^{2}J_{\mathbf{HCH}}$ = 13.52 Hz and $^{2}J_{\mathbf{HCH}}$ = 13.73 Hz for **3** and **4**, respectively) and the five bond couplings ($^{5}J_{\mathbf{P}OCCC\mathbf{H}}$ = 2.91 Hz and $^{5}J_{\mathbf{P}OCCC\mathbf{H}}$ = = 2.01 Hz for **3** and **4**, respectively). The difference of these protons in compounds **3** and **4** may be explained by the hydrogen bonding with N atoms on the cyclotriphosphazene ring. According to the crystallographic data, the –CH_2– protons in compound **1** form weak intermolecular hydrogen bonds with nitrogen atoms of the cyclotriphosphazene ring.[5] The protons of each *tert*-butyl group give a singlet (δ 1.38, 1.40 and δ 1.28, 1.59 ppm). The NH signal is broad for compound **3**, while it is a doublet (J = $^{2}J_{\mathbf{PNH}}$ = 5.92 Hz) for compound **4**. The phenyl protons **Haa'** and **Hbb'** are doublets of doublets (6.94 and 7.04 ppm and 7.17 and 7.22 ppm) because of the three and four bond coupling ($^{3}J_{\mathbf{HCCH}}$ = 6.69 and 8.62 Hz, $^{4}J_{\mathbf{HCCCH}}$ = 2.23 and 2.05 Hz for **3** and **4,** respectively). The coupling of **Haa'** with the P atom is $^{4}J_{\mathbf{P}OCC\mathbf{H}}$ = 5.17 and 8.61 Hz for **3** and **4**, respectively. The **Hcc'** protons of compounds **3** and **4** gave a doublet at δ 7.29 and 7.32 ppm, respectively.

According to the proton decoupled ^{13}C-NMR spectra, compounds **3** and **4** have nine signals (Table I). C9 is coupled with the P atom (δ 31.45 ppm, *d*, 6C, $^{3}J_{\mathbf{PNC}}$: 5.0 Hz) in compound **3**, while it is not coupled with the P atom (δ 26.25 ppm, *s*, 6C) in compound **4**.

The proton decoupled ^{31}P-NMR spectra of compounds **3** and **4** were interpreted as a result of a simple ABX and A_2B spin system (Table I). According to the pattern of the proton coupled ^{31}P-NMR spectra of compounds **3** and **4**, it was concluded that only *gem*-diamino architectures are possible.

The electron impact MS spectrum of compounds **3** and **4** showed a well-defined parent ion at *m/z* 617 (100 and 18 %) with the expected isotope pattern. The peaks at *m/z* values of 543 and 279 correspond to the loss of *tert*-BuNH)and $CH_2(OArCl)_2Cl_2$ groups, respectively. The N_3P_3 ring system in **3** and **4** is not stable (the dominant ion was not observed at *m/z* 134) during the fragmentation, which indicates the loss of *tert*-butylamino, phenoxy and chloride fragments. The fragmentation pattern of **3** was similar to that of **4**.

TABLE I. ^{1}H-NMR, ^{13}C-NMR and ^{31}P-NMR spectral data in $CDCl_3$; chemical shifts (δ) are reported in ppm

Atom	Compound	
	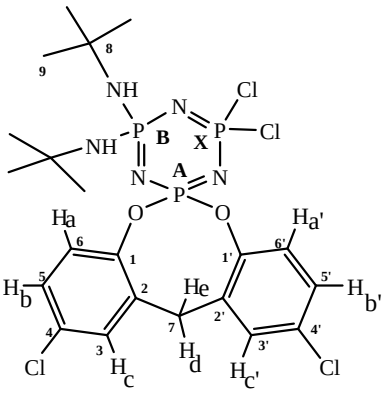 (**3**)	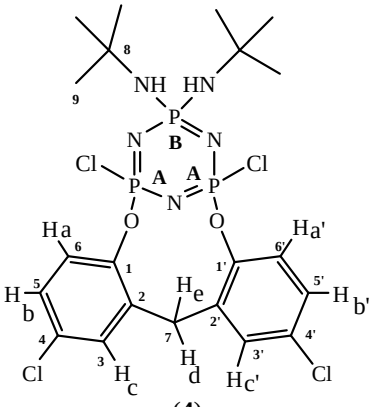 (**4**)
Haa'	6.94 (2H, *d–d*, $^{3}J_{\mathbf{HH}}$ = 6.69 Hz, $^{4}J_{\mathbf{POArH}}$ = 5.17 Hz)	7.04 (2H, *d–d*, $^{3}J_{\mathbf{HH}}$ = 8.62 Hz, $^{4}J_{\mathbf{POArH}}$ = 8.61 Hz)
Hbb'	7.17 (2H, *d–d*, $^{3}J_{\mathbf{HH}}$ = 6.69 Hz, $^{4}J_{\mathbf{HH}}$ = 2.23 Hz)	7.22 (*d–d*, 2H), ($^{3}J_{\mathbf{HH}}$ = 8.62 Hz, $^{4}J_{\mathbf{HH}}$ = 2.05 Hz)
Hcc'	7.29 (2H, *d*, $^{4}J_{\mathbf{HH}}$ = 2.23 Hz)	7.32 (2H, *d*, $^{4}J_{\mathbf{HH}}$ = 2.05 Hz)
Hd, He	4.01 (2H, *q*, $^{2}J_{\mathbf{HH}}$ = 13.52 Hz, $^{5}J_{\mathbf{POCH}}$ = 2.91Hz)	4.00 (2H, *q*, $^{2}J_{\mathbf{HH}}$ = 13.73 Hz, $^{5}J_{\mathbf{POCH}}$ = 2.01 Hz)
CH_3	1.38 (9H, *s*), 1.40 (9H, *s*)	1.28 (9H, s), 1.59 (9H, *s*)
NH	2.40 (2H, broad)	3.70 (2H, *d*, $^{2}J_{\mathbf{PNH}}$= 5.92 Hz)
C11'	147.21 (*d*, $^{2}J_{\mathbf{POC}}$ = 8.92 Hz)	146.6 (*d*, $^{2}J_{\mathbf{POC}}$ = 7.73 Hz)
C22'	131.02 (*d*, $^{3}J_{\mathbf{POC}}$ = 2.7 Hz)	131.69 (*s*)
C33'	129.94 (*s*)	130.13 (*s*)
C44'	133.57 (*d*, $^{5}J_{\mathbf{POC}}$ = 3.7 Hz)	133.37 (*s*)
C55'	128.54 (*s*)	128.79 (*s*)
C66'	124.04 (*d*, $^{3}J_{\mathbf{POC}}$ = 5.0 Hz)	123.95 (*d*, $^{3}J_{\mathbf{POC}}$ = 4.52 Hz)
C7	51.76 (*s*)	33.24 (*s*)
C8	33.35 (*s*)	29.71 (*s*)
C9	31.45 (*d*, $^{3}J_{\mathbf{PNC}}$ = 5.0 Hz)	26.25 (*s*)
Spin system	ABX	A_2B
P_A	0.76 (1P, *q*, $^{2}J_{\mathbf{PANPB}}$ = 70.49 Hz,	1.65 (2P, *d*, $^{2}J_{\mathbf{PANPB}}$ = 73.22 Hz)
P_B	$^{2}J_{\mathbf{PANPX}}$ = 71.96 Hz)	25.53(1P, *t*, $^{2}J_{\mathbf{PANPB}}$ = 73.22 Hz)
P_X	5.58 (1P, *q*, $^{2}J_{\mathbf{PANPB}}$ = 70.96 Hz, $^{2}J_{\mathbf{PBNPX}}$ =71.15 Hz) 21.65 (1P, *q*, $^{2}J_{\mathbf{PANPX}}$ = 71.96 Hz, $^{2}J_{\mathbf{PBNPX}}$ = 71.15 Hz)	–

X-ray crystallography

The conditions employed for crystal data collection and the parameters of the refinement process are summarized in Table II and selected bond distances

and angles are listed in Table III. The molecular structure with the atom-numbering scheme is shown in Fig. 1.[21] The structure of **3** shows pseudo-mirror symmetry. The mirror plane runs through the atoms N3, P1, C7, as confirmed by the torsion angles. The dihedral angle between the cyclotriphosphazene ring and phenyl ring planes is 58.98(7)°. The endocyclic bond angles (123.9(6)° and 118.5(5)°) for compound **3** are larger than those of the standard compound, $N_3P_3Cl_6$ (121.4(3)° and 118.3(2)°).[22] In compound **3**, the endocyclic angles of the substituents (*tert*-butylamine) that are bonded to the phosphorus atoms, N2A––P2A–N3A, N2B–P2B–N3B are smaller than the other endocyclic angles. The exocyclic N4A–P2A–N5A, N4B–P2B–N5B angles (105.5(4)°; 105.3(6)°) are larger than the other exocyclic angles due to the replacement of the bulky *tert*-butylamino group by Cl atoms. According to the study of Bullen and Tucker,[23] the phosphazene bond lengths are correlated with the electronegativities of exocyclic substituents bound to a particular phosphazene core. The lengths of the P–N bonds depend on the electronegativities of the substituents. In compound **3**, the 2,2'-methylenebis(4-chlorophenoxy) group attached to P1 seems to have a strong electron withdrawing character while the *tert*-butylamino group attached to P2 seems to have a strong electron releasing character. Thus, the lengths of the P–O and P–N bonds are changed considerably. The P–N bond lengths in $N_3P_3R_6$ are generally the same provided that all the substituents R are the same. However when R is a difunctional bulky substituent[24] or contains different substituents, the P–N bonds may show significant variations.[25,26] In the structure **3**, the P–N bond lengths vary between 1.547(4) and 1.632(5) Å due to the influence of the difunctional bulky substituent and the *tert*-butylamino group. According to the earlier report of Allcock *et al.*,[12] the P–O bond lengths are not unusual, however the P1A–O1 (1.542(4)] and the P1B–O2 [1.493(8)) bond lengths are shorter than P–O single bonds of 1.577(2) and 1.61 Å.[5] These lengths are shorter than the P–O single bond (1.61 Å), which suggests some exocyclic delocalization of electrons. The determined P–Cl bond lengths are in good agreement with the expected values.[5,27–29]

The crystal structure is stabilized by a weak intermolecular hydrogen bond and the molecules are stacked *via* weak C–H…π ring interactions in compound **3**.

TABLE II. Crystal data and structure refinements of compound **3**

Formula	$C_{21}H_{28}O_2N_5P_3Cl_4$
Formula weight	617.19
Crystal system	Monoclinic
Space group	P 21/n
Crystal dimension	0.20 x 0.39 x 0.70 mm^3
Temperature collection	296(2) K
Unit cell parameters	a = 10.842(4) Å, b = 9.375(5) Å, β = 99.25(3)°, c = 29.104(11) Å

TABLE II. Continued

V	2920(2) Å^3
Z	4
D_C / g cm^{-3}	1.404
μ(MoKα) / mm^{-1}	0.598
F(000)	1272
$2\theta_{max}$	52.00°
h, k, l Range	$-13 \leq h \leq 13$; $-11 \leq k \leq 11$; $-35 \leq l \leq 35$
No. of measured reflections	41048
No. of independent reflections	5752
No. of observed reflections	3469
Data / restraints / parameters	3469 / 350 / 479
Goodness-of-fit on F^2	0.991
Measurement	STOE IPDS 2
Program system	STOE X-AREA
Structure determination	SHELXS-97
Refinement method	Full-matrix least-squares on F^2
R, R_W ($I > 2\sigma(I)$)	0.0545, 0.1844
$(\Delta\rho)_{max}$–$(\Delta\rho)_{min}$ / e Å^{-3}	0.451–0.524

TABLE III. Some selected bond lengths (Å) and bond angles (°) of compound **3**

Lengths			
Cl3A–P3A 2.001(3)	P2A–N4A 1.575(5)	Cl3B–P3B 1.987(6)	P1B–O1 1.665(6)
Cl4A–P3A 2.019(3)	P2A–N2A 1.591(5)	Cl4B–P3B 2.006(6)	P2B–N2B 1.596(8)
P1A–O1 1.542(4)	P2A–N3A 1.632(5)	P1B–O2 1.493(8)	P2B–N3B 1.619(8)
P1A–N2A 1.561(5)	P2A–N5A 1.654(6)	P1B–N2B 1.559(8)	P2B–N4B 1.685(8)
Angles			
O1–P1A–N2A 105.1(2)		N3B–P2B–N4B 101.9(4)	
N2A–P1A–O2 107.4(2)		C13–O2–P1B 126.8(4)	
O1–P1A–N1A 115.0(2)		N3B–P3B–N1B 122.5(5)	
N2A–P2A–N5A 105.8(3)		C13–O2–P1A 124.8(3)	
O1–P1A–O2 104.5(2)		N3B–P3B–Cl4B 110.3(3)	
N1B–P1B–O1 98.9(3)		P1A–N2A–P2A 123.9(3)	
O2–P1B–O1 104.6(4)		N1B–P3B–Cl4B 105.5(3)	
N2B–P2B–N3B 115.6(5)		P3A–N3A–P2A 122.0(3)	

EXPERIMENTAL

Reagents and techniques

The ^{1}H-, ^{13}C- and ^{31}P-NMR spectra were recorded on a Bruker DPX FT-NMR spectrometer operating at 400, 101.6 and 161.99 (spectral data in $CDCl_3$) MHz, respectively. The ^{1}H- and ^{13}C-NMR chemical shifts were measured using $SiMe_4$ as an internal standard; the ^{31}P-NMR chemical shifts were measured using 85 % H_3PO_4 as an external standard. The infrared absorption spectra were recorded on a Perkin Elmer BX II spectrometer in KBr discs and are reported in cm^{-1} units. The electron impact (70 eV, *ca.* 1.12×10^{-17} J) mass spectra were obtained on a VG-ZAPSPEC spectrometer with an ion source temperature of 240 °C. Carbon, nitrogen and hydrogen analyses were performed on a LECO CHNS-932 analyzer.

The melting points were measured on an Electro Thermal IA 9100 apparatus using a capillary tube. Hexachlorocyclotriphosphazene was purchased from Aldrich. It was recrystallized from hexane and purified by fractional vacuum sublimation at 55 °C before use. Tetrahydrofuran and hexane were purchased from Merck, distilled over sodium/benzophenone and stored over molecular sieves. Sodium (Merck), *tert*-butylamine (Merck), 2,2'-methylenebis(4-chlorophenol) (Aldrich), and silica gel (Aldrich, 70–230 mesh, 60 Å) were used as received. All reactions were monitored using Kieselgel 60 F 254 (silica gel) pre-coated TLC plates. All reactions and manipulations were performed under an atmosphere of dry argon.

*Synthesis of 2,4',4',6',6',10-hexachloro-4',4',6',6'-tetrahydrospiro[12*H*-dibenzo[*d,g*]-[1,3,2]dioxaphosphocin-6,2'λ^5-[1,3,5,2,4,6]triazaphosphorine] (spiro) (**1**) and 2,6,8,8,10,14-hexachloro-8,8-dihydro-6*H*-6λ^5,10λ^5-nitrilo-10*H*,16*H*-dibenzo[*h,k*]-[1,7,3,5,2,4,6]-dioxadiazatriphosphacyclododecine (ansa) (**2**)*

Compounds (**1**) and (**2**) were prepared according to the published procedure.[5]

*Synthesis of 4,4'-bis(*tert*-butylamino)-2,6',6',10-tetrachloro-4',4',6',6'-tetrahydrospyro[12*H*--dibenzo[*d,g*][1,3,2]dioxaphosphocin-6,2'λ^5-[1,3,5,2,4,6]-triazaphosphozine] (spiro) (**3**)*

tert-Butylamine (0.670 g; 9.20×10^{-3} mol) in dry THF (50 mL) was added drop wise to a stirred solution of compound **1** (0.50 g; 9.2×10^{-4} mol) in dry THF (150 mL) at –20 °C over 1 h, with argon flowing over the reaction mixture. Then the mixture was allowed to come to ambient temperature, boiled under reflux (24 h) using a condenser fitted with a $CaCl_2$ drying tube. The precipitated amine hydrochloride was filtered off and the solvent removed by rotary evaporation. The crude product was left to dry under *vacuo* and chromatographed (silica gel, 60 g, eluent; $CHCl_3$/*n*-hexane, 3:1) to give compound **3**. Then, it was recrystallized from $CHCl_3$/petroleum ether (50:70) by the slow diffusion method whereby a white solid formed, yield 0.182 g.

*Synthesis of 8,8-Bis(*tert*-butylamino)-2,6,10,14-tetrachloro-8,8-dihydro-6*H*-6λ^5,10λ^5-nitrilo-10*H*,16*H*-dibenzo[*h,k*][1,7,3,5,2,4,6]-dioxadiazatriphosphacyclododecine (ansa)(**4**)*

tert-Butylamine (0.61 g; 8.30×10^{-3} mol) in dry THF (50 mL) was added drop wise to a stirred solution of compound **2** (0.45 g; 8.30×10^{-4} mol) in dry THF (150 mL) at –20 °C for over 1 h, with argon flowing over the reaction mixture. Compound **4** was prepared and purified as compound **3,** white solid, yield 0.153 g.

Crystal structure

The data collection for **3** was performed on a STOE IPDS-2 diffractometer employing graphite-monochromatized MoKα radiation (λ = 0.71073Å). The collected intensities were corrected for Lorentz and polarization factors; absorption correction was performed (μ = 0.598 mm^{-1}) by the integration method *via* X-RED software [30] and the cell parameters were determined using X-AREA software.[30] The structure was solved using direct methods in the WINGX implementation of SHELXS-97 [31] and refined with SHELXL-97.[32] A total of 479 crystallographic parameters were refined. Throughout the refinement process, the Cl3, Cl4, P1, P2, P3, N1, N2, N3, N4, N5, C14, C15, C16, C17, C18, C19, C20, C21 atoms were treated as a disordered group. The site occupation factors of the disordered atoms were refined to 0.71(2) and 0.29(2). All hydrogen atoms were located geometrically using a riding model. The crystallographic data (excluding structure factors) for the structure reported in this paper have been deposited with the Cambridge Crystallographic Data Centre as supplementary publication No. CCDC 644277.[33]

Acknowledgements. The authors are grateful to the Scientific and Technical Research Council of Turkey (TÜBİTAK) for the financial support of this work, grant number 106T108.

ИЗВОД

СИНТЕЗА И СПЕКТРОСКОПСКЕ КАРАКТЕРИСТИКЕ ГЕМИНАЛНИХ-БИС(*терц*-БУТИЛАМИНО)ФОСФАЗЕНА ДОБИЈЕНИХ РЕАКЦИЈОМ СПИРО И АНСА ФЕНОКСИФОСФАЗЕНА СА *терц*-БУТИЛАМИНОМ И СТРУКТУРА КРИСТАЛА 4,4'-БИС(*терц*-БУТИЛАМИНО)-2,6',6',10-ТЕТРАХЛОРО-4',4',6',6'-ТЕТРАХИДРОСПИРО[12*H*-ДИБЕНЗО[*d*,*g*][1,3,2]ДИОКСАФОСФОЦИН-6,2'λ^5-[1,3,5,2,4,6]-ТРИАЗАФОСФОРИНА]

DİĞDEM ERDENER[1], MUSTAFA YILDIZ[1], HÜSEYİN ÜNVER[2], NAZAN OCAK İSKELELİ[3] и TAHSİN NURİ DURLU[2]

[1]*Department of Chemistry, Faculty of Science and Arts, Çanakkale Onsekiz Mart University, TR-17100 Çanakkale,* [2]*Department of Physics, Faculty of Science, Ankara University, TR-06100 Tandoğan, Ankara и* [3]*Department of Physics, Faculty of Science and Arts, Ondokuz Mayıs University, TR-55139 Kurupelit, Samsun, Turkey*

Реакција кондензације супституисаних спиро и анса феноксициклотрифосфазена **1** и **2** са *терц*-бутиламином даје дисупституисане геминалне-бис(*терц*-бутиламино)феноксициклотрифосфазенске деривате (**3** и **4**). Структура ових једињења је окарактерисана елементалном анализом, IC, ^{1}H-, ^{13}C-, ^{31}P-NMR спектроскопијом и масеном спектрометријом. Структура једињења **3** испитана је и кристалографском анализом и утврђено је да једињење кристалише у моноклиничној просторној групи $P2_1/n$ са јединичним параметрима: a = = 10,842(4), b = 9,375(5), c = 29,104(11) Å, β = 99,25(3)°, V = 2920(2) Å^3, D_x = 1,404 g cm^{-3}.

(Примљено 22. јула 2010, ревидирано 7. јануара 2011)

REFERENCES

1. C. W. Allen, *Chem. Rev*. **91** (1991) 119
2. H. R. Allcock, *Chem. Rev*. **72** (1972) 315
3. J. F. Labarre, *Top. Curr. Chem*. **129** (1985) 173
4. M. Yıldız, Z. Kılıç, T. Hökelek, *J. Mol. Struct*. **510** (1999) 227
5. M. Yıldız, D. Erdener, H. Ünver, N. O. İskeleli, *J. Mol. Struct*. **753** (2005) 165
6. H. R. Allcock, S. Al-Shali, D. C. Ngo, K. B. Visscher, M. Parvez, *J. Chem. Soc. Dalton Trans*. (1996) 3549
7. T. Hökelek, A. Kılıç, S. Begeç, Z. Kılıç, *Acta Crystallogr. C* **55** (1999) 783
8. A. Kılıç, S. Begeç, B. Çetinkaya, T. Hökelek, Z. Kılıç, N. Gündüz, M. Yıldız, *Heteroat. Chem*. **7** (1996) 249
9. T. Hökelek, Z. Kılıç, A. Kılıç, *Acta Crystallogr. C* **50** (1994) 453
10. T. Hökelek, A. Kılıç, S. Begeç, Z. Kılıç, M. Yıldız, *Acta Crystallogr. C* **52** (1996) 3243
11. H. R. Allcock, D. C. Ngo, M. Parvez, K. B. Visscher, *J. Chem. Soc. Dalton Trans*. (1992) 1687
12. H. R. Allcock, D. C. Ngo, M. Parvez, R. R. Whittle, W. J. Birdsall, *J. Am. Chem. Soc*. **113** (1991) 2628
13. T. Hökelek, H. Dal, Z. Kılıç, *Acta Crystallogr. E* **57** (2001) o1063-o1066 Part 11
14. L. Öztürk, T. Hökelek, H. Dal, Z. Kılıç, *Acta Crystallogr. E* **58** (2002) o20-o23, Part 1
15. C. W. Allen, *Coord. Chem. Rev*. **130** (1994) 137
16. M. A. Olshavsky, H. R. Allcock, *Macromolecules* **28** (1995) 6188

17. H. R. Allcock, S. Al-Shali, D. C. Ngo, K. B. Visscher, M. Parvez, *J. Chem. Soc. Dalton Trans.* (1995) 3521
18. H. R. Allcock, C. Kim, *Macromolecules* **24** (1991) 2846
19. S. Cohen, W. C. Bano, K. B. Visscher, M. Chow, H. R. Allcock, R. Langer, *J. Am. Chem. Soc*. **112** (1990) 7832
20. S. W. Bartlett, S. J. Coles, D. B. Davies, M. B. Hursthouse, H. İbişoğlu, A. Kiliç, R. A. Shaw, İ. Ün, *Acta Crystallogr. B* **62** (2006) 321
21. L. J. Farrugia, *J. Appl. Crystallogr*. 30 (1997) 565
22. G. J. Bullen, *J. Chem. Soc. A* (1971) 1450
23. G. J. Bullen, P. A. Tucker, *J. Chem. Soc. Dalton Trans*. (1972) 1651
24. K. Kubono, N. Asaka, S. Isoda, T. Kabayashi, T. Taga, *Acta Crystallogr. C* (1994) 324
25. J. K. Fincham, M. B. Hursthouse, H. G. Parkers, L. S. Shaw, R. A. Shaw, *Acta Crystallogr. B* **42** (1986) 462
26. S. R. Contractor, M. B. Hursthouse, L. S. Shaw, R. A. Shaw, H. Yılmaz, *Acta Crystallogr. B* **41** (1985) 122
27. S. R. Contractor, M. B. Hursthouse, H. G. Parkes, L. S. Shaw, R. A. Shaw, H. Yılmaz, *J. Chem. Soc. Chem. Commun*. (1984) 675
28. S. Kumaraswamy, M. Vijjulatha, C. Muthiah, K. C. Kumara Swamy, U. Engelhardt, *J. Chem. Soc. Dalton Trans*. (1999) 891
29. N. Satish Kumar, K. C. Kumara Swamy, *Acta Crystallogr. C* (2001) 1421
30. *X-AREA (Version 1.18) and X-RED32 (Version 1.04)*, Stoe & Cie, Darmstadt, Germany, 2002
31. G. M. Sheldrick, *SHELXS-97, Program for the solution of crystal structures*, Univ. of Göttingen, Germany, 1997
32. G. M. Sheldrick, *SHELXL-97, Program for the refinement of crystal structures*, Univ. of Göttingen, Germany, 1997
33. Further information may be obtained from: Cambridge Crystallographic Data Centre (CCDC), 12 Union Road, Cambridge CB21EZ, UK, by quoting the depository number CCDC 644277 (E-mail: deposit@ccdc.cam.ac.uk).

Journal of the Serbian Chemical Society
JSCS-info@shd.org.rs • www.shd.org.rs/JSCS
J. Serb. Chem. Soc. 76 (6) 841–845 (2011) UDC 582.998.1+543.422.25:547.562:547.458.3
JSCS–4164 *Short communication*

SHORT COMMUNICATION

A new trisaccharide derivative from *Prenanthes purpurea*

MICHAELA POSCH[1], KARIN JÖHRER[2], SERHAT SEZAI CICEK[1], RICHARD GREIL[2,3], ERNST P. ELLMERER[4] and CHRISTIAN ZIDORN[1]*

[1]*Institut für Pharmazie der Universität Innsbruck, Abteilung Pharmakognosie, Josef-Moeller-Haus, Innrain 52, A-6020 Innsbruck,* [2]*Tyrolean Cancer Research Institute, Innrain 66, A-6020 Innsbruck,* [3]*Laboratory for Immunological and Molecular Cancer Research, Third Medical Department, Medical University Salzburg, Müllner Hauptstrasse 48, 5020 Salzburg and* [4]*Institut für Organische Chemie der Universität Innsbruck, Innrain 52a, A-6020 Innsbruck, Austria*

(Received 10 December 2010, revised 26 January 2011)

Abstract: A methanolic extract of *Prenanthes purpurea* L. leaves yielded 1,6”-di-*O*-cinnamoyl-*β*-D-glucopyranosyl-(1→3)-*O*-*α*-L-rhamnopyranosyl-(1→6)-*O*-*β*-D-glucopyranoside. The NMR and physical data of this new natural compound are reported.

Keywords: Asteraceae; Cichorieae; Hypochaeridinae; phenolic acids; *Prenanthes purpurea* L.; trisaccharides.

INTRODUCTION

Prenanthes purpurea L. is distributed over Central and Southern Europe and the Caucasus.[1] Recent molecular results revealed that the genus *Prenanthes* is monotypic and a member of the Hypochaeridinae subtribe within the Cichorieae tribe of the Asteraceae family.[2] The present communication deals with the isolation and structure elucidation of 1,6”-di-*O*-cinnamoyl-*β*-D-glucopyranosyl-(1→3)-*O*-*α*-L-rhamnopyranosyl-(1→6)-*O*-*β*-D-glucopyranoside, a new di-*O*-cinnamoyl-trisaccharide derivative from a methanolic extract of leaves of *P. purpurea* of Austrian origin. The structure elucidation was based on extensive NMR studies as well as HR-MS data.

RESULTS AND DISCUSSION

Compound **1** was isolated from the ethyl acetate layer of the methanolic extract of *P. purpurea* leaves employing silica gel column chromatography (CC), repeated Sephadex LH-20 CC and semi-preparative RP-18 HPLC.

* Corresponding author. E-mail: Christian.H.Zidorn@uibk.ac.at
doi: 10.2298/JSC101210072P

Physical data. Amorphous white compound, glass transition above 141 °C; FTIR (ZnSe, cm^{-1}): 3420 (br), 2920, 1710, 1636, 1578, 1529, 1496, 1450, 1332, 1312, 1283, 1204, 1174, 1074, 914, 865, 840, 807, 769, 713, 685. HRMS (*m*/*z*): 771.2520 $[M+Na]^+$, calculated for $C_{36}H_{44}O_{17}Na^+$: 771.2471. UV (MeOH) (λ_{max} / / nm (log ε)) 278 (4.22); $[a]_D^{20}$ –10° (MeOH; *c* 0.0267 g ml^{-1}).

The ESI mass spectrum of compound **1** displayed signals at *m*/*z* = 771 $[M+Na]^+$, 641 $[M–cinnamoyl+Na]^+$, and 511 $[M–2\text{-}cinnamoyl+Na]^+$ in the positive mode. Together with the ^{1}H-NMR and ^{13}C-NMR data, which showed signals of three sugar moieties and two cinnamoyl moieties, these major mass signals were indicative of a molecular formula of $C_{36}H_{44}O_{17}$. Based on one- and two-dimensional NMR experiments (Table I), the three sugar moieties were identified as two glucose and one rhamnose moiety. Linkage from the anomeric carbon of the rhamnose moiety to *O*-6 of the first glucose moiety was revealed by an HMBC crosspeak from H-1' to C-6. Likewise, an HMBC crosspeak from the anomeric proton of the second glucose moiety (H-1") to C-3' of the glucose moiety indicated linkage of the second glucose moiety to the rhamnose moiety in this position. Based on their ^{1}H-NMR coupling constants, the anomeric protons were identified as β-configured for the two glucose moieties and α-configured for the rhamnose moiety. Thus, the sugar backbone of the structure was identified as a β--D-glucopyranosyl-(1→3)-*O*-α-L-rhamnopyranosyl-(1→6)-*O*-β-D-glucopyranoside.

TABLE I. NMR data, δ / ppm, of 1,6"-di-*O*-cinnamoyl-β-glucopyranosyl-(1→3)-*O*-α-rhamnopyranosyl-(1→6)-*O*-β-D-glucopyranoside (**1**) isolated from *P. purpurea* (measured in DMSO-d_6 at 600 and 150 MHz for ^{1}H and ^{13}C, respectively; referenced to solvent residual signals and solvent signals of DMSO-d_6, ^{1}H-NMR: 2.50 ppm and ^{13}C-NMR: 39.50 ppm, respectively; coupling constants in Hz)

Position	^{1}H-NMR	^{13}C-NMR	Position	^{1}H-NMR	^{13}C-NMR
	Glucose **1**			Glucose **2**	
1	5.48 1H, *d* (7.5)	94.1	1"	4.46 1H, *d* (7.5)	104.2
2	3.24 1H, *m*[a]	72.1	2"	3.10 1H, *br t* (8.0)	73.5
3	3.30 1H, *m*[a]	75.9	3"	3.24 1H, *m*[a]	75.6
4	3.06 1H, *br t* (9.0)	69.6	4"	3.19 1H, *m*[a]	69.5
5	3.13 1H, *m*[a]	76.5	5"	3.47 1H, *m*[a]	76.1
6	3.80 1H, *m*[a]	66.9	6"	4.33 1H, *dd* (12.0, 2.0)	63.4
	3.40 1H, *m*[a]			4.25 1H, *dd* (12.0, 6.0)	
	Cinnamoyl **1**			Cinnamoyl **2**	
1"'	–	133.8	1""	–	133.9
2"'/6"'	7.41 2H, AA'BB'C	128.9	2""/6""	7.41 2H, AA'BB'C	128.9
3"'/5"'	7.70 2H, AA'BB'C	128.4	3""/5""	7.70 2H, AA'BB'C	128.4
4"'[b]	7.43 1H, AA'BB'C	130.4	4""[b]	7.43 1H, AA'BB'C	130.6
7"'	7.70 1H, *d* (16.0)	145.6	7""	7.62 1H, *d* (16.0)	144.6
8"'	6.57 1H, *d* (16.0)	117.5	8""	6.61 1H, *d* (16.0)	117.9
9"'	–	164.8	9""	–	166.2

TABLE I. Continued

Position	^{1}H-NMR	^{13}C-NMR
	Rhamnose	
1’	4.49 1H, *d* (1.5)	100.3
2’	3.83 1H, *m*[a]	69.3
3’	3.54 1H, *m*[a]	81.6
4’	3.40 1H, *m*[a]	70.5
5’	3.51 1H, *m*[a]	67.7
6’	1.14 3H, *d* (6.0)	17.8

[a]Overlapping signals; [b]signals might be exchangeable

This trisaccharide is known as a constituent of other natural products, *e.g.*, flavonoids found in tea (*Camellia sinensis* (L.) Kuntze).[3,4] Esterification of the anomeric C of the first glucose moiety was also proven by an HMBC experiment, which revealed a crosspeak from H-1 to the carbonyl moiety (C-9”’) of one of the two cinnamoyl moieties of the molecule. HMBC crosspeaks from the two protons in position 6’ of the second glucose moiety to the carbonyl (C-9””) of the second cinnamoyl moiety revealed that the second cinnamoyl moiety was attached *via* an ester linkage in this position. Conclusively, compound **1** was identified as 1,6”-di-*O*-cinnamoyl-*β*-glucopyranosyl-(1→3)-*O*-*α*-rhamnopyranosyl--(1→6)-*O*-*β*-glucopyranoside (Fig. 1). This compound represents a new natural product.

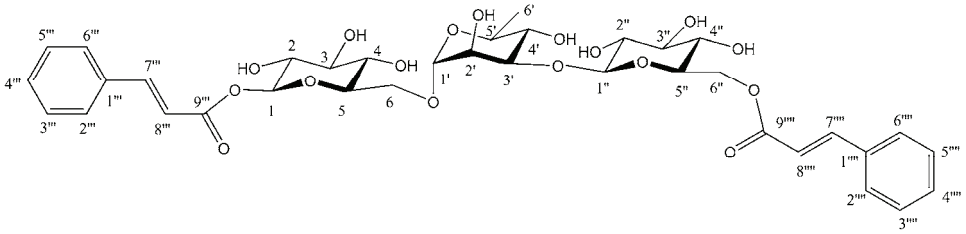

Fig. 1. 1,6”-Di-*O*-cinnamoyl-*β*-D-glucopyranosyl-(1→3)-*O*-*α*-L-rhamnopyranosyl-(1→6)-*O*-*β*-D-glucopyranoside (**1**) isolated from the leaves of *Prenanthes purpurea* L.

Additionally, extracts of flowering heads and leaves were analyzed separately for the occurrence of known phenolic acids using established protocols.[5,6] In the course of these investigations, in extracts of both leaves and flowering heads, the following caffeic acid derivatives were detected by HPLC/DAD and HPLC/MS: caffeoyltartaric acid, cichoric acid, chlorogenic acid, 3,5-dicaffeoylquinic acid, and 4,5-dicaffeoylquinic acid.

Induction of apoptosis was measured by flow cytometry in human CCRF-CEM and in human NCI-H929 cells.[7] Both after 24 h and after 48 h, compound **1** showed no cytotoxicity up to the highest concentration tested (100 μM).

EXPERIMENTAL

Plant material

Leaves of *Prenanthes purpurea* L. were collected in August 1996 NW Wieserberg, Zell/Salzburg/Austria at 1200 m above mean sea level (coordinates (WGS84): N 47°27'; E 12°46'). Voucher specimens were deposited in the herbarium of the Institut für Pharmazie (CZ-960930i) and the private herbarium of CZ.

Extraction and isolation

Air-dried, ground leaves (468 g) of *P. purpurea* were exhaustively macerated with MeOH to yield 64.1 g of crude extract after evaporation of the solvent *in vacuo*. The crude extract was re-dissolved in a mixture of MeOH and H_2O (1/2, v/v) and successively partitioned with petroleum ether 40–60 °C , EtOAc, and *n*-BuOH. The EtOAc layer was brought to dryness *in vacuo* to yield 7.95 g of residue. This residue was first fractionated by silica gel column (150 cm×2.0 cm) chromategraphy using a gradient of CH_2Cl_2 and MeOH. Fractions containing **1** were successively (three times) fractionated on Sephadex LH-20 using a mixture of methanol, acetone and water (3/1/1, v/v/v) as the mobile phase. Impure compound **1** (98.5 mg) was finally purified using semi-preparative RP-18 HPLC (Dionex-P580 pump, ASI-100 autosampler, UVD170U UV-detector, and Gilson-206 fraction collector; Waters (7.8 mm×100 mm) XTerra-Prep-MS-C18 column (5 μm)) using a gradient of H_2O and CH_3CN to yield 44.5 mg of **1**.

Characterization

Melting point/glass transition: Kofler hot-stage microscope, uncorrected. FTIR: Bruker IFS 25; samples were applied to a ZnSe disk and measured in the transmission mode. UV: Shimadzu U-2000 UV–Vis photometer. Optical rotation: Perkin Elmer Polarimeter 341. ESIMS and HRMS: Daltronics-Esquire-3000 (ion trap) and Finnigan-SSQ-7000 (quadrupole) mass spectrometers, respectively. NMR: Bruker Ultrashield 600 Plus.

Bioactivity

Induction of apoptosis was measured in human CCRF-CEM (T-acute lymphocytic leukemia cell line) and in human NCI-H929 (multiple myeloma cell line) cells by flow cytometry using established protocols.[7] Briefly, 0.5×10^6 cells ml^{-1} were incubated for 24 and 48 h with or without compound (1, 10, 50 or 100 μM) dissolved in DMSO. Analyses were performed in quadruplicate and appropriate solvent controls were included. The extent of apoptosis was calculated as percentage of AnnexinV/PI negative cells compared to the controls.

Acknowledgements. The authors wish to thank R. Spitaler (Innsbruck/Austria) for proofreading and three anonymous reviewers for valuable suggestions to amend the manuscript.

ИЗВОД

НОВИ ТРИСАХАРИДИ ИЗОЛОВАНИ ИЗ *Prenanthes purpurea*

MICHAELA POSCH[1], KARIN JÖHRER[2], SERHAT SEZAI CICEK[1], RICHARD GREIL[2,3], ERNST P. ELLMERER[4] и CHRISTIAN ZIDORN[1]

[1]*Institut für Pharmazie der Universität Innsbruck, Abteilung Pharmakognosie, Josef-Moeller-Haus, Innrain 52, A-6020 Innsbruck,* [2]*Tyrolean Cancer Research Institute, Innrain 66, A 6020 Innsbruck,* [3]*Laboratory for Immunological and Molecular Cancer Research, Third Medical Department, Medical University Salzburg, Müllner Hauptstrasse 48, 5020 Salzburg и* [4]*Institut für Organische Chemie der Universität Innsbruck, Innrain 52a, A-6020 Innsbruck, Austria*

Из метанолног екстракта лишћа биљке *Prenanthes purpurea* L. Изоловани су 1,6”-ди-*O*-цинамоил-*β*-D-глукопиранозил-(1→3)-*O*-*α*-L-рамнопиранозил-(1→6)-*O*-*β*-D-глукопиранозиди. Приказани су НМР спектри и аналитички подаци нових природних једињења.

(Примљено 10. децембра 2010, ревидирано 26. јануара 2011)

REFERENCES

1. H. Meusel, E. J. Jäger, *Vergleichende Chorologie der zentraleuropäischen Flora*, Vol. 3, Gustav Fischer Verlag, Jena, Germany, 1992, p. 540
2. N. Kilian, B. Gemeinholzer, H. W. Lack, in *Systematics, Evolution, and Biogeography of Compositae*, V. A. Funk, A. Susanna, T. F. Stuessy, R. J. Bayer, Eds., IAPT, Vienna, Austria, 2009, pp. 343–383
3. A. Finger, U. H. Engelhardt, V. Wray, *J. Sci. Food Agric.* **55** (1991) 313
4. S. Scharbert, N. Holzmann, T. Hofmann, *J. Agric. Food Chem.* **52** (2004) 3498
5. P. Fusani, C. Zidorn, *J. Food Comp. Anal.* **23** (2010) 658
6. C. Zidorn, B. Schubert, H. Stuppner, *Biochem. Syst. Ecol.* **33** (2005) 855
7. G. Koopman, C. P. Reutelingsperger, G. A. M. Kuijten, R. M. J. Keehnen, S. T. Pals, M. H. J. van Oers, *Blood* 84 (1994) 1415.

Journal of the Serbian Chemical Society
JSCS-info@shd.org.rs • www.shd.org.rs/JSCS
J. Serb. Chem. Soc. 76 (6) 847–855 (2011)
JSCS–4165
UDC 547.867.6+547.16+543.42+548.7:547.233+547.264
Original scientific paper

Digestibility of β-lactoglobulin following cross-linking by *Trametes versicolor* laccase and apple polyphenols

ZIYAD TANTOUSH, LUKA MIHAJLOVIĆ#, BOJANA KRAVIĆ#, JANA OGNJENOVIĆ#, RATKO M. JANKOV#, TANJA ĆIRKOVIĆ VELIČKOVIĆ# and DRAGANA STANIĆ-VUČINIĆ#*

Faculty of Chemistry, University of Belgrade, Studentski trg 16, P. O. Box 158, 11001 Belgrade, Serbia

(Received 1 December 2010, revised 17 January 2011)

Abstract: β-Lactoglobulin (BLG) is an important nutrient of dairy products and an important allergen in cow's milk allergy. The aim of this study was to investigate the potential of laccase to cross-link BLG in the presence of an apple phenolic extract (APE) and to characterize the obtained products for their digestibility by pepsin and pancreatin. The composition of the apple phenolics used for cross-linking was determined by liquid chromatography–electrospray ionization-mass spectrometry (LC–ESI-MS). The apple phenolic extract contained significant amounts of quercetin glycosides, catechins and chlorogenic acid. The laccase cross-linked BLG in the presence of apple phenolics. The polymerization rendered the protein insoluble in the reaction mixture. Sodium dodecyl sulfate–polyacrylamide gel electrophoresis (SDS-PAGE) analysis of the cross-linking reaction mixture revealed a heterogeneous mixture of high molecular masses (cross-linked BLG), with a fraction of the BLG remaining monomeric. Enzymatic processing of BLG by laccase and apple polyphenols as mediators can decrease the biphasal pepsin–pancreatin digestibility of the monomeric and cross-linked protein, thus decreasing its nutritional value. In addition, reduced BLG digestibility can decrease its allergenic potential. Apple polyphenols can find usage in the creation of new, more functional food products, designed to prevent obesity and hypersensitivity-related disorders.

Keywords: apple polyphenols; β-lactoglobulin; laccase; allergen; digestibility.

INTRODUCTION

Enzymatic processing of food proteins for improvement of food texture and functionality is a good replacement for chemical additives. Laccase is a polyphenol oxidase that acts on phenolic compounds and can facilitate the cross-linking

* Corresponding author. E-mail: dstanic@chem.bg.ac.rs
# Serbian Chemical Society member.
doi: 10.2298/JSC101201077T

of proteins.[1–3] The cross-linking of tyrosine-containing peptides by laccase has been shown to proceed *via* tyrosyl radicals that form primarily isodityrosine, and also a small amount of dityrosine bonds.[4,5] The formation of disulfide bonds by the oxidation of cysteines into cystine is another way of cross-linking proteins, which laccase can induce in flour dough using ferulic acid as a mediator.[3] Enzymatic cross-linking of food proteins can have beneficial effect on their safety and can influence their digestibility by digestive enzymes.[6] Reductions of allergenicity were shown for beta-casein cross-linked by laccase/caffeic acid and tyrosinase/caffeic acid,[7] peanut proteins cross-linked by polyphenol oxidase,[8] roasted peanut allergens treated with peroxidase [9] and major cherry allergen exposed to tyrosinase in the presence of various polyphenols.[10] Thus, the usage of enzymes was anticipated as a novel approach for the production of hypoallergenic foods.[11]

β-Lactoglobulin (BLG) accounts for approximately 10–15 % of the total milk proteins.[12,13] It also represents a serious health risk in cow's milk allergic patients as it is known as one of the major milk allergens[14–16] and is one of the most resistant proteins to enzymatic digestion by pepsin.[17] Under physiological conditions, it is a very soluble protein, thereby easily passing the transepithelial barrier and is able to cause systematic anaphylactic reactions.[18] It was recently shown that enzymatic processing by laccase and the employment of sour cherry phenolic extract as the mediator of enzymatic reaction may improve BLG safety and availability of peptides following digestion by pepsin, while conserving its bioactivity.[19]

Apples contain significant levels of polyphenols, possessing strong antioxidative[20] and potent immunomodulatory activity.[21] Recently, plant polyphenols have been defined as one class of gammadelta T cell agonist and appear to preferentially activate the mucosal T cell population.[22]

In this study, the cross-linking potential of laccase on purified BLG in the presence of an apple polyphenol extract (APE), as a source of phenolic mediators, and the digestibility of cross-linked BLG under simulated conditions of the gastrointestinal tract were investigated.

EXPERIMENTAL

Chemicals

Pepsin (from porcine stomach mucosa, 2650 U mg^{-1} solid), pancreatin (from porcine pancreas), Folin–Ciocalteu's phenol reagent, gallic acid, ABTS (2,2'-azino-bis(3-ethylbenzothiazoline-6-sulfonic acid) and laccase (from *Trametes versicolor*, 30.6 U mg^{-1} of solid) were purchased from Sigma-Aldrich (Taufkirchen, Germany). Anti-rabbit IgG labeled with alkaline phosphatase was also from Sigma. Urea and disodium hydrogen phosphate (analysis grade) were purchased from Merck (Darmstadt, Germany). The deionized water (DW) used in the experiments was purified in a Milli-Q system (Millipore, Molsheim, France).

Purification of β-*lactoglobulin and determination of protein*

BLG was purified from raw milk essentially as described previously.[23] The purity of the protein was assessed by sodium dodecyl sulfate polyacrylamide gel electrophoresis (SDS–PAGE). The concentration of the BLG was determined by spectrophotometry at 280 nm (ε = 0.943 mg^{-1} mL cm^{-1}).

Preparation and characterization of the apple phenolics

Apple peel extract, 250 mg, (Applepoly, Apple Poly™, USA) was dissolved in 5 mL of HPLC grade ethanol, centrifuged for 15 min at 13400 rpm, and the supernatant was submitted to LC–MS analysis of the APE composition. The components of apple extract were identified according to their *m*/*z* values, UV/Vis absorption spectra and retention times. Relative quantities of phenolics were calculated from the peak areas on the chromatograms. The total phenolics in the APE were determined by spectrophotometric analysis using Folin–Ciocalteu's reagent [24] and are expressed as mg gallic acid equivalents (GAE)/100 mL of APE.

LC–MS analysis

Chromatographic separation was performed on Agilent 1100 series high-performance liquid chromatography–electrospray ionization-mass spectrometry-time of flight (HPLC–ESI-MS-TOF), equipped with a diode array detector (DAD). The separations were realized on a Zorbax C18 1.7 μm column (4.6 mm×50mm). The mobile phase consisted of water containing 0.1 % formic acid (A) and acetonitrile containing 0.1 % formic acid (B). The separation was performed on a linear gradient of acetonitrile in water (0–90 % B) during 20 min. The injection volume for all samples was 1 μL. Mass detection was performed on an Agilent 6520 TOF detector coupled to the chromatographic system. The mass spectra were obtained at a mass-to-charge ratio (*m*/*z*) scan range from 100 to 3200. The following MS parameters were used for the analysis: charging voltage, 2000 V; capillary voltage, 4000 V; nebulizer pressure, 45 psig; drying gas flow rate, 12 L min^{-1}. The samples were analyzed in the negative mode. Data was processed using Analyst QS 1.1 from Applied Biosystems and Chemspider database for the structure search.

Polymerization of apple phenolics by Trametes versicolor *laccase*

In order to obtain polymeric catechins, apple phenolics were treated with laccase. Laccase activity was determined using ABTS (2,2'-azinobis(3-ethylbenzothiazoline-6-sulfonic acid)) as the substrate.[3] 20 μL of laccase (0.1mg mL^{-1} final concentration) was added to 430 μL of apple phenolics extract (50 mg GAE mL^{-1}) and 50 μL of 200 mM acetic buffer pH 4.5. After incubation for 24 h at 37 °C, the mixture was centrifuged for 15 min at 13400 rpm and supernatant was submitted to LC–MS analysis.

Electrophoresis

SDS–PAGE was realized using a Hoefer Scientific Instrumentation apparatus (Amersham Biosciences, Uppsala, Sweden) with a discontinuous buffer system. The Protein components were resolved on 12 and 10 % polyacrylamide gels and stained using Coomassie Brilliant Blue R-250 (Sigma–Aldrich).

Cross-linking of BLG by laccase in the presence of APE

To prepare the laccase-treated samples, 1.6 mg mL^{-1} BLG, APE in the range of phenol concentration (0.06 to 0.99 mg mL^{-1} of gallic acid equivalents) and 30.95 U mL^{-1} laccase in 40 mM acetate buffer, pH 4.5 were incubated for 2 h at 37 °C with shaking and the reaction was stopped by addition of 1 mM ethylenediaminetetraacetic acid (EDTA) in final and the sample was immediately frozen. The control samples were prepared in the same manner but

the laccase and mediator were omitted. For digestibility analysis, cross-linked BLG was prepared using 0.33 mg mL^{-1} of gallic acid equivalents APE, 30.95 U mL^{-1} laccase and 1.6 mg mL^{-1} BLG in a reaction mixture of 0.6 mL. After cross-linking, the reaction mixture was centrifuged for 30 min at 12340 rpm. The pellet was washed with 50 mM acetate buffer pH 4.5 two times and pellet was resuspended in 0.6 mL of 50 mM acetate buffer.

Digestion of the cross-linked BLG by pepsin and pancreatin

In vitro gastric fluid digestion of BLG was performed as described previously,[23] with some modifications. Briefly, fifty microliters of BLG control and laccase-treated BLG (1.6 mg mL^{-1}), with or without APE solutions (0.24 mg mL^{-1} of GAE), were diluted with 10 μL of DW, warmed to 37 °C, and 20 μL of pre-warmed 0.4 M HCl containing 8 g L^{-1} of NaCl and 1.28 g L^{-1} of pepsin were added (1 U of pepsin/μg of protein). Digestion proceeded at 37 °C with continuous shaking for 18 h. The digestion was stopped with 5 μL of 2 M Na_2CO_3, and samples were vortexed vigorously and mixed with 21.25 μL of five times concentrated sample buffer for SDS–PAGE analysis. Thirteen microliters of each sample were applied per lane (10 μg of BLG, laccase-treated BLG or laccase/APE treated BLG per well). A pepsin control was set up in the same manner but with no addition of BLG. BLG, laccase-treated BLG and laccase/APE treated BLG controls were prepared without pepsin. For bi-phasal pepsin–pancreatin digestion, pepsin digestion was performed as described above and the digestion was stopped with 5 μL of 2 M Na_2CO_3. To 85 μL of the reaction mixture, 9.5 μL of pancreatin (10 mg mL^{-1}) in ten times concentrated phosphate buffered saline (PBS) was added and digestion proceeded for 4 h. An aliquot of 17 μL was diluted with 46 μL of water to make 63 μL of mixture for analysis, which was centrifuged at 13400 rpm for 20 min. Both supernatant and pellet samples (re-suspended in 32 μL of PBS) were mixed with five times concentrated sample buffer (16 and 8 μL, respectively) for SDS–PAGE analysis and the reaction of pancreatin digestion was stopped by boiling at 95 °C for 5 min.

RESULTS AND DISCUSSION

The main constituents of APE are chlorogenic acid, phloretine glucosides and mono-, di- and trimeric catechines (Fig. 1A, Table I). The composition of APE used in this study was similar to previously described phenolic contents of polyphenols extracted from apple peals, although the number of components was reduced because of extensive purification.[20] Exposing APE to laccase induced polymerization of the polyphenol compounds (Fig. 1A) giving extensive precipitate that could not be analyzed. The soluble fraction of APE treated with laccase was subjected to LC–MS analysis and the components identified are presented in Fig. 1B and Table I. It can be observed that the spectra of the untreated and laccase-treated APE are very similar. The only significant difference is the reduction in the (–)epicatechin content after treatment. The percent (–)epicatechin decreased from 25.74 to 14.17 % of the total phenolics after laccase treatment. A very slight increase in the concentration of procyanidine C (epicatechin trimer) was also observed, *i.e.*, from 3.63 % before laccase treatment to 4.8 % after, indicating that polymerization reactions occurred, depleting the content of catechin, and increasing the content of higher oligomers. Oligomers with more than 3 catechin units were not detected, probably due to the ionization techniques used and/or their precipitation from the reaction mixture.

APE was able to mediate the cross-linking of BLG by laccase. Proteins also became insoluble in the reaction mixture. Highly polymerized BLG could be seen at the top of the running and stacking gel after SDS PAGE. Increasing concentration of APE and ratio of APE: BLG did not increase the amount of the cross-linked protein, although an extensive pellet was obtained due to formation of condensed polyphenols (tannins). The tannin network apparently captures soluble BLG, resulting in its disappearance from the reaction mixture (Fig. 2). In addition, the products of enzymatic conversion of polyphenols were able to inhibit the laccase. Therefore, the BLG cross-linking could not proceed to completion. Similar results were obtained with sour cherry phenols-mediated cross-linking of BLG. A small truncation of the BLG could also be observed, due to the presence of endoprotease in the commercial laccase preparation.[23]

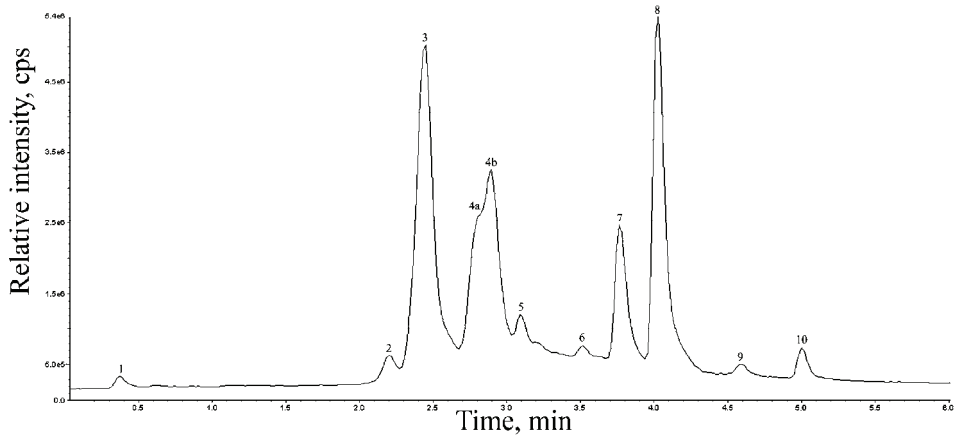

(A)

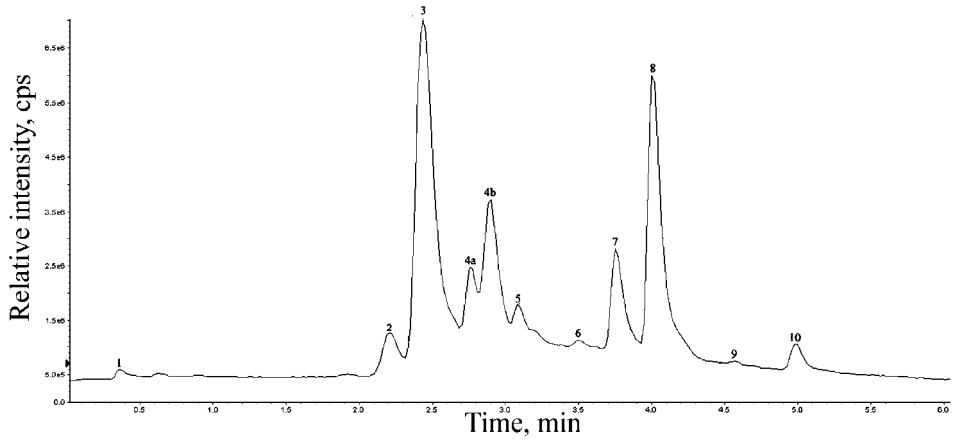

(B)

Fig 1. LC–MS chromatograms of apple phenolic extract: A) untreated B) treated with laccase.

TABLE I. The main phenol components of apple phenolic extract untreated and treated with laccase, determined by LC–ESI–MS

Main phenol components	*m/z*	Peak	Untreated APE		Laccase treated APE	
			t_R / min	% in extract	t_R / min	% in extract
Quinic acid	191	1	0.37	0.56	0.36	0.41
Proanthocyanidin B	577	2	2.20	1.57	2.21	3.42
Chlorogenic acid	353	3	2.44	31.72	2.4	38.19
Neochlorogenic acid	353	4a	2.80	n/a	2.76	5.92
Epicatechin, coumaroylquinic acid	289	4b	2.89	25.74	2.89	14.18
Proanthocyanidin C	865	5	3.09	3.63	3.08	4.81
Proanthocyanidin B, quercetin glucoside	577	6	3.51	0.79	3.50	0.57
Phloretin xyloglucoside	567	7	3.77	8.97	3.75	7.85
Phlorizin	435	8	4.02	23.35	4.00	22.89
Quercetine	301	9	4.59	0.59	4.59	0.31
Phloretin	273	10	5.00	1.63	4.99	1.77

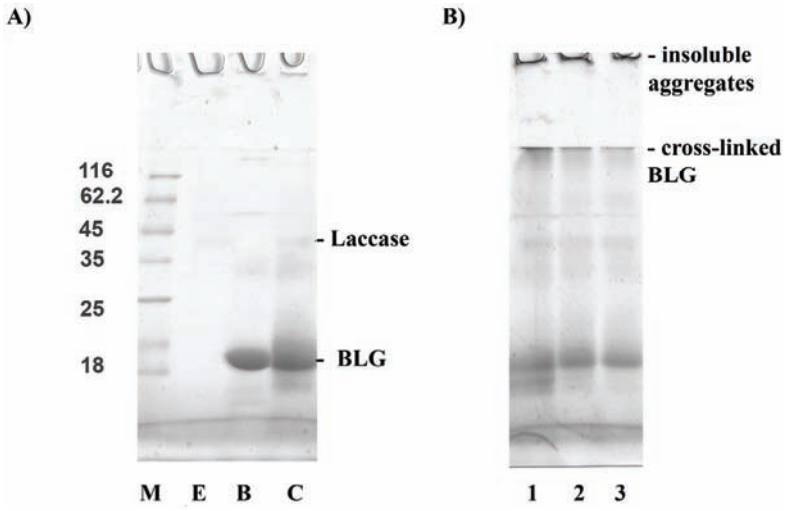

Fig 2. A) Cross-linking of BLG by laccase analyzed by 12 % SDS PAGE; M – molecular markers, E – laccase, B – BLG, C – APE/laccase cross-linked BLG. B) Influence of different concentration of APE on the cross-linking of BLG by laccase: 1 – 0.33 mg mL^{-1} GAE APE, 2 – 0.66 mg mL^{-1} GAE APE, 3 – 0.99 mg mL^{-1} GAE APE.

To test the metabolic prediction for novel proteins, *in vitro* studies with simulated digestive solutions have been widely used. Typically, most food allergens tend to be stable to the peptic and acidic conditions of the digestive system in order to reach and pass through the intestinal mucosa to elicit an allergic response. Therefore, consideration of the resistance of proteins to proteolytic digestion (digestion in simulated gastric or intestinal fluids or by pepsin) has been in-

cluded as one of the components of a comprehensive weight-of-evidence approach to assessing allergenic potential by Codex Alimentarius.[25] Cross-linked BLG was exposed to biphasal digestion by pepsin and pancreatin. Due to insolubility of the cross-linked BLG and the formed tannins, the excess of soluble proteins (laccase, BLG) and soluble polyphenols were removed from reaction mixture by centrifugation and several washing steps before digestion. The control (untreated BLG) was resistant to pepsin digestion, but very susceptible to pancreatin digestion (Fig. 3), as described previously.[26] Cross-linked BLG remained undigested by pancreatin, even after prolonged digestion. The undigested protein remaining in the insoluble fraction of the cross-linked BLG was probably protected from enzyme exposure by a complex network of condensed polyphenols.

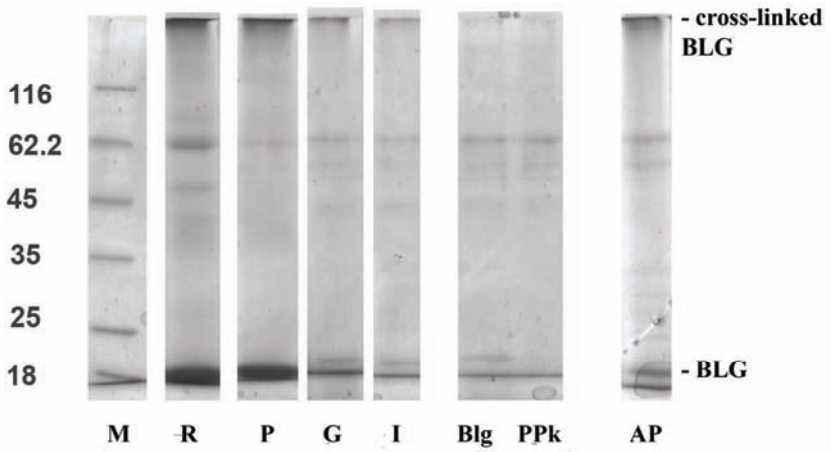

Fig 3. Digestibility of cross-linked BLG by pepsin and pepsin/pancreatin, analyzed by 10 % SDS PAGE; M – molecular markers, R – APE/laccase cross-linked BLG, P – resuspended APE/laccase cross-linked BLG after washing, G – pepsin digestion of APE/laccase cross-linked BLG, I – pepsin/pancreatin digestion of APE/laccase cross-linked BLG, Blg – pepsin/pancreatin digestion of BLG, PPk – control (pepsin and pancreatin), AP – insoluble pellet after pepsin/pancreatin digestion of APE/laccase cross-linked BLG.

It is well known that proteins resistant to both gastric and intestinal digestion are not allergenic. Very recently, the intestinal digestibility of gastric-resistant proteins has been proposed to have implications on oral tolerance to food allergens.[27] An intermediate digestion seems to be required to provide both sensitizing and lack of oral tolerance inducing the capability of a food sensitizer. The data from animal models also show that both gastric and intestinal-resistant allergens do not carry strong food allergy risk or induce oral tolerance, simply because both food allergy and oral tolerance are major histocompatibility complex (MHC) class II-dependent processes and require antigen presentation to the immune system, *i.e.*, readily available peptides in the intestinal fluids.[28] The im-

plications of the present findings are a decreased concentration of intact protein and larger peptides in the intestinal fluids in the case of APE-mediated cross-linking of BLG, leading to lower concentrations of allergen/allergenic peptides in the intestinal fluids. In addition, the anti-nutritive properties of APE-mediated cross-linking of food proteins could find employment in the creation of dietetic preparations, thus helping in the control of obesity and related disorders.

CONCLUSIONS

Apple polyphenolic extract is able to mediate enzymatic cross-linking of a major whey allergen, β-lactoglobulin, by laccase. Parallel formation of condensed products (tannins) and a protein-polyphenol network decreased the solubility of BLG and its digestibility by pepsin and pancreatin. The results of the study showed the potential of enzymatic processing in producing new and safer food with improved functional properties.

Acknowledgments. The authors acknowledge the financial support through the grant No. 172024 of the Ministry of Education and Science of the Republic of Serbia and the FP7 project FCUB ERA, GA No 256716.

И З В О Д

ДИГЕСТИБИЛНОСТ β-ЛАКТОГЛОБУЛИНА НАКОН ЊЕГОВОГ УНАКРСНОГ ПОВЕЗИВАЊА ДЕЈСТВОМ ЛАКАЗЕ ИЗ *Trametes versicolor* И ПОЛИФЕНОЛА ИЗ ЈАБУКЕ

ZIYAD TANTOUSH, ЛУКА МИХАЈЛОВИЋ, БОЈАНА КРАВИЋ, ЈАНА ОГЊЕНОВИЋ, РАТКО М. ЈАНКОВ, ТАЊА ЋИРКОВИЋ ВЕЛИЧКОВИЋ и ДРАГАНА СТАНИЋ-ВУЧИНИЋ

Хемијски факултет, Универзитет у Београду, Студентски трг 16, 11001 Београд

β-Лактоглобулин (BLG) је важан нутријент млечних производа и важан алерген код алергија на кравље млеко. Циљ ове студије је било испитивање потенцијала лаказе да унакрсно повеже BLG у присуству фенолног екстракта јабуке (APE), као и карактеризација добијених производа са аспекта њихове дигестибилности пепсином и панкреатином. Композиција фенола јабуке коришћених за унакрсно повезивање одређена је помоћу LC–ESI-MS. Фенолни екстракт јабуке садржи знатне количине гликозида кверцетина, катехине и хлорогенску киселину. BLG је унакрсно повезан лаказом у присуству фенола јабуке, при чему је полимеризација учинила BLG нерастворним у реакционој смеши. SDS-PAGE анализа показала је да реакциона смеша садржи хетерогену смешу великих молекулских маса (унакрсно повезан BLG), као и део заосталог мономерног BLG. Ензимско процесовање BLG лаказом, у присуству полифенола јабуке као медијатора, може смањити бифазну пепсин–панкреатинску дигестибилност како мономерног, тако и унакрсно повезаног BLG, и на тај начин смањити њеегову нутритивну вредност. Такође, смањена дигестибилност BLG може смањити његов алергени потенцијал. Полифеноли јабуке могу се користити за креирање нових, функционалнијих прехрамбених производа, дизајнираних за превенцију како гојазности, тако и болести везаних за преосетљивост.

(Примљено 1. децембра 2010, ревидирано 17. јануара 2011)

REFERENCES

1. L. Canfora, G. Iamarino, M. A. Rao, L. Gianfreda, *J. Agric. Food Chem.* **56** (2008) 1398
2. R. Lantto, E. Puolanne, K. Kruus, J. Buchert, K. Autio, *J. Agric. Food Chem.* **55** (2007) 1248
3. E. Selinheimo, K. Autio, K. Kruus, J. Buchert, *J. Agric. Food Chem.* **55** (2007) 6357
4. S. Rodriguez Couto, J. L. Toca Herrera, *Biotechnol. Adv.* **24** (2006) 500
5. K. Koschorreck, S. M. Richter, A. Swierczek, U. Beifuss, R. D. Schmid, V. B. Urlacher, *Arch. Biochem. Biophys.* **474** (2008) 213
6. T. Cirkovic Velickovic, J. Radosavljevic, D. Stanic, *CAB Rev.*: *Perspect. Agr. Vet. Sci. Nutr. Natl. Res.* **4** (2009) 1
7. D. Stanic, E. Monogioudi, E. Dilek, J. Radosavljevic, M. Atanaskovic-Markovic, O. Vuckovic, L. Raija, M. Mattinen, J. Buchert, T. Cirkovic Velickovic, *Mol. Nutr. Food Res.* **54** (2010) 1273
8. S. Y. Chung, Y. Kato, E. T. Champagne, *J. Sci. Food Agric.* **85** (2005) 2631
9. S. Y. Chung, S. J. Maleki, E. T. Champagne, *J. Agric. Food Chem.* **52** (2004) 4541
10. P. Gruber, S. Vieths, A. Wangorsch, J. Nerkamp, T. Hofmann, *J. Agric. Food Chem.* **52** (2004) 4002
11. E. N. Mills, A. R. Mackie, *Curr. Opin. Allergy Clin. Immunol.* **8** (2008) 249
12. D. W. Wong, W. M. Camirand, A. E. Pavlath, *Crit. Rev. Food Sci. Nutr.* **36** (1996) 807
13. G. Kontopidis, C. Holt, L. Sawyer, *J. Dairy Sci.* **87** (2004) 785
14. L. P. Shek, L. Bardina, R. Castro, H. A. Sampson, K. Beyer, *Allergy* **60** (2005) 912
15. G. Ball, M. J. Shelton, B. J. Walsh, D. J. Hill, C. S. Hosking, M. E. Howden, *Clin. Exp. Allergy* **24** (1994) 758
16. H. Y. Lam, E. van Hoffen, A. Michelsen, K. Guikers, C. H. van der Tas, C. A. Bruijnzeel-Koomen, A. C. Knulst, *Clin. Exp. Allergy* **38** (2008) 995
17. J. D. Astwood, J. N. Leach, R. L. Fuchs, *Nat. Biotechnol.* **14** (1996) 1269
18. F. Roth-Walter, M. C. Berin, P. Arnaboldi, C. R. Escalante, S. Dahan, J. Rauch, E. Jensen-Jarolim, L. Mayer, *Allergy* **63** (2008) 882
19. Z. Tantoush, D. Stanic, M. Stojadinovic, J. Ognjenovic, L. Mihajlovic, M. Atanaskovic-Markovic, T. Cirkovic Velickovic, *Food Chem.* **125** (2011) 84
20. G. M. Huber, H. P. Rupasinghe, *J. Food Sci.* **74** (2009) C693
21. M. Jung, S. Triebel, T. Anke, E. Richling, G. Erkel, *Mol. Nutr. Food Res.* **53** (2009) 1263
22. J. Holderness, J. F. Hedges, K. Daughenbaugh, E. Kimmel, J. Graff, B. Freedman, M. A. Jutila, *Crit. Rev. Immunol.* **28** (2008) 377
23. D. Stanic, J. Radosavljevic, N. Polovic, M. Jadranin, M. Popovic, O. Vuckovic, L. Burazer, R. Jankov, T. Cirkovic Velickovic, *Int. Dairy J.* **19** (2009) 746
24. E. A. Ainsworth, K. M. Gillespie, *Nat. Protoc.* **2** (2007) 875
25. Codex Alimentarius Commission, *Alinorm 03/34: Appendix III. Guideline for the conduct of food safety assessment of foods derived from recombinant DNA plants*; *Annex IV. Annex on the assessment of possible allergenicity*, Rome, Italy, 2003, p. 47
26. T. T. Fu, U. R. Abbott, C. Hatzos, *J. Agric. Food Chem.* **50** (2002) 7154
27. C. C. Bowman, M. K. Selgrade, *Toxicol. Sci.* **102** (2008) 100
28. C. C. Bowman, M. K. Selgrade, *Toxicol Sci.* **106** (2008) 435.

Journal of the Serbian Chemical Society
JSCS-info@shd.org.rs • www.shd.org.rs/JSCS
J. Serb. Chem. Soc. 76 (6) 857–863 (2011)
JSCS–4166
UDC *Dorema ammoniacum*:665.52/.54:615.28–188(55)
Original scientific paper

Composition and *in vitro* antimicrobial activity of the essential oil of *Dorema ammoniacum* D. Don. fruit from Iran

MORTEZA YOUSEFZADI[1]*, MOHAMMAD HOSSEIN MIRJALILI[2], NABA ALNAJAR[3], AMINEH ZEINALI[1] and MITRA PARSA[1]

[1]Department of Ecology and Systematic, Research Institute of Applied Science, ACECR, Shahid Beheshti University. Tehran, [2]Department of Agriculture, Medicinal Plants and Drugs Research Institute, Shahid Beheshti University, G. C., Tehran and [3]Department of Biology, Faculty of Science, Shahid Beheshti University, Tehran, Iran

(Received 30 August, revised 1 November 2010)

Abstract: The genus *Dorema* (Apiaceae) is represented in the flora of Iran with seven species of which two, *D. ammoniacum* D. Don. and *D. aucheri* Boiss. are endemic. Ripe fruits of *D. ammoniacum* collected just in the deciduous time were subjected to hydrodistillation to yield the essential oil, which was subsequently analyzed by GC and GC–MS. Twenty-nine compounds were identified and quantified, representing 95.1 % of the total oil. (*Z*)-Ocimenone (22.3 %) and (*E*)-ocimenone (18.1 %) were the main components of the oil. *In vitro* antimicrobial activity of the oil was evaluated against seven Gram-positive and Gram-negative bacteria (*Bacillus subtilis*, *Enterococcus faecalis*, *Staphylococcus epidermidis*, *Staphylococcus aureus*, *Escherichia coli*, *Pseudomonas aeruginosa* and *Klebsiella pneumoniae*) and three fungi (*Candida albicans*, *Saccharomyces cerevisiae* and *Aspergillus niger*). The results of the antimicrobial assay of the oil by the disc diffusion method and the MIC *values* indicated that the oil exhibited moderate to high antimicrobial activity, especially against *B. subtilis and S. epidermidis* with *MIC* value of 3.75 mg ml^{-1}.

Keywords: *Dorema ammoniacum*; Apiaceae; essential oil composition; antimicrobial activity; ocimenone; (*Z*)-ocimenone; (*E*)-ocimenone.

INTRODUCTION

Essential oils obtained from many plants have recently gained in popularity and scientific interest. Many plants are used for different purposes, such as food, drugs and perfumes. Researchers are interested in biologically active compounds isolated from plant species for the eradication of pathogenic microorganisms because of the resistance that microorganisms have acquired against antibiotics.[1]

* Corresponding author. E-mail: morteza110110@gmail.com
doi: 10.2298/JSC100830074Y

The genus *Dorema* D. Don. (Apiaceae) is represented in the flora of Iran by seven species, among which two are endemic, *D. ammoniacum* D. Don. and *D. aucheri* Boiss.[2,3] *D. ammoniacum*, a vulnerable species, grows to a height of about 1–2 m and in spring and early summer contains a milky juice. It is one of the most important endemic medicinal plants in many arid and semi-arid regions of Iran, such as the Yazd, Isfahan and Semnan provinces, which are known by the local Persian names of Kandal, Vasha and Koma-kandal.[2–4] *D. ammoniacum* produces a medicinal gum resin, commonly known as ammoniacum gum, which is found in cavities in stems, roots, and petioles.[5] The resin exudes from punctures in the stem, which can occur from insect attack. The resin serves as a carminative, diaphoretic, mild diuretic, expectorant, poultice, stimulant, antimicrobial, and vasodilator agent.[6] It is still used in Indian and Western Medicine and is listed in the British pharmacopoeia[4] as an antispasmodic and expectorant. It is occasionally used for chronic bronchitis and persistent coughs.[5] The antimicrobial activity of the dichloromethane–methanol (1:1) extract of the plant gum was previously reported.[7] A literature survey revealed that the essential oil compositions of *D. aucheri* aerial parts[8] and *D. ammoniacum* leaves[9] have already been reported. However, the chemical composition and antimicrobial activity of the essential oil of *D. ammoniacum* fruit has not hitherto been investigated, and hence the present study was focused on the possible uses of this oil in pharmacy and pathogenic systems.

EXPERIMENTAL

Plant material

Ripe fruits of *D. ammoniacum* were collected just in deciduous time from the Semnan Road toward Firoozkuh after Bashm Defile (35° 46’ 11” N, 52° 52’ 38” E and altitude of 1300 m), Semnan Province, Iran. A voucher specimen (AS-85406) was deposited at the Herbarium of Ecology and Systematic Department, Research Institute of Applied Science, Shahid Beheshti University, Tehran, Iran.

Isolation of the essential oil

Dried fruits of the plant (500 g) were hydrodistilled using a Clevenger type apparatus for 3 h according to the method recommended in the British Pharmacopoeia (1993).[10] The resulting essential oil was dried over anhydrous sodium sulfate and stored at 4 °C until analyzed and tested.

GC and GC–MS analyses

The GC–FID analysis of the oil was conducted using a Thermoquest-Finnigan instrument equipped with a DB-5 fused silica column (60 m×0.25 mm i.d., film thickness 0.25 μm). Nitrogen was used as the carrier gas at the constant flow of 1.1 ml min^{-1}. The split ratio was 1.50. The oven temperature was increased from 60 to 250 °C at a rate of 5 °C min^{-1}. The injector and detector (FID) temperatures were maintained at 250 and 280 °C, respectively. The GC–MS analysis was performed on a Thermoquest-Finnigan Trace GC–MS instrument equipped with the same column and temperature programming as given for the GC analysis. The transfer line temperature was 250 °C. Helium was used as the carrier gas at a flow rate of

1.1 ml min^{-1} with a split ratio of 1/50. The constituents of the essential oil were identified by calculation of their retention indices under temperature-programmed conditions for *n*-alkanes (C6–C24) and the oil on a DB-5 column under the same conditions. Identification of individual compounds was made by comparison of their mass spectra with those of the internal reference mass spectra library (Wiley 7.0) or of authentic compounds and confirmed by comparison of their retention indices with those of authentic compounds or with those reported in the literature.[11] Semi-quantitative data was obtained from the FID area percentages without the use of correction factors.

Microbial strains

Ten microbial strains were used which included; *Bacillus subtilis* (ATCC 465), *Enterococcus faecalis* (ATCC 29737), *Staphylococcus aureus* (ATCC 25923), *Staphylococcus epidermidis* (ATCC 12228), *Escherichia coli* (ATCC 25922), *Klebsiella pneumoniae* (ATCC 10031), *Pseudomonas aeruginosa* (ATCC 85327), *Aspergillus niger* (ATCC 16404), *Candida albicans* (ATCC 10231) and *Saccharomyces cerevisiae* (ATCC 9763).

Antimicrobial screening

The antimicrobial activity of essential oil was determined by the disk diffusion method.[12] Briefly, 0.1 ml of a suspension of the test microorganism (10^8 cells ml^{-1}) was spread on Mueller–Hinton Agar plates for bacteria and Sabouraud Dextrose Agar for the fungi. Sterile 6 mm disks, each containing 10 µl of essential oil were placed on the microbial lawns. The plates were incubated at 37 °C for 24 h for the bacteria and at 30 °C for 48 h for the fungi. The diameters of the zones of inhibition were measured and are reported in mm. Triplicate tests were performed in all experiments.

*Determination of minimum inhibitory concentration (*MIC*)*

The *MIC* values were determined by the broth microdilution assay.[13] Serial two-fold dilutions of the essential oil were made in Mueller–Hinton Broth containing 0.5 % Tween 80 for the bacteria and Sabouraud Dextrose Broth with 0.5 % Tween 80 for the fungi in 96-well micro titer plates. Fresh microbial suspensions prepared from overnight-grown cultures in the same media were added to give a final concentration of 5×10^5 organisms ml^{-1}. Controls of medium with microorganisms or the essential oil alone were included. The microplates were incubated at 37 °C for 24 h for the bacteria and 30 °C for 48 h for the fungi. The first dilution with no microbial growth was recorded as the *MIC*.

RESULTS AND DISCUSSION

Essential oil analysis

The hydrodistillation of *D. ammoniacum* fruits gave a yellow oil in 0.09 % (w/w) yield, based on the dry weight of the fruit. Twenty-nine components were identified representing 95.1 % of the total oil. The qualitative and quantitative essential oil compositions are presented in Table I, in which the compounds are listed in order of their elution on the DB-5 column. The major constituents of the oil were (*Z*)-ocimenone (22.3 %), (*E*)-ocimenone (18.1 %) and *β*-cyclocitral (9.9 %). (*Z*)- and (*E*)-ocimenone were previously reported as the main compounds of the essential oil of *Ferula latisecta* (Apiaceae).[14] The classification of the identified compounds based on the major groups is summarized at the end of Table I and shows that oxygenated monoterpenes (58.4 %) were the main group of com-

pounds. In an earlier investigation on the essential oil composition of *D. ammoniacum* leaves,[9] α-gurjunene (49.5 %), β-gurjunene (19.0 %) and α-selinene (4.6 %) were found to be the main constituents while, in the present study, (*Z*)- and (*E*)-ocimenone, β-cyclocitral and *ar*-curcumene were characterized as the major components, which could be attributed to their ecological variability or plant part. Masoudi *et al*. reported α-eudesmol (31.2 %) and δ-cadinene (10.9 %) as the main components of the essential oil of *D. aucheri* aerial part.[8]

TABLE I. Essential oil composition of *D. ammoniacum* fruit (*RI*: retention indices relative to C6–C24 *n*-alkanes on a DB-5 column)

No.	Compound	*RI*	Content, %
1	1,3,8-*p*-Menthatriene	1119	0.5
2	(*E*)-Tagetone	1126	2.2
3	(*Z*)-Tagetone	1133	3.2
4	(*E*)-5-Undecen-3-yne	1163	0.7
5	*trans*-2-Caren-4-ol	1178	2.2
6	β-Cyclocitral	1189	9.9
7	(*Z*)-Ocimenone	1213	22.3
8	(*E*)-Ocimenone	1220	18.1
9	*p*-Mentha-1,8-diene	1246	0.5
10	Piperitenone oxide	1293	0.5
11	α-Cubebene	1356	0.4
12	α-Copaene	1385	3.2
13	β-Bourbonene	1395	4.1
14	Italicene	1414	1.0
15	Di-epi-α-Cedrene	1427	2.9
16	α-Longipinene	1430	0.9
17	β-Cedrene	1433	0.5
18	β-Barbatene	1457	3.0
19	α-Humulene	1462	1.1
20	*ar*-Curcumene	1475	6.4
21	(*Z*)-(*E*)-Farnesene	1481	0.6
22	Germacrene D	1487	3.0
23	Bicyclogermacrene	1502	0.9
24	Cuparene	1506	2.9
25	δ-Cadinene	1522	0.8
26	Spathulenol	1576	1.2
27	Caryophyllene oxide	1583	0.7
28	Heptadecanoic acid	2069	1.4
Monoterpene hydrocarbons		–	1
Oxygenated monoterpenes		–	58.4
Sesquiterpene hydrocarbons		–	31.7
Oxygenated sesquiterpenes		–	1.9
Others		–	2.1
Total identified		–	95.1

Antimicrobial activity

The essential oil of *D. ammoniacum* was tested against four Gram-positive and three Gram-negative bacteria, as well as three fungi. The results of antimicrobial activity of the essential oil according to the disc diffusion method and *MIC* values indicated that the essential oil has moderate to high inhibitory activity against the tested bacteria, except for two microorganisms, *P. aeruginosa* and *A. niger* (Table II). The most sensitive microorganisms were *B. subtilis*, *S. epidermidis* and *S. aureus* with inhibition zones of 23, 22, 17 mm and *MIC* values of 3.75, 3.75 and 7.5 mg ml^{-1}, respectively. Five microbial strains, *E. coli*, *E. faecalis*, *K. pneumoniae*, *S. cerevisiae* and *C. albicans* were found to be less sensitive to the oil. The obtained results showed that Gram-negative bacteria and fungi are more tolerant to the antimicrobial activity of the essential oil than Gram-positive bacteria.

TABLE II. Antimicrobial activity of the essential oil of *D. ammoniacum* fruit (values are given as means ± standard deviation)

Microorganism	Essential oil		Standard antibiotics					
			Tetracycline (30 μg disc^{-1})		Gentamicin (10 μg disc^{-1})		Nystatine (30 μg disc^{-1})	
	IZ[a]	*MIC*[b]	*IZ*	*MIC*	*IZ*	*MIC*	*IZ*	*MIC*
B. subtilis	23±0.2	3.75	21±0.8	3.2	–	nt	nt	nt
E. faecalis	13±0.4	15	9±0.4	6.4	–	nt	nt	nt
S. aureus	17±0.3	7.5	20±0.4	3.2	–	nt	nt	nt
S. epidermidis	22±0.8	3.75	34±0.8	1.6	–	nt	nt	nt
E. coli	14±0.2	15	–	nt	23±0.8	3.2	nt	nt
K. pneumoniae	12±0.4	15	–	nt	20±0.8	3.2	nt	nt
P. aeruginosa	–	nt	–	nt	12±0.4	6.4	nt	nt
A. niger	–	nt	nt	nt	nt	nt	16±0.4	6.4
C. albicans	10±0.4	>10	nt	nt	nt	nt	18±0.4	3.2
S. cerevisiae	11±0.2	>10	nt	nt	nt	nt	18±0.8	1.6

[a]Zone of inhibition (in mm) includes diameter of the disc (6 mm); [b]minimum inhibitory concentration values as mg ml^{-1}. (–) inactive; (7–13) moderately active; (> 14) highly active; nt, not tested

CONCLUSIONS

Chemical characterization and antimicrobial screening studies on plant-based essential oils could lead to the discovery of new natural antimicrobials. Although the antimicrobial activity of the dichloromethane–methanol (1:1) extract of the plant gum was previously studied,[7] the present study is the first report on the antimicrobial activity of the essential oil from the fruits of *D. ammoniacum*. The oil showed promising antimicrobial activity against *B. subtilis*, *S. epidermidis* and *S. aureus*. Rajani *et al*. reported that ammoniacum gum extract has excellent antimicrobial activity.[7] The present results also indicate that the essential oil of *D. ammoniacum* has antimicrobial activity; hence a scientific basis is

provided for the traditional use of *D. ammoniacum* for bronchitis, respiratory infections, fever, cold and flu.[7]

Acknowledgement. We are grateful to the Academic Center for Education, Culture and Research (ACECR) for financial support of this work (Grant No.: 1542-11).

ИЗВОД

САСТАВ И АНТИМИКРОБНА АКТИВНОСТ ЕТАРСКОГ УЉА ПЛОДА *Dorema ammoniacum* D. DON. ИЗ ИРАНА

MORTEZA YOUSEFZADI[1], MOHAMMAD HOSSEIN MIRJALILI[2], NABA ALNAJAR[3], AMINEH ZEINALI[1] и MITRA PARSA[1]

[1]*Department of Ecology and Systematic, Research Institute of applied science, ACECR, Shahid Beheshti University, Tehran,* [2]*Department of Agriculture, Medicinal Plants and Drugs Research Institute, Shahid Beheshti University, G. C., Tehran и* [3]*Department of Biology, Faculty of Science, Shahid Beheshti University, Tehran, Iran*

Род *Dorema* (Apiaceae) у Ирану представља седам врста биљака, од којих су две ендемске: *D. ammoniacum* D. Don. и *D. aucheri* Boiss. Зрели плодови *D. ammoniacum* су подвргнути дестилацији воденом паром ради добијања етарског уља које је анализирано методама GC и GC–MS. Идентификовано је двадесет девет састојака који су чинили 95,1 % уља. (*Z*)-оцименон (22,3 %) и (*E*)-оцименон (18,1 %) су били главни састојци. *In vitro* антимикробна активност уља је тестирана спрам седам Грам-позитивних и Грам-негативних бактерија (*Bacillus subtilis*, *Enterococcus faecalis*, *Staphylococcus epidermidis*, *Staphylococcus aureus*, *Escherichia coli*, *Pseudomonas aeruginosa* и *Klebsiella pneumoniae*) и три гљиве (*Candida albicans*, *Saccharomyces cerevisiae* и *Aspergillus niger*). Метода дифузије на диску и *MIC* вредности су показали да уље има средњу до велику антимикробну активност, посебно спрам *B. subtilis* и *S. epidermidis*, уз *MIC* вредност од 3,75 mg ml^{-1}.

(Примљено 30. августа, ревидирано 1. новембра 2010)

REFERENCES

1. B. Tepe, D. Daferera, A. Sokmen, M. Sokmen, M. Polissiou, *Food Chem*. **90** (2005) 333
2. V. Mozaffarian, *A Dictionary of Iranian Plant Names*, Farhang Moaser, Tehran, Iran, 1996, p. 190
3. V. Mozaffarian, *Bot. Zhurn. (Leningrad)* **88** (2003) 88
4. K. H. Rechinger, *Flora Iranica*. *Umbelliferae*, Akademische Druck- und Verlagsanstalt, Graz, Austria, 1980, p. 380
5. J. H. Langenheim, *Plant resins: chemistry, evolution, ecology, and ethnobotany*, Timber Press, Portland, OR, USA, 2003, p. 412
6. N. Irvani, M. Solouki, M. Omidi, A. Z. Zare, S. Shahnazi, *Plant Cell Tiss. Organ Cult.* **100** (2010) 293
7. M. Rajani, N. Saxena, M. N. Ravishankara, N. Desai, H. Padh, *Pharm. Biol*. **40** (2002) 534
8. S. Masoudi, A. Esmaeili, M. A. Khalilzadeh, A. Rustaiyan, N. Moazami, M. R. Akhgar, M. Varavipoor, *Flavour Fragr. J.* **21** (2006) 801
9. S. E. Sajjadi, N. Ghassemi, P. Mohammadzamani, *Revue des régions Arides* **1** (2007) 194
10. British pharmacopoeia, HMSO, London, UK, 1993

11. R. P. Adams, *Identification of essential oils components by gas chromatogramphy/quadrupole mass spectroscopy*, Allured Publishing Co., Carol Stream, IL, USA, 2001
12. National Committee for Clinical Laboratory Standards (NCCLS), *Performance standards for antimicrobial disk susceptibility test*, 6th ed., Approved Standard, M100-A6, Wayne, PA, USA, 1997
13. National Committee for Clinical Laboratory Standard (NCCLS), *Performance standards for antimicrobial susceptibility testing*, 9th International Supplement, M100-S9, Wayne, PA, USA, 1999
14. Z. Habibi, P. Salehi, M. Yousefi, Y. Hejazi, A. Laleh, V. Mozaffarian, S. Masoudi, A. Rustaiyan, *Chem. Nat. Compd*. **42** (2006) 689.

Journal of the Serbian Chemical Society
JSCS-info@shd.org.rs • www.shd.org.rs/JSCS
J. Serb. Chem. Soc. *76* (6) 865–877 (2011)
JSCS–4167
UDC 546.881–31+547.576:548.7:543.422.25
Original scientific paper

Transition metal complexes with thiosemicarbazide-based ligands. Part 58. Synthesis, spectral and structural characterization of dioxovanadium(V) complexes with salicylaldehyde thiosemicarbazone

LJILJANA S. VOJINOVIĆ-JEŠIĆ[#], VUKADIN M. LEOVAC*[#], MIRJANA M. LALOVIĆ[#], VALERIJA I. ČEŠLJEVIĆ[#], LJILJANA S. JOVANOVIĆ[#], MARKO V. RODIĆ[#] and VLADIMIR DIVJAKOVIĆ

Faculty of Sciences, University of Novi Sad, Trg D. Obradovića 3, 21000 Novi Sad, Serbia

(Received 17 December 2010, revised 24 January 2011)

Abstract: The first two complexes of dioxovanadium(V) with salicylaldehyde thiosemicarbazone (SALTSC), of the coordination formulas $[VO_2(SALTSC–H)]\cdot H_2O$ (**1**) and $NH_4[VO_2(SALTSC–2H]$ (**2**), were synthesized and characterized by elemental analysis, conductometric measurements, IR and UV–Vis spectroscopy and X-ray analysis. The complexes were obtained in the reaction of an aqueous ammoniacal solution of NH_4VO_3 and SALTSC. The results of the characterization showed that SALTSC was coordinated in the usual ONS tridentate mode as monoanion in complex **1** and dianion in complex **2**. In both complexes, the vanadium atom is in a deformed square-pyramidal environment and is slightly shifted towards the apical oxo-ligand (≈ 0.52 Å).

Keywords: dioxovanadium(V) complexes; salicylaldehyde thiosemicarbazone; crystal structure; spectra.

INTRODUCTION

Thiosemicarbazones have been the subject of studies not only for coordination chemistry reasons, but for pharmacological as well, due to their good complexing properties and significant biological activity.[1] Among the most examined compounds of this group is certainly salicylaldehyde thiosemicarbazone (SALTSC) and its metal complexes.

Usually, SALTSC is coordinated as a tridentate monoanionic ligand through the oxygen atom of the deprotonated phenolic OH-group, the azomethine nitrogen atom N3 and the thionic sulfur atom. The result of such coordination is the formation of two metallocycles: a six-membered (salicylidene) and five-mem-

* Corresponding author. E-mail: vukadin.leovac@dh.uns.ac.rs
# Serbian Chemical Society member.
doi: 10.2298/JSC101217078V

bered (thiosemicarbazide) (Fig. 1a). Experiments have shown that SALTSC can also be coordinated as a tridentate dianion (Fig. 1b) after deprotonation of the thiosemicarbazide residue in its thiol form, which is regulated by the pH value. Another two coordination modes of this ligand are bidentate through N3 and S1, by which one 4-membered metallocycle is formed (Fig. 1c)[2] and monodentate through S1.[3] Only one exception to this rule is known and that is the complex of MoO_2(VI), in which SALTSC is coordinated as a tridentate ONN ligand, *via* the amide N1 atom instead of the usual thionic S1 atom (Fig. 1d).[4] This coordination mode is characteristic for *S*-alkyl-thiosemicarbazide derivates, *i.e.* isothiosemicarbazides and isothiosemicarbazones.[5]

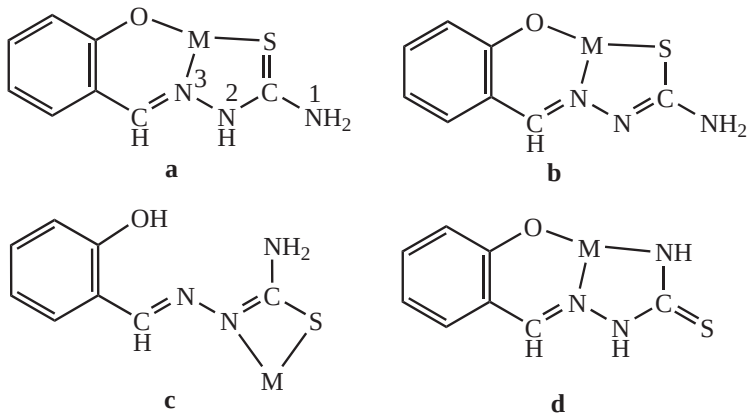

Fig. 1. Selected coordination modes of SALTSC.

The syntheses of the complexes [V(SALTSC–H)(SALTSC–2H)], NH_4[V(SALTSC–2H)$_2$] and [VO(SALTSC–2H)A] (A = *o*-phen, α,α'-dipy) confirm that this versatile ligand can stabilize +3 and +4 oxidation states of vanadium.[6,7] The two new complexes of VO_2^+(V), of the formulas [VO_2(SALTSC–H)]·H_2O and NH_4[VO_2(SALTSC-2H)], presented in this paper, certify that the SALTSC can stabilize the maximum oxidation state of vanadium.

EXPERIMENTAL

Reagents

All chemicals used were commercial products of analytical reagent grade, except for the ligand salicylaldehyde thiosemicarbazone, which was prepared by the reaction of EtOH solutions of salicylaldehyde and thiosemicarbazide.[8]

Synthesis of the complexes

*[VO_2(SALTSC-H)]·H_2O (**1**) and NH_4[VO_2(SALTSC-2H)] (**2**).* A mixture of NH_4VO_3 (0.060 g, 0.5 mmol) and SALTSC (0.098 g, 0.5 mmol) was overpoured with 5 cm^3 ccNH_3 (aq) and heated for 5 min to complete the dissolution. After 12 days of standing at the room

temperature, the yellow (**1**) and orange (**2**) single crystals obtained from the orange solution were filtered and washed with EtOH. Yield (of the mixture): 0.025 g.

Analytical methods

Elemental analyses (C, H, N and S) of air-dried complexes were realized by standard micromethods in the Center for Instrumental Analyses, ICTM in Belgrade.

Molar conductivities of freshly prepared H_2O and DMF complex solutions ($c = 1.0\times10^{-3}$ mol dm^{-3}) were measured on a Jenway 4010 conductivity meter.

IR spectra were recorded using KBr pellets on a Thermo Nicolet (NEXUS 670 FTIR) spectrophotometer in the range of 4000–400 cm^{-1}.

UV–Vis spectra in DMF solutions were recorded on a T80+ UV/Vis spectrometer PG Instruments Ltd., in the spectral range of 270–1100 nm.

*Single crystal X-ray experiment of [VO_2(SALTSC–H)]·H_2O (**1**) and NH_4[VO_2(SALTSC–2H)] (**2**)*

Single crystals of **1** and **2** were selected and glued on a glass fiber. Diffraction measurements were performed on an Oxford Diffraction Gemini S diffractometer equipped with a Sapphire CCD detector. The crystal to detector distance was 45 mm, and graphite monochromated MoKα (0.71073 Å) radiation was used. The data were reduced using the Oxford Diffraction program CrysAlisPRO. A semi-empirical absorption-correction was applied, and the data were corrected for Lorentz, polarization, and background effects. The structures were solved by the direct method using SIR92[9] and refinement was performed by full-matrix least-square methods on F^2 using the SHELXL-97 program.[10] All non-H atoms were refined with anisotropic displacement parameters. The positions of all H atoms were found by inspection of ΔF maps. In the final stage of refinement, the H atoms belonging to SALTSC were positioned geometrically (N–H, 0.86; C–H, 0.93 and 0.97 Å for CH and CH_3, respectively) and refined using the riding model with U_{iso} equal to 1.2 (for NH and CH) and 1.5 (for CH_3) U_{eq} of the parent atoms. Positions of the H atoms corresponding to H_2O in complex **1** and NH_4^+ in **2** were refined with restrained N–H and O–H distances (O–H = 0.82; N–H = 0.86 Å) with U_{iso} equal to 1.5 U_{eq} of the parent atoms. The material for publication was prepared by the WINGX[11] and PLATON[12] programs. The crystal data and refinement parameters are listed in Table I.

TABLE I. Crystal data and refinement parameters for [VO_2(SALTSC–H)]·H_2O (**1**) and NH_4[VO_2(SALTSC–2H)] (**2**)

Empirical formula	$C_8H_{10}N_3O_4SV$ (**1**)	$C_8H_{11}N_4O_3SV$ (**2**)
Formula weight	295.19	294.21
Temperature, K	295(2)	295(2)
Wavelength, Å	0.71073	0.71073
Crystal system	Monoclinic	Monoclinic
Space group	*Cc*	$P2_1/c$
Unit cell dimensions, Å	a = 7.7751(3)	a = 14.104(5)
	b = 11.2828(5)	b = 6.363(5)
	c = 12.8995(4)	c = 13.829(5)
	β = 92.254(4)°	β = 113.169(5)°
Volume, Å^3	1130.73(8)	1141.0(11)
Z	4	4
D_c, g cm^{-3}	1.734	1.713
Absorption coefficient, μ / mm^{-1}	1.068	1.054

TABLE I. Continued

$F(000)$	600	600
Crystal size, mm	0.5 × 0.2 × 0.1	0.6 × 0.3 × 0.1
Color/shape	Yellow/prism	Orange/prism
Theta range, °	3.16–25.00	2.96–25.00
Index ranges $-h\ +h$; $-k\ +k$; $-l\ +l$	–9 +7; –9 +13; –15 +14	–10 +16; –7 +7; –16 +16
Reflections collected	2307	5554
Unique reflections	1433 (R_{int} = 0.0204)	2011 (R_{int} = 0.0285)
Reflections with $I > 2\sigma I_o$	1346	1680
Refinement methods	Full matrix L. S. on F^2	Full matrix L. S. on F^2
Data/restraints/parameters	1433/2/162	2011/4/170
Goodness-of-fit on F^2	1.045	1.101
Final R indices [$F_o > 4\sigma F_o$]	$R1$ = 0.0308	$R1$ = 0.0398
R indices (all data)	$R1$ = 0.0338, $wR2$ = 0.0654	$R1$ = 0.0519, $wR2$ = 0.0921
Extinction coefficient	no	no
Larg. diff. peak and hole, eÅ^{-3}	0.26 and –0.21	0.36 and –0.23

RESULTS AND DISCUSSION

Synthesis

The ligand, SALTSC, was obtained by the reaction of warm EtOH solutions of salicylaldehyde with thiosemicarbazide in the mole ratio 1:1. The reaction of warm ammonia solutions of NH_4VO_3 and SALTSC in a mole ratio 1:1 resulted in the formation of two types of complexes: the neutral yellow [VO_2(SALTSC–H)]·H_2O (**1**) and the monoanionic orange NH_4[VO_2(SALTSC–2H)] (**2**) (Scheme 1). In both complexes, SALTSC is coordinated in its usual ONS tridentate mode as a monoanion (complex **1**), formed by the deprotonation of the phenolic hydroxyl, and as a dianion (complex **2**), formed by further deprotonation of the thioureido –NH–C(=S)–NH_2 group.

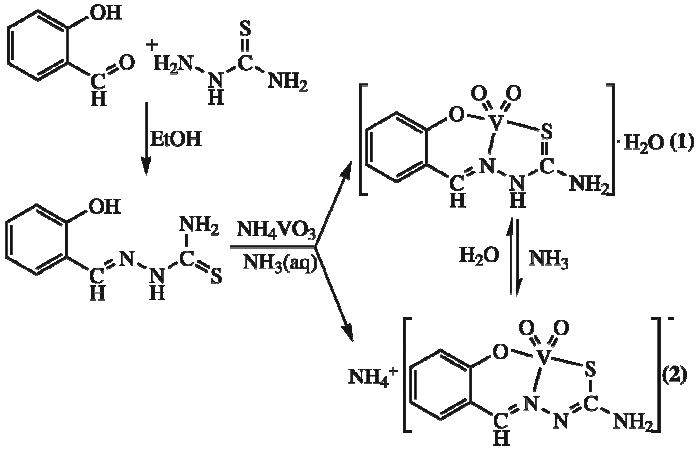

Scheme 1. Reaction scheme for the synthesis of SALTSC ligand.

Magnetic measurements showed that the obtained complexes are diamagnetic, which is further evidence of the isolation of V(V) complexes.

Complexes are stable in air, soluble in DMF, and sparingly soluble in MeOH and EtOH. Unlike complex **1**, complex **2** is soluble in water.

Molar conductivity of **1** in DMF indicates its non-electrolytic nature while the molar conductivity of **2** in both H_2O and DMF points to 1:1 electrolyte type, which is in accordance with the coordination formulas.[13,14]

Since **2** is a strong base, the protonation of the nitrogen atom N2 of the coordinated thiosemicarbazide moiety in aqueous solution leads to the formation of **1**. The reconversion to the complex **2** can be achieved by deprotonation of the neutral complex **1** in NH_3. A similar reversible reaction was described for the complex $NH_4[VO_2(salhyph)]$, where salhyph stands for the dianion of the tridentate ONO Schiff base derived from salicylaldehyde and benzoic acid hydrazide.[15]

The presented reactions involved no essential chemical transformations of SALTSC. This is emphasized here because it is known that the reaction in a similar environment, *i.e.*, aqueous–ammonia solution of $VOSO_4$ and SALTSC, leads to the partial decomposition of SALTSC to thiosemicarbazide and salicylaldehyde moieties.[7] Here, salicylaldehyde is condensed with an amide NH_2-group of the undecomposed SALTSC and a square-pyramidal complex of VO^{2+} with *in situ* obtained tetradentate O_2N_2 ligand bis(salicylidene)-thiosemicarbazide is formed. This leads to the conclusion that, unlike VO^{2+}, VO_2^+ is not a suitable template center for the mentioned SALTSC transformation.

Analytical and spectral characteristics

*$[VO_2(SALTSC–H)]\cdot H_2O$ (**1**).* Anal. Calcd. for $C_8H_{10}N_3O_4SV$ (*FW* = 295.19): C, 32.55; H, 3.41; N, 14.23; S, 10.86 %. Found: C, 32.48; H, 3.30; N, 14.08; S, 10.49 %. FTIR (KBr, cm^{-1}): 3154, 1638, 1549, 915, 902, 761. UV–Vis (λ_{max} / nm (log (ε / mol^{-1} dm^3 cm^{-1})): 276 (4.20), 307*sh* (4.11), 336 (3.53), 350*sh* (3.08), 382 (3.28) (*sh*-shoulder). λ_M (DMF, 1.0×10^{-3} mol dm^{-3}): 9.5 S cm^2 mol^{-1}.

*$NH_4[VO_2(SALTSC–2H)]$ (**2**).* Anal. Calcd. for $C_8H_{11}N_4O_3SV$ (*FW* = 294.20): C, 32.66; H, 3.77; N, 19.04; S, 10.90 %. Found: C, 32.48; H, 3.66; N, 18.83; S, 10.69 %. FTIR (KBr, cm^{-1}): 3144, 1620, 1550, 915, 890, 767. UV–Vis (λ_{max} / nm (log (ε / mol^{-1} dm^3 cm^{-1})): 275*bp* (4.15), 320*sh* (3.28), 384 (3.73) (*bp*-broad peak). λ_M (H_2O, 1.0×10^{-3} mol dm^{-3}): 99 S cm^2 mol^{-1}. λ_M (DMF, 1.0×10^{-3} mol dm^{-3}): 47 S cm^2 mol^{-1}.

IR spectra

X-Ray analysis of the obtained complexes (*vide infra*) showed that the SALTSC was coordinated in the usual way,[8] *i.e.*, *via* the phenolic group oxygen, azomethine nitrogen and sulfur atom of the thionic (complex **1**) or thiolic (complex **2**) group. This mode of coordination was confirmed by the IR spectra.

In the IR spectrum of SALTSC, the characteristic ν(OH) band is observed at 3444 cm^{-1}. The absence of this band in the IR spectra of the complexes indicates the coordination through the phenolic oxygen O1. Additional evidence of O1 coordination is the positive shift of the ν(C–O) band (≈10 cm^{-1}) in the IR spectra of the complexes, compared to the IR spectrum of the ligand.[16]

The IR band ν(CH=N) appearing at 1616 cm^{-1} in the free ligand spectrum is shifted towards higher wavenumbers in the spectra of the complexes (1638 and 1620 cm^{-1}, respectively) due to the involvement of the azomethine nitrogen in coordination.[16–22]

Unlike aforementioned bands, the ν(C=S) band is shifted to the lower energy region in the IR spectra of both complexes (761 and 767 cm^{-1}) in comparison to the IR spectrum of the free SALTSC (777 cm^{-1}).[17]

The strong band at 3170 cm^{-1} can be attributed to ν(N^2–H) vibrations. In free SALTSC, the N2 is involved in a H-bond with the sulfur atom of an adjacent molecule,[22] but in the complexes this bond disappears as a consequence of sulfur atom coordination. However, in the structure of complex **1**, instead of the N2––H···S1, an H-bond with O4 is formed. Since the H-bond with oxygen is stronger than with the sulfur atom, ν(N^2H) is found to undergo a downfield shift after complexation.

Very strong bands observed in the region characteristic for the *cis*-VO_2 group, *i.e.*, 915 and 902 cm^{-1} in **1** and 915 and 890 cm^{-1} in **2**, arise from $\nu_{sym/asym}(VO_2^+)$ vibrations.[23,24]

Electronic spectra

In the available spectral range in DMF (270–1100 nm), the two complexes absorbed only at wavelengths up to 450 nm. The spectral characteristics resemble those reported previously for iron(III) complexes with the same deprotonated ligand forms in this solvent.[25,26] Generally, the absorptions at $\lambda < 350$ nm appear as unresolved bands resulting from the intraligand transitions ($\pi \rightarrow \pi^*$ and $n \rightarrow \pi^*$). Similarly to the mentioned Fe(III) and other previously reported VO_2^+ complexes with pyridoxal thiosemicarbazone derivatives,[23] the band registered at higher λ (≈380 nm) is attributable to ligand-to-metal charge-transfer (LMCT) complex. As expected, no d–d interactions could be observed in the visible spectral range.

*Crystal structure of $[VO_2(SALTSC–H)]\cdot H_2O$ (**1**) and $NH_4[VO_2(SALTSC–2H)]$ (**2**)*

Molecular structures of the obtained complexes are shown in Figs. 2 and 3, respectively, and selected bond distances and angles for the complexes and free ligand are given in Table II. The asymmetric unit of **1** contains the neutral complex molecule and one water molecule involved in H-bonding with the complex molecule. The complex molecule consists of a tridentate monodeprotonated li-

gand, chelating the VO_2^+. In the asymmetric unit of **2**, there are the complex anion and the NH_4^+, which are linked by a dominant electrostatic interaction and a moderate H-bond.

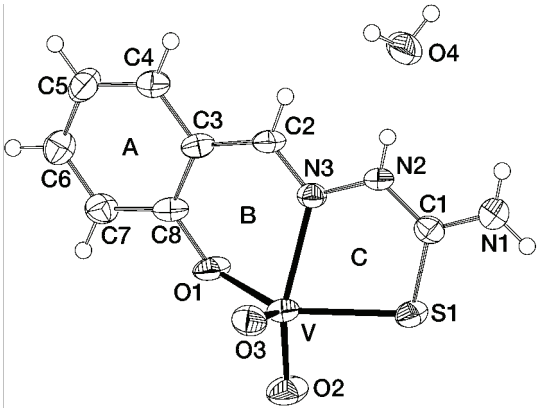

Fig. 2. Molecular structure of $[VO_2(SALTSC–H)]\cdot H_2O$ (**1**).

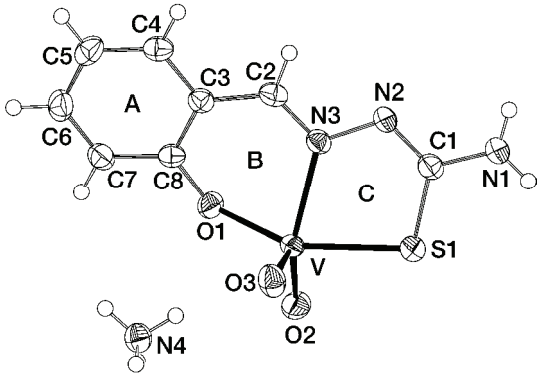

Fig. 3. Molecular structure of $NH_4[VO_2(SalTSC–2H)]$ (**2**).

In both complexes, tridentate coordination of the SALTSC results in a square–pyramidal configuration usual for VO_2^+-complexes with one oxo-ligand in the basal plane and the other in the apical position. It is interesting to notice that the vanadium atom is in an almost ideal square-pyramidal environment (τ = 0.052) in **2**, unlike the vanadium atom in **1,** in which the square-pyramidal environment is significantly distorted. The vanadium atom is shifted from the basal O1–N3––S1–O2 plane towards the apical oxo-ligand in both complexes (≈ 0.52 Å). The VO_2-group is in the *cis*-configuration with the usual value of the O–V–O angle[23] (108.2(2) in **1** and 108.7(1)° in **2**). As mentioned above, the SALTSC is coordinated in a common tridentate ONS mode, which results in the formation of two metallocycles: one six-membered (B, salycilidene) and one five-membered (C, thiosemicarbazide). In **1**, the SALTSC is coordinated as a monoanion formed by

deprotonation of the phenolic OH-group. However, in **2**, a further deprotonation of the thiolic group occurs, resulting in a dianion of the ligand.

TABLE II. Selected bond distances and bond angles for $[VO_2(SALTSC–H)]·H_2O$ (**1**), $NH_4[VO_2(SALTSC–2H)]$ (**2**) and SALTSC

Bond	Distance, Å		SALTSC
	1	**2**	
V–O1	1.895(2)	1.906(2)	–
V–N3	2.217(4)	2.186(3)	–
V–S1	2.383(1)	2.358(2)	–
V–O2	1.626(3)	1.639(3)	–
V–O3	1.629(3)	1.631(2)	–
O1–C8	1.336(5)	1.340(4)	1.356(3)
C2–N3	1.287(5)	1.296(4)	1.276(3)
N3–N2	1.382(5)	1.394(4)	1.380(4)
C1–N2	1.319(5)	1.300(4)	1.346(4)
C1–N1	1.324(5)	1.350(5)	1.317(4)
C1–S1	1.717(4)	1.734(3)	1.689(4)
	Angle, °		
	1	**2**	
O3–V–O2	108.3(2)	108.7(1)	–
O1–V–S1	139.32(9)	149.44(8)	–
N3–V–O2	155.6(1)	146.3(1)	–
O1–V–O2	98.5(1)	95.6(1)	–
O2–V–S1	88.2(1)	87.63(9)	–
S1–V–N3	76.99(9)	77.30(7)	–
N3–V–O1	81.2(1)	83.6(1)	–

Based on a previously known crystal structure of the free ligand[27] and two new structures of its complexes with VO_2^+ presented in this paper, it is possible to make comparative analysis of the corresponding geometric parameters. In neutral, uncoordinated SALTSC, the thiocarbonylic sulfur atom is in a *trans*-position with respect to the other two ligators N3 and O1. In the complexation reaction, rotation around the C1–N2 bond brings all the ligators into *cis*-positions that are maintained in the complexes.

The chelate ligand donors–vanadium bond distances V–O1, V–N3 and V–S1 in **1** are 1.895(2), 2.217(4) and 2.383(1) Å and in **2** 1.906(2), 2.186(3) and 2.358(2), respectively. In **1**, the V–N3 bond is slightly longer compared to the same bond in **2**, probably because of the stronger *trans*-influence of the O2 oxygen, which in this complex is placed at a shorter distance from the vanadium atom. It is noticeable that the V–S1 bond is shorter in **2** than in **1**, which is in accordance with better electron-donor properties of the thiol compared to the thione sulfur atom. The two oxo-ligands are at the almost same distance from the vanadium atom in **1**, unlike the complex **2** in which apical oxo-ligand O2 forms a

shorter bond with vanadium atom than the basal oxygen O3. Since the thiosemicarbazide residue is in its thiolate form, both oxo-ligands in **2** are further from the vanadium atom than in **1**.

The average V=O distances 1.627 Å in **1** and 1.635 Å in **2**, being slightly longer than the normal V=O double bond length of 1.595 Å, indicate that the oxygens are involved in moderate hydrogen-bonding interactions.[24]

The C2–N3 and N3–N2 bond distances have the values of localized double and single bond, respectively, in both complexes and in the free ligand as well. However, the slight elongation of these bonds in the complexes is a consequence of the involvement of the nitrogen N3 in the coordination. The other two C–N bonds, *i.e.*, C1–N1 and C1–N2, in the complexes are, due to the delocalization, shorter than a formal single, but longer than a formal double bond.[2]

It is also worth mentioning that the C1–N1 bond in free SALTSC is shorter (1.317(4) Å) than in the complexes, especially in **2**. This is evidence of the effect of the sulfur atom on the movement of electron density towards the metal atom. The shortening of the C1–N2 bond in **2** compared to the bond length in **1** can be explained by the deprotonation of the nitrogen atom N2, as well as by the involvement of an additional electron in the delocalization.

As expected, it was found that the thioketo C1–S1 bond in **1** is longer than the same bond in the free ligand, due to the coordination effect. In **2**, the increased single-bond character expected in the deprotonated form of the thioureido group makes this bond even longer. A similar elongation trend of the C1–S1 bond was found in some other structures containing the thioketoureido fragment.[28] In both complexes, the C8–O1 bond is shorter than the single C(sp^2)–O bond found in the free ligand (1.356(3) Å). Namely, the oxygen atom O1 is deficient in electron density as a consequence of the coordination, and the π-electron cloud is shifted from the benzene ring towards the oxygen O1. This process results in contraction of the C8–O1 bond.

As expected, the whole ligand molecule, which possesses an extended system of conjugated double bonds, in **1** is planar (the maximum distance of the mean plane 0.110 Å for the N3). Hence, the five-membered chelate ring (C) has an envelope conformation (E_1) and the six-membered (B) is in the conformation close to a half-chair. In **2**, the ligand is distorted and twisted along the C2–C3 bond with a torsion angle C8/C2/C3/N2 of –10.4°, and, as a result, the C ring becomes planar, but the B ring remains in the conformation close to a half-chair. These conformations of the B and C rings result in a decreased difference between the trans-basal angles and, therefore, in a decreased value of the τ-parameter with respect to **1**.

The crystal lattice of both complexes is stabilized by an inter- and intramolecular hydrogen-bond network. The H-bond parameters are given in Tables III and IV.

In the asymmetric unit of **1**, the complex molecule is linked by the moderate H-bond[29] N2–H2N···O4 to water, and in **2**, by the moderate H-bond N4––H4B···O3 formed between the complex anion and NH_4^+.

TABLE III. Hydrogen-bonding geometry in $[VO_2(SALTSC–H)]·H_2O$ (**1**); equivalent positions: *i*) *x*+1/2, –*y*+3/2, *z*–1/2; *ii*) *x*+1/2, *y*–1/2, *z*; *iii*) *x*+1/2, –*y*+3/2, *z*–1/2; *iv*) *x*, –*y*+2, *z*–1/2

Distance, Å			*D*–H···*A* angle, °
D–H···*A*	*D*–*A*	H···*A*	
N2–H2N···O4	2.653(5)	1.79	179.1
N1–H1A···O2^{i}	3.043(5)	2.24	155.8
N1–H1B···O3^{ii}	2.917(5)	2.12	153.7
O4–HW1···O1^{iii}	2.820(5)	2.01(7)	166(6)
O4–HW2···O3^{iv}	2.698(5)	1.86(9)	163(8)

TABLE IV. Hydrogen-bonding geometry in $NH_4[VO_2(SALTSC–2H)]$ (**2**); equivalent positions: *i*) –*x*+2, –*y*+1, –*z*+2; *ii*) –*x*+1, –*y*, –*z*+2; *iii*) –*x*+1, *y*–1/2, –*z*+3/2; *iv*) *x*, –1+*y*, *z*

Distance, Å			*D*–H···*A* angle, °
D–H···*A*	*D*–*A*	H···*A*	
N4–H4B···O3	2.850(4)	2.00(3)	169(4)
N1–H1A···N2^{i}	3.050(4)	2.30	146.4
N4–H4A···O1^{ii}	3.028(4)	2.17(3)	173(4)
N4–H4C···O2^{iii}	2.866(4)	2.04(3)	158(3)
N4–H4D···O3^{iv}	2.904(4)	2.01(3)	175(4)

The packing of the structural units in **1** is shown in Fig. 4, from which it can be seen that the complex molecules form C-layers that are parallel to the *ab* plane

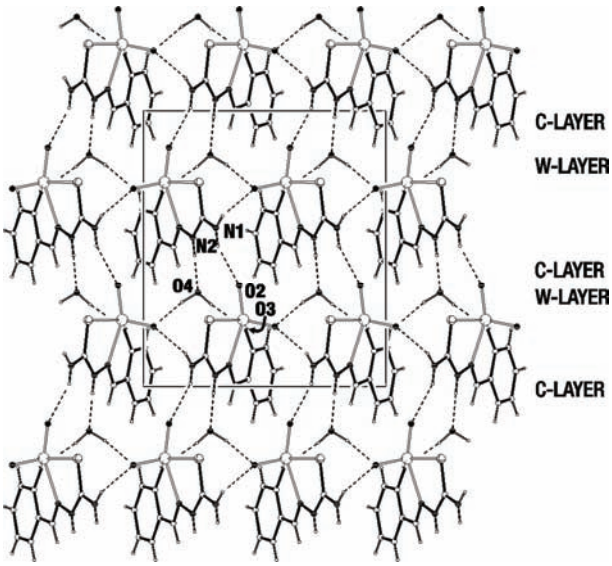

Fig. 4. Crystal packing diagram of complex **1** viewed perpendicular to the *bc* plane.

at the levels $c = 0$, $c = 1/2$ and $c = 1$. At the levels $c = 1/4$ and $c = 3/4$, water molecules form a W-layer, with one apical oxo-ligand between two water molecules. Within one C-layer, there is the N1–H1B···O3 H-bond, linking the molecules and another H-bond, N1–H1B···O3, which ties in the adjacent C-layers. Three moderate H-bonds, *i.e.*, N2–H2N···O4, O4–HW1···O1 and O4–HW2···O3, associate the W-layer with the neighboring C-layers.

The packing of the structural units in **2** is shown in Fig. 5. C-double layers are formed by the complex anions placed in the *bc* plane at the levels $a = 0$ and $a = 1$ linked by the N1–H1A···N2 H-bond. The NH_4^+ ions form A-layers parallel to the *bc* plane at $a = 1/2$. Between the C-double-layers and the A-layers, there are moderate H-bonds, *i.e.*, N4–H4B···O3, N4–H4A···O1, N4–H4C···O2 and N4––H4D···O3. A similar layered structure was reported for the abovementioned complex $NH_4[VO_2(salhyph)]$.[15]

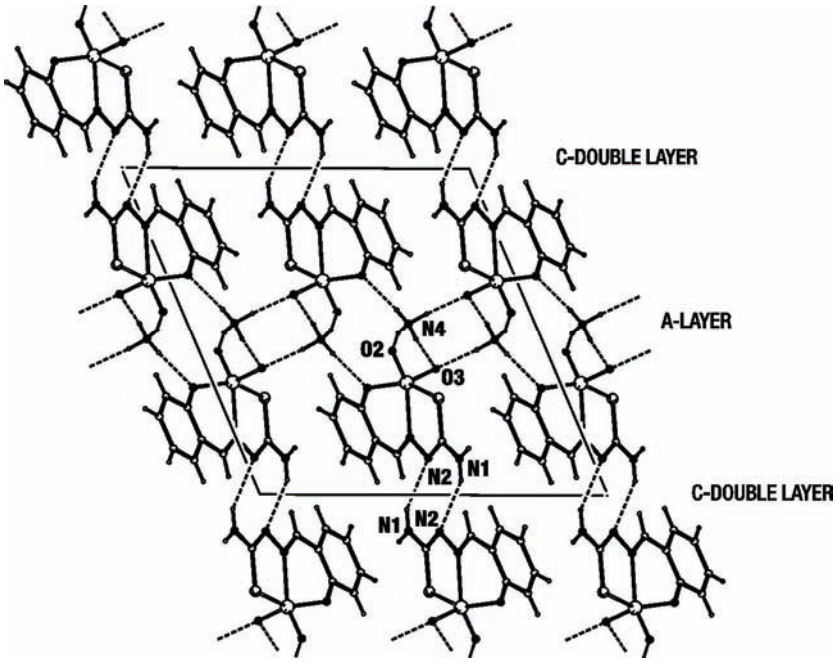

Fig. 5. Crystal packing diagram of complex **2** viewed perpendicular to the *ac* plane.

Crystallographic data reported for the complex $[VO_2(SALTSC–H)]\cdot H_2O$ and $NH_4[VO_2(SALTSC–2H)]$ have been deposited under the CCDC Nos. CCDC-801721 and 801722. Copies of the data can be obtained free of charge *via* www.ccdc.cam.ac.uk (or from the Cambridge Crystallographic Data Centre, 12, Union Road, Cambridge, CB2 1EZ, UK; fax: +44 1223 336033; or deposit@ccdc.cam.ac.uk).

Acknowledgement. This work was supported by the Ministry of Science and Technological Development of the Republic of Serbia (Grant No. 172014).

И З В О Д

КОМПЛЕКСИ ПРЕЛАЗНИХ МЕТАЛА СА ЛИГАНДИМА НА БАЗИ ТИОСЕМИКАРБАЗИДА. ДЕО 58. СИНТЕЗА, СПЕКТРАЛНА И СТРУКТУРНА КАРАКТЕРИЗАЦИЈА КОМПЛЕКСА ДИОКСОВАНАДИЈУМА(V) СА ТИОСЕМИКАРБАЗОНОМ САЛИЦИЛАЛДЕХИДА

ЉИЉАНА С. ВОЈИНОВИЋ-ЈЕШИЋ, ВУКАДИН М. ЛЕОВАЦ, МИРЈАНА М. ЛАЛОВИЋ, ВАЛЕРИЈА И. ЧЕШЉЕВИЋ, ЉИЉАНА С. ЈОВАНОВИЋ, МАРКО В. РОДИЋ и ВЛАДИМИР ДИВЈАКОВИЋ

Prirodno–matemati~ki fakultet, Univerzitet u Novom Sadu, Trg D. Obradovi}a 3, 21000 Novi Sad

Описане су синтезе и структуре прва два комплекса диоксованадијума(V) са тридентатним ONS тиосемикарбазоном салицилалдехида (SALTSC), формула $[VO_2(SALTSC–H)]\cdot H_2O$ (**1**) и $NH_4[VO_2(SALTSC–2H)]$ (**2**). Комплекси су добијени као смеша кристала у реакцији водено-амонијачног раствора NH_4VO_3 и SALTSC. Комплекси су окарактерисани елементалном и рендгено-структурном анализом, кондуктометријским мерењима, IR- и UV–Vis спектрима. Рендгено-структурна анализа је показала да комплекс **1** има деформисану, а комплекс **2** скоро идеалну квадратно-пирамидалну геометрију са атомом ванадијума померeним ка апикалном оксо-лиганду за око 0,52 Å.

(Примљено 17. децембра 2010, ревидирано 24. јануара 2011)

REFERENCES

1. T. S. Lobana, R. Sharma, G. Bawa, S. Khanna, *Coord. Chem. Rev.* **253** (2009) 977 and references therein
2. F. Basuli, S.-M. Peng, S. Bhattacharya, *Inorg. Chem*. **36** (1997) 5645
3. H.-G. Zheng, D.-X. Zeng, X.-Q. Xina, W.-T. Wong, *Polyhedron* **16** (1997) 3499
4. M. Cindrić, V. Vrdoljak, N. Strukan, B. Kamenar, *Polyhedron* **24** (2005) 369
5. V. M. Leovac, V. I. Češljević, *Coordination Chemistry of Isothiosemicarbazide and Its Derivatives*, Faculty of Science, Novi Sad, 2002 (in Serbian)
6. N. V. Gerbeleu, *Zh. Neorg. Khim.* **13** (1968) 2467
7. N. V. Gerbeleu, M. D. Revenco, *Zh. Neorg. Khim.* **16** (1971) 1046
8. V. M. Leovac, Lj. S. Vojinović, K. Mészáros Szécsényi, V. I. Češljević, *J. Serb. Chem. Soc.* **68** (2003) 919
9. A. Altomare, G. Cascarano, C. Giacovazzo, A. Gualardi, *J. Appl. Cryst.* **26** (1993) 343
10. G. M. Sheldrick, *Acta Crystallogr. A* **64** (2008) 112
11. L. J. Farrugia, *J. Appl. Cryst.* **32** (1999) 837
12. A. L. Spek, *Acta Crystallogr. D* **65** (2009) 148
13. Yu. N. Kukushkin, *Himiya koordinacionnyh soedinenii*, Vysshaya shkola, Moskva, 1985.
14. W. J. Geary, *Coord. Chem. Rev.* **7** (1971) 81
15. W. Plass, H.-P. Yozgatli, *Z. Anorg. Allg. Chem.* **629** (2003) 65
16. S. Purohit, A. P. Koley, L. S. Prasad, P. T. Manoharan, S. Ghosh, *Inorg. Chem*. **28** (1989) 3735
17. R. Raina (Née Kalloo), T. S. Srivastava, *Inorg. Chim. Acta* **67** (1982) 83
18. D. X. West, J. P. Scovill, J. V. Silverton, A. Bavoso, *Transition Met. Chem.* **11** (1986) 123

19. P. Souza, F. Sánchez-Kaister, J. R. Masaguer, A. Arquero, *Transition Met. Chem.* **12** (1987) 128
20. B. S. Garg, M. R. Prathapachandra Kurup, S. K. Jain, Y. K. Bhoon, *Transition Met. Chem.* **13** (1988) 247
21. M. Belicchi Ferrari, G. Gasparri Fava, C. Pelizzi, G. Pelosi, P. Tarasconi, *Inorg. Chim. Acta* **269** (1998) 297
22. F. Basuli, M. Ruf, C. G. Pierpont, S. Bhattacharya, *Inorg. Chem*. **37** (1998) 6113
23. V. M. Leovac, V. Divjaković, M. D. Joksović, Lj. S. Jovanović, Lj. S. Vojinović-Ješić, V. I. Češljević, M. Mlinar, *J. Serb. Chem. Soc*. **75** (2010) 1063
24. A. Hazra, A. K. Barik, S. Pal, S. Gupta, S. Roy, R. J. Butcher, S.-M. Peng, G. H. Lee, S. K. Kar, *Polyhedron* **26** (2007) 773
25. V. M. Leovac, L. Bjelica, Lj. Jovanović, *Polyhedron* **4** (1985) 233
26. L. J. Bjelica, Lj. S. Jovanović, F. F. Gaál, *Rev. Res. Fac. Sci. Univ. Novi Sad* **13** (1983) 37
27. D. Chattopadhyay, S. K. Mazumdar, T. Baneriee, S. Gosh, T. C. W. Mak, *Acta Crystallogr. C* **44** (1988) 1025
28. A. G. Bingham, H. Bögge, A. Müller, E. W. Ainscough, A. M. Brodie, *J. Chem. Soc. Dalton Trans.* (1987) 493
29. G. Gilli, P. Gilli, *The Nature of the Hydrogen Bond*, Oxford University Press, Oxford, 2009.

Journal of the Serbian Chemical Society
JSCS-info@shd.org.rs • www.shd.org.rs/JSCS
J. Serb. Chem. Soc. 76 (6) 879–890 (2011)
JSCS–4168
UDC 665.344.2+547.521:539.125.4:519.677
Original scientific paper

A theoretical study of the intramolecular proton transfer and calculation of the nucleus independent chemical shift in juglone and some of its derivatives

ESMAIL VESSALLY[1], EHSAN FEREYDUNI[2]*, MAHDI KAMAEE[3] and SHAHRAM MORADI[4]

[1]*Payame Noor University (PNU), Zanjan, Iran,* [2]*Department of Chemistry, Tabriz Branch, Islamic Azad University, Tabriz, Iran,* [3]*Department of Chemistry, Shahid Chamran University, Ahvaz, Iran and* [4]*Faculty of Chemistry, Islamic Azad University, North Tehran Branch, Tehran, Iran*

(Received 30 September 2010)

Abstract: In the present study, first, the intramolecular proton transfer (IPT) process of juglone and its derivatives were theoretically investigated in the gas phase and the effect of electron-withdrawing and electron-releasing substituents in different positions of the phenyl and benzoquinone rings of juglone on the IPT process was studied in which the geometries, energies and thermodynamic functions of the compounds were obtained using density functional theory (DFT) calculations at the B3LYP/6-31+G(2d,p) level. Next, the influence of IPT on changing the aromaticity of the phenyl and benzoquinone rings was investigated. To determine the aromaticity of the rings, nuclear independent chemical shift (*NICS*) values were calculated for the ground state and transition state structures (GS_1, TS and GS_2) using the continues set of gauge transformations (CSGT) procedure at the B3LYP/6-311+G(2d,p) level.

Keywords: juglone; *NICS*; aromaticity; intramolecular proton transfer; DFT.

INTRODUCTION

1,4-Naphthoquinones are widely distributed in plants, fungi and some animals[1] and many are found to exhibit an interesting range of pharmacological properties, including antibacterial,[2,3] antimicrobial,[4] antiviral,[5] trypanocidal,[6] anticancer,[7] antimalarial,[8,9] and antifungal[10] activities, especially when a hydroxyl group is present at the C5 position.[11] Juglone is a quinone produced in the roots, leaves and bark of walnut trees.[12,13] It contains an intramolecular hydrogen bond (IAHB) between hydroxyl and keto groups. The IAHB can be formed between donor and acceptor groups of the same molecule when the molecular configu-

* Corresponding author. E-mail: e_fereyduni@yahoo.com
doi: 10.2298/JSC100930080V

ration and conformation bring them within hydrogen bond geometry. Studies on IAHB became increasingly popular in the past[14,15] and hydrogen bonding complexes have been extensively studied with a wide range of experimental techniques and calculations.[16,17] One of the most significant structures capable of bearing hydrogen bond is the O–H···O unit which is studied in this paper. Sometimes, an IAHB decisively influences the stability of molecular conformations and favors tautomerization *via* an intramolecular proton transfer (IPT) process. In juglone as well, a hydrogen atom can transfer from hydroxyl to a keto group *via* the IPT process. IPT reactions are among the most important processes that occur in chemistry and biology.[18,19] Juglone is a natural ligand and many complexes can be formed *via* IPT reactions. Therefore juglone and its analogues can act as absorbent or carrier of metal ions and amino acids in biologic systems. Substituent effects are among the most important concepts of structural effects influencing the chemical, physico-chemical, and biochemical properties of chemical species.[20]

Juglone is an aromatic organic compound and aromaticity is one of the most characteristic phenomena associated strongly with a cyclic π-electron delocalization.[20] Aromaticity fundamentally characterizes the molecular structure, physical properties and chemical reactivity from both thermodynamic and kinetic standpoints,[21,22] which is used as a powerful predictive tool for compounds which had not been prepared previously. Aromaticity seems to be significant in any logical application of organic chemistry. However, a more detailed investigation of aromatic molecules requires a quantitative estimation of the degree of aromaticity of cyclic conjugated systems. There are several criteria used frequently for a compound to be considered aromatic, *i.e.*, stability of cyclic π-system, near planarity, bond length equalization, delocalized π-electrons satisfying the Hückel ($4n$+2) electron counting rule and unusual magnetic properties, such as magnetic susceptibilities.[23,24] π-Electron delocalization, is a concept that covers various structural situations, is a fundamental concept in the definition of aromaticity.[20] Aromaticity is a quantity which cannot be directly measured. Therefore, its magnitude is evaluated in terms of a few criteria, such as structural, energetic and magnetic ones. However, magnetic properties have the closest relationship to aromaticity, since they are directly dependent on the induced ring currents associated with cyclic electron delocalization. There are several methods for evaluating the magnetic aromaticity,[25,26] such as NMR,[27–29] exaltation of magnetic susceptibilities,[29–31] nucleus independent chemical shifts (*NICS*),[26,32–34] ring current density plots,[35–37] and aromatic ring current shieldings (ARCS).[38] *NICS* which was proposed by Schleyer *et al.*,[32] was found to be an easy computed and generally applicable criterion and has been widely used to evaluate the aromaticity and anti-aromaticity of rings,[39,40] clusters,[41,42] transition states,[43,44] and transition metal complexes.[45]

Some new theoretical[46,47] and experimental[48,49] studies have been made on juglone. In the present work, a theoretical study of the IPT process of juglone and its derivatives was realized. Several derivatives of juglone were supposed by placing electron-withdrawing (EW) and electron-releasing (ER) substituents at different positions of phenyl and benzoquinone rings and the effect of substituents on the IPT process was investigated. Next, the influence of IPT on the change of the aromaticity of the phenyl and benzoquinone rings was investigated using magnetic aromaticity indices.

COMPUTATIONAL DETAILS

Density functional theory (DFT) calculation of juglone and its derivatives was conducted in which geometries, energies and thermodynamic functions $\Delta G^{\ominus}$, $\Delta H^{\ominus}$ and $S^{\ominus}_{298}$ values for all structures were calculated at the B3LYP/6-31+G (2d,p) level. The intramolecular proton transfer (IPT) process was performed by ADDREDUNDANT keyword by scanning a proton at the B3LYP/6-31+G (2d,p) level to reach a final optimization. QST2 keyword was used to investigate the transition state structures between the primitive (GS_1) and final (GS_2) structures. The magnetic shielding at the center of a ring system was determined by calculating the chemical shift of "ghost" atoms. By convention, the *NICS* value is the negative of computed isotropic shielding value. Large negative values indicate aromaticity while large positive values represent anti-aromaticity, and near-zero values introduce non-aromaticity. To obtain a measure of the aromaticity in juglone rings, *NICS* values were calculated at two points as illustrated in Fig. 1.

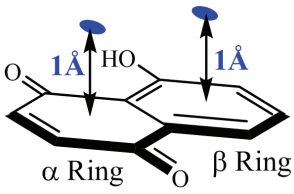

Fig. 1. Definition of the points at which the *NICS* values were calculated.

NICS calculations were performed at 1 Å above the centre of the α- and β-rings for all systems at the B3LYP/6-311+G (2d,p) level and NMR shielding tensors were computed with the continuous set of gauge transformations (CSGT) method. All computations were realized using the Gaussian 98W program package.[50] Data in this article extracted among more than 300 Gaussian program output files.

RESULTS AND DISCUSSION

Geometries and barrier energies

All structures (**MM** and **JG1**–**JG20**) included in this study are shown in Fig. 2. Taking juglone **MM** as the mother molecule, the other structures (**JG1**–**JG20**) can be obtained by placing –OMe, –Br, –Cl and $–NO_2$ substituents at different ring positions of **MM**. The geometry calculations showed all frameworks are almost planar structures. The average bond lengths and bond angles of **MM** and its analogues related to the six-membered ring which formed *via* IPT are given in Table I. The length of the H-bond in the ground state (GS_1) is up to 2 Å; there-

fore, strong hydrogen bonds exist in all **MM** derivatives. During the IPT process, the average interatomic distance between the donor oxygen (O5) and H6 increased while the distance between the acceptor oxygen (O1) and H6 decreased. In addition, the O1–C2 and C3–C4 bonds lengthened, whereas the C2–C3 and C4–O5 bonds shortened (Table I).

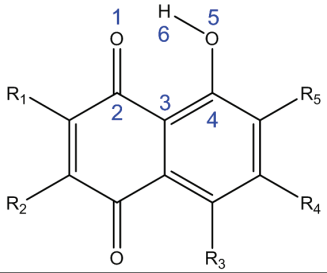

Substituents			Species
R_2=R_3=R_4=R_5= H,	R_1=	H	**MM**
		NO_2	**JG1**
		Cl	**JG6**
		Br	**JG11**
		OMe	**JG16**
R_1=R_3=R_4=R_5= H,	R_2=	H	**MM**
		NO_2	**JG2**
		Cl	**JG7**
		Br	**JG12**
		OMe	**JG17**
R_1=R_2=R_4=R_5= H,	R_3=	H	**MM**
		NO_2	**JG3**
		Cl	**JG8**
		Br	**JG13**
		OMe	**JG18**
R_1=R_2=R_3=R_5= H,	R_4=	H	**MM**
		NO_2	**JG4**
		Cl	**JG9**
		Br	**JG14**
		OMe	**JG19**
R_1=R_2=R_3=R_4= H,	R_5=	H	**MM**
		NO_2	**JG5**
		Cl	**JG10**
		Br	**JG15**
		OMe	**JG20**

Fig. 2. Juglone and its derivatives studied in this work, together with the atom numbering.

In continuation, the IPT of juglone and its derivatives was studied to understand the effect of the location of ER and EW substituents on the IPT process. Since juglone and its derivatives are analogous, their reaction paths are similar. The values of the energy and some thermodynamic functions related to the GS_1, TS and GS_2 structures are filed in Table II. The barrier energies (E_{rel}, kcal mol^{-1})*

* kJ = 4.1868 kcal

of the IPT of the phenolic hydrogen to the carbonyl group for all structures (**MM** and **JG1**–**JG20**) are depicted in Fig. 3. Some substituents at particular positions facilitate the IPT process (when the E_{rel} value is less than that of mother molecule **MM**); however, some others make the progress of the process more arduous (having an E_{rel} value greater than that of **MM**). Two ways are suggested to interpret the effect of substituents on the IPT:

i) locating a particular substituent in different positions (R_1 to R_5) and its effect on the barrier energy; as an example, on placing $–NO_2$ at R_1 to R_5, the activation barriers (E_{rel}) of the IPT increase in the order of R_3 (17.69 kcal mol^{-1}) < < R_4 (19.08 kcal mol^{-1}) < R_2 (19.33 kcal mol^{-1}) < R_5 (20.75 kcal mol^{-1}) < R_1 (22.63 kcal mol^{-1}). According to the E_{rel} of **MM** (18.28 kcal mol^{-1}), it can be concluded that substituting a nitro group at the R_3 position facilitates the IPT, while placing it at the other positions, especially at R_1, impedes the reaction. The large effects of substituents at R_1 and R_5 on proton transfer could be related to these substituents neighboring the IPT center, which increases the sensitivity of the IPT to substituents at R_1 and R_5. The influence of substituents located at the other positions can be easily understood according to Fig. 3.

TABLE I. Average bond lengths (Å) and bond angles (degree) in juglone and its derivatives, shown in Fig. 2

Bond	State		
	GS_1	TS	GS_2
	Bond length, r / Å		
O1–C2	1.117	1.259	1.285
C2–C3	1.476	1.230	1.370
C3–C4	1.395	1.421	1.457
C4–O5	1.322	1.258	1.222
O5–H6	0.956	1.290	1.490
H6–O1	1.421	1.175	1.406
	Bond angle, θ / °		
O1–C2–C3	102.2	104.6	122.9
C2–C3–C4	122.9	120.3	120.5
C3–C4–C5	120.0	116.5	123.2
C4–O5–H6	123.7	120.1	104.7
O5–H6–O1	140.7	155.3	156.9

TABLE II. Total energies (Hartree), activation barrier energies (E_{rel} / kcal mol^{-1}), zero-point vibrational energies (*ZPVE* / kcal mol^{-1}), $\Delta G^{\ominus}$, $\Delta H^{\ominus}$ and $S^{\ominus}_{298}$ calculated at the B3LYP/6--31+G(2d,p) level for all structures shown in Fig. 2

Species	State	B3LYP/6-31+G(2d,p)	E_{rel}	*ZPVE*	$G^{\ominus}_{298} - G^{\ominus}_{0}$	$H^{\ominus}_{298} - H^{\ominus}_{0}$	$S^{\ominus}_{298}$
MM	GS_1	–606.8297	(0.00)	93.384	–0.0345	0.0098	93.347
	TS	–606.8006	(18.28)	90.326	–0.0340	0.0093	91.200
	GS_2	–606.8049	(15.55)	88.072	–0.0332	0.0089	88.575
	GS_1	–810.3016	(0.00)	95.525	–0.0385	0.0114	106.873

TABLE II. Continued

Species	State	B3LYP/6-31+G(2d,p)	E_{rel}	*ZPVE*	$G^{\ominus}_{298} - G^{\ominus}_{0}$	$H^{\ominus}_{298} - H^{\ominus}_{0}$	$S^{\ominus}_{298}$
JG1	TS	–810.2655	(22.63)	92.442	–0.0380	0.0109	104.989
	GS_2	–810.2703	(19.66)	95.360	–0.0385	0.0114	106.929
	GS_1	–810.2975	(0.00)	95.504	–0.0386	0.0114	107.313
JG2	TS	–810.2667	(19.33)	92.442	–0.0381	0.0111	105.133
	GS_2	–810.2728	(15.50)	95.360	–0.0384	0.0114	106.998
	GS_1	–810.2967	(0.00)	95.468	–0.0383	0.0114	106.487
JG3	TS	–810.2685	(17.69)	92.454	–0.0378	0.0108	104.469
	GS_2	–810.2724	(15.25)	95.289	–0.0385	0.0114	107.021
	GS_1	–810.3101	(0.00)	95.481	–0.0388	0.0114	107.684
JG4	TS	–810.2797	(19.08)	92.463	–0.0385	0.0016	106.107
	GS_2	–810.2842	(16.25)	95.289	–0.0128	0.0375	108.042
	GS_1	–810.3016	(0.00)	95.525	–0.0385	0.0630	106.874
JG5	TS	–810.2685	(20.75)	92.457	–0.0380	0.0118	104.948
	GS_2	–810.2784	(14.54)	95.447	–0.0384	0.0123	106.742
	GS_1	–1065.7223	(0.00)	87.038	–0.0365	0.0110	100.155
JG6	TS	–1065.6919	(19.07)	83.975	–0.0360	0.0105	97.950
	GS_2	–1065.6959	(16.57)	82.616	–0.0351	0.0100	95.138
	GS_1	–1065.7229	(0.00)	87.048	–0.0386	0.0110	100.147
JG7	TS	–1065.6934	(18.48)	83.968	–0.0381	0.0105	97.950
	GS_2	–1065.6982	(15.49)	82.561	–0.0384	0.0100	95.138
	GS_1	–1065.7134	(0.00)	86.806	–0.0371	0.0111	101.594
JG8	TS	–1065.6875	(16.25)	83.819	–0.0362	0.0106	98.512
	GS_2	–1065.6917	(13.64)	83.448	–0.0350	0.0996	94.832
	GS_1	–1065.7266	(0.00)	86.896	–0.0365	0.0110	100.130
JG9	TS	–1065.6979	(18.00)	83.847	–0.0392	0.0105	98.018
	GS_2	–1065.7026	(15.06)	82.549	–0.0362	0.0100	95.293
	GS_1	–1065.7226	(0.00)	86.988	–0.0364	0.0110	99.969
JG10	TS	–1065.6946	(17.57)	83.954	–0.0360	0.0037	97.936
	GS_2	–1065.6993	(14.62)	82.952	–0.0416	0.0105	95.398
	GS_1	–3176.3125	(0.00)	86.710	–0.0376	0.0112	102.679
JG11	TS	–3176.2823	(18.96)	83.662	–0.0370	0.0107	100.468
	GS_2	–3176.2861	(16.55)	86.577	–0.0374	0.0112	102.264
	GS_1	–3176.3127	(0.00)	86.713	–0.0376	0.0112	102.679
JG12	TS	–3176.2834	(18.41)	83.631	–0.0370	0.0104	100.482
	GS_2	–3176.2881	(15.44)	86.633	–0.0375	0.0112	102.396
	GS_1	–3176.3033	(0.00)	86.556	0.0382	0.0113	104.282
JG13	TS	–3176.2774	(16.26)	83.566	–0.0372	0.0108	101.041
	GS_2	–3176.2814	(13.73)	86.482	–0.0377	0.0112	102.977
	GS_1	–3176.3160	(0.00)	86.546	–0.0376	0.0113	102.822
JG14	TS	–3176.2871	(18.14)	83.484	–0.0371	0.0108	100.691
	GS_2	–3176.2918	(15.21)	86.498	–0.0375	0.0112	102.621
	GS_1	–3176.3131	(0.00)	86.699	–0.0375	0.0112	102.544
JG15	TS	–3176.2852	(17.49)	83.654	–0.0370	0.0108	100.527
	GS_2	–3176.2898	(14.62)	86.659	–0.0375	0.0112	102.404
	GS_1	–720.7170	(0.00)	115.329	–0.0382	0.0125	106.998
JG16	TS	–720.6871	(18.73)	112.257	–0.0376	0.0120	104.675

TABLE II. Continued

Species	State	B3LYP/6-31+G(2d,p)	E_{rel}	*ZPVE*	$G^{\ominus}_{298} - G^{\ominus}_{0}$	$H^{\ominus}_{298} - H^{\ominus}_{0}$	$S^{\ominus}_{298}$
JG16	GS_2	–720.6911	(16.23)	110.680	–0.0354	0.0107	97.187
	GS_1	–720.7225	(0.00)	115.700	–0.0377	0.0113	105.259
JG17	TS	–720.6949	(17.31)	112.601	–0.0370	0.0108	103.064
	GS_2	–720.6980	(15.34)	110.945	–0.0353	0.0096	96.767
	GS_1	–720.7076	(0.00)	115.163	–0.0380	0.0125	106.399
JG18	TS	–720.6809	(16.78)	112.129	–0.0375	0.0120	104.319
	GS_2	–720.6861	(13.47)	110.968	–0.0350	0.0107	96.803
	GS_1	–720.7230	(0.00)	115.483	–0.0378	0.0124	105.630
JG19	TS	–720.6937	(18.43)	112.359	–0.0374	0.0119	103.956
	GS_2	–720.6972	(16.21)	110.554	–0.0354	0.0107	97.141
	GS_1	–720.7142	(0.00)	115.567	–0.0377	0.0123	105.530
JG20	TS	–720.6862	(17.53)	112.530	–0.0372	0.0118	103.237
	GS_2	–720.6924	(13.68)	115.615	–0.0160	0.0122	105.064

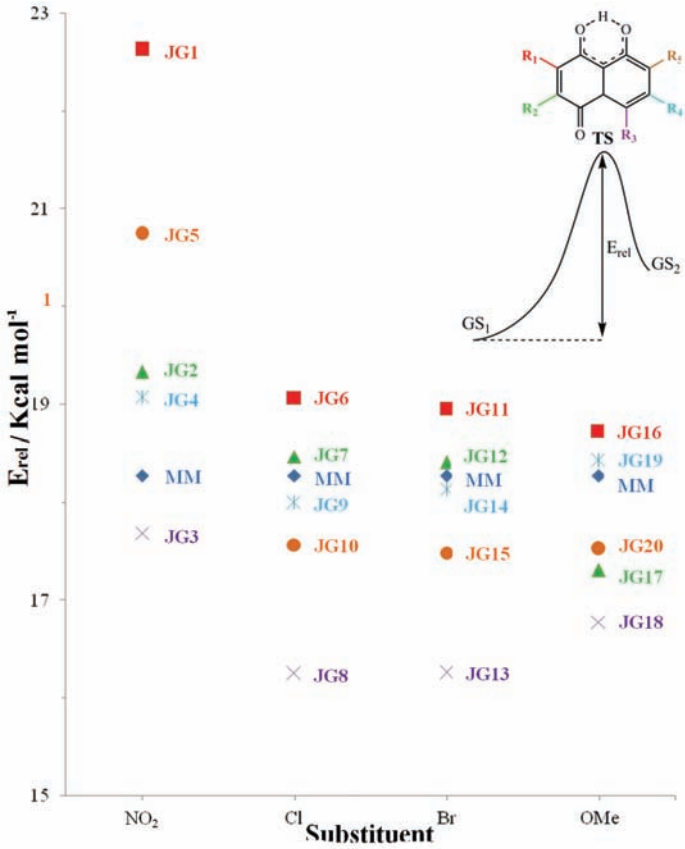

Fig. 3. The barrier energies (E_{rel} / kcal mol^{-1}) for the IPT of **MM** and the **JG1**–**JG20** analogues included in this study. (R_1 = square sign, R_2 = triangle sign, R_3 = multiplication sign, R_4 = star sign, R_5 = circle sign. **MM** showed by rhombic sign).

ii) Placing different substituents at a particular position and their influence on the barrier energy; For instance, locating the above-mentioned groups at the R_5 position indicated that –OMe, –Br and –Cl groups have promoting effects on the IPT whereas $–NO_2$ has retarding effects on the reaction. The strong conjugation of the $–NO_2$ group with the aromatic ring with respect to other substituents leads the IPT reaction being hindered. In addition, substituting R_1 with any group encumbers the IPT since **MM** has a lower E_{rel} value than all the R_1-substituted compounds (E_{rel}: **MM** < **JG16** < **JG11** < **JG6** < **JG1**). The highest relative barrier energy for the $–NO_2$ group at **JG1** may be attributed to the repulsion energy between the non-bonding electrons on the oxygen atoms of the $–NO_2$ substituent and the –OH group, which is greater than the repulsion energy between the $–NO_2$ substituent and the –CO group. By the same interpretation, substituting R_3 with any group facilitates the IPT.

Effect of the IPT on the NICS value of the rings

Perturbation of the π-electron density distribution depends on the electronic properties of the substituents and can be studied using *NICS* values. Hence, *NICS* values for the GS_1, TS and GS_2 structures of all **MM** derivatives were calculated and are given in Table III, from which, it can be clearly seen that all structures in GS_1 have negative *NICS* values in the β-ring due to the aromaticity of this ring and have positive ones in the α-ring because of the localized quinone ring. Furthermore, by comparing the *NICS* values of the GS_1 and GS_2 structures, it was

TABLE III. *NICS*(1) values (ppm) obtained using the CSGT procedure at the B3LYP/6--311+G(2d,p) level for the ground states and transition state structures of each species

Substituent	State	Position									
		R_1		R_2		R_3		R_4		R_5	
		Ring									
		α	β	α	β	α	β	α	β	α	β
–H	GS_1	2.0	–8.0	2.0	–8.0	2.0	–8.0	2.0	–8.0	2.0	–8.0
	TS	1.5	–5.1	1.5	–5.1	1.5	–5.1	1.5	–5.1	1.5	–5.1
	GS_2	1.1	–2.3	1.1	–2.3	1.1	–2.3	1.1	–2.3	1.1	–2.3
$–NO_2$	GS_1	1.6	–8.0	1.7	–7.9	0.7	–8.0	1.7	–8.5	1.8	–8.1
	TS	0.6	–4.7	1.6	–5.2	0.5	–5.9	1.5	–5.9	1.5	–5.5
	GS_2	0.3	–2.3	0.5	–2.2	0.4	–3.1	1.0	–3.3	0.8	–3.0
–Cl	GS_1	2.0	–8.2	1.9	–7.9	1.5	–7.8	2.0	–7.7	1.9	–8.1
	TS	1.4	–5.2	1.7	–5.2	0.8	–5.1	1.6	–5.1	1.6	–5.2
	GS_2	0.8	–2.3	0.9	–2.3	0.6	–2.9	1.2	–2.7	1.0	–2.5
–Br	GS_1	1.7	–8.2	1.8	–7.9	1.8	–7.9	1.6	–7.8	1.3	–8.1
	TS	1.4	–5.2	1.7	–5.0	1.5	–5.1	1.7	–5.0	1.6	–5.2
	GS_2	0.4	–2.5	1.0	–2.3	0.8	–2.5	0.5	–3.4	0.0	–2.8
–OMe	GS_1	1.7	–8.0	2.0	–7.9	3.0	–8.1	1.7	–7.4	2.0	–7.7
	TS	1.6	–5.2	1.9	–5.5	1.1	–5.3	0.9	–4.8	1.3	–5.0
	GS_2	0.9	–2.3	1.4	–2.9	0.1	–1.9	1.9	–4.8	0.6	–2.0

found that during IPT from the *β*- to the *α*-ring, the aromatic properties and the π-electron delocalization in *β*-ring decreased, whereas the π-electron delocalization in the *α*-ring increased for all **MM** analogues (Table III and Fig. 4). In continuation, the changing rate of the aromatic properties and the π-electron delocalization due to placing substituents at different positions on the rings were studied. Thus the, *NICS* value of the initial state (GS_1) was subtracted from that of the final state (GS_2), *i.e.*, $\Delta(NICS) = NICS_{(GS2)} - NICS_{(GS1)}$. Analysis of the $\Delta(NICS)$ values for the *α*-ring showed that highest and lowest rates of increase in π-electron delocalization in this ring were with –OMe at the R_3 (2.9 ppm) and R_4 (0.2 ppm) positions, respectively. The same analysis for the *β*-ring indicated that maximum and minimum rates of decrease in π-electron delocalization were with –OMe at the R_3 (6.2 ppm) and –Br at the R_4 (4.4 ppm) positions, respectively.

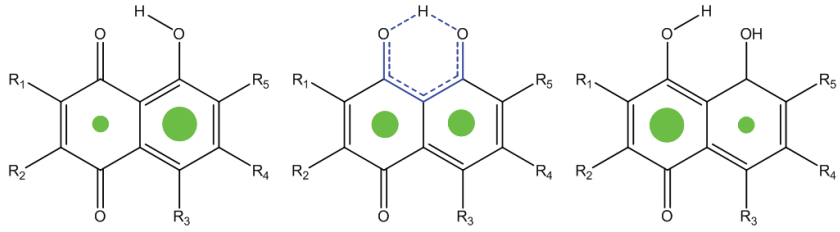

State	GS_1		TS		GS_2	
Ring	α	β	α	β	α	β
NICS (1)	1.85 ±1.15	-7.95 ±0.55	1.20 ±0.70	-5.30±0.60	0.95 ±0.95	-3.35 ±1.45

Fig. 4. Distribution of the hanging π-electron density during IPT (shown by green circles) and range of *NICS* (1) values (ppm) in the *α*- and *β*-rings for the GS_1, TS and GS_2 structures (shown under the figure).

CONCLUSIONS

In the present study, intramolecular proton transfer of juglone and 20 of its derivatives were studied. Placing a number of groups at certain ring positions facilitated the IPT, whereas placing some others at specific positions impeded the reaction. As noticeable examples, locating –Cl and –Br groups in the R_3 position (**JG8** and **JG13** analogues, respectively) resulted in a significant decrease in the activation barrier which effectively increased the realization of the IPT more than other analogues, whereas placing an $–NO_2$ group at the R_1 position (**JG1** analogue) remarkably increased the activation barrier, which hindered the progress of the reaction compared to the other derivatives.

Analysis of the *NICS* values showed that all GS_1 structures had negative *NICS* values in the *β*-ring (due to the aromaticity of the *β*-ring) and positive ones in the *α*-ring (because of the localized quinone ring). Furthermore, during IPT from the *β*- to the *α*-ring, the aromatic properties in the *β*-ring downgraded (due

to destruction of the aromatic cycle), whereas the π-electron delocalization in the α-ring were upgraded (because of the newly formed double bond) for all **MM** analogues. It should be noted that all derivatives showed different rates of change of the aromatic properties of the α- and β-rings.

Since Juglone is a natural ligand and IPT can be a basis for formation of complexes, juglone and its analogues can be utilized as absorbents or carriers of metal ions and amino acids in biologic systems. According to the calculation results, it can be rationalized which derivates of juglone can be utilized as an absorbent (derivatives which facilitate the IPT) and which ones as a carrier (derivatives which hinder the progress of the IPT) of metal ions and amino acids.

И З В О Д

ТЕОРИЈСКО ИСТРАЖИВАЊЕ ИНТРАМОЛЕКУЛСКОГ ТРАНСФЕРА ПРОТОНА И ОД ЈЕЗГРА НЕЗАВИСНОГ ХЕМИЈСКОГ ПОМАКА У ЈУГЛОНУ И ЊЕГОВИМ ДЕРИВАТИМА

E. VESSALLY[1], E. FEREYDUNI[2], M. KAMAEE[3] и S. MORADI[4]

[1]*Payame Noor University (PNU), Zanjan,* [2] *Department of Chemistry, Tabriz Branch, Islamic Azad University, Tabriz,* [3]*Department of Chemistry, Shahid Chamran University, Ahvaz u* [4]*Faculty of Chemistry, Islamic Azad University, North Tehran Branch, Tehran, Iran*

У раду се прво истражује интрамолекулски трансфер протона (IPT) у југлону и његовим дериватима. Ова истраживања односе се на утицај електрон-привлачних и електрон-одбојних супституената у различитим положајима у југлону. Проучавани су IPT процеси у којима су геометрије, енергије и термодинамичке функције једињења одређене методом функционалне теорије густине (DFT), на нивоу B3LYP/6-31+G(2d,p). Затим је проучаван утицај IPT на промену ароматичности фенил и бензохинонског прстена. За то су израчунате *NICS*-вредности прстенова, за основна и прелазна стања (GS_1, TS и GS_2) примењујући CSGT процедуру на нивоу B3LYP/6-31+G(2d,p).

(Примљено 30. септембра 2010)

REFERENCES

1. R. H. Thomson, *Naturally Occurring Quinones*, Academic Press, London, 1971
2. S. A. A. Osman, A. A. Abdalla, M. O. Alaib, *J. Pharm. Sci.* **72** (1983) 68
3. I. M. Roushdi, E. S. A. Ibrahim, N. S. Habib, *Pharmazie* **31** (1976) 856
4. B. A. Kulkari, V. D. Kelker, P. L. Kukarni, *Indian J. Pharm. Sci.* **45** (1983) 21
5. R. I. Brinkworth, D. P. Fairlie, *Biochim. Biophys. Acta* **1253** (1995) 5
6. L. Salmon-Chemin, E. Buisine, V. Yardley, S. Kohler, M. A. Debreu, V. Landry, C. Sergheraert, S. L. Croft, L. R. Krauth-Siegel, E. Davioud-Charvet, *J. Med. Chem.* **44** (2001) 548
7. B. Hazra, P. Sur, D. K. Roy, B. Sur, A. Banerjee, *Planta. Med.* **51** (1984) 295
8. V. Yardley, D. Snowdon, S. Croft, B. Hazra, *Phytother. Res.* **10** (1996) 559
9. F. J. Bullock, J. F. Tweedie, D. D. McRitchie, M. A. Tucker, *J. Med. Chem.* **13** (1970) 550
10. N. B. Perry, J. W. Blunt, *Nat. Prod.* **54** (1991) 978
11. H. Bobich, A. Stern, *J. Appl. Toxicol.* **13** (1993) 353
12. J. J. Inbaraj, C. F. Chignell, *Chem. Res. Toxicol.* **17** (2004) 55

13. Z. Varga, L. Bene, C. Pieri, S. Damjanovich, R. Gaspar, *Biochem. Biophys. Res. Commun.* **218** (1996) 828
14. A. Kovacs, I. Mascari, I. Hargittai, *J. Phys. Chem. A* **103** (1999) 3110
15. M. Cuma, S. Scheiner, T. Kar, *J. Mol. Struct. THEOCHEM* **467** (1999) 37
16. S. F. Tayyari, H. Raissi, F. Milani-Nejad, I. S. Butler, *Vib. Spectrosc.* **26** (2001) 187
17. R. Kakkar, V. Katoch, *J. Mol. Struct. THEOCHEM* **578** (2002) 169
18. D. Devault, *Quantum Mechanical Tunnelling in Biological Systems*, Cambridge Univ. Press, London, 1984
19. L. I. Krishtalik, *Biochim. Biophys. Acta* **1458** (2000) 6
20. T. M. Krygowski, B. T. Stepien, *Chem. Rev.* **105** (2005) 3482
21. T. M. Krygowski, M. K. Cyranski, Z. Czarnocki, G. Haefelinger, A. R. Katritzky, *Tetrahedron* **56** (2000) 1783
22. F. D. Proft, P. Geerlings, *Chem. Rev.* **101** (2001) 1451
23. X. Li, A. E. Kuznetsov, H. F. Zhang, A. I. Boldyrev, L. S. Wang, *Science* **291** (2001) 859
24. E. D. Jemmis, B. Kiran, *Inorg. Chem.* **37** (1998) 2110
25. J. A. N. F. Gomes, R. B. Mallion, *Chem. Rev.* **101** (2001) 1349
26. Z. Chen, C. S. Wannere, C. Corminboeuf, R. Puchta, P. v. R. Schleyer, *Chem. Rev.* **105** (2005) 3842
27. R. H. Mitchell, *Chem. Rev.* **101** (2001) 1301
28. F. Faglioni, A. Ligabue, S. Pelloni, A. Soncini, R. G. Viglione, M. B. Ferraro, R. Zanasi, P. Lazzeretti, *Org. Lett.* **7** (2005) 3457
29. J. A. Pople, *J. Chem. Phys.* **24** (1956) 1111
30. D. W. Davies, *The theory of the electric and magnetic properties of molecules*, Wiley, London, 1967
31. R. C. Benson, W. H. Flygare, *J. Am. Chem. Soc.* **92** (1970) 7523
32. P. v. R. Schleyer, C. Maerker, A. Dransfeld, H. Jiao, N. J. R. v. E. Hommes, *J. Am. Chem. Soc.* **118** (1996) 6317
33. M. K. Cyranski, T. M. Krygowski, A. L. Katritzky, P. v. R. Schleyer, *J. Org. Chem.* **67** (2002) 1333
34. C. Corminboeuf, T. Heine, G. Seifert, P. v. R. Schleyer, J. Weber, *Phys. Chem. Chem. Phys.* **6** (2004) 273
35. E. Steiner, P. W. Fowler, *Chem. Commun.* (2001) 2220
36. T. M. Krygowski, K. Ejsmont, B. T. Stepien, M. K. Cryanski, J. Poater, M. J. Sola, *Org. Chem.* **69** (2004) 6634
37. T. M. Krygowski, B. T. Stepien, M. K. Cryanski, K. J. Ejsmont, *Org. Chem.* **18** (2005) 886
38. J. Juselius, D. Sundholm, *Phys. Chem. Chem. Phys.* **1** (1999) 3429
39. G. Subramanian, P. v. R. Schleyer, H. Jiao, *Angew. Chem. Int. Ed. Engl.* **35** (1996) 2638
40. T. Zywietz, H. Jiao, P. v. R. Schleyer, A. de Meijere, *J. Org. Chem.* **63** (1998) 3417
41. A. Hirsch, Z. Chen, H. Jiao, *Angew. Chem. Int. Ed.* **39** (2000) 3915
42. M. Bühl, A. Hirsch, *Chem. Rev.* **101** (2001) 1153
43. F. P. Cossio, I. Marao, H. Jiao, P. v. R. Schleyer, *J. Am. Chem. Soc.* **121** (1999) 6737
44. S. P. Verevkin, H. D. Beckhaus, C. Rückhardt, R. Haag, S. I. Kozhushkov, T. Zywietz, A. de Meijere, H. Jiao, P. v. R. Schleyer, *J. Am. Chem. Soc.* **120** (1998) 11130
45. P. v. R. Schleyer, B. Kiran, D. V. Simon, T. S. Sorensen, *J. Am. Chem. Soc.* **122** (2000) 510

46. R. Jin, *J. Mol. Struct. THEOCHEM* **939** (2010) 9
47. S. Sharma, B. K. Sharma, Y. S. Prabhakar, *Eur. J. Med. Chem.* **44** (2009) 2847
48. Y.-B. Ji, Z.-Y. Qu, X. Zou, *Exp. Toxicol. Pathol.* **63** (2011) 69
49. B. K. Aithal, M. R. S. Kumar, B. N. Rao, N. Udupa, B. S. S. Rao, *Cell. Biol. Int.* **33** (2009) 1039
50. *Gaussian 98 software package*, Gaussian Inc., Wallingford, CT, 1998.

Journal of the Serbian Chemical Society
JSCS-info@shd.org.rs • www.shd.org.rs/JSCS
J. Serb. Chem. Soc. *76* (6) 891–902 (2011)
JSCS–4169
UDC 665.52/.54:544.022:544.723.232
Original scientific paper

A quantitative structure–retention relationship for the prediction of retention indices of the essential oils of *Ammoides atlantica*

PARVIZ ABEROMAND AZAR[1], MEHDI NEKOEI[1], SIAVASH RIAHI[2,3]*, MOHAMMAD R. GANJALI[3] and KARIM ZARE[1]

[1]*Department of Chemistry, Faculty of Basic Sciences, Science and Research Branch, Islamic Azad University, Tehran,* [2]*Institute of Petroleum Engineering, College of Engineering, University of Tehran, P. O. Box 11365–4563, Tehran and* [3]*Center of Excellence in Electrochemistry, Faculty of Chemistry, University of Tehran, P. O. Box 14155–6455, Tehran, Iran*

(Received 19 October, revised 23 December 2010)

Abstract: A simple, descriptive and interpretable model, based on a quantitative structure–retention relationship (QSRR), was developed using the genetic algorithm-multiple linear regression (GA-MLR) approach for the prediction of the retention indices (*RI*) of essential oil components. By molecular modeling, three significant descriptors related to the *RI* values of the essential oils were identified. A data set was selected consisting of the retention indices for 32 essential oil molecules with a range of more than 931 compounds. Then, a suitable set of the molecular descriptors was calculated and the important descriptors were selected with the aid of the genetic algorithm and multiple regression method. A model with a low prediction error and a good correlation coefficient was obtained. This model was used for the prediction of the *RI* values of some essential oil components which were not used in the modeling procedure.

Keywords: chemometrics; QSRR; genetic algorithms; multiple linear regression; retention indices; essential oils.

INTRODUCTION

Essential oils are valuable natural products used as raw materials in many fields, including folk medicine, perfumes, cosmetics, aromatherapy, phytotherapy, spices and nutrition. They are mixtures of more than 200 compounds that can be grouped basically into two fractions, a volatile fraction, which constitutes 90–95 % of the whole oil and contains monoterpenes and sesquiterpene hydrocarbons and their oxygenated derivatives, together with aliphatic aldehydes, al-

* Corresponding author. E-mail: riahisv@khayam.ut.ac.ir
doi: 10.2298/JSC100219076A

cohols and esters, and a nonvolatile residue, that constitutes 5–10% of the whole oil and contains hydrocarbons, fatty acids, sterols, carotenoids, waxes, coumarins, psoralens and flavonoids.[1]

Ammoides atlantica is of the *Apiaceae* family. The plant is used in infusions for the treatment of headache, fever and diarrhea. It is also used in compresses, alone or soaked in alcohol or vinegarand mixed with henna, to treat children affected by mental debility as reported by Laouer *et al.*[2]

GC and GC–MS are the main methods for the identification of these plant oils. Seeking a quantitative relationship between the molecular structure and the gas chromatographic retention indices has been a basic task in chemistry. Correlations between the GC retention indices and the molecular structures can provide more profound insights into the interactions between the eluents and the stationary phases from a theoretical viewpoint. In addition, they can provide very important information about the effect of the chemical structures on the retention behavior and the possible mechanism of absorption and elution.

Prediction of physico–chemical properties of materials based on their molecular structure has been one of the wishes of scientists and engineers for a long time. One of the best methods which has been applied for this purpose is quantitative structure–property relationships (QSPR). QSPR analysis is now a well-established and highly respected technique to correlate diverse simple and complex physico–chemical properties of a compound with its molecular structure, through a variety of descriptors. The basic strategy of QSPR analysis is to find optimum quantitative relationships, which can then be used for the prediction of the properties from molecular structures. Once a reliable relation has been obtained, it is possible to use it to predict that same property for other structures not yet measured or even not yet prepared.[3]

Quantitative structure–retention relationships represent statistical models that quantify the relation between the structure of molecules and their chromategraphic retention indices, allowing the prediction of the retention indices of novel compounds. QSRR on the retention indices have been reported for different types of organic compounds.[4–8]

The application of these techniques usually requires variable selection for building well-fitted models. In this work, the genetic algorithm selection method was employed for the variable selection in the MLR method. Nowadays, GA is well-known as an interesting and widely used variable selection method.[9–11]

The aim of this work was to search for an efficient method to build an accurate quantitative relationship between the molecular structure and the retention indices of *A. atlantica* essential oils by GA–MLR.

EXPERIMENTAL

Computer hardware and software

A Pentium IV personal computer (CPU at 3.06 GHz) with the Windows XP operating system was used. The geometry optimization was performed with HyperChem (Version 7.0 Hypercube, Inc). For the calculation of the molecular descriptors, Dragon 2.1 software was used.[12] SPSS software (version 11.50, SPSS, Inc.) was employed for the simple MLR analysis. The GA–MLR regression and the other calculations were performed in Matlab (Version 7.0, Math works, Inc).

Data set

The data set of the GC retention indices was taken from the values reported by Laouer *et al*.[13] The Kovats retention indices were obtained according to the following equation:

$$I = 100N + 100\left[\frac{\log x_i - \log x_z}{\log x_{(z+1)} - \log x_z}\right] \quad (1)$$

where x refers to the adjusted retention volume or time, z is the number of carbon atoms of the *n*-alkane eluting before and z+1 is the number of carbon atoms of the *n*-alkane eluting after the peak of interest. These values were obtained after subtracting the number of the carbons in the main chain ties 100 from Kovats indices (*KI*).

The molecules in the data set, including the essential oils from *Ammoides atlantica*, are shown in Table I. The retention indices of all compounds were determined by GC and GC–MS under a single set of conditions. An apolar fused silica capillary column Perkin Elmer Elite-5 MS (5 % phenylmethylsiloxane, 30 m×0.25 mm, 0.25 μm film thickness) was used. The column oven temperature was programmed from 60–185 °C at 1.5 °C min^{-1}, held isothermal at 185 °C for 1 min and then raised to 275 °C at 9 °C min^{-1}.

The data set was split into a training set and a prediction set. The prediction set of 6 compounds was selected randomly from the original 32 of essential oil components, with the remaining compounds constituting the training set. The training set of 26 compounds, with *RI* values in the range 931–1582, was used to adjust the parameters of the model, and the test set of 6 compounds, with *RI* in the range 954–1545, was used to evaluate its predictive ability.

Determination of molecular descriptors

Molecular descriptors are defined as numerical characteristics associated with chemical structures. The molecular descriptor is the final result of a logic and mathematical procedure which transforms chemical information encoded within a symbolic representation of a molecule into a useful number applied to correlate physical properties.

The Dragon software was used to calculate the descriptors in this research and a total of 1481 molecular descriptors, from 18 different types of theoretical descriptors, were calculated for each molecule. Since the values of many descriptors are related to the bonds length and bonds angles *etc*., the chemical structure of every molecule must be optimized before calculating its molecular descriptors. For this reason, the chemical structure of the 32 studied molecules were drawn with Hyperchem software and saved with the HIN extension. To optimize the geometry of these molecules, the AM1 geometrical optimization was applied. After optimizing the chemical structures of all compounds, the molecular descriptors were calculated using Dragon. A wide variety of descriptors have been reported in the literature, having been used in QSAR analysis.[14–19]

Genetic algorithm for descriptor selection

In QSPR studies, after calculating the molecular descriptors from optimized chemical structures of all the components available in the data set, the problem is to find a linear equation that can predict the desired property with the least number of variables as well as highest accuracy.

In other words, the problem is to find a subset of variables (most statistically effective molecular descriptors for the *RI*) from all the available variables (all molecular descriptors) that can predict *RI* with the minimum error in comparison to the experimental data.

A generally accepted method for this problem is the genetic algorithm based multivariate linear regression (GA-MLR). In this method, the genetic algorithm is applied for the selection of the best subset of variables with respect to an objective function. This algorithm was presented by Leardi *et al*. for the first time.[20]

The GA is a stochastic method to solve the optimization problems defined by fitness criteria, applying the evolution hypothesis of Darwin and different genetic functions, *i.e*., crossover and mutation.

To select the most relevant descriptors, the evolution of the population was simulated.[21–23] The population of the first generation was selected randomly. Each individual member in the population, defined by a chromosome of binary values, represented a subset of descriptors. The number of the genes at each chromosome was equal to the number of the descriptors. A gene was given the value of 1, if its corresponding descriptor was included in the subset; otherwise, it was given the value of zero. The number of the genes with the value of 1 was kept relatively low to have a small subset of descriptors.[24] As a result, the probability of generating 0 for a gene was set greater (at least 60 %) than the value of 1. The operators used here were crossover and mutation. The application probability of these operators was varied linearly with a generation renewal (0.0–0.1 % for mutation and 60–90 % for crossover). The population size was varied between 50 and 250 for different GA runs. For a typical run, the evolution of the generation was stopped when 90 % of the generations took the same fitness.

MLR Modeling

The general purpose of multiple regressions is to quantify the relationship between several independent or predictor variables and a dependent variable. A set of coefficients defines the single linear combination of independent variables (molecular descriptors) that best describes retention indices. The retention indices value for each essential oil component would then be calculated as a composite of each molecular descriptor weighted by the respective coefficients. A multi-linear model can be represented as:

$$y = \beta_0 + \beta_1\chi 1 + \beta_2\chi 2 + \beta_3\chi 3 + \cdots + \beta_k\chi k + \varepsilon \quad (2)$$

where k is the number of independent variables, $\beta_1,\ldots, \beta_k$ the regression coefficients and y is the dependent variable. The regression coefficients represent the independent contributions of each calculated molecular descriptor. The algebraic MLR model is defined in Eq. (1) and in matrix notation:

$$y = Xb + e \quad (3)$$

when X is of full rank, the least-squares solution is $b = (X^TX)^{-1}X^Ty$, where b is the estimator for the regression coefficients in b and X^T is a transpose of X.

A single MLR model was developed for essential oil compounds using SPSS software (version 11.50, SPSS Inc., USA). The MLR model was built using a training set and validation using an external prediction set. Multiple linear regression (MLR) techniques based on least-

squares procedures are very often employed for estimating the coefficients involved in a model equation.[25]

RESULTS AND DISCUSSION

MLR Analysis

The multiple linear regression method (MLR) is one of the most used modeling methods in QSRR. Thus, MLR analysis was performed to derive the best QSAR model. A small number of molecular descriptors proposed by our team were used to establish a QSRR model. The MLR technique was performed on the molecules of the training set shown in Table I. After regression analysis, a few suitable models were obtained, from which the best model was selected and is presented in Eq. (3). A small number of molecular descriptors (*RDF*035*m*, *PCD* and *Q*2) proposed were used to establish the QSRR model. Additional validation was performed on an external data set consisting of 6 essential oil compounds. MLR Analysis provided a useful equation that can be used to predict the RI of essential oil based upon these parameters. The best equation obtained for the RI of the essential oil compounds is:

$$RI = 590.81 + 20.56RDF035m + 107.41PCD + 839.37Q2 \quad (4)$$

TABLE I. The data set and the corresponding observed and predicted *RI* values by GA-MLR for the training and test set (*E* – relative error)

No.	Compound	*RI* (Exp)	*RI* (GA-MLR)	*E* / %
	Training set			
1	*α*-Thujene	931	993.31	6.69
2	*α*-Pinene	941	967.82	2.85
3	Sabinene	975	976.75	0. 18
4	*β*-Pinene	980	968.41	–1.18
5	*α*-Phellandrene	1007	1051.05	4.37
6	*δ*-3-Carene	1013	998.54	–3.38
7	*p*-Cymene	1026	1112.58	8.43
8	Limonene	1030	995.12	–3.38
9	*γ*-Terpinene	1064	1010.16	–5.05
10	*cis*-Sabinene hydrate	1069	989.20	–7.46
11	Linalool	1099	1178.61	7.24
12	*cis*-*p*-Menth-2-en-1-ol	1123	1193.25	6.25
13	*α*-Terpineol	1186	1118.92	–5.65
14	Methyl thymol	1236	1290.56	4.41
15	Thymol	1292	1265.62	–2.04
16	Carvacrol	1297	1257.97	–3.00
17	*β*-Caryophyllene	1420	1394.21	–1.81
18	*α*-Amorphene	1486	1490.01	0.26
19	*γ*-Cadinene	1516	1399.89	–7.65
20	*δ*-Cadinene	1527	1517.06	–0.65
21	Germacrene B	1560	1572.98	0.83
22	Caryophyllene oxide	1582	1617.89	2.26

TABLE I. Continued

No.	Compound	*RI* (Exp)	*RI* (GA-MLR)	*E* / %
		Prediction set		
1	Camphene	954	1039.2	8.93
2	Myrecene	993	997.8	0.48
3	α-Terpinene	1020	1012.2	–0.76
4	1,8-Cineole	1032	1082.3	4.88
5	Terpinolene	1088	985	–9.45
6	Terpinen-4-ol	1177	1119.5	–4.87
7	Methyl carvacrol	1244	1272.5	2.29
8	α-Copaene	1379	1382.8	0.28
9	α-Muurolene	1501	1482.9	–1.19
10	Selina-3,7(11)-diene	1545	1406.2	–8.98

Positive values of the regression coefficients indicate that the indicated descriptor contributes positively to the value of *RI*, whereas negative values indicate that the greater the value of the descriptor, the lower is the value of *RI*. In other words, increasing *RDF*035*m*, *PCD* and *Q*2 will increase the extent of the *RI* of essential oil compounds.

For an evaluation of the predictive power of the generated MLR, the optimized model was applied for prediction of the *RI* values of 6 compounds in the prediction set, which were not used in the optimization procedure. For the constructed models, the predictive ability of the MLR model was evaluated by calculation of statistical parameters.

The data set and the corresponding experimental and predicted *RI* values of all the molecules studied in this work are summarized in Table I. Plots of the values predicted by the GA-MLR against the experimental values of the retention indices of the training and prediction sets are shown in Fig. 1. The residuals (experimental *RI* − predicted *RI*) obtained by the GA-MLR modeling *versus* the experimental *RI* values are shown in Fig. 2. The distribution of the residuals on both sides of the zero line indicates there is no systematic error in the GA-MLR model.

Statistical parameters

For an evaluation of the predictive power of the generated MLR, the optimized model was applied for the prediction of the *RI* values of the test compounds in the prediction set, which were not used in the optimization procedure. For the constructed models, two general statistical parameters were selected to evaluate the prediction ability of the model for *RI* values. For this case, the predicted *RI* of each sample in the prediction step was compared with the experimental *RI*.

The root mean square error of prediction (*RMSEP*) is a measurement of the average difference between predicted and experimental values, at the prediction

stage. The *RMSEP* can be interpreted as the average prediction error, expressed in the same units as the original response values. The *RMSEP* was obtained using the following formula:

$$RMSEP = \frac{100}{\bar{y}}\left[\frac{1}{n}\sum_{i=1}^{n}(y_i - \hat{y}_i)^2\right]^{0.5} \quad (5)$$

The second statistical parameter was the relative error of prediction (*REP*) that shows the predictive ability of each component, and is calculated as:

$$REP\ (\%) = \frac{100}{\bar{y}}\left[\frac{1}{n}\sum_{i=1}^{n}(\hat{y}_i - y_i)^2\right]^{0.5} \quad (6)$$

where y_i is the experimental *RI* value of the essential oil in the sample *i*, $\hat{y}_i$ represents the predicted *RI* value of the essential oil in the sample *i*, $\bar{y}$ is the mean of experimental *RI* values in the prediction set and *n* is the total number of samples used in the prediction set.

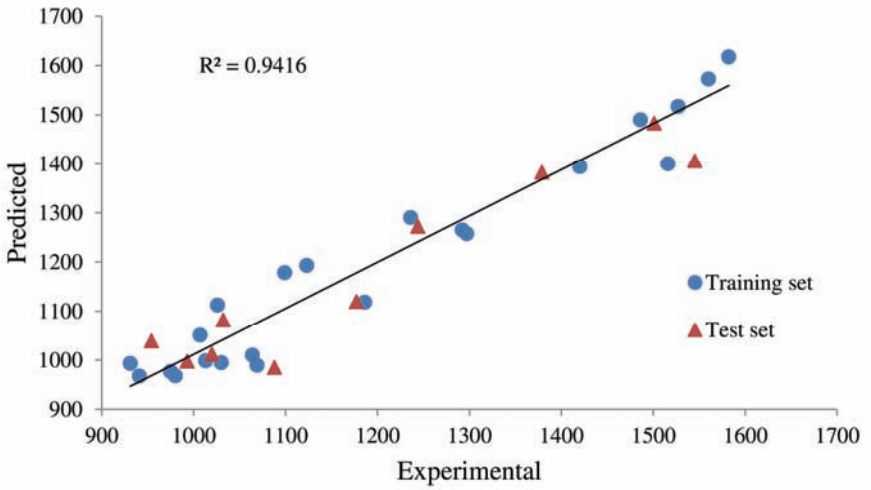

Fig. 1. The *RI* values predicted by the MLR modeling *vs.* the experimental *RI* values.

The statistical parameters calculated for the GA–MLR model are listed in Table II.

Topliss and Edwards[26] demonstrated that the more independent variables screened, the more independent variables are available for selection in a multiple linear regression model and the more likely a model will be found by chance. These authors recommended that in order to reduce the risk of chance correlations, there should be a certain ratio of data points to the number of independent variables available. A solution for the detection of a chance correlation is the *Y*-randomization test.[27] In order to assess the robustness of the model, the *Y*-ran-

domization test was applied in this study. The dependent variable vector (*RI*) was randomly shuffled and a new QSPR model was developed using the original independent variable matrix. The new QSPR models (after several repetitions) are expected to have low R^2 and Q^2 values (Table III). If the R^2 and Q^2 values of these models were much lower than those of the original model, it could be considered that the model was reasonable and had not been obtained by the chance.

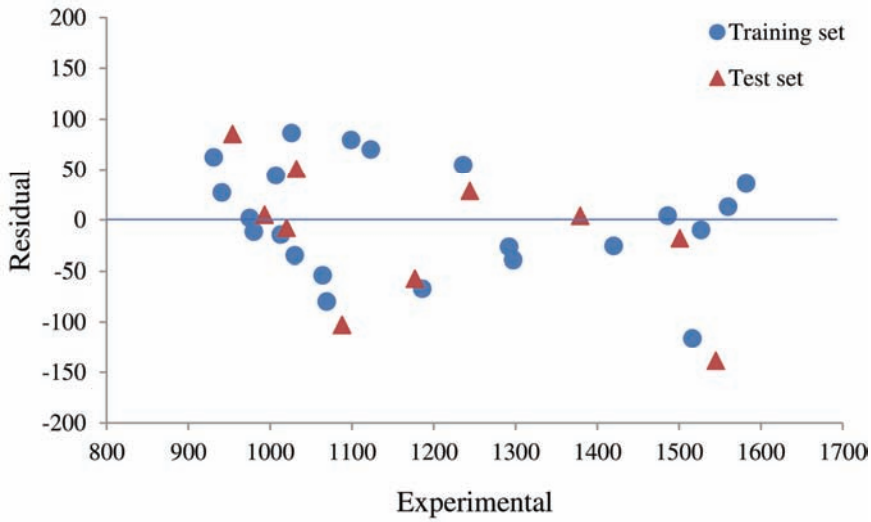

Fig. 2. Plot of the residuals against the experimental values of the retention indices.

TABLE II. Statistical parameters obtained by application of the MLR method to the test set

Parameter	Value
RMSEP	66.473
REP / %	5.570
R^2	0.894
Number of descriptors	3

TABLE III. R^2 train and Q^2LOO values after several *Y*-randomization tests

Iteration	R^2	Q^2
1	0.1568	0.0031
2	0.1217	0.0013
3	0.2186	0.0122
4	0.0729	0.0096
5	0.1354	0.0197
6	0.0097	0.2751
7	0.1877	0.0026
8	0.3235	0.1193
9	0.0814	0.0506
10	0.2099	0.0059

Description of the models descriptors

The retention indices in GC depend on the relative solubility of the solute in the mobile and stationary phases, which depend on the molecular structure and chemical properties of the solute. Differences between these properties govern the retention behavior through the column.

In this work, three descriptors were selected including *RDF*035*m*, *PCD* and Q2 for the prediction of the retention indices values. A brief description of the descriptors is presented in Table IV. The methods for the calculations of these descriptors and their meaning have been explained in the Handbook of Molecular Descriptors by Todeschini *et al.*[14]

TABLE IV. A brief description of the descriptors used in this study

No.	Descriptor	Definition
1	*RDF*035*m*	Radial distribution function – 3.5/weighted by atomic mass
2	*PCD*	Difference of multiple path counts to path counts
3	*Q2*	Total squared charge

The first descriptor is *RDF*035*m*, which is one of the radial distribution function (*RDF*) descriptors. A *RDF* in this form meets all the requirements for a 3D structure descriptor. It is independent of the atom number (*i.e.*, the size of a molecule), it is unique regarding the three-dimensional arrangement of the atoms and it is invariant against translation and rotation of the entire molecule.

Formally, a radial distribution function of an ensemble of N atoms can be interpreted as the probability distribution to find an atom in a spherical volume of radius r.[21] The following equation represents the radial distribution function code as it was used in this investigation:

$$g(r) = f \sum_{i}^{N-1} \sum_{j}^{N} A_i A_j e^{-B(r-r^4)^2} \quad (7)$$

where f is a scaling factor and N is the number of atoms. By including characteristic atomic properties A of the atoms i and j, the *RDF* codes can be used in different tasks to fit the requirements of the information to be represented. The exponential term contains the distance r_{ij} between the atoms i and j and a smoothing parameter B, which defines the probability distribution of the individual distances. $g(r)$ was calculated at a number of discrete points with defined intervals. The atomic properties A_i and A_j used in this equation enable the discrimination of the atoms of a molecule for almost any property that can be attributed to an atom. Such a distribution function provides, besides information about interatomic distances in the whole molecule, the opportunity to gain access to other valuable information, *e.g.*, bond distance, ring types, planar and non-planar systems and atom types. This fact is a most valuable consideration for a computer-assisted

code elucidation. The radial distribution function in this form meets the entire requirement mentioned above, especially the invariance against linear translations.[28]

Additionally, the *RDF* descriptors can be restricted to specific atom types or distance ranges to represent specific information in a certain three-dimensional structure space (*e.g.*, to describe the steric hindrance or the structure/activity properties of a molecule). *RDF*035*m* displays a positive sign, which indicates that a retention index is directly related to this descriptor.

The second descriptor of this model was the difference of multiple path counts to path counts (*PCD*) that describes information related to bonds and distances (bond orders, saturation and ratio of multiple bonds to single bonds).[14] Its effect on the retention indices was positive, which indicates that the retention time is directly related to this descriptor.

The final descriptor of this model was the total squared charge (*Q2*)[29–31] that is obtained by the following formula:

$$Q2 = \sum_{i}^{N} Q_i^2 \tag{8}$$

where Q_i is the amount of charge on atom i and N is the number of atoms of that molecule. This descriptor had a positive effect on the retention indices.

The correlation coefficient matrix for the descriptors used in this study (GA-MLR), is listed in Table V. The data indicate there is a very low correlation between the descriptors used in this research. Therefore, the ability of the resulting QSRR regression models to enable accurate prediction of the retention indice is not related to co-linearity between the variables.

TABLE V. The correlation coefficient matrix for the descriptors used in this study

	PCD	*Q2*	*RDF*035*m*
PCD	1	–	–
Q2	0.259	1	–
*RDF*035*m*	0.108	0.532	1

CONCLUSIONS

In this paper, a simple QSRR model was presented for the prediction of the *RI* of essential oils. This model is a multivariate linear model, which has three variables (molecular descriptors). These three molecular descriptors were selected using the GA-MLR technique. These variables are calculated based on the chemical structure of the molecules. The QSRR model with the simply calculated molecular descriptors could be employed to estimate the retention indices for new compounds, even in the absence of standard candidates.

ИЗВОД

КВАНТИТАТИВНА РЕЛАЦИЈА ИЗМЕЂУ СТРУКТУРЕ И РЕТЕНЦИЈЕ ЗА ПРЕДВИЂАЊЕ ИНДЕКСА РЕТЕНЦИЈЕ ЕСЕНЦИЈАЛНИХ УЉА ИЗ *Ammoides atlantica*

PARVIZ ABEROMAND AZAR[1], MEHDI NEKOEI[1], SIAVASH RIAHI[2,3], MOHAMAD R. GANJALI[3] и KARIM ZARE[1]

[1]*Department of Chemistry, Faculty of Basic Sciences, Science and Research Branch, Islamic Azad University, Tehran,* [2]*Institute of Petroleum Engineering, College of Engineering, University of Tehran, P. O. Box 11365–4563, Tehran u* [3]*Center of Excellence in Electrochemistry, Faculty of Chemistry, University of Tehran, Iran*

Развијен је једноставан, дескриптиван и интерпретативан модел, заснован на квантитативној релацији између структуре и ретенције (QSRR), уз примену генетичког алгоритма са линеарном регресијом (A-MLR). Помоћу тог модела предвиђају се ретенциони индекси (*RI*) за компоненте есенцијалних уља. Помоћу молекулског моделовања идентификована су три битна дескриптора за опис *RI*. Састављена је база података која се састоји из *RI* за 32 молекула који су садржани у есенцијалним уљима, од више од 931 познатих. Затим је израчунат погодан скуп молекулских дескриптора и најбитнији међу њима су одређени помоћу GA-MLR. Добијен је модел са ниском грешком и добрим коефицијентом корелације. Модел је онда употребљен за предвиђање *RI* вредности за неке компоненте есенцијалних уља које нису коришћене за добивање QSRR модела.

(Примљено 19. октобра, ревидирано 23. децембра 2010)

REFERENCES

1. N. Achak, A. Romane, M. Alifriqui, R. P. Adams, *J. Essent. Oil Res.* **20** (2008) 200
2. H. Laouer, M. M. Zerroug F. Sahli, A. N. Chaker, G. Valentini, G. Ferretti, M. Grande, J. Anaya, *J. Essent. Oil Res.* **15** (2003) 135
3. A. R. Katritzky, D. G. Fara, *Energy Fuels* **19** (2005) 922
4. M. Jalali-Heravi, M. H. Fatemi, *J. Chromatogr. A* **915** (2001) 177
5. Z. Garakani-Nejad, M. Karlovits, W. Demuth, T. Stimpfl, W. Vycudilik, M. Jalali-Heravi, K. Varmuza, *J. Chromatogr. A* **1028** (2004) 287
6. J. Acevedo-Martinez, J. C. Escalona-Arranz, A. Villar-Rojas, F. Tellez-Palmero, P. R. Roses, L. Gonzalez, R. Carrasco-Velar, *J. Chromatogr. A* **1102** (2006) 238
7. P. Tulasamma, K. S. Reddy, *J. Mol. Graphics Modell.* **25** (2006) 507
8. K. Heberger, T. Kowalska, *Chemom. Intell. Lab. Syst.* **47** (1999) 205
9. U. Depczynski, V. J. Frost, K. Molt, *Anal. Chim. Acta* **420** (2000) 217
10. B. K. Alsberg, N. Marchand-Geneste, R. D. King, *Chemom. Intell. Lab. Syst.* **54** (2000) 75
11. D. Jouanrimbaud, D. L. Massart, R. Leardi, O. E. De Noord, *Anal. Chem.* **67** (1995) 4295
12. Dragon 6, R. Todeschini, V. Consonni, M. Pavana, available at http://www.talete.mi.it/ /products/dragon_description.htm
13. H. Laouer, N. Boulaacheb, S. Akkal, G. Singh, P. Marimuthu, C. De Heluani, C. Catalan, N. Baldovini, *J. Essent. Oil Res.* **20** (2008) 266
14. R. Todeschini, V. Consonni, *Handbook of Molecular Descriptors*, Wiley-VCH, Weinheim, Germany, 2000.
15. L. B. Kier, L. H. Hall, *Molecular Connectivity in Structure–Activity Analysis*, RSP-Wiley, Chichester, UK, 1986.
16. E. V. Kostantinova, *J. Chem. Inf. Comp. Sci.* **36** (1997) 54

17. G. Rucker, C. Rucker, *J. Chem. Inf. Comp. Sci.* **33** (1993) 683
18. J. Galvez, R. Garcia, M. T. Salabert, R. Soler, *J. Chem. Inf. Comp. Sci.* **34** (1994) 520
19. P. Broto, G. Moreau, C. Vandicke, *J. Med. Chem.* **19** (1984) 66
20. R. Leardi, R. Boggia, M. Terrile, *J. Chemom.* **6** (1992) 267
21. J. Hunger, G. Huttner, *J. Comput. Chem.* **20** (1999) 455
22. S. Ahmad, M. M. Gromiha, *J. Comput. Chem.* **24** (2003) 1313
23. C. L. Waller, M. P. Bradley, *J. Chem. Inf. Comput. Sci.* **39** (1999) 345
24. J. Aires-de-Sousa, M. C. Hemmer, J. Casteiger, *Anal. Chem.* **74** (2002) 80
25. J. N. Miller, J. C. Miller, *Statistics and Chemometrics for Analytical Chemistry*, Prentice Hall, London, 2000
26. J. G. Topliss, R. P. Edwards, *J. Med. Chem.* **22** (1979) 1238
27. A. Tropsha, P. Gramatica, V. K. Gombar, *QSAR Comb. Sci.* **22** (2003) 69
28. M. P. Gonzalez, Z. Gandara, Y. G. Gomez, *Eur. J. Med. Chem.* **43** (2008) 1360
29. N. Bodor, Z. Gabanyi, C. K. Wong, *J. Am. Chem. Soc.* **111** (1989) 3783
30. L. Buydens, D. Massart, P. Geerlings, *Anal. Chem.* **55** (1983) 738
31. M. Karelson, S. Victor, *Chem. Rev.* **96** (1996) 1027.

Journal of the Serbian Chemical Society
JSCS-info@shd.org.rs • www.shd.org.rs/JSCS
J. Serb. Chem. Soc. 76 (6) 903–922 (2011)
JSCS–4170
UDC 665.944+544.142.3+546.482+546.817:66.081.2:544.4
Original scientific paper

Characterization of hydroxybenzoic acid chelating resins: equilibrium, kinetics, and isotherm profiles for Cd(II) and Pb(II) uptake

BHAVNA A. SHAH[1]*, AJAY V. SHAH[2] and RITESH V. TAILOR[1]

[1]*Department of Chemistry, Veer Narmad South Gujarat University, Surat-7, Gujarat and* [2]*Science and Humanity Department, Polytechnic, Vidyabharti Trust, Umrakh, Bardoli-1, Gujarat, India*

(Received 1 June, revised 8 November 2010)

Abstract: Chelating ion-exchange resins were synthesized by polycondensation of *ortho*/*para* hydroxybenzoic acid with resorcinol/catechol employing formaldehyde as cross-linking agent at 80±5 °C in DMF. The resins were characterized by FTIR and XRD. The uptake behaviour of synthesized resins for Cd(II) and Pb(II) ions have been studied depending on contact time, pH, metal ion concentration and temperature. The sorption data obtained at optimized conditions were analyzed by the Langmuir and Freundlich isotherms. Experimental data of all metal–resin system were best represented by the Freundlich isotherm. The maximum obtained sorption capacity for cadmium was 69.53 mg g^{-1} and 169.32 mg g^{-1} for lead. The adsorption process follows first order kinetics and the specific rate constant K_r was obtained by the application of the Lagergan equation. Thermodynamic parameters ΔG^{ads}, ΔS^{ads} and ΔH^{ads} were calculated for the metal–resin systems. The external diffusion rate constant (K_s) and the intra-particle diffusion rate constant (K_{id}) were calculated by the Spahn––Schlunder and Weber–Morris models, respectively. The sorption process was found to follow an intra-particle diffusion phenomenon.

Keywords: chelating resin; SEM; kinetics; isotherm; distribution coefficient.

INTRODUCTION

In recent years, there has been a growing concern for the immobilization of metal ions introduced into water and wastewater bodies by increasing human technological activities. It has been established beyond doubt that heavy metal ions in the environment (water, soil and air) pose a very serious threat to human health. With the exponentially increasing population, there is a need for control-

* Corresponding author. E-mail: bhavna606@gmail.com
doi: 10.2298/JSC100601081S

ling heavy metal discharge before the toxic metal ions enter the complex ecosystem.

Separation, removal, and enrichment of trace metals in aqueous solutions play an important role in the analysis of wastewaters, industrial and geological samples. Solid phase extraction of metal ion has gained rapid acceptance because of its various advantages over other methods. The extraction of metal ions using chelating ion exchange resin is a green analytical method since it does not involve the use of toxic chlorinated organic solvents, which are very frequently used in conventional liquid–liquid extraction techniques. The main objective of most of the research on chelating resins was the preparation of insoluble functionalized polymers that can provide more flexible working conditions together with good stability and high capacity for metal ions.

The use of modified clay minerals for the adsorption of metal ions from aqueous solutions for water purification or industrial wastewater treatment has been widely studied. These clay minerals, when used as colloids or powders, have been found to be equally efficient as ion exchange resin but it is difficult to recover such adsorbents from filters after use. This further renders the regeneration and possible reuse of clay adsorbents very difficult.

The kinetics of the adsorption of toxic metal ions is required in order to predict the rate at which the toxic metal ions are removed from the aqueous solution. Adsorption kinetics also provides an insight into the mechanism of adsorption.[1]

A number of kinetic investigations have been performed on the adsorption of Pb(II) onto peat,[2] Pb(II) onto decaying leaves,[3] Cd(II) onto hydrous ferric oxide,[4] Cu(II) and Pb(II) onto a polysulphone and algae complex,[5] Cr(IV) onto peat,[6] Pb(II) on palm kernel fibre,[7] Pb(II) onto orthophosphate-modified Kaolinite clay,[8] Pb(II) and Cd(II) onto tripolyphosphate-modified Kaolinite clay,[9] to mention but a few. However, although these adsorbents all showed good potential as low cost adsorbents in the adsorption of metal ions, they either exist in aqueous solution as colloids or dispersed particles that are difficult to recover from filters.

To address the problem of recovery of adsorbent after use from filters, this study focuses on the production of a water-stable and mechanically strong adsorbent by the synthesis of chelating ion exchange resins. These were subsequently employed for the adsorption of Pb(II) and Cd(II).

This study further considers the kinetics of the adsorption of Pb(II) and Cd(II) onto chelating ion exchange resin adsorbents. The effects of pH, metal ion concentration, temperature, the pseudo-second order and pseudo first order rate constants and the kinetics of adsorption of Pb(II) and Cd(II) for all the resins were investigated. The obtained kinetic adsorption data were modelled against existing kinetic adsorption models.

EXPERIMENTAL

Reagents and solutions

Analytical reagent (A.R.) grade chemicals were used unless otherwise stated. Stock solutions (500 mM) of metal ions were prepared by dissolving appropriate amounts of $CdAc_2$ and $PbAc_2$ in deionised water acidified with 5 cm^3 of the corresponding acid. The metal ion solutions were standardized by complexometric titration with ethylenediaminetetraacetic acid (EDTA) using standard procedures.[10] The working solutions of metal ions were obtained by dilution of the stock solutions with deionised water. The solutions were adjusted to a particular pH using buffers. Acetate buffer was used to adjust the pH in the ranges 3.5 to 6.5. The water samples from industry were collected, immediately acidified with 2 % HNO_3, filtered, and stored in glass bottles. Solutions of acids and alkalis were prepared by dissolving appropriate amounts of the particular compound in deionised water and standardized by literature methods.[10]

Instruments

A flame atomic absorption spectrometer (AAS, Electronic Corporation of India Ltd., Hyderabad, India, model 4129) was used for the measurements of the metal concentrations, employing an air–acetylene flame (air and acetylene flow rates: 10 dm^3 min^{-1} and 2.0 dm^3 min^{-1}, respectively). The line selected for monitoring Cd and Pb were 228.8 and 217.0 nm, respectively. The analysis of each metal ion was realised by AAS after appropriate dilution. The infrared spectra of the synthesized resin in KBr pellets were recorded on an FTIR spectrophotometer (Shimadzu, model-8201PC, Japan). The X-ray diffraction (XRD) analysis was performed using an advanced diffractometer (Bruker, AXE D8, UK). The surface morphology was analyzed using an optical microscope (Olympus, SZX12, Japan) and a scanning electron microscope (Philips, XL30, Netherlands) at different magnifications. The sorption–desorption studies of both metal ions were performed by the batch technique and using columns of 0.5 cm internal diameter. For the batch sorption technique, a mechanical shaker equipped with an incubator (Hindustan Scientific, New Delhi, India) at a speed of 200 strokes min^{-1} was used throughout the equilibration.

Resin synthesis

Salicylic acid/*p*-hydroxybenzoic acid (13.5 g, 0.1 mol) was taken in a 250 cm^3 round bottom flask and dissolved in dimethyl formamide (DMF) solvent (20 cm^3) to give a clear solution. A solution of resorcinol/catechol (11 g, 0.1 mol) in 10 cm^3 DMF was added to the solution and stirred for 2 h. Formaldehyde (0.3 mol, 37 %) was added and stirred for an hour. The salicylic acid–formaldehyde–resorcinol (SFR), salicylic acid–formaldehyde–catechol (SFC), *p*-hydroxybenzoic acid–formaldehyde–resorcinol (*p*HFR) and *p*-hydroxybenzoic acid–formaldehyde–resorcinol (*p*HFC) resins were synthesized by refluxing the corresponding mixture at 80±5 °C in a water bath for 2–3 h under constant stirring, during which the mixture gelled to a soft dark brown mass. A gel was separated from the reaction vessel and cured in an oven at 80–90 °C for 12 h. As carboxylic acid groups normally decompose above 100 °C, the resin was cured below 90 °C. The resulting resins were washed with DMF to remove monomer impurities and finally with deionised water. After the complete washing cycle, the yields of the resins were in the range 78–85 %. These purified and dried resins were finely ground and passed through a 50-mesh sieve and then a 20-mesh sieve to obtain a uniform particle size (20–50 mesh). The sieved resins were again washed with water, air dried at room temperature and stored in airtight polyethylene bottles.

To convert the resin samples into the H^+ form, resins of uniform particle size were equilibrated with 1 M HCl solution for 24 h and washed with deionised water until chloride-free,

checked with silver nitrate solution. The H^+ form of the resins were used for the batch and column studies. The physico-chemical properties, *viz*. moisture content, % solid, apparent density, true density, void volume fraction and sodium exchange capacity were studied according to literature methods.[11]

Batch sorption experiments

The sorption properties, *i.e*., as the effect of contact time, the effect of pH, the effect of metal ion concentration and the effect of temperature, were studied by the batch equilibration method at 30±2 °C according to literature methods.[12]

To study the effect of contact time on the sorption of Cd(II) and Pb(II), accurately weighed (0.250±0.001 g) amounts of the H^+ form of the dry resins with a uniform particle size (20–50 mesh) were taken in different glass-stoppered flasks and equilibrated with buffer solutions of optimum pH value (pH of the highest exchange) for 6 h. After decanting the buffer solution, 50 cm^3 (200 mM) of metal ion solutions of the same pH were added. After the equilibration time, the solutions were filtered through a 0.02 μm membrane filter to separate the resin and solution. The amounts of non-adsorbed metal ions were determined by AAS at fixed time intervals.

To study the effect of pH on the uptake of Cd(II) and Pb(II), different sets of accurately weighed (0.250±0.001 g) dry resin were equilibrated with buffers of different pH values in glass-stoppered flasks for 6 h for the resin to attain the desired pH value. After 6 h, the buffer solutions were decanted and 50cm^3 of 200 mM metal ion solutions of varying pH from 3 to 7 were added. The metal ion solutions were equilibrated at room temperature (30±2 °C) for 6 h with intermittent shaking. The pH of the filtrate was measured and it was found that the pH remained stable throughout the experiment (±0.2). The non-adsorbed metal ions were estimated after filtration.

To study the effect of metal ion concentration on the uptake of Cd(II) and Pb(II) ions by the synthesized resins, accurately weighed (0.250±0.001 g) buffered resins were equilibrated with different concentrations of metal ion solutions (50 cm^3) in the range 50–300 mM at the same pH value at room temperature for 6 h with intermittent shaking. After 6 h, the metal ion solutions were filtered and the residual metal ions were estimated by AAS.

To study the effect of temperature, equilibrium experiments were performed at fixed metal ion concentration (200 mM) for a fixed resin loading (0.250±0.001g) and initial pH (different optimum pH for different resins for Cd(II) and Pb(II) ions) at four different temperatures: 30, 40, 50 and 60 °C.

Column chromatography

Column/ion exchange chromatography is a technique in which the separation of components of a mixture is realised by taking advantage of their different selectivity coefficients/retention capacity of the column adsorbent/resin. The differences in the selectivity coefficient/retention capacity lead to different migration rates on through the column. The study of column chromatography for the separation of mixtures and industrial effluents provides an idea of its application on a large scale.

A calibrated 50cm^3 glass column (0.5cm internal diameter) fitted with a glass wool plug at the lower end was used as ion exchange column. The resin having various particle sizes (20–50 mesh) was used to avoid choking of the column. The glass column was filled with a slurry of the resin in hot deionised water whereby air entrapment was avoided. The column was then backwashed with deionised water to ensure no air bubbles remained in the column and that the resin was uniformly distributed. This column was used for the separation of Cd(II) and Pb(II) from the mixtures.

RESULTS AND DISCUSSION

Physico–chemical properties

The physico–chemical properties of all four synthesized resins are presented in Table I. The moisture content of a resin furnishes a measure of its water loading capacity or its swelling capacity. The moisture content depends on many factors, such as the composition of the resin matrix, the degree of cross-linking or the nature of the active groups and the ionic form of the resin. The degree of cross-linking of a resin has an impact on the moisture content of the resin and the moisture content, in turn, has an impact on the selectivity. In a resin with a high moisture content, the active groups are spaced further apart from each other, for example, strong acid cation resins contain about 50 % moisture. The percentage moisture content of synthesized resins, as shown in Table I, ranged from 6.2–8.7 %. Thus, these resins have low range of percentage moisture content compared to the commercial resins. Resins synthesized from salicylic acid–furfuraldehyde–benzidine and *p*-hydroxybenzoic acid–furfuraldehyde–benzidine[13] had lower moisture contents (4.01 and 4.9 % respectively) than the present synthesized resins. The resin synthesized from salicylic–furfuraldehyde–hexamine[14] and salicylic acid–formaldehyde–*m*-cresol[15] exhibited slightly higher moisture contents (15.11 and 9.4 %, respectively) than SFR, SFC, pHFR and pHFC resins. The difference in moisture content may be due to the different experimental conditions, such as the media in which the resins were synthesized, the polymeric backbones, the degree of cross linking and functional groups involved.

TABLE I. Physico–chemical properties of the synthesized resins

Property	*SFR*	*SFC*	*p*HFR	*p*HFC	*SD*
Moisture content, %	7.0	6.2	8.7	6.5	0.5
Solid content, %	93	93.8	91.3	93.5	0.5
True density, d_{res} / g cm^{-3}	1.126	1.210	1.689	1.391	0.03
Apparent density, d_{col} / g cm^{-3}	0.842	0.883	0.931	0.916	0.006
Void volume fraction	0.453	0.483	0.448	0.341	0.005
Sodium exchange capacity, mmol g^{-1} dry resin	4.931	4.027	3.822	3.497	0.2
Concentration of fixed ionogenic groups, mmol cm^{-3}	5.02	4.473	5.893	4.548	0.200
Volume capacity, mmol cm^{-3}	2.67	2.209	3.247	2.997	0.05

The true densities of the synthesized resins, which were in the range 1.126 to 1.689 g cm^{-3}, are given in Table I. The true density of commercial resins generally lies between 1.1 to 1.7 g cm^{-3}. To avoid the floating of resin particles, the true density must be more than one. Floating of resin particles is undesirable in chromatographic studies, as it hampers the formation of a compact column. The optimum density and uniform particle size enable perfect column packing and performance of the column. The measurement of the column density, or apparent density, is necessary as commercially resins are sold on a volume basis and packed

on a weight basis. The apparent densities of the synthesized polymers are given in Table I, from which it can be seen that the apparent densities of all the resins were in the range of 0.84 to 0.93 g cm^{-3}, which is comparable to the density of commercial resins. This may be because of changes in the polymeric matrix, different functional groups and the method of synthesis. The apparent density parameter gives an idea of the required length of a packed column for an ideal column chromatographic study. The values of void volume fraction of resin are also given in Table I. The void volume fraction of the synthesized resin was in the range of 0.341 to 0.483. The appreciable values of the void volume fraction help the diffusion of the exchangeable ion on the resin and hence increase the rate of exchange of ions. The minimum essential void volume provides better diffusion of exchangeable ions and thus gives feasibility to column operation.

FTIR Spectra of resins

The FTIR spectra of the SFR, SFC, *p*HFR and *p*HFC resins are displayed in Fig. 1. The strong band at 3446–3452 cm^{-1} is attributed to ν(O–H) stretching of the phenolic group. The presence of a medium band at 2920–2926 cm^{-1} is due to the ν(C–H) stretching of the methylene group.[16] The medium strong band at 1630–1653 cm^{-1} can be assigned to ν(C=O) stretching of the aromatic acid

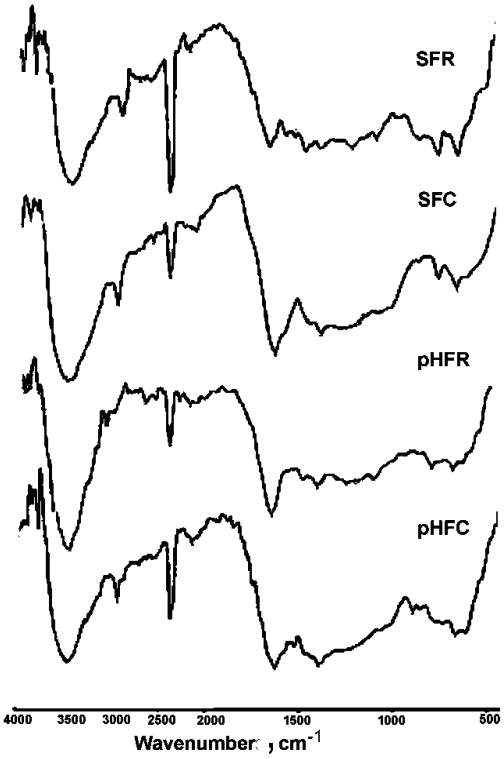

Fig. 1. FTIR Spectra of the synthesized resins.

group. The weak medium band at 1390–1462 cm^{-1} is due to δ(C–H) deformation of the methylene group.[15,17] The medium band at 769–775 cm^{-1} is due to the δ(C–H) bending of the 1,2,3,4-tetra substituted benzene ring.[18] The medium band at 664–667 cm^{-1} is attributed to the δ(C–H) bending of poly ethylene –(CH_2)– bridges.

X-Ray diffraction analysis

XRD Patterns of a compound provide information about its crystalline or amorphous nature and the regions of the compound that may co-exist.[19] The XRD patterns of all four resins (SFR, SFC, pHFR and pHFC) are shown in Fig. 2. No sharp peaks were observed in the diffractograms of the resins, which exhibited an irregular pattern, which is characteristic an amorphous compound. A phenol–formaldehyde resin exhibited a similar XRD pattern, which confirms the amorphous nature of the four synthesized resins.[20]

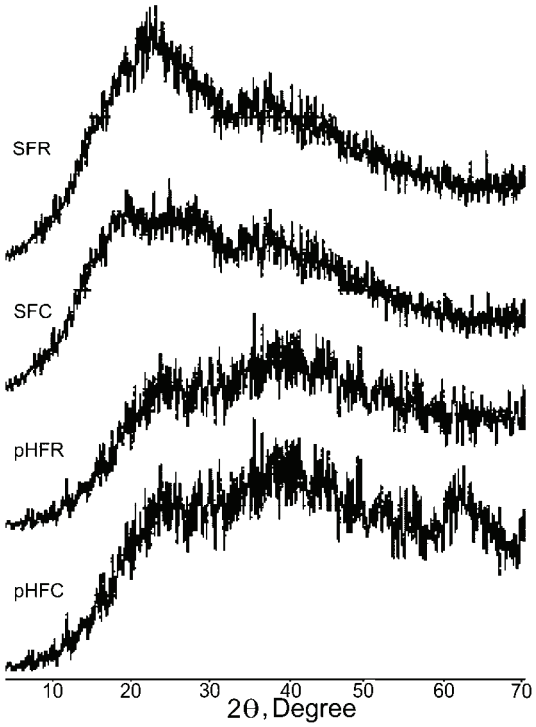

Fig. 2. XRD Patterns of the synthesized resins.

SEM and optical microscopy

Surface analysis is of great use for the understanding of the surface features of a material. Several observations were made of the resins before the photographs (SEM and optical) were taken to ensure that the photographed regions were representative of the overall resin. The optical photographs of synthesized

resins showed that the SFR resin was red in colour, whereas the pHFR resin appeared brown in colour with a rough surface, while the SFC and pHFC resins were black in colour with a smooth surface. This indicates that salicylic acid-containing resins exhibit a reddish–brown colour and the catechol-containing resins were black in colour.

The SEM photographs of all the resins are shown in Fig. 3 at 500× magnification. The SEM photographs indicate that the resin exhibits angular edges with regular fringes. The morphology of the resin shows a fringed micelle model of the crystalline–amorphous structure. The fringes represent the transition material between crystalline and amorphous phases. The SEM photographs exhibits such spherulites, which are the aggregate of some crystallites present along with some amorphous regions. SFC is more amorphous than *p*HFC, while *p*HFR is least amorphous. All four resins exhibited an amorphous character, which was confirmed by their XRD patterns.

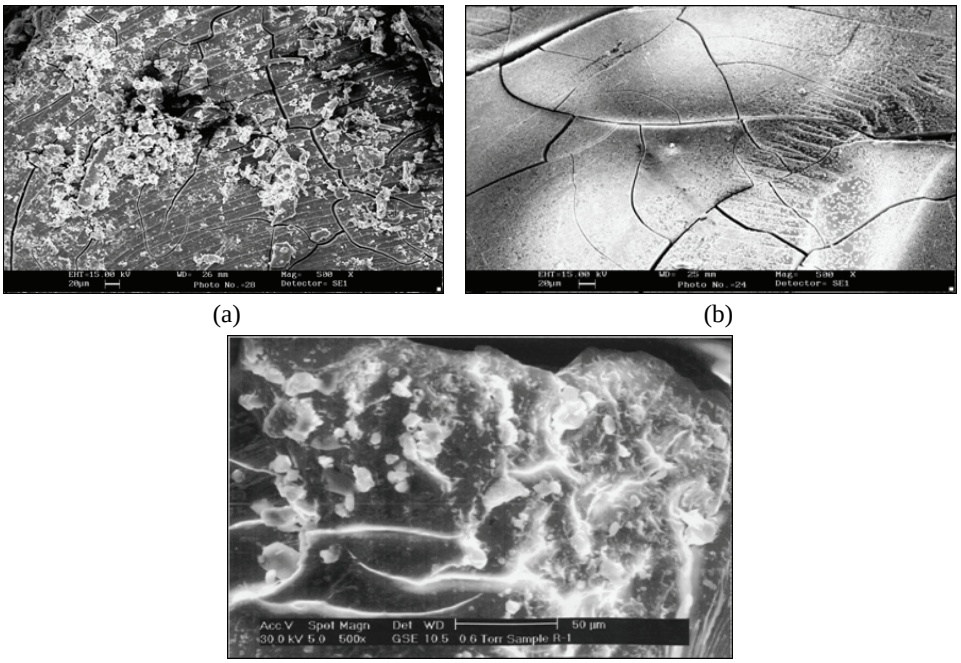

(a) (b)

(c)

Fig. 3. SEM Photographs of the synthesized resins at 500× magnification; a) *p*HFC, b) *p*HFR and c) SFC.

Effect of contact time

The rate of exchange of metal ions on the resin changed in a time dependent manner as can be seen in Fig. 4. Thus, the time required for 50 % exchange ($t_{1/2}$) of Cd(II) for the SFR and SFC resins was 50 min, for *p*HFR about 60 min and for

*p*HFC 65min. The time required for 50 % exchange ($t_{1/2}$) of Pb(II) for SFR was 45 min, for SFC 55 min, *p*HFR about 55 min and for *p*HFC 60 min. The fast rate of exchange at the beginning can be explained based on the law of mass action.[21] A faster rate of exchange is facilitated by column chromatographic separation. The kinetics of metal ion exchange mainly depends on various physical properties, such as particle size, pore size, physical core structure and diffusion of the counter ion.[15,17] Complete uptake of Cd(II) took 21 h with SFR, *p*HFR and *p*HFC and 15 h with SFC. Complete uptake of Pb(II) 12 h with SFR, 15h with SFC and 18 h with pHFR and pHFC. Hence, 24 h was considered as the optimum time for complete equilibration of Cd(II) and Pb(II) ions and was used for all further experiments.

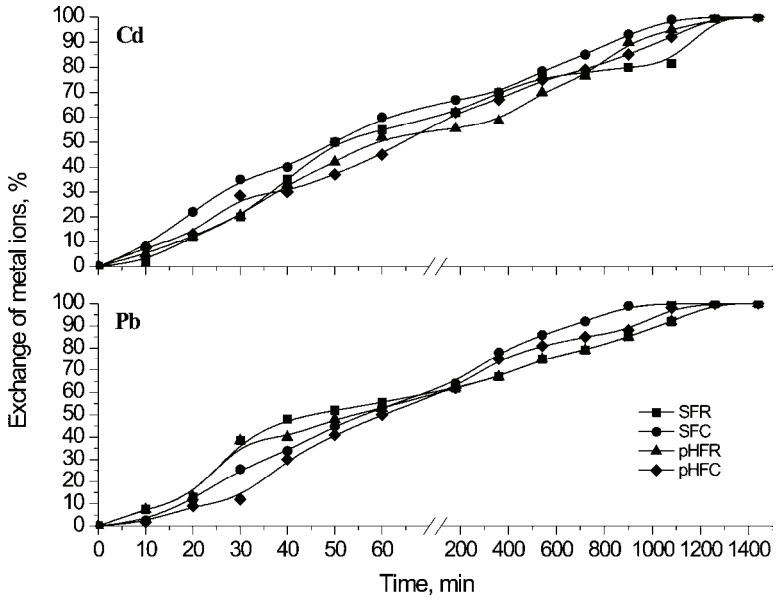

Fig. 4. Time dependence of the fraction of metal ion uptake by the synthesized resins. Conditions: c_0 = 200 mM, w = 0.25 g, V = 50 cm^3, t = 30±2 °C.

Effect of pH on the exchange capacity

The effect of pH variation on chelating ability of the synthesized resins towards Cd(II) and Pb(II) ions was studied. The removal of metal ions from aqueous solution was highly dependent on the pH of the solution that also affected the surface charge of the sorbents. The results are presented in Fig. 5 as exchange capacity against pH for both the studied metal ions. The results show that the uptake of Cd(II) and Pb(II) ions increased with increasing pH up to a certain value and thereafter decreased. The nature of the observed trend indicates that the cation exchange behaviour of these resin was similar to that of weak acid cation

exchangers,[17] because in weak acid cation ion exchanger, the exchange capacity is pH dependent.[19] The maximum uptake of SFR for Cd(II) and Pb(II) occurred at pH 5 and of SFC at pH 5.5, while *p*HFR exhibited a maximum capacity for Cd(II) at pH 5.5 and for Pb(II) at pH 5 and *p*HFC a maximum capacity for Cd(II) at pH 5 and for Pb(II) at pH 5.5.

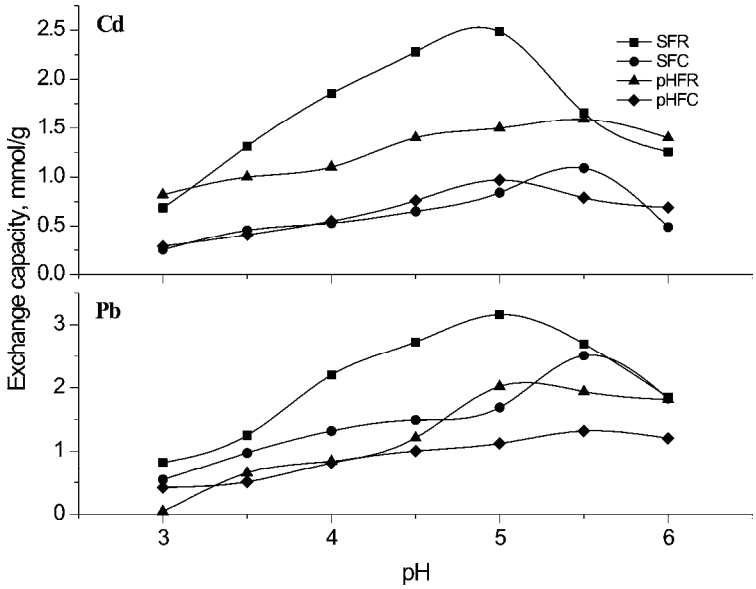

Fig. 5. Metal ion uptake capacity of the synthesized resins as a function of pH. Conditions: c_0 = 200 mM, w = 0.25 g, V = 0 cm^3, t = 30±2 °C.

The selectivity order for Pb(II) was SFR > SFC > *p*HFR > *p*HFC and for Cd(II), it was SFR > *p*HFR > SFC > *p*HFC. Chelation and ion exchange, are more favourable for the uptake of Pb(II) in case of the salicylic acid-containing resin due to its smaller hydrated ion radius. An increase in pH increased the negatively charged nature of the sorbent surface. This leads to an increase in the electrostatic attraction between the positively charged metal ions and the negatively charged sorbent, which results in an increase in the uptake of metal ions. The decrease in the removal of metal ions at lower pH is due to the higher concentration of H^+ present in the reaction mixture, which compete with the metal ions for the sorption sites on the resin surface. The observed decrease in sorption at higher pH is due to the formation of insoluble hydroxy complexes of the metal ions.[22]

Though SFC and pHFC were found to possess low cross-linking in their backbones, they exhibit comparatively higher exchange than a salicylic acid–formaldehyde–*m*-cresol resin.[15] This is due to tiny cracks and channels, which were clearly seen on the surface of the SFC and pHFC resin (SEM photographs, Fig.

3). The breaking of large particles tends to open tiny cracks and channels on the particle surface of the material, resulting in better diffusion owing to the smaller particle size.

SFR exhibited a higher exchange capacity for both Cd(II) and Pb(II), while pHFC showed a lower exchange capacity for Cd(II) and Pb(II) as compared to other synthesized resins (SFC and *p*HFR). The exchange capacity for Cd(II) was lower as compared to Pb(II) for all the synthesized resins (SFR, SFC, *p*HFR and *p*HFC). This can be explained based on the hydrated radius of Cd(II) and Pb(II), cadmium having a larger hydrated ion radius than Pb(II) ion. This results in a decrease in the electrostatic attraction between the Cd(II) and coordinating group, a lower complex stability and hence a lower the capacity.

Effect of initial metal ion concentration on the exchange capacity

The amount of metal ion uptake first increased with increasing concentration of metal ions and then remained constant with further increasing of the metal ion concentration (results not shown). At lower concentrations of metal ions, the number of metal ions available in solution was lower than the number of available sites on the sorbent.[23] However, at higher concentrations, the available sites of exchange remained the same whereas more metal ions were available for sorption and subsequently the exchange finally become almost constant. A similar trend in the sorption data was previously reported for lead and chromium onto bagasse fly ash[24] and for heavy metals onto a salicylic acid–formaldehyde–*m*--cresol chelating resin.[15] At a Cd(II) concentration of 250 mM, the sorption/ion exchange attained a limiting value for the SFR, SFC and *p*HFC and *p*HFR resins. In case of Pb(II), the uptake became constant for SFR and *p*HFC after a concentration of 200 mM, while for SFC and *p*HFC, the limiting value was reached at a concentration of 250 mM. Therefore, a 200 mM concentration was considered as the optimum concentration for all the resins and this concentration was used in the further experiments.

Effect of electrolyte concentration and pH on the distribution coefficients of the metal ions

The distribution coefficient (K_d) values of the metal ions as a function of pH and concentration of electrolyte solution were studied. The K_d value decreased with increasing the electrolyte concentration and increased with increasing pH, which is presented in Table II. In the present investigation, the distribution studies were limited up to a certain pH for each metal ion to prevent hydrolysis of the metal ions at higher pH values. To achieve a more distinct separation of metal ions in a shorter time, the maximum difference in the K_d value should be selected for optimized chromatography conditions.

TABLE II. K_d values for the synthesized resins in tartaric acid at different pH values and concentrations

Resin	Metal ion	Tartaric acid concentration, mol dm^{-3}	pH				
			3.0	3.5	4.0	5.0	6.0
SFR	Cd(II)	0.1	565.00	443.00	299.80	143.31	87.50
		0.2	370.81	215.70	153.80	98.98	50.99
		0.3	252.11	170.77	101.02	53.00	19.27
		0.5	98.23	50.09	31.13	–	–
		1.0	31.47	22.57	10.68	–	–
	Pb(II)	0.1	828.23	587.62	440.84	310.51	247.10
		0.2	517.00	473.74	301.77	250.67	189.74
		0.3	390.32	295.00	220.22	181.37	121.84
		0.5	152.71	210.13	187.15	120.91	92.31
		1.0	171.13	145.70	90.27	52.64	11.09
SFC	Cd(II)	0.1	69.5	54.3	33.5	21.3	17.5
		0.2	52.1	37.8	21.5	13.5	12.5
		0.3	29.3	21.5	14.3	9.2	–
		0.5	17.4	15.8	–	–	–
		1.0	–	–	–	–	–
	Pb(II)	0.1	143.1	129.7	103.5	81.5	52.6
		0.2	118.2	110.4	84.8	62.7	45.3
		0.3	72.9	63.1	57.6	48.3	37.5
		0.5	–	–	–	31.2	24.8
		1.0	–	–	–	–	
*p*HFR	Cd(II)	0.1	55.5	62.2	68.6	22.2	19.4
		0.2	42.3	57.2	31.7	39.3	13.6
		0.3	29.7	20.5	27.8	14.5	
		0.5		–	–	–	–
		1.0	–	–	–	–	–
	Pb(II)	0.1	96.3	81.1	74.2	54.2	33.8
		0.2	78.5	68.2	62.8	49.0	30.1
		0.3	69.2	60.5	54.8	31.5	22.0
		0.5	54.2	49.7	44.0	37.4	18.8
		1.0	–	–	–	–	–
*p*HFC	Cd(II)	0.1	37.5	22.0	30.2	19.5	19.0
		0.2	24.9	18.0	15.5	10.9	15.6
		0.3	19.5	15.0	9.5	–	–
		0.5	16.2	12.9	–	–	–
		1.0	–	–	–	–	–
	Pb(II)	0.1	60.5	39.5	28.4	25.5	16.5
		0.2	32.1	22.0	20.3	16.5	15.4
		0.3	15.1	13.6	10.1	15.2	–
		0.5	8.5	10.2	–	–	–
		1.0	–	–	–	–	–

Among all the resins under investigation, the SFR resin showed the highest K_d values, where pHFC exhibited the lowest K_d values. This may be explained based on the stability constants or the difference in the energy of the complexes

according to Irving and Williams.[25] Chromatographic separation of these two metal ions was employed using the SFR resin. From Table II, it is clear that Pb(II) had a distribution coefficient of 120.91 as compared to Cd(II) (0.0) at pH 5.0 and tartaric acid concentration of 0.5 M, indicating the feasibility of the chromatographic separation of these two metal ions. Chromatographic separation of the metal ions was achieved and the recovery of Cd(II) was 90.7 % and of Pb(II) 96.20 %, which is shown in Fig. 6.

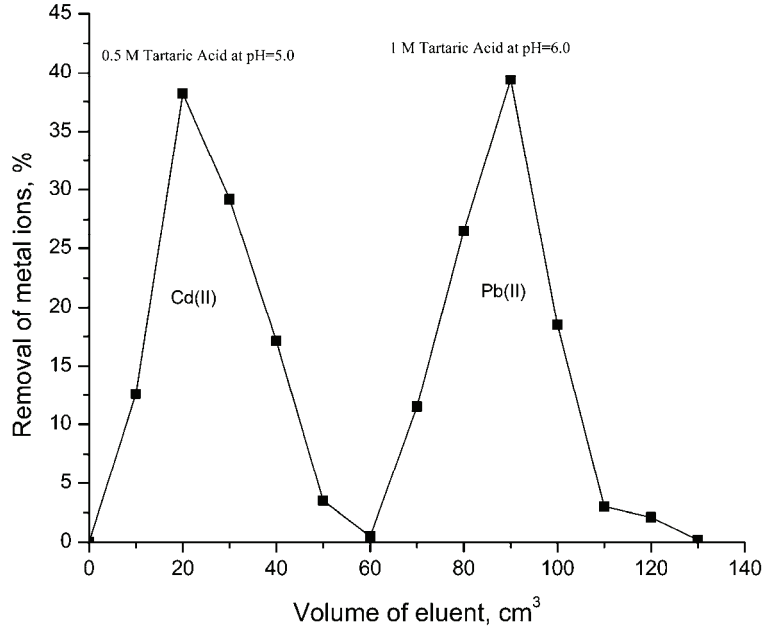

Fig. 6. Chromatographic separation of the metal ions on the SFR resin.

Effect of temperature and thermodynamic parameters

The effect of temperature on the uptake of both Cd(II) and Pb(II) on synthesized resins was studied using the optimized conditions determined in the previous experiments. The temperature was varied from 30 °C to 60 °C. It was observed that the uptake of Cd(II) and Pb(II) ions increased with increasing temperature (results not shown) for all the metal–resins systems. The exchange was enhanced due to the increased kinetic energy.[26] The phenomenon of an ion-exchange depends on the metal ion concentration and temperature. The surface energy of the SFC resin increases with temperature. Similar results were also reported previously for the ion exchange of Ni(II), Cu(II), Zn(II),Cd(II) and Pb(II) with Dowex 50[28] and Amberlite IR 120.[27]

The values of ΔH^{exch}, ΔS^{exch} and ΔG^{exch} were also calculated from the slope and intercept of the Van't Hoff plot of the exchange of metal ions on the

SFC resin using the following linear variation of ln K_d with reciprocal temperature 1/T:

$$\ln K_d = (\Delta S^{exch}/R) - (\Delta H^{exch}/RT) \quad (1)$$

where, ΔS^{exch} and ΔH^{exch} are the entropy and enthalpy change for the process, respectively. The free energy of the adsorption ΔG^{exch} was calculated using the following Van't Hoff Equation:

$$\Delta G^{exch} = -RT\ln K_d \quad (2)$$

The value of ΔH^{exch} was negative which indicates an exothermic ion exchange process and it is likely that the chelation mechanism dominates (Table III).[28] The entropy (ΔS^{exch}) is positive corresponding to an increase in degree of freedom of the system due to release of two hydrogen ions for the divalent metal ions under study.[29] The negative values of ΔG^{exch} indicate the feasibility of the process and also the spontaneity of the ion exchange process. The amount of metal ions uptake at equilibrium must increase with increasing temperature, because ΔG^{exch} decreases with increasing solution temperature.

TABLE III. Thermodynamic parameters for Cd(II) and Pb(II) adsorption on the synthesized resins

Metal ion	Resin	T / K	K_d	ΔG / kJ mol^{-1}	ΔH /kJ mol^{-1}	ΔS / J K^{-1} mol^{-1}
Cd(II)	SFR	293	7.92±0.2	–5.041	–6±0.2	17±0.2
		303	8.12±0.2	–5.276		
		313	8.41±0.2	–5.541		
		323	8.67±0.2	–5.799		
	SFC	293	4.65±0.2	–3.622	–7±0.2	19±0.2
		303	4.95±0.2	–3.712		
		313	5.10±0.2	–3.739		
		323	5.29±0.2	–4.801		
	*p*HFR	293	5.19±0.1	–4.371	–7±0.1	18±0.1
		303	5.32±0.1	–4.391		
		313	5.49±0.1	–4.406		
		323	5.69±0.1	–4.409		
	*p*HFC	293	4.41±0.1	–3.701	–5±0.1	13±0.1
		303	4.67±0.1	–3.722		
		313	4.93±0.1	–3.735		
		323	5.06±0.1	–3.739		
Pb(II)	SFR	293	9.65±0.2	–4.803	–5±0.2	11±0.2
		303	9.92±0.2	–4.812		
		313	10.51±0.2	–4.835		
		323	10.87±0.2	–4.853		
	SFC	293	8.05±0.2	–3.845	–4±0.2	12±0.2
		303	8.27±0.2	–3.892		
		313	8.63±0.2	–3.911		
		323	8.79±0.2	–3.923		

TABLE III. Continued

Metal ion	Resin	T / K	K_d	ΔG / kJ mol^{-1}	ΔH /kJ mol^{-1}	ΔS / J K^{-1} mol^{-1}
Pb(II)	*p*HFR	293	7.47±0.1	–2.588	–7±0.1	20±0.1
		303	7.61±0.1	–2.591		
		313	7.92±0.1	–2.607		
		323	8.11±0.1	–2.615		
	*p*HFC	293	7.12±0.1	–4.782	–5±0.1	15±0.1
		303	7.56±0.1	–5.094		
		313	7.73±0.1	–5.311		
		323	8.02±0.1	–5.492		

Sorption isotherms

Equilibrium can be described by isotherm equations such as the Langmuir and Freundlich isotherms. A preliminary screening of the corresponding equations showed that the Langmuir and Freundlich models best fit the experimental data and the following equations were used for the modelling of results.

Langmuir model: $(c_e/Q_e) = (1/Q^0b) + (c_e/Q^0)$ (3)

Freundlich model: $\log q_e = \log k_f + (1/n)\log c_e$ (4)

where c_e is the equilibrium concentration (mmol g^{-1}), Q_e is the amount adsorbed at equilibrium (mmol g^{-1}) and Q^0 and b are Langmuir constants related to the adsorption capacity and energy of adsorption, respectively. The liner plots of c_e/Q_e *vs.* c_e (not shown) indicate that ion uptake obeys the Langmuir model. The constants Q^0 for Cd(II) were calculated as 69.53, 43.23, 52.47 and 38.84 mg g^{-1} as the maximum capacity for SFR, SFC, *p*HFR and *p*HFC, respectively. The constant Q^0 for Pb(II) by SFR, SFC, pHFR and pHFC were calculated as 169.32, 143.23, 122.47 and 101.84 mg g^{-1}, respectively. These results are comparable to those of the commercial resin Duolite GT-73 reported by Vaughan *et al.*[30] The Q^0 value of Duolite GT-73 for Cd(II) and Pb(II) were 106 and 122 mg g^{-1},[30] respectively. The values of Q^0 for a synthetic methacrylic acid–co–ethyleneglycol dimethacrylate resin were 416.67 and 588.24 mg g^{-1} for Cu(II) and Ni(II) respectively.[23] The sorption energy constant of Cd(II) for SFR, SFC, *p*HFR and *p*HFC are 0.1048, 0.0721, 0.0831 and 0.0593 dm^3 mg^{-1}, respectively. The sorption energy constant of Pb(II) for SFR, SFC, *p*HFR and *p*HFC are 0.2732, 0.2461, 0.2382 and 0.1984 dm^3 mg^{-1}, respectively The essential characteristics of Langmuir equation can be expressed in terms of a dimensionless separation factor or equilibrium parameter, R_L.[31] The value indicates the isotherm to be either unfavourable ($R_L < 1$), linear ($R_L = 1$), favourable ($0 < R_L < 1$) or irreversible ($R_L = 0$). The values of R_L obtained for all the metal–resin systems investigated are given in Table IV. The R_L values for both the metals Cd(II) and Pb(II)) under study were between 0 and 1, indicating the sorption to be favourable.

TABLE IV. Langmuir and Freundlich isotherms constants for the metal–resin systems

Metal ion	Resin	Langmuir constant				Freundlich constant		
		b/ dm^3 mg^{-1}	Q^0/ mg g^{-1}	R_L	R^2	k_f / dm^3 g^{-1}	1/n	R^2
Cd(II)	SFR	0.1048	69.53	0.219	0.9627	35.41	0.4152	0.9886
	SFC	0.0721	43.23	0.202	0.9787	68.72	0.7215	0.9934
	*p*HFR	0.0831	52.47	0.2141	0.9791	54.70	0.5123	0.9862
	*p*HFC	0.0593	38.84	0.198	0.9687	21.35	0.5216	0.9912
Pb(II)	SFR	0. 2732	169.32	0.341	0.9892	71.75	0.7023	0.9925
	SFC	0.2461	143.23	0.322	0.9974	66.23	0.6230	0.9914
	*p*HFR	0.2382	122.47	0.281	0.9972	54.11	0.5834	0.9887
	*p*HFC	0.1984	101.84	0.263	0.9983	39.63	0.4982	0.9974

The specific rate constant, K_r, for the sorbent was determined by the Langergan Equation:

$$\log (q_e - q) = \log q_e - K_r t/2.303 \quad (5)$$

where q_e and q (mg g^{-1}) are the amounts of metal ions adsorbed at equilibrium and at time t (min), respectively. The straight-line plot of log (q_e–q) *vs.* time t, (not shown) indicates the validity of the Lagergren equation for the system and explains that the process follows first order kinetics. The values of K_r for the Cd(II)–resin systems were found to be 17.123×10^{-3}, 14.315×10^{-3}, 15.217×10^{-3}, 11.831×10^{-3} min^{-1} for SFR, SFC, *p*HFR and SFC, respectively. The values of K_r for the Pb(II)–resin systems were found to be 9.187×10^{-3}, 12.501×10^{-3}, 15.157×10^{-3} and 15.331×10^{-3} min^{-1} for SFR, SFC, pHFR and SFC, respectively. Similar K_r values were reported by Prasad *et al.* for Cu(II) (11.3×10^{-3} min^{-1}) and Ni(II) (9.9×10^{-3} min^{-1}) with a synthetic methacrylic acid–co–ethyleneglycol dimethacrylate resin.[23]

Diffusion models

Sorption kinetics are mainly controlled by various factors including *i*) solute transfer from the solution to the boundary film of the particle (bulk diffusion), *ii*) diffusion from the film to the surface of the sorbent (external diffusion), *iii*) diffusion from the surface to the intraparticular sites (intra-particle diffusion) and *iv*) solute adsorption by complexation or physico–chemical sorption or ion exchange.

By providing sufficient agitation to avoid particle and solute gradients in the batch reactor, enables bulk diffusion to be ignored.[23] The processes of intra-particle diffusion and external diffusion may be the rate controlling steps. Several models have been described to discuss the effect of external diffusion and intra-particle diffusion of solute on an adsorbent. In the present work, the Spahn and Schlunder model[33] and the Weber and Morris model[34] were chosen to describe the external diffusion and intra-particle diffusion on the resin, respectively.

The Spahn and Schlunder model

If external diffusion of metal cations (within the diffuse layers outside the sorbent) is the rate limiting step then the sorption data can be fitted by the following equation:[23,37]

$$\ln (c_t/c_0) = -K_s A t/V \quad (6)$$

where K_s is the external diffusion coefficient, c_0 is the initial metal ion concentration, c_t is the concentration at sorption time t, A is the external sorption area and V is the total solution volume. The external diffusion coefficient can be calculated from the slope of the straight line obtained from a plot of ln (c_t/c_0) *vs.* t (not shown). The external diffusion model shows excellent correlation with the sorption data, with high correlation coefficients (Table V). This would indicate that the sorption of Cd(II) and Pb(II) ions under study is a probably a surface process occurring on the exterior of the resin particle. The external diffusion coefficient (K_s) values of Cd(II) and Pb(II) for SFR, SFC, *p*HFR and *p*HFC were calculated and the values are given in Table V. The values for the external diffusion coefficient (K_s) for the synthesized resins are in the range of 0.00125–0.00425 mmol h^{-1} for Cd(II) and 0.00249–0.00680 mmol h^{-1} for Pb(II). Similar results were observed by Anand *et al.*[23] while studying the uptake behaviour of Cu(II) and NI(II) on a methacrylic acid–co–ethylene glycol dimethacrylate polymer.

TABLE V. External and intra-particle diffusion rate constants for the metal–resin systems

Metal ion	Resin	External diffusion		Intra-particle diffusion		
		K_s	R^2	K_{id}	I	R^2
Cd(II)	SFR	0.00425	0.978	0.102	0.029	0.987
	SFC	0.00125	0.977	0.0310	0.063	0.990
	*p*HFR	0.00193	0.938	0.0504	0.094	0.992
	*p*HFC	0.00187	0.987	0.0301	0.039	0.990
Pb(II)	SFR	0.00680	0.942	0.134	0.119	0.989
	SFC	0.00355	0.963	0.0807	0.187	0.997
	*p*HFR	0.00249	0.993	0.0443	0.173	0.978
	*p*HFC	0.00283	0.983	0.0439	0.062	0.995

Weber and Morris model

An empirically found functional relationship, common to the most sorption processes, is that the uptake varies almost proportionally with $t^{1/2}$, the Weber and Morris plot:[34]

$$q_t = k_{id} t^{1/2} + I \quad (7)$$

where, q_t is the amount of sorbate retained at time t, k_{id} is the intra-particle diffusion rate constant and I is thickness of the boundary layer. According to Eq. (7), a plot of q_t *vs.* $t^{1/2}$ (not shown) should be a straight line with slope k_{id} and intercept I when sorption mechanism follows an intra-particle diffusion process.

The values of intercept give an idea about the thickness of the boundary layer, *i.e.*, the larger the intercept, the greater is the boundary layer effect.[35] The values of I for all the resins for Cd(II) and Pb(II) were found in the range 0.029–0.187 mmol dm^{-3} $h^{-1/2}$. The obtained values of the intra particle coefficient (K_{id}) and I are given in Table V. From the external diffusion and intra-particle diffusion data, it can be concluded that diffusion process was mainly controlled by intra--particle diffusion.

Analytical application

Removal of toxic metal from industrial effluents. The efficiency of metal ion recovery from industrial effluent was examined using SFR as the representative of all the synthesized resins. The effluents were collected from D. P. Chemicals Pvt. Ltd. GIDC, Ankleshwer and the Plate Well, Padra Road, Atladara, Baroda for Cd(II) and Pb(II), respectively. The initial concentrations of Cd(II) and Pb (II) in the effluents were found to be 185 and 106 mg dm^{-3}, respectively.

Industrial effluent analysis was performed in a simple way using the synthesized resins. The SFR resin was filled in a column (diameter is 0.5 cm) to a length of 15 cm. The filled resin was pre-equilibrated at pH 5.0.

The pH of the industrial effluent containing Cd(II) (100 cm^3) was adjusted to 5.0 using buffer solution and passed through the resin column at flow rate of 1 cm^3 min^{-1}, followed by a thorough washing with water. The chelated cadmium was eluted with 1 M tartaric acid solution at pH 5.0. It was found that the removal and recovery of cadmium from the effluent were quantitative.

The pH of the Pb-containing effluent was adjusted to 5.0 and pass through the resin column at a flow rate 1 cm^3 min^{-1}, followed by thorough washing with deionised water. The chelated lead was eluted with 1 M tartaric acid solution at pH 6.0.

The results showed 94.3 % Cd(II) and 95.1 % Pb(II) recovery from the industrial effluents using the SFR resin. The synthesized resins can be adopted for the treatment of industrial wastewater.

CONCLUSIONS

The synthesized resins exhibited great amorphous character with cracks and channels on their surfaces. The low moisture contents of the resins indicate high degrees of cross-linking. The resins showed quite high capacities for metal uptake. The void volume fractions of the resins were relatively lower than other reported resins, indicating a lower rate of exchange. The chelating ability of the resins for Cd(II) was SFR > *p*HFR > SFC > *p*HFC and for Pb(II) was SFR > SFC > > *p*HFR > *p*HFC. The uptake of metals proceeds by both physical and chemical phenomenon, confirmed by the applicability of the Langmuir and Freundlich isotherms. Diffusion studies shows that the process of metal ion uptake is mainly governed by an intra-particle diffusion process. These synthesized resins can be

used for the removal of toxic heavy metals from aqueous media and industrial wastewater containing Cd(II) and Pb(II). The recovery of the metals from Industrial effluents gives an indication of the utilization potential of the synthesized resins for wastewater treatment.

И З В О Д

КАРАКТЕРИЗАЦИЈА ХЕЛАТНЕ СМОЛЕ ХИДРОКСИБЕНЗОЕВЕ КИСЕЛИНЕ: РАВНОТЕЖА, КИНЕТИКА И ИЗОТЕРМСКИ ПРОФИЛ ЗА ВЕЗИВАЊЕ Cd(II) И Pb(II)

BHAVNA A. SHAH[1], AJAY V. SHAH[2] и RITESH V.TAILOR[1]

[1]*Department of Chemistry, Veer Narmad South Gujarat University, Surat-7, Gujarat u* [2]*Science and Humanity Department, Polytechnic, Vidyabharti trust, Umrakh, Bardoli-1, Gujarat, India*

Хелатна јоно-измењива смола је синтетисана на 80±5 °C поликондензацијом *орто*/*пара*-хидроксибензоеве киселине и ресорцинолом/катехолом уз формалдехид у DMF као умрежавајући агенс. Смола је била карактерисана FTIC и XRD методама. Испитана је способност синтетисаних смола (SFR, SFC, *p*HFR и *p*HFC) да вежу Cd(II) и Pb(II) јоне у зависности од времена контакта, pH, концентрације јона метала и температуре. Селективност синтетисаних смола у везивању јона Pb(II) расте у низу SFR > SFC > *p*HFR > *p*HFC, а за Cd(II) SFR > > *p*HFR > SFC > *p*HFC. Сорпциони подаци добијени за оптимизоване услове су анализирани применом Langmuir-ове и Freundlich-ове изотерме. Експериментални подаци за све метал–смола системе су у најбољем слагању са Freundlich-овом изотермом. SFR показује максимални сорпциони капацитет за кадмијум од 69,5 mg/g и олово 169,3 mg/g. Адсорпциони процес је реакција првог реда, а константа брзине је одређена применом Lagergan-ове једначине. Израчунати су термодинамички параметри метал–смола система. Константе дифузије за спољашњу дифузију и дифузију унутар честице су израчунате применом Spahn–Schlunder и Weber–Morris модела, редом. Дифузија унутар честица је одговорна за процес сорпције.

(Примљено 1. јуна, ревидирано 8. новембра 2010)

REFERENCES

1. G. McKay, Y. S. Ho, *Trans. IchemE. B* **77** (1999) 165
2. Y. S. Ho, C. Y. J. Ng, G. McKay, *Sep. Sci. Technol.* **36** (2001) 241
3. R. Salim, M. M. Al-Subu, S. Qashoa, *J. Environ. Sci. Health Part A Environ. Sci. Eng.* **29** (1994) 2087
4. D. A. Dzombak, F. M. M. Morel, *J. Colloid Interface Sci.* **112** (1996) 588
5. U. S. Ramelow, C. N. Guidry, S. D. Fisk, *J. Hazard. Mater.* **46** (1996) 37
6. D. C. Sharma, C. F. Forster, *Eur. J. Soil Sci.* **46** (1994) 633
7. Y. S. Ho, A. E. Ofomaja, *Process Biochem.* **40** (2005) 3455
8. E. I. Unuabonah, K. O. Adebowale, B. I. Olu-Owolabi, *J. Hazard. Mater.* **144** (2007) 386
9. K. O. Adebowale, I. E. Unuabonah, B. I. Olu-Owolabi, *Chem. Eng. J.* **136** (2008) 99
10. A. I. Vogel, *Quantitative Inorganic Analysis*, 5th ed., Longman, London, 1989
11. A. Helfferich, *Ion exchange*, McGraw-Hills, New York, USA, 1962
12. R. Kunnin, *Ion exchange resin*, Wiley, London, 1958
13. M. V. Vyas, R. N. Kapadia, *Indian J. Technol.* **18** (1980) 411
14. M. V. Vyas, R. N. Kapadia, *Indian J. Technol.* **19** (1981) 491
15. B. A. Shah, A. V. Shah, P. M. Shah, *Iran. Polym. J.* **15** (2006) 809

16. M. Patel, R. Manavalan, *Indian J. Chem.* **22A** (1983) 117
17. B. A. Shah, A. V. Shah, R. R. Bhatt, *Iran. Polym. J.* **16** (2007) 173
18. R. M. Silverstein, G. C. Bassler, *Spectrometric Identification of Organic Compounds*, Wiley, New York, 1991
19. A. Tager, *Physical Chemistry of Polymers*, Mir Publisher, Moscow, 1978
20. S. A. Johnson, E. S. Brighan, T. E. Mollouk, *Chem. Mater.* **9** (1997) 2448
21. F. Vernon, H. Eccles, *Anal. Chim. Acta* **72** (1974**)** 331
22. B. A. Shah, A. V. Shah, B. N. Bhandari, R. R. Bhatt, *J. Iran. Chem. Soc.* **5** (2008) 252
23. P. S. Anand, H. H. Prasad, K. M. Popat, *Indian J. Chem. Technol.* **9** (2002) 385
24. V. K. Gupta, I. Ali, *J. Colloid Interface Sci.* **271** (2004) 321
25. H. R. Irving, R. J. Williams, *Chem. Rev.* **56** (1956) 221
26. E. Pehlivan, T. Altum, *J. Hazard. Mater.* **134(B)** (2006) 149
27. A. Demirbas, E. Pehlivan, F. Gode, T. Altun, G. Arslan, *J. Colloid Interface Sci.* **282** (2005) 20
28. I. S. Lima, C. Airoldi, *Thermochim. Acta* **421** (2004)133
29. A. Baraka, P. J. Hall, M. J. Heslop, *J. Hazard. Mater.* **140** (2007) 86
30. T. Vaughan, C. W. Seo, W. E. Marshall, *Bioresor. Technol.* **78** (2001) 133
31. D. K. Singh, M. Srivastava, *J. Liq. Chrom. Related Technol.* **29** (2006) 1433
32. I. B. Stephan, N. Sulochana, *Indian J. Chem. Technol.* **9** (2002) 201
33. H. Spahn, U. Schlunder, *Chem. Eng. Sci.* **30** (1975) 529
34. J. C. Morris, W. J. (Jr.) Weber, in *Proceedings of 1st Int. Conf. on Water Pollution Res.*, Pergamon Press, New York, **2** (1962) 231
35. I. D. Mall, V. C. Srivastava, N. Agarwal, I. M. Mishra, *Colloids Surf. A* **264** (2005) 17.

Journal of the Serbian Chemical Society
JSCS-info@shd.org.rs • www.shd.org.rs/JSCS
J. Serb. Chem. Soc. 76 (6) 923–932 (2011)
JSCS–4171
UDC 544.354–125.4+547.549+547.567.3+66.094.25:544.478+546.98
Original scientific paper

Altervalent cation-doped MCM-41 supported palladium catalysts and their catalytic properties

HAIHUI JIANG, LIGANG GAI* and YAN TIAN

Shandong Provincial Key Laboratory of Fine Chemicals, School of Chemical Engineering, Shandong Institute of Light Industry, Jinan 250353, Peoples' Republic of China

(Received 27 February, revised 13 December 2010)

Abstract: Metal cation-doped MCM-41 (M-MCM-41, M = Al, Ce, Co, V or Zr) supported Pd catalysts (Pd/M-MCM-41) were prepared by a solution-based reduction method. The catalysts were characterized by X-ray diffraction (XRD) analysis, infrared spectroscopy (IR), scanning electron microscopy (SEM) and transmission electron microscopy (TEM), and further evaluated by selective hydrogenation of *para*-chloronitrobenzene (*p*-CNB) in anhydrous ethanol. The metal cation-containing Pd catalysts can efficiently enhance the selectivity for *para*-chloroaniline (*p*-CAN). The highest selectivity of 96.5 % in the molar distribution for *p*-CNB to *p*-CAN was acquired over Pd (1.8 wt. %)/*V*-MCM-41 (Si/V = 30, molar ratio) catalyst, and the corresponding turnover frequency (TOF) was 1.24×10^{-2} mol *p*-CNB mol^{-1} Pd s^{-1}. Water molecules adsorbed by the support have important effects on both the catalytic activity of the sample and the selectivity for *p*-CAN. A water molecule-mediated catalytic hydrogenation is discussed.

Keywords: metal cation-doped MCM-41; *para*-chloronitrobenzene; hydrogenation; *para*-chloroaniline.

INTRODUCTION

Metal cation-doped mesoporous materials have attracted much attention due to their extensive applications in catalysis[1–5] and as sensor.[6] In general, two methods have been used for the preparation of metal cation-doped mesoporous materials, *i.e.*, *in situ* doping synthesis[1] and the traditional wet impregnation method.[2] From the viewpoint of recycling the catalyst, the former method is superior to the latter because the foreign cations embedded in the framework are more stable than those adsorbed on the surface of the matrix. Recently, incurporation of foreign cations, including transition metals[3–5] and main-group elements,[3,7,8] into the MCM-41 matrix has been intensively investigated because of

* Corresponding author. E-mail: liganggai@yahoo.com
doi: 10.2298/JSC100227073J

the facile synthesis of the modified MCM-41 and their enhanced properties in catalysis.

Catalytic hydrogenation of chloronitrobenzene (CNB) to the corresponding chloroaniline (CAN) over various metal catalysts, such as Pd, Pt, Rh, Ru, Ni, Co and Ag,[9–15] in solution is considered a simple and efficient route due to the relatively clean process. Recently, a gas phase hydrogenation over supported Ni catalysts with 100 % selectivity for CNB to CAN has been reported,[16] giving a promising clean production of CAN. In order to improve the activity and selectivity of metal catalysts in the liquid phase, many strategies have been developed, such as metal oxide-assisted,[9–12] polymer-stabilized,[13,14] carbon and carbon nanotube supported,[15] and the metal cation-promoted method.[11,14,15] Although enhanced catalytic activity and selectivity for CNB to CAN can be achieved by the polymer-stabilized and metal cation-promoted methods, limitations still exist, including difficult separation and recycling of the catalyst.[17]

Inspired by the metal cation-promoted method for the clean production of CAN, together with the large specific surface area of mesoporous molecular sieves, an *in situ* metal cation-doped MCM-41 was as the catalyst support in this study. Thus, the preparation of altervalent cation-doped MCM-41 (M-MCM-41, M = = Al, Ce, Co, V or Zr) supported Pd catalysts (Pd/M-MCM-41), and their applications in the hydrogenation of *para*-chloronitrobenzene (*p*-CNB) to *para*-chloroaniline (*p*-CAN) are reported in this paper.

EXPERIMENTAL

Materials and characterizations

Sodium aluminate ($NaAlO_2$) and palladium(II) acetate ($Pd(OAc)_2$) were of chemical purity, and the other employed reagents were of analytical grade. All the reagents were purchased from Tianjin (China) and used directly without further purification.

The X-ray diffraction (XRD) patterns were recorded on a Rigaku D/Max–2200PC diffractometer with CuKα radiation (λ = 0.15418 nm). The Fourier transform infrared (FTIR) spectra were collected on a Nicolet Nexus 670 infrared spectrometer using pressed KBr discs. Scanning electron microscopy (SEM) images and energy dispersive X-ray spectroscopy (EDS) patterns were taken on a FEI co-Holland Quanta 200E scanning electron microscope. For the EDS analysis, the sample was spread onto a conducting carbon film. Transmission electron microscopy (TEM) images and selected area electron diffraction (SAED) patterns were obtained on a Hitachi H-800 transmission electron microscope operating at 150 kV. The Pd content was measured by dissolving the sample in 20 % aqueous HF solution using a Perkin–Elmer Optima 2000 DV inductively coupled plasma-optical emission spectrometer (ICP-OES). Gas chromatography (GC) and gas chromatography/mass spectrometry (GC/MS) analyses were realized on a Shimadzu GC-2010 gas chromatograph and a GCMS-QP2010 spectromonitor, equipped with a FID detector and a DB-5 capillary column, respectively.

Preparation of M-MCM-41(M = Al, Ce, Co, V or Zr) supports

An *in situ* doping method[1] was employed for the synthesis of the M-MCM-41 supports. In a typical synthesis of Al-MCM-41, cetyltrimethylammonium bromide (CTAB) and $NaAlO_2$ were added to deionized water and stirred at 30 °C for 0.5 h. Tetraethyl orthosilicate (TEOS)

and an aqueous 1 M NaOH solution were then added dropwise to the mixture under constant stirring over 2 h. The gel mixture with a molar composition of 1.0 TEOS:0.033 $NaAlO_2$:0.2 CTAB:0.32 NaOH:84 H_2O was transferred to a Teflon container and heated at 120 °C for 48 h. The precipitate was filtered, washed with deionized water, then several times with anhydrous ethanol and dried in air at 60 °C for 12 h. The as-synthesized product was calcined in air at 550 °C for 6 h, cooled naturally to 70 °C, then transferred quickly to a desiccator and allowed to cool to room temperature in the desiccator. The sample was named Al-MCM-41 (Si/Al = 30, molar ratio based on the starting materials).

Similar procedures were utilized for the syntheses the other M-MCM-41 samples, apart from the substitutions of $NaAlO_2$ by the corresponding mole amount of $Ce(NO_3)_3{\cdot}6H_2O$, $Co(NO_3)_2{\cdot}6H_2O$, $Zr(SO_4)_2{\cdot}4H_2O$ and half mole of V_2O_5.

Preparation of Pd/M-MCM-41 catalysts

A solution-based reduction method was used for the synthesis of Pd/M-MCM-41 composites, involving an impregnation and reduction process. In a typical procedure, 45.3 mg of $Pd(OAc)_2$, 1.0 g of M-MCM-41, and 50 mL of anhydrous ethanol were placed into a 200-mL capacity stainless steel autoclave. The autoclave was vacuumed and sealed. After agitation at room temperature for 2 h, the autoclave was filled with H_2 (99.999 %) to 3 atm and then heated at 50 °C for 3 h with a stirring rate of 250 rpm. The dark gray precipitate was filtered, washed sufficiently with anhydrous ethanol and then acetone several times, and dried in a vacuum oven at 60 °C for 12 h. The mass percent of Pd in the sample was 1.8 %, as measured by ICP--OES. The newly formed dry composites were exposed to air with a relative humidity of 35 % for 24 h before usage. The final moisture-containing Pd (1.8 wt. %)/M-MCM-41 composites had a water content of ≈1 wt. %.

Hydrogenation of p-*CNB*

Hydrogenation of *p*-CNB to *p*-CAN over the Pd/M-MCM-41 composites was performed by a procedure similar to that described in the litereature.[14] Briefly, 10 mmol *p*-CNB, 0.2 g of Pd/M-MCM-41, and 50 mL of anhydrous ethanol were placed into the aforementioned autoclave. The autoclave was vacuumed, sealed, and filled with H_2 (99.999 %) to 2 atm in sequence and then heated at 50 °C for 3 h under constant stirring. The resulting product was separated by centrifugation. The supernatant liquor was collected, analyzed by GC using diphenyl as an internal standard and identified by GC/MS analysis.

RESULTS AND DISCUSSION

Characterization of the catalysts

The XRD and FTIR techniques were employed to examine the structure and composition of the supports, as shown in Figs. 1 and 2. Compared to silicon-based MCM-41 synthesized in the absence of a metal additive, each kind of metal cation-doped support possessed a mesoporous structure (Fig. 1), with little variation in the lattice parameter a_0[18] (Table I), which arises from incorporation of foreign cations into the framework of MCM-41.[3–5] Considering the IR spectra (Fig. 2), it was reported that the peak around 960–970 cm^{-1}, ascribed to the asymmetric stretching vibration (ν_{as}) of Si–O–M, is a probe to verify the doping state of foreign cations in mesoporous matrix.[4,19] In comparison with that of pure MCM--41, the peak position of ν_{as}(Si–O–M) in all the cation-doped supports was blue-

-shifted (Table II), which is indicative of the incorporation of foreign cations into the framework of the MCM-41 matrix,[4,19] which is consistent with the XRD results.

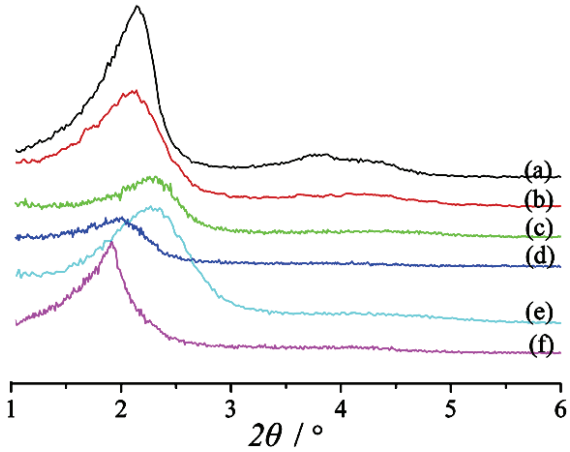

Fig. 1. Low-angle XRD patterns of M-MCM-41: a) pure MCM-41; b) Al-MCM-41; c) Ce-MCM-41; d) Co-MCM-41; e) V-MCM-41; f) Zr-MCM-41.

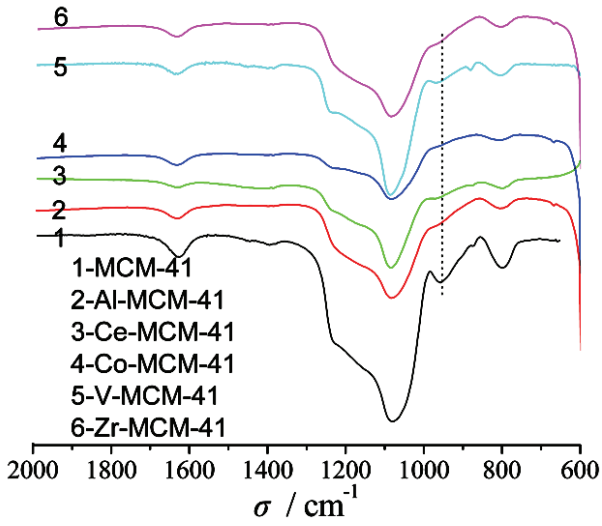

Fig. 2. IR Spectra of the M--MCM-41 supports.

TABLE I. Lattice parameter a_0 ($a_0 = 2d_{100}/\sqrt{3}$) of the M-MCM-41 supports

Sample	MCM-41	Al-MCM-41	Ce-MCM-41	Co-MCM-41	V-MCM-41	Zr-MCM-41
a_0 / nm	4.47	4.49	4.43	4.57	4.42	4.65

TABLE II. Asymmetric stretching vibration of the Si–O–M groups in the M-MCM-41 supports

Sample	MCM-41	Al-MCM-41	Ce-MCM-41	Co-MCM-41	V-MCM-41	Zr-MCM-41
ν_{as} / cm^{-1}	961	967	968	967	968	967

A typical XRD pattern of the Pd (1.8 wt. %)/V-MCM-41 sample in the 2θ range 0.5–80° is shown in Fig. 3. The diffraction peaks in the low-angle region (0.5–8°) along with a broad peak at about 23.5° correspond to amorphous mesoporous silica. The peak centered at 40.0° can be indexed to the (111) plane of cubic Pd (JCPDS No. 88-2335). An SEM image of the Pd (1.8 wt. %)/V-MCM-41 sample (Fig. 4a) shows agglomerated microparticles with an average size of ≈1 μm. The corresponding EDS pattern (Fig. 4b) displays C, O, V, Si and Pd elements, confirming the vanadium cation-doped SiO_2 supported Pd catalyst. The C element arises from the conducting carbon film. In order to further verify the composition of the sample, TEM measurements were performed. Although metal Pd nanoparticles encapsulated in the ordered channels of the MCM-41 matrix cannot be excluded, from the viewpoint of diffusion constraint, crystalline Pd nanoparticles are more easily formed on the MCM-41 surface, as shown in Fig. 4c. The typical dark-field TEM image (Fig. 4c) reveals a random distribution of bright spots, which are assigned to crystalline Pd nanoparticles according to the corresponding SAED pattern (Fig. 4d). The average size of Pd nanoparticles is ≈60 nm, as determined by counting at least 100 individual metal particles.

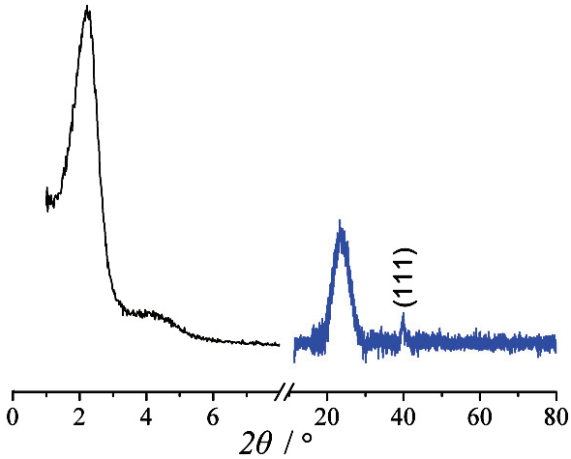

Fig. 3. A typical XRD pattern of Pd (1.8 wt. %)/V-MCM-41.

Catalytic properties for selective hydrogenation of p-*CNB*

Catalytic properties of the Pd (1.8 wt. %)/M-MCM-41 catalysts were evaluated by selective hydrogenation of *p*-CNB to *p*-CAN as summarized in Table III. It was found that conversion of *p*-CNB over each Pd(1.8 wt. %)/*M*-MCM-41 was higher than that over Pd(1.8 wt. %)/MCM-41, indicating that the foreign cations embedded in MCM-41 matrix can improve the catalytic activity of the catalyst. Moreover, the selectivity for *p*-CAN was greatly enhanced in the presence of Pd(1.8 wt. %)/*M*-MCM-41 and the highest selectivity for *p*-CAN

occurred over the Pd(1.8 wt. %)/*V*-MCM-41 catalyst. Therefore, the Pd (1.8 wt. %)/ /V-MCM-41 samples were selected for further investigation.

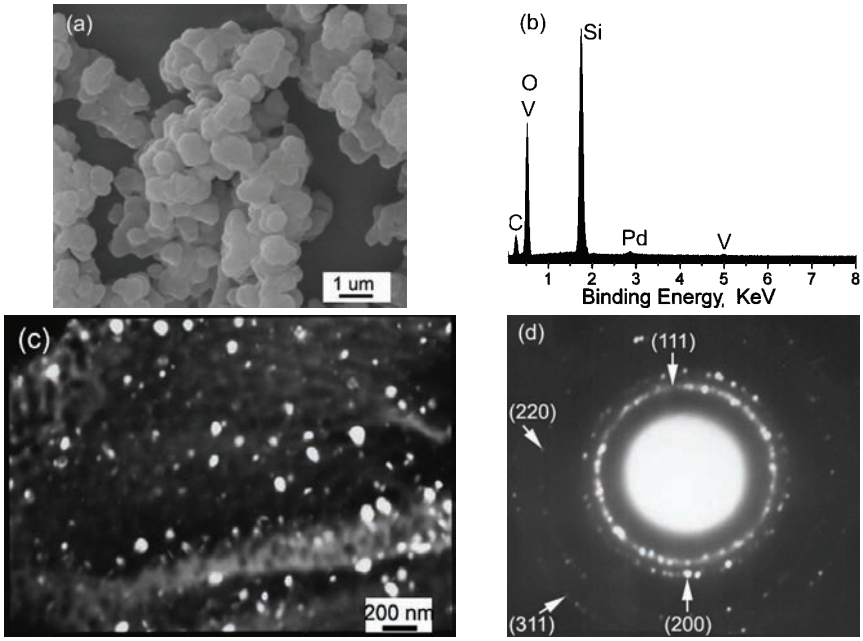

Fig. 4. a) SEM Image, b) the corresponding EDS pattern, c) TEM image and d) the corresponding SAED pattern of Pd (1.8 wt. %)/V-MCM-41.

TABLE III. Catalytic hydrogenation of *p*-CNB over different Pd (1.8wt. %)/M-MCM-41 catalysts (reaction conditions: 0.2 g catalyst, 10 mmol *p*-CNB, 50 ml anhydrous ethanol and 2 atm H_2 at 50 °C for 3 h)

Catalyst support[a]	Conversion of *p*-CNB, mol %	$TOF \times 10^2$ mol *p*-CNB mol^{-1} Pd s^{-1}	Selectivity, mol %		
			p-CAN	Aniline	Others[b]
MCM-41	24.3	0.996	64.3	32.8	2.9
Al-MCM-41	35.7	1.46	86.6	10.7	2.7
Ce-MCM-41	34.3	1.41	94.2	3.5	2.3
Co-MCM-41	30.6	1.25	93.4	1.7	4.9
V-MCM-41	30.2	1.24	96.5	0.9	2.6
Zr-MCM-41	32.6	1.34	90.1	5.1	4.8

[a]Si/M = 30 (molar ratio), M = Al, Ce, Co, V or Zr; [b]Others contain nitrobenzene, *p*-chlorophenylhydroxylamine, chlorobenzene, azo- and azoxy-dichlorobenzenes

The metal cation-promoted hydrogenation of CNB to corresponding CAN has been intensively studied.[11,14,15] A well-accepted mechanism[11] is that the introduced metal cation interacts with the $–NO_2$ group of the CNB molecule, thereby increasing the polarity of N=O bond and decreasing the polarity of the $C_{ring}–Cl$ bond. This leads to a promotion of the hydrogenation of the nitro group and an

inhibition of the dechlorination side reaction.[11] In the present case of Pd/M--MCM-41, the foreign cations incorporated into MCM-41 matrix played a similar role to that of the metal complexes previously reported,[11,14,15] as illustrated in scheme 1(a). The highest selectivity for *p*-CNB to *p*-CAN, which was acquired over Pd/V-MCM-41, can be assigned to the strong interaction between the vanadium ion and the *p*-CNB molecule, due to it having the highest valence (+5) among the employed cations. It should be noted that, unlike the polymer-stabilized and metal addition-promoting methods,[11,14,15] the absence of polymer or ligands from metal additive in the present method enables a clean production of CAN because of the stability of the foreign metal cations in the MCM-41 matrix.

In fact, the Cl atom with lone pair electrons in the CNB molecule can also coordinate with cations embedded in the support, resulting in a decrease in the strength of the C_{ring}–Cl bond as a consequence of an increase in the side reaction of dechlorination. This assumption was evidenced by the fact that the selectivity of *p*-CNB to aniline increased on decreasing the Si/V molar ratio to 15 (Table IV), which shows that an excess of foreign metal cations hampers the selective hydrogenation of CNB to CAN.

TABLE IV. Hydrogenation of *p*-CNB over different Pd (1.8 wt. %)/V-MCM-41 catalysts

Si/V molar ratio	Conversion of *p*-CNB, mol %	$TOF \times 10^2$ mol *p*-CNB mol^{-1} Pd s^{-1}	Selectivity, mol %		
			p-CAN	Aniline	Others
15	32.5	1.33	86.7	10.1	3.2
30	30.2	1.24	96.5	0.9	2.6
60	27.6	1.13	92.1	2.8	5.1
30[a]	52.5	2.15	77.9	3.0	19.1

[a]Newly formed dry catalyst was used

It is worth noting that the water molecules adsorbed by the Pd/V-MCM-41 are beneficial to the selectivity for *p*-CAN, whereas adverse to the conversion of *p*-CNB (Table IV). In the presence of the newly formed dry catalyst, a dramatic increase in the conversion of *p*-CNB was observed, while a distinct decrease in the selectivity for *p*-CAN occurred (Table IV). Furthermore, the increased product mainly concentrates on the other products including nitrobenzene, *p*-chlorophenylhydroxylamine, chlorobenzene, azo- and azoxy-dichlorobenzenes, rather than aniline.

It is known that a catalytic process proceeding on the surface of a catalyst mainly comprises three steps: 1) adsorption of the reactants, 2) the catalytic reaction and 3) desorption of the products. Compared to the moisture-containing catalyst, the newly formed dry catalyst may have relatively higher adsorption ability for adsorbing the sorbate from the viewpoint of surface potential, which facilitates the catalytic reaction under otherwise identical conditions. This justifies the dramatic increase in the conversion of *p*-CNB. Moreover, high adsorption

ability means strong interactions between the reactant molecules and the catalytically active sites, which can cause further reaction of the desired product into by-products, as mentioned above. For example, the further reaction of *p*-CAN molecules leads to formation of azo- and azoxy-dichlorobenzenes by dimolecular reactions of *p*-CNB. Therefore, the decrease in selectivity for *p*-CAN and the increase in the molar distribution of the by-products are reasonable. On the other hand, according to catalysis theory,[20] highly catalytically active sites possess high adsorption potential for the sorbate, which evens out the dechlorination and the reduction of nitro group in the case of hydrogenation of *p*-CNB. This further supports the decrease in the selectivity for *p*-CAN.

The water molecule-promoted, selective hydrogenation of *p*-CNB to *p*-CAN was previously reported,[10] when a suitable amount of water was added into the reaction system, leading to formation of water films on the surface of catalyst. The water films can depress side reactions towards by-products and favor desorption of *p*-CAN into the mixed solvent.[10] In the present case of the moisture-containing Pd/V-MCM-41, from the viewpoint of the electron effect, the water molecule-modified catalytic active sites preferentially interact with the $-NO_2$ group rather than the Cl atom of the *p*-CNB molecule through hydrogen bond (Scheme 1b), which favors the formation of *p*-CAN.

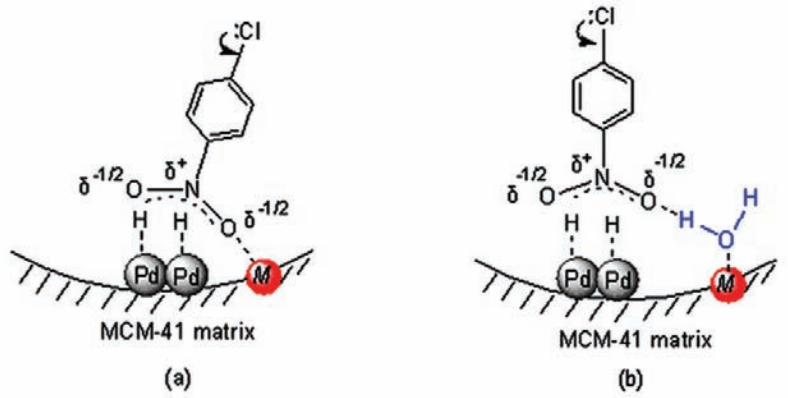

Scheme 1. Schematic illustration of the selective hydrogenation of *p*-CNB over a) Pd/M-MCM-41 and b) moisture-containing Pd/M-MCM-41; *M* denotes a metal cation embedded in the MCM-41 matrix.

CONCLUSIONS

In summary, a set of metal cation-doped MCM-41-supported Pd catalysts were prepared. Their catalytic properties were measured by selective hydrogenation of *p*-CNB to *p*-CAN. The highest conversion of *p*-CNB (35.7 %) was realized over Pd (1.8 wt. %)/Al-MCM-41 (Si/Al = 30), whereas the highest selectivity for *p*-CAN (96.5 %) occurred over Pd (1.8 wt. %)/V-MCM-41 (Si/V = 30).

The turnover frequency (*TOF*) of hydrogenation increased from 9.96×10^{-3} mol *p*-CNB mol^{-1} Pd s^{-1} over Pd (1.8 wt. %)/MCM-41 to 1.24×10^{-2} mol *p*-CNB mol^{-1} Pd s^{-1} over Pd (1.8 wt. %)/V-MCM-41 (Si/V = 30). The water molecules adsorbed by the support have an important effect on the selectivity of the hydrogenation of *p*-CNB to *p*-CAN. The metal cation-containing MCM-41 supported Pd catalysts presented herein enable their easy separation and recycling, and are promising candidates for the selective hydrogenation of CNB.

Acknowledgements. The Natural Science Foundation (Y2007F17), Doctoral Program Foundation (2008BS04009), and the Science and Technology Foundation (2007GG10003017) of the Shandong Province of China are gratefully acknowledged for partial financial support of this work.

И З В О Д

ПАЛАДИЈУМСКИ КАТАЛИЗАТОР НА MCM-41 ПОДЛОГАМА ДОПИРАНИМ КАТЈОНИМА РАЗЛИЧИТЕ ВАЛЕНЦЕ И ЊИХОВА КАТАЛИТИЧКА АКТИВНОСТ

HAIHUI JIANG, LIGANG GAI и YAN TIAN

Shandong Provincial Key Laboratory of Fine Chemicals, School of Chemical Engineering, Shandong Institute of Light Industry, Jinan 250353, Peoples' Republic of China

Паладијумски катализатори (Pd/M-MCM-41) на подлогама M-MCM-41, M = Al, Ce, Co, V или Zr, допираним јонима метала припремани су редукцијом из раствора. Катализатори су окарактерисани применом методе ренгенске дифракције из праха (XRD), инфрацрвене спектроскопије (IC), скенирајуће електронске микроскопије (SEM) и трансмисионе електронске микроскопије (TEM), а затим су тестирани у реакцији хидрогенизације *пара*-хлоронитробензена (*p*-CNB) у анхидрованом етанолу. Паладијумски катализатори који имају металне јоне могу ефективно повећавати селективност у добијању *пара*-хлороанилина (*p*--CAN). Највећа селективност од 96,5 %, у моларној дистрибуцији *p*-CNB u *p*-CAN се постиже на катализатору Pd (1,8 mas. %)/V-MCM-41 и молски однос Si/V = 30, на коме је одговарајућа фреквенција обнављања (*TOF*) катализатора $1,24\times10^{-2}$ mol *p*-CNB mol^{-1} Pd s^{-1}. Адсорпција воде на носачу катализатора утиче како на каталитичку активност тако и на селективност катализатора у добијању *p*-CAN. У раду је дискутована улога воде у реакцији каталитичке хидрогенизације.

(Примљено 27. фебруара, ревидирано 13. Децембра 2010)

REFERENCES

1. P. Tanev, M. Chibwe, T. Pinnavaia, *Nature* **359** (1994) 321
2. Y. Han, F. Xiao, S. Wu, X. Meng, D. Li, S. Lin, F. Deng, X. Ai, *J. Phys. Chem. B* **105** (2001) 7963
3. A. Corma, *Chem. Rev.* **97** (1997) 2373
4. S. Laha, P. Mukherjee, S. Sainkar, R. Kumar, *J. Catal.* **207** (2002) 213
5. Y. Kong, H. Zhu, G. Yang, X. Guo, W. Hou, Q. Yan, M. Gu, C. Hu, *Adv. Funct. Mater.* **14** (2004) 816
6. Q. Qi, T. Zhang, X. Zheng, L. Wan, *Sensors Actuators B* **135** (2008) 255
7. K. Okumura, K. Nishigaki, M. Niwa, *Microporous Mesoporous Mater.* **44–45** (2001) 509
8. R. C. Vasant, K. J. Suman, S. P. Nilesh, *Tetrahedron Lett.* **43** (2002) 1105

9. B. J. Zuo, Y. Wang, Q. L. Wang, J. L. Zhang, N. Z. Wu, L. D. Peng, L. Gui, X. Wang, R. Wang, D. Yu, *J. Catal.* **222** (2004) 493
10. J. Ning, J. Xu, J. Liu, H. Miao, H. Ma, C. Chen, X. Li, L. Zhou, W. Yu, *Catal. Commun.* **8** (2007) 1763
11. X. Xu, X. M. Liu, J. R. Chen, R. Li, X. Li, *J. Mol. Catal. A: Chem.* **260** (2006) 299
12. Y. Y. Chen, C. A. Wang, H. Y. Liu, J. S. Qiu, X. H. Bao, *Chem. Commun.* (2005) 5298
13. C. X. Xiao, H. Z. Wang, X. D. Mu, Y. Kou, *J. Catal.* **250** (2007) 25
14. X. X. Han, R. X. Zhou, X. M. Zheng, H. Jiang, *J. Mol. Catal. A: Chem.* **193** (2003) 103
15. X. X. Han, Q. Chen, R. X. Zhou, *J. Mol. Catal. A: Chem.* **277** (2007) 21016
16. 16. F. Cárdenas-Lizana, S. Gómez-Quero, M. A. Keane, *Appl. Catal., A* **334** (2008) 199
17. X. W. Jiang, G. W. Wei, X. Zhang, W. Q. Zhang, P. W. Zheng, F. Wen, L. Q. Shi, *J. Mol. Catal. A: Chem.* **277** (2007) 102
18. J. S. Beck, J. C. Vartuli, W. J. Roth, M. E. Leonowicz, C. T. Kresge, K. D. Schmitt, C. T. Chu, D. H. Olson, E. W. Sheppard, *J. Am. Chem. Soc.* **114** (1992) 10834
19. M. Chatterjee, T. Iwasaki, H. Hayashi, Y. Onodera, T. Ebina, T. Nagase, *Chem. Mater.* **11** (1999) 1368
20. Z. H. Jiang, D. Z. Sun, G. J. Shao, Eds., *Applied Surface Chemistry and Technology*, Harbin Industry University Press, Harbin, P. R. China, 2001, p. 197 (in Chinese).

Journal of the Serbian Chemical Society
JSCS-info@shd.org.rs • www.shd.org.rs/JSCS
J. Serb. Chem. Soc. 76 (6) 933–946 (2011)
JSCS–4172
UDC 551.463+504.4.054:543.000.57+639.42(497.16)
Original scientific paper

Mussels as a bio-indicator of the environmental quality of the coastal water of the Boka Kotorska Bay (Montenegro)

MIHAJLO JOVIĆ[1]*, ANA STANKOVIĆ[1], LATINKA SLAVKOVIĆ-BESKOSKI[2], ILIJA TOMIĆ[3], SANDRO DEGETTO[4] and SLAVKA STANKOVIĆ[1]

[1]*Faculty of Technology and Metallurgy, University of Belgrade, Belgrade,* [2]*Institute of Nuclear Science Vinča, University of Belgrade, Belgrade,* [3]*Institute of Chemistry, Technology and Metallurgy, University of Belgrade, Belgrade, Serbia an* [4]*ICIS-CNR, Environmental Laboratory, Padua, Italy*

(Received 7, revised 27 October 2010)

Abstract: The Mediterranean blue mussel *Mytilus galloprovincialis* was used as a pollution level indicator in the Boka Kotorska Bay of the southeastern Adriatic on the Montenegrin coast. The ever-increasing urbanization and industrialization, combined with a poor sewage system, an increase in both marine and inland traffic, as well as insufficient water circulation in the Bay itself have resulted in some level of pollution. Since heavy metals are extremely toxic and do not easily undergo biodecomposition, the results of this study supply valuable information concerning the metal pollution of the marine environment in Boka Kotorska Bay. The concentrations of the investigated metals and non-metals accumulated in the mussels were determined during the fall of 2007 using Atomic Absorption Spectroscopy (AAS) for Cr, Mn, Co, Ni, Cu, Cd, Hg, Pb, Sn and V, and Energy Dispersive X-ray Fluorescence (ED–XRF) to determine the concentrations of Fe, Zn, Si, P, S, Cl, K and Ca. ED–XRF was also used to determine the levels of non-metals and elements present in high concentrations. Comparing the data from this study in relation to data from other regions for *Mytilus galloprovincialis*, the mussel sampled from the Boka Kotorska Bay showed a moderate level of pollution.

Keywords: pollution; metals; non-metals; *Mytilus galloprovincialis*; bio-indicator.

INTRODUCTION

The Boka Kotorska Bay is located in the southeastern part of the Adriatic Sea and is deemed to be one of the most beautiful bays of the world. The Boka Kotorska Bay is naturally divided into four smaller bays: the Herceg Novi, Tivat,

* Corresponding author. E-mail: jovicmihajlo@yahoo.co.uk
doi: 10.2298/JSC101007075J

Risan and Kotor Bays. It is hypothesized that the Boka Kotorska Bay, having a coastline 105.7 km long, covering an area of 87.3 km^2, containing a volume of 2.4×10^6 km^3 of water and with a maximum depth of 60 m, was formed by fluvial erosion.

Each and every one of the four smaller bays comprising the Boka Kotorska Bay has specific hydrographic and relief characteristics, and is significantly different in its aquatic life from sea waters stretching away from Montenegro.[1]

The increased urbanization and industrialization of the Montenegrin Coast over the last two decades could lead to an increase of marine pollution of the Boka Kotorska Bay. Waste stemming from various inland human activities is directly delivered into the sea without any prior treatment, the greatest threat being old and poorly maintained sewage systems. Within the Boka Bay itself, 62 underwater untreated sewage disposal systems have been identified, all of which deliver sewage waste at a close distance to the shore. Sewage disposal systems in the Kotor, Tivat and Risan Bays are neither long nor deep enough, disposing waste immediately at the coastal line of the Bays. Moreover, many privately owned estates have sewage disposal systems which are not part of the municipal sewage system, thereby adding even more to the pollution of the Bay.[1]

Pollution and contamination of the Boka Kotorska Bay ecosystem arise from both anthropogenic sources of pollution and natural weathering. Industrial waste from the steel, soap and pharmaceutical industries, as well as waste produced by shipyards, hotels and hospitals located within the Boka Kotorska Bay itself, is allowed to freely flow into the sea, polluting it with heavy and other metals, causing significant environmental damage. The total quantity of wastewater delivered into the sea from the three towns together (Herceg Novi, Tivat and Kotor) is 7700 and 4900 m^3 per day from industries and households, respectively.[1]

Moreover, the Boka Kotorska Bay is known as one of the regions in Europe with the highest amount of precipitation, and the quantity of pollutants reaching the sea from this source cannot be neglected. Adding to this are the ever increasing volume of marine and inland traffic, as well as a growing number of tourists over the last decade.

All of the above-mentioned factors significantly contribute to the accumulating pollution of the Boka Kotorska Bay, the highest danger stemming from heavy metal pollution, such as mercury (Hg), lead (Pb), cadmium (Cd) and other metals.

Heavy metals are extremely toxic and do not easily undergo biodecomposition.[2] Living organisms have as of more recently been used as water pollution biomonitors, especially for purposes of identifying heavy metals, as the standard chemical analysis methods do not provide information about the presence and accumulation of these metals in water.[3] Furthermore, the concentrations of me-

tals in water are often below the instrument detection limit, making aquatic organisms an even more attractive method for their determination.[3]

As marine organisms absorb and accumulate matter from their habitat, they serve as excellent heavy metal water pollution bio-indicators.[4,5] In addition to heavy metals, marine organisms serve as bio-indicators for metals and compounds otherwise difficult to identify and quantify.[6]

Not all marine organisms are suitable as water pollution bio-indicators. The criteria required for an acceptable bio-indicator are that it must be able to tolerate large concentrations of pollutants and accumulate them in addition to being able to withstand changes in temperature and salinity. It should be representative of a location, *i.e.*, static and easy to identify, sample and handle. It should have a long enough life cycle to ensure sampling over specified and extended time frames, in addition to having a sufficient amount of tissue required for chemical analysis.[5,6] Of marine organisms generally, mussels and benthic fish are selected as suitable indicator species of coastal pollution, as they give complementary information on the bio-availability of chemicals in the water column and sediments, respectively. Bioaccumulation patterns of the different pollutants vary substantially among species. Habitat, season and food chain play key roles in the bioaccumulation process. Filter feeder organisms accumulate most of the pollutants at levels higher than those found in the water column; hence, they permit the quality of coastal environments to be assessed. Being sedentary and easy to sample, the blue mussel *Mytilus galloprovincialis* fulfills most of the above-mentioned criteria,[7] thus it was chosen to serve as the bio-indicator of heavy metal water pollution in the Boka Kotorska Bay.

The goal of this work was to determine levels of heavy metals and other elements in the marine environment of the Boka Kotorska Bay using the mussel *M. galloprovincialis* as a bio-indicator and to compare the obtained data with other regional data. The aim was to establish the environmental quality of the coastal waters in the Boka Kotorska Bay.

EXPERIMENTAL

Sampling, storage and sample preparation

Mytilus galloprovincialis was sampled from seven different locations in the fall of 2007: Krašići, Kukuljina, Tivat, Opatovo, Sv. Stasija, Perast and Herceg Novi as indicated in Fig. 1. The seven sampling sites are spread throughout the entire Boka Kotorska Bay and are in close proximity to large towns, ports and industries of the Bay.

Mussels, of similar shell lengths, from each sampling site were sampled. Sampling was performed using a stainless steel blade. The sampled mussels were placed in plastic bags together with sea water and so transported to the laboratory. The mussels were rinsed additionally with distillated water and the soft tissue separated from the shells. After that, the mussel soft tissue was rinsed with de-ionized water, whereupon it was subjected to lyophilization – freeze drying (Christ, Alpha 2-4 LD plus, Germany) under vacuum and at a temperature of –40 °C for 48 h to remove any remaining water. Dried samples of 25–30 mussels

from each station were pulverized and homogenized using a mill. The application of different methods to analyze the metal concentrations in the mussels required the preparation of both liquid and solid samples.

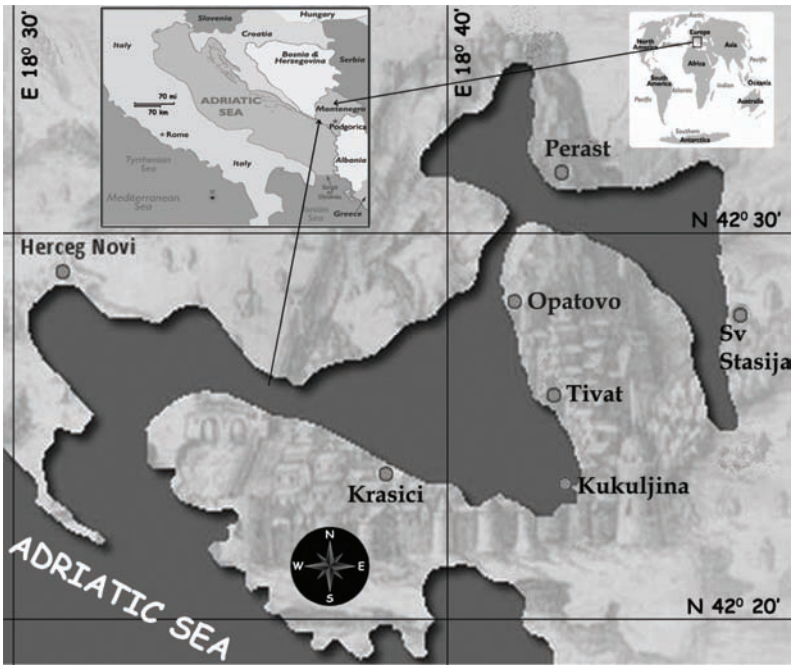

Fig. 1. Sampling sites of *Mytilus galloprovincialis* in the Boka Kotorska Bay, Montenegro, southeastern Adriatic Sea.

Solid samples for Energy dispersive X-ray tluorescence (ED-XRF) analyses were prepared as follows: the dried material (post-lyophilization) was pulverized in a vibration mill in the presence of paraffin wax. The added wax allowed for homogenization of the sample and served as a binding material for making pellets (whilst not interfering with the analysis itself). The pellets (d = 40 mm) were made by pressing 5 g of material from the mill in a mold of the desired shape under high pressure.

Liquid samples for Atomic absorption spectrometry (AAS) analyses were prepared as follows: about 0.5 g of dried mussel tissue was digested under high pressure with a mixture containing 7 ml HNO_3 (65 % Merck, Suprapur) and 2 ml H_2O_2 (30 % Merck, Suprapur) in a high microwave digestion system (CEM Corporation, MDS-2100) for 30 min, diluted to 25 ml with ultrapure water and stored in polyethylene bottles until analysis. A blank digest was performed in the same manner.

Chemical analysis

The manganese (Mn), cobalt (Co), nickel (Ni), copper (Cu), cadmium (Cd) and vanadium (V) concentrations in the mussel samples were determined using flame atomic absorption spectrometry (Perkin–Elmer, AAnalyst 200) with an air–acetylene flame. Analyses of lead (Pb) and chromium (Cr) were performed using a graphite furnace AAS (Perkin–Elmer, 4100ZL, with Zeeman background correction). Hydride generation and cold vapor techniques

were used for the analyses of mercury (Hg) and tin (Sn) (PerkinElmer, AAnalyst 200). The Iron (Fe), zinc (Zn), silicon (Si), phosphorus (P), sulfur (S), chlorides (Cl), potassium (K) and calcium (Ca) concentrations were determined using the energy dispersive X-ray fluorescence method (Oxford, ED 2000).

RESULTS AND DISCUSSION

For the first time, the concentrations of the investigated elements were measured in the mussel *Mytilus galloprovincialis* at the coastal area of the south-eastern Adriatic Sea, Montenegro, using the mussel as a bio-indicator.

The information related to the collected samples and the physical parameters of the sea water at the seven investigated sites are given in Table I. The Perast site had the lowest water temperature (21.3 °C) and salinity (30.28 ‰), but the pH value was in the range of the all the other measured pH values, 8.16.

TABLE I. Information related to the collected sample

Location	Coordinate	Depth m	Shell length cm	Water temperature °C	Water oxygen mg l^{-1}	Water conductivity mS cm^{-1}	Water pH
Krasici	42°23’11”N 18°42’10”E	0.5	6.7	26.0	3.08	52.0	8.12
Kukuljina	42°25’34”N 18°42’17”E	0.5	6.5	26.5	2.86	52.9	8.22
Tivat	42°25’45”N 18°41’46”E	0.5	6.3	26.7	3.12	52.3	8.15
Opatovo	42°26’58”N 18°41’09”E	0.5	6.8	26.2	3.20	53.1	8.16
Sv. Stasija	42°28’13”N 18°45’50”E	0.5	7.2	26.5	3.05	47.3	8.08
Perast	42°29’09”N 18°41’55”E	0.5	6.1	21.3	2.94	45.2	8.16
H. Novi	42°26’58”N 18°32’08”E	0.5	7.2	21.7	2.70	53.8	8.19

Determined mean concentrations (mg kg^{-1} dry weight) of Cr, Mn, Fe, Co, Ni, Cu, Zn, Cd, Hg, Pb, Sn, V, Si, P, S, Cl, K and Ca using *M. galloprovincialis* as a bio-indicator of the pollution of the Boka Kotorska Bay are given in Table II. The values of the *MCL*s[8] (metal contamination levels) for Cr, Ni, Cu, Cd, Pb, Hg and Zn are shown in Table II. These *MCL*s could denote contamination. Recommended values of *MCL*s for the remaining elements do not exist in the literature.

The mean concentrations of investigated elements in the soft tissue of mussels from the Boka Kotorska Bay were: 0.67 (Hg), 0.77 (V), 1.64 (Cr), 1.76 (Sn), 2.33 (Cd), 8.00 (Pb), 8.86 (Ni), 9.44 (Cu), 12.60 (Co), 17.69 (Mn), 293 (Zn), 303 (Fe), 3,057 (Ca), 5,714 (P), 7,657 (K), 26,543 (Si), 11,629 (S) and 32,243 (Cl) in mg kg^{-1} dry weight.

TABLE II. Concentration of the elements found in the soft tissues of *M. galloprovincialis* (mg kg^{-1} dry weight)

Element	Location							
	Krašići	Kukuljina	Tivat	Opatovo	Sv. Stasija	Perast	H. Novi	*MCLs*[8]
				AAS				
Cr	1.30	2.20	2.40	1.75	1.62	0.74	1.45	2.5
Mn	10.89	18.88	28.68	23.96	12.71	13.07	15.61	–
Co	11.71	13.17	14.63	13.25	11.90	11.71	11.85	–
Ni	8.75	11.00	10.55	8.90	7.20	7.80	7.85	3.9
Cu	13.22	7.21	15.62	10.22	6.61	7.81	5.41	10
Cd	2.34	1.59	2.66	1.65	1.56	3.91	2.61	3.7
Pb	8.00	5.50	14.50	9.00	6.50	7.00	5.50	3.2
V	0.60	0.60	0.90	0.50	0.10	2.30	0.40	–
Hg	0.65	0.32	0.42	1.61	0.37	0.90	0.45	0.23
Sn	1.80	1.70	2.60	1.50	1.40	1.80	1.50	–
				ED-XRF				
Fe	250	680	410	250	150	180	200	–
Zn	310	200	570	280	190	220	280	200
K	7,600	8,100	8,700	7,800	7,300	7,000	7,100	–
Ca	2,800	2,700	5,900	2,200	1,400	1,600	4,800	–
Si	26,200	27,700	26,900	26,200	26,300	26,100	26,400	–
P	5,700	5,400	6,500	5,400	6,300	5,600	5,100	–
S	12,500	11,700	14,000	11,800	10,600	9,800	11,000	–
Cl	37,000	32,700	43,400	37,300	22,100	22,000	31,200	–

In relation to the values of *MCL*s for the mean concentrations of Ni, Cu, Cr, Cd, Pb, Hg and Zn (Table II), only the measured Cr levels in investigated mussels from the Boka Kotorska Bay were lower than *MCL* for this element. The higher levels of the other measured elements than the respective *MCL* value in the investigated mussel can also be caused by the bay mineralogy.

The highest concentrations of Cr, Mn, Co, Cu, Zn, Pb, K, Ca, P, S, Cl and Sn were detected in mussels at the Tivat location, as expected. This is the site with most anthropogenic activities, known as an agricultural area with military port, shipyard and airport nearby. Mussels sampled from the Kukuljina site contained the highest levels of Fe, Ni and Si; but the highest Hg level was found at the Opatovo site, while the highest levels of Cd and V were found at the Perast site.

Nickel (Ni) levels determined in *M. galloprovincialis* varied between 7.20––11.00 mg kg^{-1} for all sampling sites; the maximum level was in mussels from the Kukuljina site (11.00 mg kg^{-1}) and the minimum value was measured at Sv. Stasija (7.20 mg kg^{-1}). In comparison to other literature reports on the Ni content in mussels,[9–11] its content in mussels from the Boka Kotorska Bay may be considered as elevated. It is suspected that the elevated levels of Ni are primarily the consequence of human activities in the Bay.

The concentration levels of Mn and Cr in the mussels at the seven sites ranged between 10.89–28.68 and 0.74–2.40 mg kg^{-1}, respectively. The maximum concentrations of manganese and chromium were recorded at the Tivat site. An analysis of the metal content of the Boka Bay sediments prior to its Industrialization period indicated that the sea bed of the Bay is rich in Mn and Cr,[12] and that their presence in the mussel soft tissue cannot be entirely anthropogenic.

The Cu concentrations ranged from 5.41 to 15.62 mg kg^{-1}. The maximum Cu level was found in the Tivat and the minimum in the Herceg Novi mussels. Copper is an essential trace element required by all forms of life. In comparison to other literature reports on the Cu content in mussels, Table III, the Cu levels found in the present study were lower than the literature data.

TABLE III. A comparison of the metal and non-metal concentrations in *M. galloprovincialis* found for this study with literature data from other sea world regions (mg kg^{-1} dry weight)

Element	Croatia[27]	Italy[10]	Slovenia[28]	Turkey[9]	Morocco[29]	Spain[30]	Spain[31]	This study
Cu	3.7–11.1	17.9–156	6.5–49	90–260	4.1–43.1	4.42–9.65	6.8–29.9	5.41–15.62
Si	–	–	–	–	–	–	–	26,100–27,700
Cd		0.6–1.0	0.44–1.09	2–4	2.12–34.71	0.36–2.84	0.2–0.77	1.56–3.91
Cr	1–2.9	–	2.7–10.3	1–3	1.9–28.9	–	2.2–45.7	0.74–2.40
P	–	–	–	–	–	–	–	5,100–6,500
Fe	53.4–719	45.1–754		1,150–4,030	–	–	174–715	150–680
Ni	0.8–5	1.3–7.6	2.8–8.0	1–6	11.7–31.7	–	0.85–19	7.20–11.00
S	–	–	–	–	–	–	–	9,800–14,000
Co	–	–	0.31–2.09	—	–	–	0.45–2.69	11.71–14.63
Pb	2–7	2.0–9.0	0.79–11.5	5–21	0.1–26.45	0.52–8.22	0.3–6.1	5.50–14.50
Sn	–	0.6–3.9	–	–	–	–	6.7–21	1.40–2.60
V	–	–	–	–	–	–	–	0.10–2.30
K	–	–	–	4,230–7,960	–	–	–	7,000–8,700
Ca	–	–	–	6,960–20,400	–	–	–	1,400–5,900
Cl	–	–	–	–	–	–	–	22,000–43,400
Zn	59.1–273	60.9–189	73–249	180–630	107.4–365.7	134–462	85–447	190–570
Hg	–	<0.5	–	–	0.01–2.31	0.08–0.88	0.1–0.63	0.32–1.61
Mn	2–13	72.9–83.1	9.6–29.8	41–59	7.2–27.5	–	4.3–15.8	10.89–28.68

Cobalt is a relatively rare element, present at 0.0025% w/v in the Earth's crust and 4×10^{-8} % (w/v) in seawater. It is usually found in Ni, Ag, Pb, Cu and Fe ores.[13] The cobalt levels found in the mussel soft tissue were in the range 11.71–14.63 mg kg^{-1}; the maximum found level was at the Tivat (14.63 mg kg^{-1}) and the minimum at the Perast and Krasici sampling sites (11.71 mg kg^{-1}). The relatively high levels of Co in the Boka Bay samples may be explained by its use as an alloying ingredient together with nickel, chromium, molybdenum and other elements. It is an important constituent of magnets and batteries, and is also used as a pigment for glass, ceramics and paints. Additionally, it can be used as a paint drier and as a catalyst in the petroleum and chemical industries. Many fertilizers are enriched with cobalt in order to amend agricultural soils that are cobalt-deficient. It can be claimed that the Co pollution of the Boka Bay is of anthropogenic nature, especially in the Tivat area, known as an agricultural area.

The non-essential metals Cd, Pb and Hg are toxic at relatively low concentrations.[14] Human activities and industrial processes lead to an increase of these metals in the environment and changes in their levels are good indicators of increased anthropogenic impact.[14,15]

Mussels can accumulate cadmium in their tissues at levels up to 100,000 times higher than the levels observed in the water in which they live.[14] Cd concentrations in *M. galloprovincialis* from this coastal area were in the range of 1.56–3.91 mg kg^{-1}. Cd occurs naturally in ores together with Zn, Cu and Pb. Cd compounds are used as stabilizers in PVC products, pigments and in nickel–cadmium batteries. The cadmium sources in the investigated mussel samples most likely originate from pigments in paints for ships and phosphate fertilizers, since the highest Cd concentrations were found at locations with a port (Perast, Tivat and H. Novi) and at the Tivat location, known for its high usage of phosphate fertilizers.

Elevated levels of lead were detected in port towns with a high volume of marine and inland traffic. Pb levels ranged from 5.50 to 14.50 mg kg^{-1}, the maximum level having been found in Tivat. Lead is known to accumulate in the environment and is dispersed due to anthropogenic activities. Hence, it comes as no surprise that highest Pb concentrations were found in mussels sampled from the Tivat location, the site with most anthropogenic activities.

Mercury is the most toxic of the heavy metals, especially in its organic form. It dramatically impedes bivalve growth. A significant amount of mercury introduced into coastal waters precipitates due to the very low solubility of its resulting compounds, and it is retained in sediments of the coastal area. Due to biological activity, inorganic mercury may be converted to methyl mercury and released into the water, where it becomes available to marine organisms.[16] Marine organisms accumulate mercury both by ingestion of contaminated food and by direct adsorption from the water.[16] Levels of Hg for the seven sites were in the

0.32–1.61 mg kg^{-1} range. The maximum Hg level was found at the Opatovo and the minimum value at the Kukuljina site. Such high levels of mercury can indeed be somewhat ascribed to anthropogenic factors, but is important to emphasize that the Mediterranean is extremely rich in Hg; its basin containing about 65 % of the total world Hg mineral resources.[17,18] Hence, naturally occurring mercury levels are significant and might in the case of the Boka Bay outweigh anthropogenic factors.

The maximum concentration of tin was found at the Tivat site (2.60 mg kg^{-1}), while the minimum value was found at the Sv. Stasija site (1.40 mg kg^{-1}). Tin may be released into the environment from natural (component of many soils) and anthropogenic (agricultural activities, gases, dusts and fumes containing tin may be released from smelting and refining processes, industrial uses of tin, waste incineration, and burning of fossil fuels) sources. There is no evidence that tin is essential for organisms and, in general, tin-containing compounds are mainly released into the environment from anthropogenic sources. Most of the tin found in a marine environment comes from boat paints containing tributyltin – TBT,[19] which could explain the high Sn content in the mussels sampled at the Tivat location.

Vanadium concentrations were in the 0.10–2.30 mg kg^{-1} range. The maximum value of V was found in Perast (2.30 mg kg^{-1}), while the minimum value was measured at the Sv. Stasija site (0.10 mg kg^{-1}). As there is no naturally occurring free vanadium, this metal occurs in seawater either by its absorption from the atmosphere or by dissolution of sediment as it is found to be a component of some minerals. Industrially, vanadium is mostly used as an additive in the steel industry and in petrochemical products. It is an essential element for marine organisms and its concentration found in mussels was a thousand times higher than in seawater.[20]

Elements such as Fe, Zn, K, Ca, Si, P, S and Cl were determined using the ED–XRF technique for two reasons: all of the elements analyzed were present in very high concentrations, and P, S and Cl are non-metals which cannot be determined by AAS.

The iron concentrations were in the 150–680 mg kg^{-1} range. The maximum concentration of Fe was found at Kukuljina (680 mg kg^{-1}) while the minimum value was found at Sv. Stasija (150 mg kg^{-1}). Iron is an essential trace element required by all forms of life. In comparison with literature data, it is clear that the measured Fe concentrations were lower than in other examined areas, Table III, indicating that there is no major pollution caused by this element in Boka Kotorska Bay.

The concentrations of zinc ranged from 190–570 mg kg^{-1}. The maximum value of Zn was found at Tivat (570 mg kg^{-1}), while the minimum value was found at Sv. Stasija (190 mg kg^{-1}). Zinc is an essential element and its *in vivo*

levels are regulated by most organisms.[21] Zinc is not biomagnified. The absorption of zinc by aquatic organisms tends to be from water rather than food.[22] Only dissolved zinc tends to be bioavailable and the bioavailability depends on the physical and chemical characteristics of the marine environment, such as: pH, dissolved organics, water hardness, competing ions, soluble ligands and biological processes.[23] The increased concentrations of Zn in the investigated samples compared to other regions, Table III, could be explained by fact that Zn is used as a dietary supplement, as well as in the chemical industry and all industries located along the coastal area of the Bay.[23]

The concentrations of Si, K, P and S do not vary much amongst the investigated locations, which may indicate common local inputs and similar dispersion processes in the study area, with the exception of Ca and Cl. The concentrations of these two elements are also main factors of seawater salinity, which is obviously related to Perast and St. Stasija, Tables I and II. Simultaneously it can be noticed that the concentrations of all the investigated elements in mussels were generally lower from the sites Sv. Stasija and Perast, except some elements such as Cr (Sv. Stasija) and V (Perast). It could be concluded that salinity has high impact on metal accumulation in mussels. Some elements (Cu, Cd, Pb, V and Hg) were present at lower levels in the mussel from H. Novi (salinity at H. Novi was higher compared to Perast) than in mussel from Perast, but it could be explained by the mixing of bay water with open-sea water at the mouth of the Bay.

The silicon concentrations were in the range 26,100–27,700 mg kg^{-1}. Silicon constitutes 25.7 % of the Earth's crust by weight and is the second most abundant element. It is found largely in the form of silicon oxides such as sand (silica), quartz, rock crystal, amethyst, jasper and opal. Si is the main constituent of clay,[20] and clay is being the main constituent of the Bay bottom. As in the case of Mn and Cr, it can be concluded that Si is naturally present in the seawater and mussels of the Bay, explaining its similar and increased level.

The maximum value of P was found at Tivat (6,500 mg kg^{-1}), while the minimum value was found in H. Novi (5,100 mg kg^{-1}). Phosphorus is a natural and anthropogenic component of an aquatic environment.[24] The most important anthropogenic inputs of this element in the Boka Kotorska Bay ecosystem are through the use of fertilizers and detergents.

Chlorides are the most common component of sea water, together with Na, Mg and SO_4, it makes up almost 97 % of the concentrations of all ions.[25] After them, K and Ca are the most common and it is not surprising that the largest concentrations of these three elements, Cl, K and Ca, were found in the samples: Cl (22,000–43,400 mg kg^{-1}), K (7,000–8,700 mg kg^{-1}) and Ca (1,400–5,900 mg kg^{-1}). Anthropogenic input of these three elements is possible because they are used in many processes and products. Chlorine is used in the production of drinking water, in the production of paper products, textiles, petroleum products, me-

dicines, insecticides, solvents, paints and plastics; K is used in the preparation of potassium phosphates for liquid detergents and fertilizers; while Ca is commonly used in cement factories.[20]

The concentrations of sulfur (S) ranged from 9,800–14,000 mg kg^{-1}. Sulfur is a natural and anthropogenic component of an aquatic environment. Natural sulfur is primarily derived from the dissolution of dead marine organisms, plants and animals. The formation of sulfur intermediates in marine sediments principally occurs through the oxidation of sulfide produced during bacterial sulfate reduction.[26] The most important anthropogenic input of this element to a marine ecosystem is through the use of fuel oil and its presence in fungicides.[20] This was confirmed by the highest concentration of S obtained for mussels sampled at Tivat (14,000 mg kg^{-1}), already mentioned as location with the greatest number of possible pollution sources.

Literature data and data from this study are given in Table III to compare element concentration levels in the *M. galloprovincialis*.

The sampled mussels are compared with the available literature data of other areas of the Adriatic Sea, (Italy, Croatia and Slovenia),[10,27,28] and of other Mediterranean areas.[9,29–31] From Table III, it can be concluded that the heavy metal concentrations of Cd, Pb, Ni, Hg, Co and Zn are generally higher in the Boka Kotorska Bay than in mussels from other parts of the Adriatic (Italy, Croatia and Slovenia). However, this is not case when the levels of these metal are compared with most industrialized and developed areas in the Mediterranean area (Spain, Turkey and Morocco)[9,29–31] In this case, the concentrations of Cd, Pb, Hg and Ni in the mussels from the bay are generally lower, Table III.

Of all seven investigated locations, the mussel sampled at the Tivat site had the highest levels of heavy and other metals, suggesting that the highest seawater pollution is at this site in Boka Kotorska Bay. The total quantity of wastewater delivered into the sea at the Tivat location is second, compared to Herceg Novi, indicating that other pollution sources play a role in the case of Tivat: the proximity of the airport, a military harbor, shipyards, oil tankers and a high usage of agricultural fertilizers in the hinterland of Tivat. Nevertheless, the hydrological positions of Tivat and Herceg Novi in the Bay cannot be disregarded: Herceg Novi is located nearer to the entrance of the bay, experiencing higher seawater flux and water exchange with the open sea in comparison to Tivat.

CONCLUSIONS

More intensive mussel cultivation in the Boka Kotorska Bay, their increasing consumption, and the possibility of their export to other countries imposes the need for regular monitoring of seasonal and annual trends of metal concentrations in the mussels of the Bay, to assess the environmental quality of this marine

ecosystem as the determined concentrations of Ni, Cu, Cd, Pb, Hg and Zn were higher than the corresponding *MCL* value.

It was found that of all of the investigated locations in the Boka Kotorska Bay, the mussels sampled at the Tivat location contained the highest levels of toxic metals, primarily due to anthropogenic activities.

The results of this investigation, *i.e.*, the determination of the concentrations of metal and non-metal elements in mussels, indicate that the degree of pollution of the Boka Kotorska Bay, which is influenced by anthropogenic activities, is comparable to other marine environments. A comparison of the concentrations of the investigated elements found in mussels from the Boka Kotorska Bay to the other areas of the Adriatic Sea show that the levels Zn and Co, and also of the heavy metals Ni, Pb, Cd and Hg in the Boka Kotorska Bay are generally higher. Additionally, it was found that the concentrations of a few very toxic elements, Cd, Pb, Hg and Ni, were generally lower compared to those determined in mussels sampled from other Mediterranean regions.

Mytilus galloprovincialis as a bio-indicator of metal pollution has and can continue to provide information about water quality not only in the Boka Kotorska Bay, but also along the whole coast of Montenegro on the southeastern Adriatic Sea.

Acknowledgement. This research was financed by the Ministry of Education and Science of the Republic of Serbia, Contract No. III 43009 and EAR, Contract No. 04SER02/05/007.

И З В О Д

ДАГЊЕ КАО БИОИНДИКАТОР КВАЛИТЕТА МОРСКЕ ВОДЕ ПРИОБАЉА БОКОКОТОРСКОГ ЗАЛИВА (ЦРНА ГОРА)

МИХАЈЛО ЈОВИЋ[1], АНА СТАНКОВИЋ[1], ЛАТИНКА СЛАВКОВИЋ-БЕСКОСКИ[2], ИЛИЈА ТОМИЋ[3], SANDRO DEGETTO[4] и СЛАВКА СТАНКОВИЋ[1]

[1]Технолошко–металуршки факултет, Универзитет у Београду, Београд, [2]Институт за нуклеарне науке Винча, Универзитет у Београду, Београд, [3]Институт за хемију, технологију и металургију, Универзитет у Београду, Београд и [4]ICIS-CNR, Envinronmental lab, Padova, Italy

Медитеранска плава шкољка *Mytilus galloprovincialis* (дагња) је коришћена као индикатор нивоа загађења Бококоторског залива, Црногорско приморје – југоисточни Јадран. Све већа урбанизација и индустријализација, лош канализациони систем, све интензивнији поморски и копнени саобраћај, слабо струјање и мала циркулација воде, доводе до све већег загађења овог залива. Како су тешки метали веома токсични и не подлежу лако биодеградацији, резултати овог истраживања нуде вредне информације о загађењу металима и неметалима приобаља Бококоторског залива коришћењем дагњи. Концентрације елемената у дагњама узоркованих у току јесени 2007 године одређиване су применом атомске апсорпционе спектоскопије (AAS) за Cr, Mn, Co, Ni, Cu, Cd, Hg, Pb, Sn i V, а енергетски дисперзивна рендгенска флуоресцентна анализа (ED-XRF) за одређивање Fe, Zn, Si, P, S, Cl, K i Ca. ED-XRF је коришћена да би се одредио ниво неметала и елемената присутних у високим концентрацијама. Поредећи резултате овог истраживања са већ публикованим

радовима из других региона, дагње узорковане у Бококоторском заливу су показале умерен ниво загађења.

(Примљено 7., ревидирано 27. Октобра 2010)

REFERENCES

1. Government of Montenegro, *Spatial Plan of Montenegro Until 2020*, http://www.gov.me/files/1216637502.pdf (last accessed: September, 2010)
2. A. Ikem, N. O. Egiebor, *J. Food Compos. Anal.* **18** (2005) 771
3. J. Morillo, J. Usero, I. Gracia, *Chemosphere* **58** (2005) 1421
4. F. Regoli, Arch. Environ. Contam. Toxicol. **34** (1998) 48
5. R. T. Angelo, M. S. Cringan, D. L. Chamberlain, A. J. Stahl, S. G. Haslouer, C. A. Goodrich, *Sci. Total Environ.* **384** (2007) 467
6. M. Roméo, C. Frasila, M. G. Barelli, G. Damiens, D. Micu, G. Mustata, *Water Res.* **39** (2005) 596
7. U. Sunlu, *Environ. Monit. Assess.* **114** (2006) 273
8. A.Y. Cantillo, *Mar. Pollut. Bull.* **36** (1998) 712
9. U. Çevik, N. Damla, A. I. Kobya, V. N. Bulut, C. Duran, G. Dalgic, R. Bozaci, *J. Hazard. Mater.* **160** (2008) 396
10. D. Desideri, M. A. Meli, C. Roselli, L. Feduzi, *J. Radioanal. Nucl. Chem.* **279** (2009) 591
11. P. Szefer, B. S. Kim, C. K. Kim, E. H. Kim, C. B. Lee, *Environ. Pollut.* **129** (2004) 209
12. S. Degetto, C. Cantaluppi, D. Desideri, M. Schinitu, S. Stankovic, Z. Kljajic, in *Proceeding of 7th Int. Conf. Methods and Applications of Radioanalytical Chemistry – MARC VII*, 2006, Kailua-Kona, Hawaii, USA, 2006, p. 83
13. J. Nechev, K. Stefanov, D. Nedelcheva, S. Popov, *Comp. Biochem. Physiol. B* **146** (2007) 568
14. S. T. Culha, M. Y. Celik, M. Culha, I. Karayucel, A. Gundogdu, *J. Anim. Vet. Adv.* **7** (2008) 1618
15. F. X. Han, A. Banin, Y. Su, D. L. Monts, M. J. Plodinec, W. L. Kingery, G. E. Triplett, *Naturwissenschaften* **89** (2002) 497
16. N. Odzak, T. Zvonaric, Z. Kljakovic Gaspic, M. Horvat, A. Baric, *Sci. Total Environ.* **261** (2000) 61
17. S. R. Aston, S. W. Fowler, *Sci. Total Environ.* **43** (1985) 13
18. R. Bargagli, R. Ferrara, B. E. Maserti, *Sci. Total Environ.* **72** (1988) 123
19. International Programme on Chemical Safety INCHEM, *Tin and inorganic tin compounds*, http://www.inchem.org/documents/cicads/cicads/cicad65.htm (last accessed: September, 2010)
20. *Web Elements: the periodic table on the web*, http://www.webelements.com (last accessed: September, 2010)
21. D. G. Heijerick, C. R. Janssen, C. Karlen, I. O. Wallinder, C. Leygraf, *Chemosphere* **47** (2002) 1073
22. L. T. Sun, S. S. Jeng, *Zool. Stud.* **37** (1998) 184
23. B. Simon-Hertich, A. Wibbertmann, D. Wagner, L. Tomaska, H. Malcolm, *Environ. Health Criteria* **221** (2000) 1
24. Y. Liu, G. Villalba, R. U. Ayres, H. Schroder, *J. Ind. Ecol.* **12** (2008) 229
25. F. Culkin, in *Chemical Oceanography*, Vol. I, J. P. Riley, G. Skirrow, Eds., Academic Press, London, UK, 1965, p. 121

26. B. B. Jørgensen, *Mar. Biol.* **41** (1977) 7
27. V. Orescanin, I. Lovrencic, L. Mikelic, D. Barisic, Z. Matasin, S. Lulic, D. Pezelj, *Nucl. Instrum. Methods B* **245** (2006) 495
28. J. Scancar, T. Zuliani, T. Turk, R. Milacic, *Environ. Monit. Assess.* **127** (2007) 271
29. M. Maanan, *Environ. Toxicol.* **22** (2007) 525
30. V. Besada, J. Fumega, A. Vaamonde, *Sci. Total Environ.* **288** (2002) 239
31. R. Beiras, J. Bellas, N. Fernandez, J. I. Lorenzo, A. Cobelo-Garcia, *Mar. Environ. Res.* **56** (2003) 531.